Eddy-Mean Flow Interactions
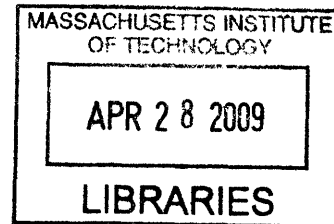# in Western Boundary Current Jets

by

Stephanie N. Waterman

Submitted in partial fulfillment of the
requirements for the degree of

Doctor of Philosophy

at the

MASSACHUSETTS INSTITUTE OF TECHNOLOGY ARCHIVES

and the

WOODS HOLE OCEANOGRAPHIC INSTITUTION

February 2009

Author . . . . :
....
Joint Program in Physical Oceanography
Massachusetts Institute of Technology
Woods Hole Oceanographic Institution
January 20, 2009

Certified by . .
....
Steven R. Jayne
Associate Scientist
Thesis Supervisor

Certified by . .
....
Nelson G. Hogg
Scientist Emeritus
Thesis Supervisor

Accepted by
....
Raffaele Ferrari
Chair, Joint Committee for Physical Oceanography
Massachusetts Institute of Technology
Woods Hole Oceanographic Institution

Eddy-Mean Flow Interactions
in Western Boundary Current Jets

by

Stephanie N. Waterman

Abstract

This thesis examines the nature of eddy-mean flow interactions in western boundary
current jets and recirculation gyre dynamics from both theoretical and observational
perspectives. It includes theoretical studies of eddy-mean flow interactions in idealized
configurations relevant to western boundary current jet systems, namely (i) a study
of the mechanism by which eddies generated from a localized forcing drive mean
recirculation gyres through the process of nonlinear rectification; and (ii) a study of
the role of eddies in the downstream evolution of a baroclinic jet subject to mixed
instabilities. It also includes an observational analysis to characterize eddy-mean flow
interactions in the Kuroshio Extension using data from the downstream location of
maximum eddy kinetic energy in the jet.

New insights are presented into a rectification mechanism by which eddies drive the
recirculation gyres observed in western boundary current systems. Via this mecha-
nism, eddies drive the recirculations by an up-gradient eddy potential vorticity flux
inside a localized region of eddy activity. The effectiveness of the process depends
on the properties of the energy radiation from the region, which in turn depends
on the population of waves excited. In the zonally-evolving western boundary cur-
rent jet, eddies also act to stabilize the unstable jet through down-gradient potential
vorticity fluxes. In this configuration, the role of eddies depends critically on their
downstream location relative to where the unstable time-mean jet first becomes sta-
bilized by the eddy activity. The zonal advection of eddy activity from upstream
of this location is fundamental to the mechanism permitting the eddies to drive the
mean flows. Observational results are presented that provide the first clear evidence
of a northern recirculation gyre in the Kuroshio Extension, as well as support for the
hypothesis that the recirculations are, at least partially, eddy-driven. Support for
the idealized studies' relevance to the oceanic regime is provided both by indications
that various model simplifications are appropriate to the observed system, as well as
by demonstrated consistencies between model predictions and observational results
in the downstream development of time-mean and eddy properties.

Thesis Supervisor: Steven R. Jayne
Title: Associate Scientist

Thesis Supervisor: Nelson G. Hogg
Title: Scientist Emeritus

Acknowledgments

Carlos Moffatt, Katie Silverthore, Beatriz Pena-Molino, Rachel Horwiz and Holly Dail in particular. Tribute must also be paid to the "aesthetics committee" of 1417 for all of their advice in response to my frequent consultation. I thank the students of 12.800 in the fall of 2007 for giving me one of my most rewarding experiences in graduate school.

I thank all of my friends from WHOI and MIT who have given me so much happiness during my years here. It is because of you I am most sad to say goodbye. I thank my parents for their unconditional and unending support through what was a longer-than-average career as a student. Steve, I thank-you for everything you did to make me happy in this chapter, and for all of the happiness the anticipation of the next chapter has given me.

Finally I thank Barry Ruddick, for telling me I should be an oceanographer.

Contents

3   Eddy-Mean Flow Interactions in the Downstream Evolution of an Idealized Western Boundary Current Jet   73

Chapter 1

Introduction

This thesis is an effort to extend our understanding of the role of eddy variability and eddy-mean flow interactions in the dynamics of western boundary current (WBC) jets and their recirculation gyre systems. It was motivated by the Kuroshio Extension System Study (KESS), which provides an unprecedented suite of observations uniquely suited to study the jet, its eddy variability, and their interactions. As such, there existed a unique opportunity to understand how our theoretical ideas about eddy-mean flow interactions in various idealized configurations apply to the actual oceanic system.

1.1 Background and Motivation

The Gulf Stream (GS) and the Kuroshio Extension (KE) current systems are among the most energetic current systems in the world ocean and are dominant features of the North Atlantic and North Pacific Oceans circulations respectively. After separating from their respective coasts at Cape Hatteras and the Boso peninsula, these WBCs turn eastwards, and flow into the deep ocean. Here they are no longer constrained by topography, and they become free, inertial, unstable jets, characterized by large amplitude meanders and pinched-off eddies (Figure 1-1). These WBC jets are of fundamental importance to the dynamics of steady basin-scale circulations, as regions of enhanced exchange of potential vorticity (PV) and energy, and by acting to restore
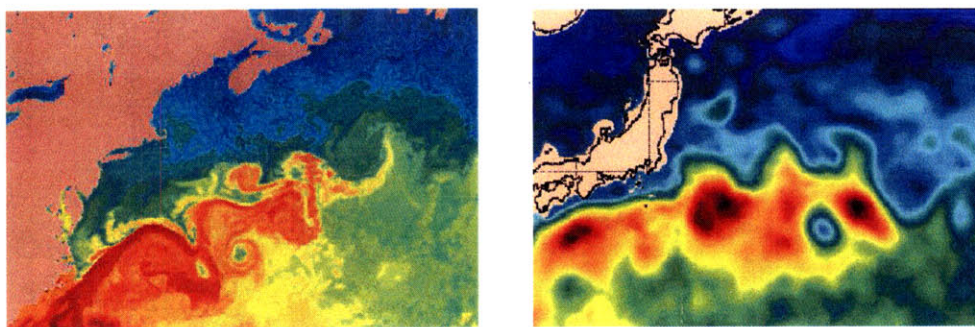
Figure 1-1: Instantaneous snapshots of the GS (*left*) and KE jets (*right*) (from Sea-WiFS satellite measure of ocean color (*left*) and sea surface height in the 1/16° global Naval Research Laboratory (NRL) Layered Ocean Model (NLOM) (*right*)).

global balances between forcing and dissipation. Understanding their dynamics is fundamental to improving our understanding of the ocean general circulation.

Observations of various types in all oceans indicate that eddy kinetic energy (EKE) is strongly (orders of magnitude) spatially inhomogeneous, reaching maxima in the vicinity of strong currents such as these WBC jets (Ducet and Le-Traon, 2001) (Figure 1-2). The GS and KE regions are prime examples of this, where the meandering of the streams results in an increase in the eddy kinetic and potential energies by orders of magnitude along the climatological mean path of the jet at all depths (Schmitz, 1984; Hogg, 1988; Bower and Hogg, 1992; Malanottte-Rizzoli, 1994). Given such high levels of eddy activity in these regions, our description of WBC jet dynamics clearly needs to include an understanding of the effects of this eddy variability.

An investigation into the role of eddy variability in WBC jet dynamics is important because eddies (defined for the remainder of this discussion as simply the deviation from an appropriately defined temporal mean) can play an important role in the dynamics of the system. Through their fluxes of momentum and vorticity, eddies can be important in determining the character of the mean flow, not only as a source of dissipation but also as a driving force through nonlinear eddy-eddy and eddy-mean flow interactions. In addition, eddy fluxes of active tracers such as temperature, salinity, momentum and PV can significantly influence the overall dynamics of the system. In WBC jet systems in particular, some examples of the anticipated effects
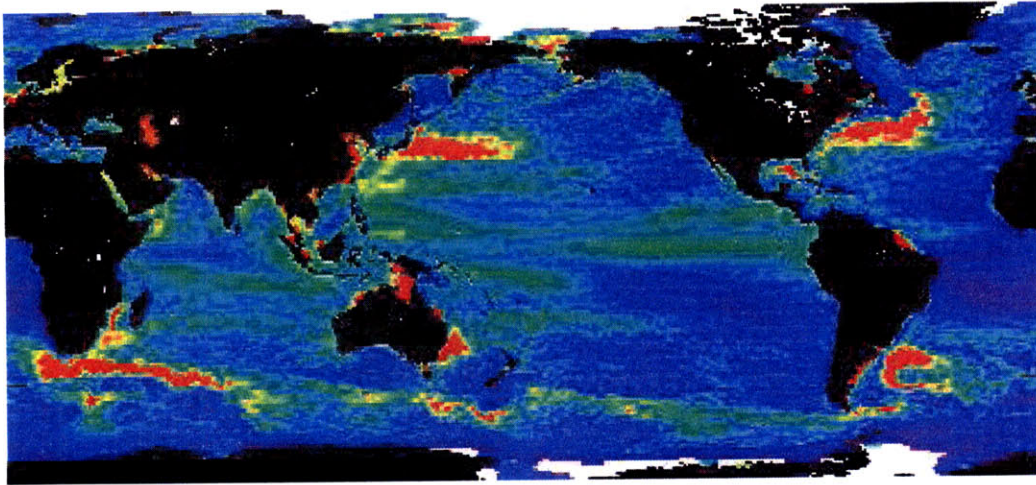
Figure 1-2: Ocean circulation variability (root mean square of variations in dynamic topography) derived from combined observations by the TOPEX/Poseidon, ERS-1 and ERS-2 satellites between October 1992 and November 1998 (from Centre National d'Etudes Spatiales (CNES)).

of eddy variability on system dynamics include:

1. Altering mean jet strength, structure and stability: It has been suggested that eddy variability may be playing a role in driving the mean jet, given that the observed mean circulation in these regions contains short meridional scales similar to the EKE distribution (Schmitz, 1980) and has a strength several times that expected from wind or buoyancy forcing. Analysis of *in situ* observations in the GS (Thompson, 1977, 1978; Dewar and Bane, 1989; Hogg, 1992) confirm this, suggesting that eddy variability is not only playing a role in altering the mean jet strength, but also its structure and stability properties, and how these characteristics evolve in time and downstream.

2. Driving recirculations through fluxes of potential vorticity: Eddies also play a potential role in driving recirculations, the phenomenon through which the down-stream transport of the separated jet is increased many-fold by flanking, weakly depth-dependent gyres (*e.g.* Richardson, 1985; Hogg, 1992; Schmitz and McCartney, 1993) (Figure 1-3). A number of dynamical explanations have been offered for the existence of these gyres. A consequence of eddy form drag resulting from baroclinic
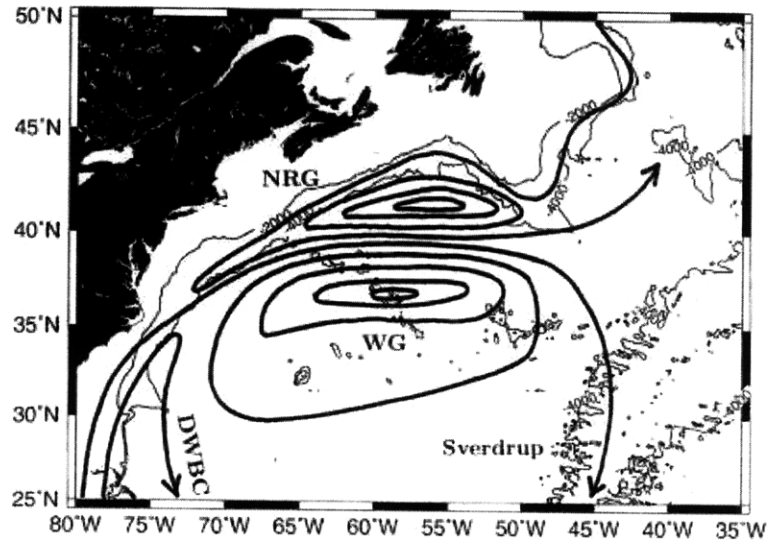
Figure 1-3: Scheme for the recirculation in the GS system that is consistent with transport observations made by current meters. Heavy lines are streamlines. To the north of the central jet is the northern recirculation gyre (NRG) carrying 40-60 Sv and to the south of the jet is the Worthington gyre (WG) also carrying 40-60 Sv (from Sheremet (2002); adapted from Hogg (1992)).

instability in the westward moving Sverdrup flow (Rhines and Holland, 1979) to more direct driving by eddies in the jet itself (*e.g.* Thompson, 1978; Haidvogel and Rhines, 1983; Spall, 1994; Jayne et al., 1996; Jayne and Hogg, 1999) are potential candidates.

3. Driving deep abyssal motions: In addition, eddy variability appears to be important in coupling the strong motions in these baroclinic jets to deep abyssal circulations. One of the primary (and unexpected) scientific results of the Synoptic Ocean Prediction Experiment (SYNOP) was the discovery of strong, transient, nearly depth-independent cyclones in the deep ocean that formed beneath the large amplitude GS meander troughs that routinely formed in the GS's path (Shay et al., 1995; Howden, 2000; Watts et al., 2001) (Figure 1-4). While strong velocities in the deep ocean near this location had been observed before (Luyten, 1977; Hogg, 1981), it was not until SYNOP that these flows were clearly seen to be part of well-organized mesoscale cyclones, strongly coupled to the evolution of the GS path in the upper ocean and in particular the troughs of the baroclinic jet.
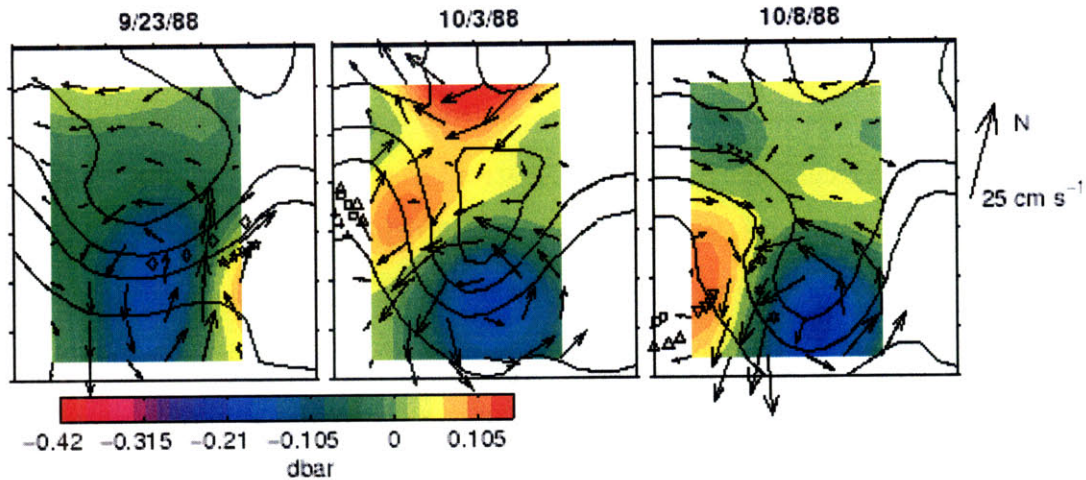
Figure 1-4: Case study of a GS meander trough steepening over a two-week period illustrating the spin-up of a deep cyclone beneath from SYNOP analysis. Four different measurements are superimposed: thermocline depth (thin solid lines, contour interval 200 m), the perturbation pressure field at 3500 m (in color), velocity vectors at 3500 m (speeds proportioned to the compass arrow), and locations of several RAFOS floats (triangles and squares) (from Howden (2000)).

And these deep eddies, through their fluxes, likely have a significant effect on the mean circulation, both in the baroclinic jet and in the abyssal ocean. Cronin (1996) demonstrated that in the GS statistics of eddy fluxes and their divergences observed during SYNOP, eddies played an important role in affecting the mean flow, controlling both the speed and direction of the time-mean GS jet. In addition, these eddy fluxes are likely to be important in driving the deep recirculation gyres. Hogg (1983, 1985, 1993) examined the issue of eddy effects on the deep circulations from the point of view of vorticity dynamics, and suggested that (given relatively large error bars) lateral relative vorticity and thickness eddy fluxes appear to have gradients of the proper sign and strength to drive a deep recirculation of the right order of magnitude.

4. *Modulating low-frequency variability:* Finally, eddies and eddy-mean flow interactions are potentially important in modulating the low-frequency variability observed in these systems. Both the GS and KE exhibit low-frequency fluctuations in

their transport, the degree of their meandering intensity / EKE, and their associated recirculation structure (*e.g.* Lee and Cornillon, 1995; Kelly et al., 1996; Qui and Chen, 2005), transitioning back and forth from a state with a weakly meandering jet and strong recirculation to one with a strongly meandering jet and small recirculation. There are many possible explanations for the source of this variability ranging from external (*e.g.* atmospheric) forcing (Qui, 1995) to multiple state equilibria associated with highly inertial dynamics (*e.g.* McCalpin and Haidvogel, 1996; Berloff and Meacham, 1998; Primeau, 1998; Berloff and McWilliams, 1999; Meacham, 2000). Eddy effects may be important as well. For example, Spall (1996), Qui (2000) and Berloff et al. (2007a) have all shown that the process of eddies fluxing PV away from the detached jet can lead to natural low-frequency oscillations (*i.e.* even without atmospheric coupling) in jet/recirculation gyre systems. It is likely that the source of the low-frequency variability in the oceanic system is a complicated mixture from a number of sources, with atmospheric forcing, inertial dynamics, and eddy effects all contributing. An appreciation of any potential roles of eddy effects alone however can be thought of as an important step in sorting out this complicated picture.

In summary, understanding WBC jet dynamics is important in our overall understanding of the large-scale ocean circulation, and given the importance of eddy variability in these systems, this understanding must include an appreciation of the effects of the eddy-mean flow interactions in the system. Eddy effects are potentially of first order importance in altering the strength, structure and stability of the mean jet, driving recirculations, coupling the strong motions in these baroclinic jets to deep abyssal circulations, and finally in modulating the low-frequency variability observed in these systems. An understanding of all of these features, and the role of eddy variability in them, is a necessary part of our overall picture of the WBC jet system.

1.2   Past Work and Present State of Knowledge

Given the importance of WBC jets and their recirculation gyres, work on the subject of their dynamics, and in particular the role that eddy variability may play, has had
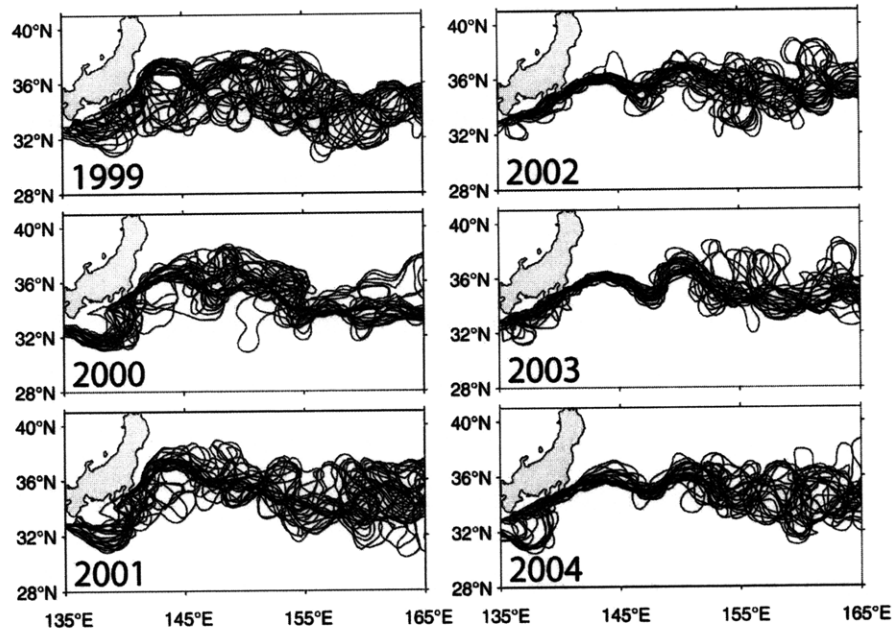
Figure 1-5: The contrast in the jet's meandering in the strongly meandering state (1999-2001) vs. the weakly meandering state (2002-2004) as seen by superimposed paths of the Kuroshio and Kuroshio Extension defined by the 170-cm contours in the weekly SSH fields. Here paths are plotted every 14 days (from Qui and Chen, 2005).

a long history.

(a) Theoretical Studies

Much has been learned about these systems, and their recirculation gyres in particular, through idealized theoretical studies, *i.e.* via analytical analysis or a numerical simulation of the solutions of various forms of the simplified equations of motion in simplified configurations. Theoretical studies that lay the foundation onto which the work described here will build can be thought of dividing into the following three categories:

1. inertial theories in which time-mean recirculation gyres can arise from the steady-state time-mean advection of PV alone (*e.g.* Fofonoff, 1954; Marshall and Nurser, 1986; Greatbatch, 1987; Cessi, 1990)

2. eddy-driven theories in which the effects of a directly prescribed vorticity forcing generates mean rectified flows through eddy-mean flow and eddy-eddy interactions (*e.g.* Haidvogel and Rhines, 1983; Cessi et al., 1987; Malanotte-Rizzoli et al., 1995; Berloff, 2005)

3. unstable jet studies in which the generation of mean recirculations arise from unstable jets in which eddy effects (arising from jet instabilities) and inertial effects can both play a role (*e.g.* Spall, 1994; Jayne et al., 1996; Beliakova, 1998; Jayne and Hogg, 1999)

Collectively these approaches demonstrate that recirculations can arise from the steady-state inertial terms, or the rectification of eddy fluxes, or potentially both. Steady-state inertial theories show that closed recirculation gyres are steady solutions to the nonlinear equations of motion forced by a balance between the inertial term (the mean advection of PV) and dissipation. At the same time, time-dependent numerical simulations demonstrate that zonal flows and closed recirculations can be generated solely from rectification effects through nonlinear eddy-mean flow and eddy-eddy interactions. Finally, rectified mean flows can also result from forcing by an unstable jet.

In this case, mean recirculations to the north and south of the jet are produced by eddies, generated by the jet's instability, acting to smooth the PV anomalies associated with the jet, and in the process produce homogenized regions in which essentially inertial recirculations can develop. It is interesting that recirculations generated in this way in barotropic models are able to predict recirculation strength quite accurately in spite of their reliance on the barotropic instability mechanism.

(b) Observational Studies

It is challenging to obtain enough observational data to accurately calculate various eddy statistics. As a consequence, diagnostic studies of the relation between the mean or low-frequency state and eddies using direct observations of the ocean circulation have been rare. Some attempts have been made with limited data on regional scales. For example, several investigators have attempted to infer crude properties of the eddy-mean flow interactions in the vicinity of the GS through the analysis of current meter data, attempting to evaluate either quantities related to the effective eddy forcing on the mean (such as the sign of the eddy momentum flux gradients or the eddy vorticity flux divergence), or by examining various terms in the eddy energy budget (*e.g.* Thompson, 1977, 1978; Dewar and Bane, 1989; Hogg, 1993; Cronin and Watts, 1996; Cronin, 1996). With similar aims, Chester et al. (1994) used acoustic tomography to estimate the eddy potential vorticity flux to diagnose the properties of eddy-mean flow interactions in the GS jet. In general, the overall picture was greatly expanded by SYNOP, that resulted in important new insights into the workings of the meandering jet and its relationship to the surrounding ocean, and a fundamental change in the scientific community's understanding of the interconnected system of currents, recirculations and eddies (see Hogg, 1992; Watts et al., 1995; Johns et al., 1995; Shay et al., 1995; Bower and Hogg, 1996).

Collectively, the work of these investigators demonstrate that eddy variability, in certain circumstances, has an order one importance in the dynamics of the mean GS. Observations suggest that eddies may be playing a role in the net driving of the mean jet by transferring momentum between the jet and the nearby inshore counter-

current via cross-stream momentum flux convergences and divergences, making "eddy-driving" a possible source for the excess momentum needed to drive the mass transport in the GS above the expected Sverdrup value (Thompson, 1977, 1978). In the abyssal ocean too, observations suggest eddies play a role in driving mean flows. For example, abyssal ocean measurements by Hogg (1993) suggest that the eddy relative vorticity flux divergence is of the right order of magnitude to drive a recirculation of the observed strength. The role of eddies however appears to have important variations in the vertical, with important implications for an eddy effect on jet stability. In current meter records analyzed by Dewar and Bane (1989), eddies acted to accelerate flows at abyssal levels but had the opposite effect (acting as a brake) for the mean flow at thermocline depths, a signature of baroclinic energy conversion of the standard type. The eddies therefore were acting not only to drive deep mean flows, but also to alter the structure of the inertial jet which gave rise to them. In this way, eddy variability may be playing a role in the evolving stability of the WBC jet, acting to exchange PV in the cross-stream direction or in the vertical, thereby removing the PV anomaly carried by it and driving the jet towards a state of marginal stability downstream. Cronin and Watts (1996) and Cronin (1996) also suggest that eddy fluxes and their divergences in the GS are playing a role in stabilizing the GS jet. They argue this effect is via episodic large-amplitude trough formation events that are a classic example of eddy-mean flow interactions whereby the GS, a baroclinically unstable jet, generates eddies which in turn act back on the mean flow. The eddy effect is to make the flow more barotropic (*i.e.* stable) through a divergent eddy stretching potential vorticity flux that acts to spin up and accelerate the deep layer flow.

In summary, theoretical and observational studies have both contributed to a detailed understanding of the potential role of eddies in driving recirculation gyres, as well as the role of eddies and eddy-mean flow interactions in real oceanic WBC jets. Despite this however, several questions regarding the essential physics of WBC jet and recirculation gyre systems and, in particular, the role of eddies in their dynamics, are

still unresolved. What are the essential mechanisms of eddy-mean flow interaction in WBC jet configurations and how do they depend on system parameters? How does zonal dependence change our understanding of the zonal-mean eddy-mean flow interaction problem? How does baroclinicity change our understanding of the essential physics of the eddy rectification effects seen in idealized barotropic jet models? What is the relative importance of inertial *vs.* eddy forcing in WBC jet systems? How representative are the observations of eddy-mean flow interaction in the GS of WBC jets in general? Are the dynamics at play significantly different in the KE? What can improved remote-sensing, *in situ* observational, and computing abilities relative to the days of SYNOP teach us further about eddy-mean flow interactions in actual WBC jet systems? It is in essence these questions, and the opportunity provided by the new KESS observations in the KE to make progress on them, that motivate the work presented here.

1.3   Thesis Objectives

Motivated by these questions and the KESS dataset, this thesis addresses the nature and the importance of eddy-mean flow interactions in WBC jets and recirculation gyre dynamics from both theoretical and observational perspectives. The objectives are:

1. to examine eddy-mean flow interactions in idealized configurations relevant to WBC jet systems, in particular (i) the mechanism by which eddies drive mean recirculation gyres through the rectification of a localized, transient forcing, and (ii) the role of eddies and eddy-mean flow interactions in the downstream evolution of a baroclinic jet subject to mixed instabilities.

2. to characterize eddy-mean flow interactions in the Kuroshio Extension using KESS observations, satellite data, and data from past observational programs in the region.

3. to test the relevance of the theoretical understanding derived from the idealized

studies to the dynamics of the actual Kuroshio Extension jet-recirculation gyre system.

It is the hope that the theoretical approach of studying idealized models will permit a more lucid understanding of the essential physics of the system, while the observational analysis can provide the necessary reality check to help understand the relevance of the idealized system and the theoretical framework derived from it to the real oceanic system. Taken together, the goal is to construct a tractable theoretical framework in which to think about eddy-mean flow interactions in WBC jet systems, that gives both an understanding of the dynamics from first principles, as well as an understanding of its relevance to the actual oceanic system.

1.4 Thesis Outline

Work towards achieving these goals is presented in the following three chapters. Chapter 2 presents the first of the theoretical studies of eddy-mean flow interactions in idealized configurations relevant to WBC jet systems, that of eddy-driven recirculations from the rectification of a localized, transient forcing. Here new insights into the rectification mechanism, as well as explorations into how its effectiveness is influenced by the variation of forcing parameters, stratification, the presence of a mean background flow, and the degree of nonlinearity of the forced wave / eddy field, are presented. Chapter 3 describes the second of the theoretical studies, that of eddy-mean flow interactions in the downstream evolution of an idealized WBC jet. Here a diagnosis of the eddy effect on the time-mean circulation, an examination of the mechanism that permits the eddies to drive the time-mean recirculation gyres, a discussion of the relative importance of eddy *vs.* steady-state inertial terms, and a comparison of these mechanisms in barotropic, baroclinic and mixed instability jets is given. Finally, Chapter 4 addresses the second and third thesis objectives by presenting the results of the observational study of eddy-mean flow interactions in the KE jet. Here a characterization of the time-mean jet, its eddy variability, and indicators of their interactions during the observational period, as well as an evaluation of the relevance

of the idealized WBC jet study to the oceanic system by considering both the model set-up and its results relative to observations, is given. Note that each of these chapters is self-contained and can stand alone, independently describing the problem, the methods, the results, and their implications. Chapter 5 summarizes the conclusions for the thesis as a whole, as well as discussing implications of the work as a whole, and suggesting directions for future research.

Chapter 2

Eddy-Driven Recirculations From A Localized, Transient Forcing

Abstract

The generation of time-mean recirculation gyres from the nonlinear rectification of a vorticity forcing that is localized in space and oscillatory in time is re-examined both analytically and numerically. I present new insights into the rectification mechanism and explore how its effectiveness is influenced by the variation of forcing parameters, stratification and the presence of a mean background flow. From this exploration emerges an understanding that the effectiveness of the rectification depends on the properties of the energy radiation from the forcing, which in turn depends on the population of the waves that participate in the process. This population is selected by the relation of the forcing parameters to the available free Rossby wave spectrum. An enhanced response is achieved if the parameters of the problem are such to select the Rossby wave with zero zonal group velocity and maximum meridional group velocity which is optimal for producing rectified flows. Although formulated in a weakly nonlinear wave limit, simulations in the fully turbulent (and more oceanically relevant) system suggest that this understanding of the mechanism remains useful in the strongly nonlinear regime with the addition of wave-mean flow interaction that needs to taken into account. The problem is idealized but has general application in the understanding of eddy-eddy and eddy-mean flow interactions as the contrasting limit to that of spatially broad (basin-wide) forcing, and is relevant given many sources of oceanic eddies are localized in space.

2.1 Introduction

The effect of transient eddies on the time-mean state is a fundamental problem in the theoretical studies of the circulation of the atmosphere and ocean. By redistributing momentum, heat, and vorticity in a systematic fashion, eddy flux divergences of momentum and potential vorticity (PV) are capable of having an important impact on the large-scale, time-mean state.

One way eddies can affect the larger scale circulation is through the driving of mean motions. Here I examine this phenomenon through a study of nonlinear rectification, the generation of non-zero mean flow from a forcing with zero mean, in an idealized set-up. Specifically I examine the time mean-flow response of a barotropic and equivalently barotropic fluid subject to a simple vorticity forcing that is localized in space and oscillatory in time. The emergence of the mean flow is a result of nonlinear terms producing finite time-mean fluxes (Reynolds stresses) of momentum and relative vorticity, whose convergences and divergences act as a driving force for the time-mean flow.

2.1.1 Motivation

Interest in the problem was originally motivated by its potential relevance to the specific application of the dynamics of deep recirculation gyres observed with the eastward jet extensions of western boundary current (WBC) systems such as the Gulf Stream and Kuroshio (Figure 2-1). One hypothesis for the driving of these abyssal recirculations originating in historic eddy-resolving ocean circulation studies (*e.g.* Holland and Rhines, 1980) is through the action of energetic surface eddies in and above the thermocline, which act to provide localized sources and sinks of vorticity ("plungers" of Ekman pumping velocity) to the deep ocean through fluctuating thickness fluxes. It is my hope that understanding the details of the idealized rectification problem considered here will aid in evaluating the relevance of this mechanism to the deep recirculation gyres seen in recent WBC observations (*e.g.* Hogg, 1992; Bower and Hogg, 1996; Chen et al., 2007; Jayne et al., 2008).

The problem however has more general application in our understanding of wave/eddy rectification from a localized forcing, serving as the contrasting limit to spatially broad (basin-scale) forcing (*e.g.* Pedlosky, 1965; Veronis, 1966) and important given many sources of ocean eddies are intermittent in space. For example, rectification from localized forcing has potential relevance to the response of the ocean to a spatially localized wind-stress pattern or a spatially localized concentration of eddy activity as say generated by mean-flow instability. More generally, the generation of mean zonal motion by the action of locally forced eddies, as is considered here, has relation to the phenomenon of zonal jet formation, observed to occur spontaneously in turbulent β-plane flows (*e.g.* Rhines, 1975, 1977; Williams, 1978). This process has recently received renewed interest given the discovery of deep zonal jets in ocean observations (Maximenko et al., 2005) and ocean GCMs (Richards et al., 2006). Finally, the problem can be considered a small contribution towards improving our understanding of the varied effects of eddies on the large-scale and time-mean state, critical in our search for better ways to parameterize unresolved eddy effects in general circulation models.

2.1.2 Past Work

The work presented here extends earlier studies of eddy-driven mean flow from localized forcing, specifically the pioneering laboratory experiments by Whitehead (1975) and numerical simulations by Haidvogel and Rhines (1983) (hereafter HR83). The former was the first experimental demonstration of the generation of mean zonal currents from localized, periodic forcing, whereas the latter examined this phenomenon numerically through simulations of two-dimensional flow on a mid-latitude β-plane.

In their analysis, HR83 make many insights into the rectification mechanism that are important as a starting point for the present study. First, they show the usefulness of an analytical solution in the form of a time-periodic Green's function in understanding the numerically simulated forced primary wave field. Second, from analysis of their numerical simulations, they propose that the dynamics of the rectified circulation is related to the mean eddy PV flux, $\overline{v'q'}$, that a turbulent Sverdrup

27
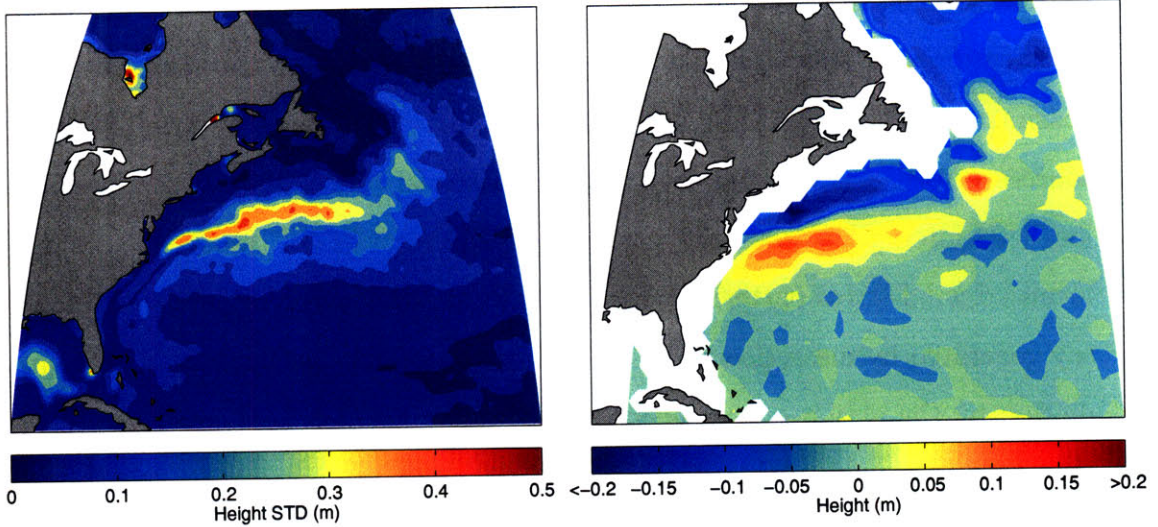
Figure 2-1: Time-mean sea surface height variance (measured by altimetry, source: AVISO) (*left*) showing a localized concentration of eddy energy along the axis of the Gulf Stream. The time-mean dynamic pressure field at 1000 m (measured by subsurface floats) (source: Jayne (2006))(*right*) showing the pair of counter-rotating deep recirculation gyres that exist below.

balance ($\beta v = -\nabla \cdot \overline{v'q'}$) dominates in nearly all parts of the flow, and that regions of counter (up) gradient potential vorticity fluxes provide the propulsion necessary for fluid particles to cross the mean quasi-geostrophic contours. Finally, they show that the strength of the induced circulation has a roughly quadratic dependence on forcing amplitude and forcing scale, and decreases with increasing bottom friction and decreasing forcing period.

2.1.3 Present Work Objectives

The present work seeks to extend this earlier study in a number of different ways. Specifically the work presented here aims to:

1. examine the rectification mechanism in more detail from the perspective of eddy-mean flow interactions (*i.e.* through examination of the eddy flux convergences of momentum and vorticity, and eddy enstrophy generation).

2. extend the study of parameter variations (both of the forcing (amplitude, frequency and length-scale) and the flow (the non-dimensional beta parameter)),

and to understand the mean-flow dependence on forcing parameters in terms of the dynamics of the rectification mechanism.

3. consider the effects of stratification via the use of an equivalently barotropic model.

4. consider the effects of a background mean flow.

5. extend these results from a weakly non-linear limit to the fully nonlinear regime, and to examine which results from the small amplitude limit break-down and why.

Finally, I seek to comment on the potential relevance of the mechanism in driving mean-flows in an oceanic / atmospheric context.

2.1.4   Chapter Outline

This chapter is organized as follows: In Section 2.2, I outline my approach to the problem that includes the use of both an analytical solution and numerical simulations. Here details about the model set-up, the numerical method, and the design of the numerical experiments are presented. In Sections 2.3 - 2.7 I present the results. In Section 2.3 I present new insights into the rectification mechanism from both an analytical expansion solution (valid in the weakly nonlinear limit) and from examining the nonlinear eddy-mean flow interaction terms in the fully nonlinear numerical simulations. In Section 2.4 I discuss the results of numerical model parameter studies, describing the dependence of the strength of the mean flow generated on various forcing and flow parameters, and interpreting this dependence in terms of the rectification effectiveness of the population of waves selected by the parameters of the problem. In Sections 2.5 and 2.6 I examine the effects of stratification and a mean background flow respectively, and similarly interpret their effect on rectification effectiveness in terms of the rectification effectiveness of the population of waves they select. Finally, in Section 2.7, I extend the numerical experiments from a weakly nonlinear regime to a strongly nonlinear regime, and examine which aspects of our understanding of the

problem formed from an analysis of the weakly nonlinear case remain valid, and also where and why weakly nonlinear results break-down. In the final section, I summarize the lessons learned from the study and discuss its relevance to atmospheric and oceanic applications.

2.2 Methodology

Following HR83, I consider the problem via both analytical and numerical approaches.

2.2.1 Analytical Analysis

To gain insight into the rectification mechanism and the relation between forcing parameters and rectified flow, like HR83, I appeal to an analytical description of the forced waves. To introduce the effects of nonlinearity responsible for the rectification, a solution to the nonlinear equation in terms of an expansion in the amplitude of the forcing is sought. This provides a framework by which to connect the second order mean flow to forcing by the time-mean Jacobian (relative vorticity flux divergence) of the first order, linear forced wave field, a description that is valid in the weakly non-linear limit (see Appendix A for details). I then compare the wave or eddy flux divergence forcing and the mean flow it generates for various linear solutions to the Rossby wave equation for different forcing functions. In particular I consider the time-periodic Green's function solution (for which an analytical form exists and which was considered by HR83) and the solution for a forcing function with a finite spatial extent (a particular solution obtained through the numerical integration of the Green's function convolution integral). As it will be seen, this comparison will demonstrate the critical roles of the forcing extent and the east-west asymmetric radiation of energy in the rectification mechanism. I also generalize the analytical solution of HR83 to include the effects of stratification and comment on its influence on rectification.

2.2.2 Numerical Simulations

To examine the effect of the full nonlinearities on the problem, both in a weakly nonlinear and fully nonlinear regime, I also perform numerical simulations.

The numerical model is essentially the one described in Jayne and Hogg (1999) with the jet inflow and outflow conditions replaced by a prescribed forcing function in the form of a narrow plunger fixed at the center of the basin. It is quasi-geostrophic, barotropic or reduced gravity baroclinic, and on a mid-latitude β plane. It solves the potential vorticity equation:

$$\frac{\partial q}{\partial t} + J(\psi, q) = F(x, y)e^{i\omega t} - R\nabla^2\psi \tag{2.1}$$

with

$$q = \nabla^2\psi - \frac{1}{Bu}\psi + \beta y \tag{2.2}$$

ψ being the streamfunction, Bu the Burger number (the square of the ratio of the Rossby radius of deformation to the length scale of the motion), and R a non-dimensional bottom friction coefficient.

Various forms of the forcing function $F(x, y)$ were considered. For the mechanism that will be described here, it is important only that the forcing be sufficiently localized in space (an understanding of what "sufficiently localized" means will follow as we gain insight into the rectification mechanism). To allow a large range of amplitudes to be considered, it was convenient to use a forcing function of the form of a normalized Gaussian:

$$F(x, y) = A\left(\frac{2 - 4\left(\frac{x}{L}\right)^2}{L^2} + \frac{2 - 4\left(\frac{y}{L}\right)^2}{L^2}\right)e^{-\left(\frac{x}{L}\right)^2 - \left(\frac{y}{L}\right)^2} \tag{2.3}$$

such that at any instant in time, the basin-integral of the PV input due to the forcing is zero. Results presented here will be from a forcing of this form. Note however that the results described remain robust for other forms of $F(x, y)$ including a standard Gaussian as in HR83.

31

Details on the numerical method can be found in Jayne and Hogg (1999). Briefly, integration in time and space is done using a scheme that is center differenced in the two spatial dimensions (an "Arakawa A-grid") and forward stepped in time using a third-order Adams-Bashforth scheme (Durran, 1991). Advective terms are handled using the vorticity conserving scheme of Arakawa (1966). Dissipative sponge layers, 50 grid points wide, are placed next to all boundaries to absorb all waves leaving the domain. Away from the sponge layers the explicit friction, $R = 4x10^{-5}$ (non-dimensional), is chosen to be as low as possible consistent with numerical stability (dimensional values for the dissipation time scale range from ~ 10 years at a non-dimensional β, $\beta = \frac{\beta_{dim}L^2}{U}$, value of 0.01 to ~ 100 years at $\beta = 0.15$). The non-dimensional grid spacing is 0.2 and the number of grid points is 751 (E-W) by 401 (N-S). With the origin at the center of the domain this puts the western boundary at $x = -75$ and the northern boundary at $y = 40$ non-dimensional units.

The governing equation is solved in non-dimensional form with time scaled by the advective time scale, $T = \frac{L}{U}$. L and U are typical horizontal length and velocity scales of the motions respectively. Values for the non-dimensional β parameter ($\beta = \frac{\beta_{dim}L^2}{U}$ where β_{dim} is the meridional gradient of the earth's planetary voriticty, hence the ratio of the scales of the horizontal gradient in relative vorticity to that of the horizontal gradient in planetary vorticity), as well as non-dimensional forcing parameters A (the forcing amplitude), ω (the forcing frequency) and L_F (the forcing length scale) are specified. A typical run (around which parameter studies are varied) has a value of β of 0.05 and forcing parameters $L_F = 5.0$, $\omega = 0.01$ and $A = 0.001$. Dimensionally these would correspond to (taking a typical velocity scale of $U = 1$ m/s) a forcing scale $L_{F\,dim}$ of ~ 250 km, a forcing period ω_{dim} of ~ 60 days and a forcing amplitude A_{dim} corresponding to an Ekman pumping velocity of $\sim 1x10^{-3}$ m/s (or equivalently a wind stress of ~ 0.4 N/m^2). Hence a typical run has scales typical of oceanic synoptic scales. For reference, a summary of the suite of numerical experiments varying various parameters that are reported on here, as well as their corresponding dimensional scales to put the experiments in a physical context, are summarized in Table 2.1.

Table 2.1: Summary of Numerical Experiments

Parameter	Range of Non-Dimensional Values	Range of Dimensional Scales
β	0.01 - 0.15	~ 1 m/s $\geq$ U $\leq \sim 0.1$ m/s
ω	0.001 - 0.015	~ 100 days $\geq T \geq \sim 10$ days
L_F	1 - 15	~ 50 km $\leq L_F \leq \sim 750$ km
Bu^{-1}	0 - 0.3	$infinite \geq R_D \geq \sim 100$ km
U	-0.1 - 0.1	$\sim$-1 cm/s $\leq U \leq \sim 1$ cm/s
A	0.001 - 0.015	~ 0.1 N/ms$^2 \leq \tau \leq \sim 1$ N/ms^2
		~ 1 x 10^{-4} m/s $\leq w_{Ek} \leq \sim 1$ x 10^{-3} m/s

Here Bu^{-1} is the inverse Burger number used to vary the importance of stratification, and U is a mean background flow. See Sections 2.5 and 2.6 for more details.

2.3 Results: Insights into the Rectification Mechanism

As a first step in the analysis, I attempt to understand the mechanism by which the waves or eddies rectify to produce the time-mean recirculation gyres. Insights are gained from both the analytical expansion solution and an examination of the fully nonlinear solution obtained by numerical simulation.

2.3.1 Insights From Analytical Analysis

An analytical solution in terms of an expansion in the amplitude of the forcing relates the second order mean flow to forcing by the time-mean Jacobian (relative vorticity flux divergence) of the first order, linear forced wave field. In particular, the order amplitude squared rectified flow is given by the zonal integral of the eddy relative vorticity flux divergence of the order amplitude waves (for details see Appendix A). This relation provides a way to relate forcing parameters to properties of the rectified mean-flow valid in a weakly nonlinear limit.

I compare the eddy relative vorticity flux divergence and its zonal integral for wave solutions to the linear forced Rossby wave equation for various forcing functions.

From this I learn that a finite forcing extent is critical to produce rectified flow. As is shown in Figure 2-2, the Green's function solution (*i.e.* approximating the spatial dependence of the forcing function by a delta function, as considered by HR83 and for which a closed-form solution exists) produces an east-west anti-symmetric pattern of vorticity flux divergence that, because of its exact zonal asymmetry and the dependence of the rectified flow on the zonal integral of the flux divergence, does not produce rectified flow outside the immediate vicinity of the forcing. In contrast, the particular solution for a forcing function with finite spatial extent (here a localized Gaussian spatial dependence) does produce a pattern of vorticity flux divergence whose zonal integral is consistent with the two gyre circulation pattern.

This observation highlights the fact that, at least in the weakly nonlinear limit, it is necessary for the forcing to have a finite length scale in order to generate rectified flow in the far field, a lesson that provides us with a new understanding of the rectification mechanism. It implies that the mechanism that is generating the rectified flow is occurring inside the forcing region (where the Green's function and particular solution differ) and not by the waves in the far field (where they do not). As it will be seen, it is also highlighting the importance of introducing a zonal asymmetry in the wave radiation pattern that is critical to the production of rectified flow, something that will be elaborated on in subsequent sections.

2.3.2 Insights From Numerical Simulations

Examining various eddy-mean flow interaction diagnostic terms from the fully non-linear numerical solutions expands our picture of the mechanism by which the wave or eddy terms produce the rectified flow. In particular, visualization of the nonlinear eddy fluxes (Reynolds stresses) of vorticity and momentum provide important insights.

(a) Insights from eddy fluxes of vorticity

Examination of the Reynolds stresses of relative vorticity (Figure 2-3) show that the key to the eddy generation of mean flows is a systematic up-gradient (northward)
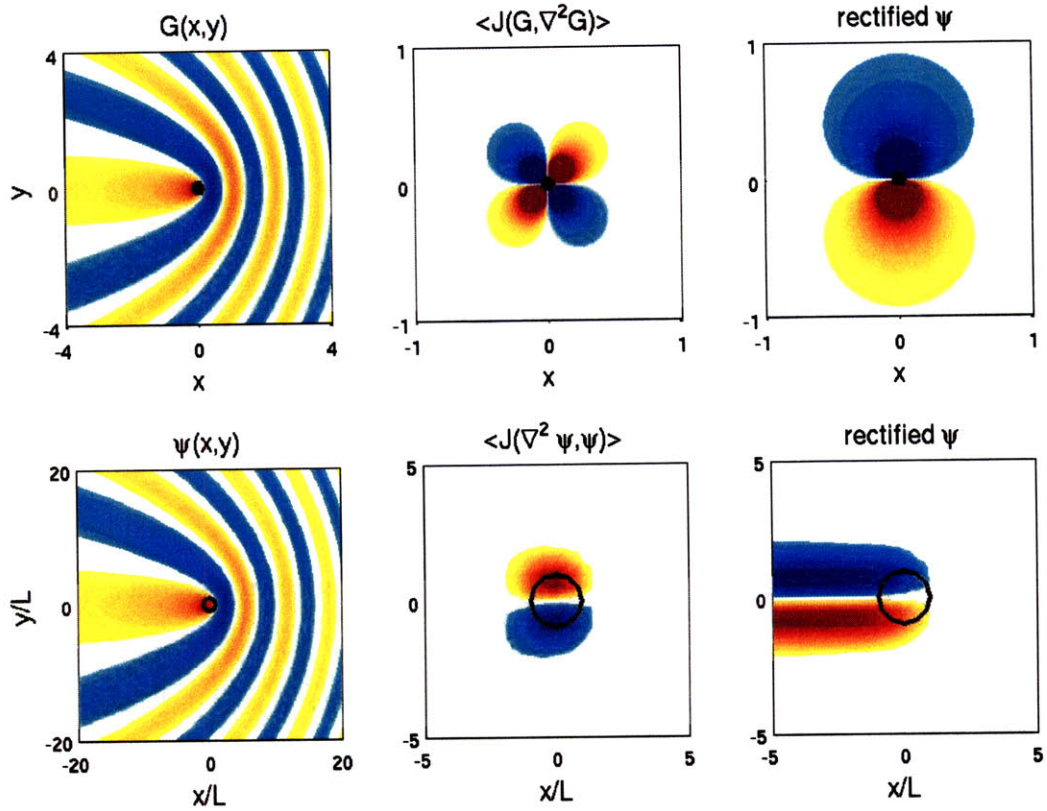
Figure 2-2: A comparison of properties of the analytical solutions for 1. a forcing function with a Green's function spatial dependence (*top*) *vs.* 2. a forcing function with a Gaussian spatial dependence (*bottom*). The wave fields (*left*) show no qualitative difference, but the two solutions do exhibit a fundamental difference in the vorticity flux divergence patterns (*center*) and consequently the time-mean rectified flow forced by this flux divergence pattern (*right*).
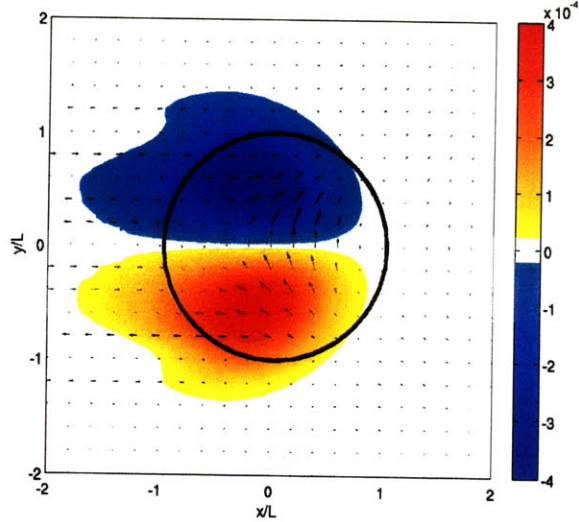
Figure 2-3: Eddy relative vorticity transport $(\overline{u'q'}\vec{i} + \overline{v'q'}\vec{j})$ (vectors) overlaid on the eddy relative vorticity transport divergence $(\overline{J(\psi',\nabla^2\psi')})$ (color), which in a small amplitude limit is understood to force the mean rectified flow through the relation $\overline{\psi} = \frac{-1}{\beta}\int \overline{J(\psi',\nabla^2\psi')}dx$. The black circle indicates the plunger radius.

eddy flux of vorticity that occurs inside the forcing region. This eddy transport produces a flux convergence in the northern half and a flux divergence in the southern half of the forced region that is responsible for the forcing of the time-mean recirculation gyres that extend outside the vicinity of the forcing. Given this picture, I hypothesize that the properties of the mean-flow generated will therefore be closely related to the process of eddy vorticity transport in the vicinity of the plunger.

Understanding rectification as a consequence of up-gradient eddy vorticity transport provides further insights into the requirements for rectification. First, given up-gradient transport is permitted only in the forcing region because of the source of vorticity supplied there, one can now understand the requirement for a finite forcing extent that one finds in the analytical analysis: with no (specifically meridional) extent to the forcing region, no up-gradient flux is possible. Second, based on eddy enstrophy budget considerations to be outlined below, one can also understand the requirement that the forcing be "sufficiently localized".

The requirement for an up-gradient eddy vorticity transport is equivalent to the requirement that the eddy enstrophy generation term in the eddy enstrophy equation
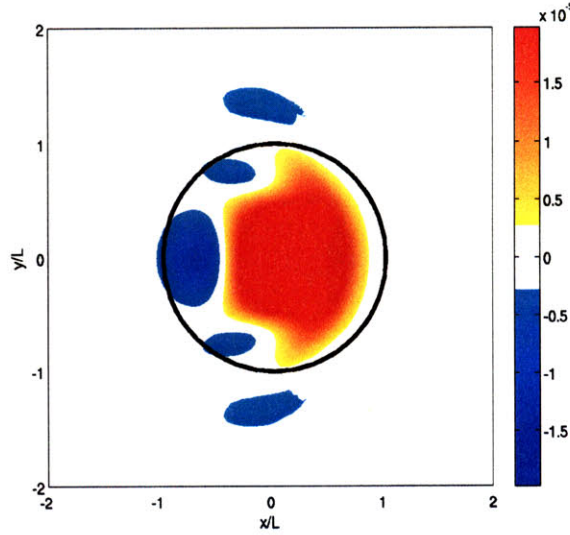
Figure 2-4: Eddy enstrophy destruction ($\overline{\vec{u}'\zeta'}\cdot\nabla\overline{\zeta}$) (color) which indicates the direction of the eddy vorticity transport relative to the prevailing gradient (positive implies an eddy vorticity flux up the mean vorticity gradient; negative implies an eddy vorticity flux down the mean vorticity gradient).

$(-\overline{\mathbf{u}'\zeta'} \cdot \nabla\overline{q})$ is negative (*i.e.* eddy enstrophy destruction, $-\overline{\mathbf{u}'\zeta'} \cdot \nabla\overline{q}$, is positive). This condition is met if the balance of the remaining terms in the time-mean eddy enstrophy budget $(-\overline{\chi'\zeta'} + \overline{\mathbf{u}} \cdot \nabla\overline{\frac{1}{2}\zeta'2}$, where χ' represents the fluctuating relative vorticity forcing) is negative, a condition that is met if (1) the stirring is the same sign as the forcing so $\overline{\chi'\zeta'} > 0$ (*i.e.* the forcing is "sufficiently localized") and (2) mean advection is small relative to the forcing. Visualization of the eddy enstrophy destruction term for a typical set of parameters (Figure 2-4) confirms that indeed these conditions are met and eddy enstrophy destruction is positive inside the forcing region in the cases where rectified flow is produced. Given this picture, I hypothesize that the rectification mechanism will be robust as long as this enstrophy balance is maintained.

(b) Insights from eddy fluxes of momentum

Examination of the Reynolds stresses of momentum (Figure 2-5) provide an alternative understanding of the rectification mechanism. In this framework, one understands the mean zonal flows to be driven by eddy forces that arise from a systematic eddy flux of zonal momentum towards the forcing region. This pattern of
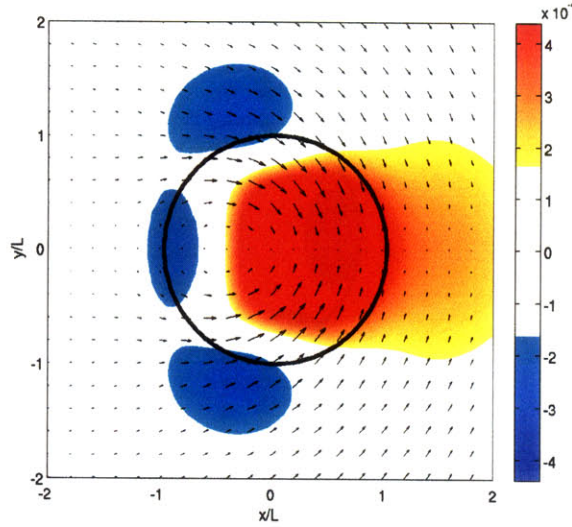
Figure 2-5: Eddy zonal momentum transport $(\overline{u'u'}\vec{i} + \overline{v'v'}\vec{j})$ (vectors) overlaid on the negative of the eddy zonal momentum transport divergence $(-\frac{\partial}{\partial x}\overline{u'u'} + \frac{\partial}{\partial y}\overline{u'v'})$ (color), the latter which can be interpreted as a parameterization of an effective steady zonal eddy force in the prognostic non-eddy-resolving momentum equations of the large-scale or slowly-varying flow.

eddy flux is a result of the outward energy radiation of the Rossby waves emanating from the forcing, as first discussed by Thompson (1971). This produces an eddy momentum flux convergence in the forced zone and eddy momentum flux divergences north and south of the forcing. Through the interpretation of this eddy flux divergence quantity as a parameterization of an effective steady zonal eddy force in the prognostic momentum equations of the large-scale or slowly-varying flow in a non-eddy-resolving model, this pattern then translates to a positive (eastward) eddy force at the latitude of the forcing and negative (westward) eddy forces north and south of the forcing. In this way, eddies are seen to act to accelerate the eastward jet at the forced latitudes and drive the flanking westward flows. Given this picture, I hypothesize that the properties of the eddy-driven mean-flow will therefore be closely tied to the properties of the wave energy radiation away from the forcing.

38

2.4 Results: Dependence on System Parameters

I examine the sensitivity of the rectification mechanism to various system parameters to gain further insight. Specifically I vary the non-dimensional β parameter, $\beta = \frac{\beta_{dim}L^2}{U}$ where β_{dim} is the meridional gradient of planetary vorticity and L and U are typical length and velocity scales of the flow (to be thought of as a measure of the relative importance of the relative vorticity of the flow to the planetary vorticity), the forcing frequency ω, and the plunger size L. Results from these parameter studies are presented here.

2.4.1 Effect on Rectification Effectiveness

The most basic result of the parameter studies is the observation that rectification effectiveness (the strength of the mean-flow generated as measured by the maximum time-mean gyre transport, $\overline{\psi}_{max} - \overline{\psi}_{min}$) is a function of the various forcing and environmental parameters. This dependence on β and plunger size L in physically relevant parameter ranges is shown in Figure 2-6. A non-monotonic dependence of mean flow strength on both of these parameters generates new questions about what sets which parameter values generate an enhanced response.

2.4.2 Interpretation Via Wave Rectification

Examining this non-monotonic behavior provides additional understanding of the rectification mechanism. In particular it highlights the importance of the relationship between the scales of the forcing and the free Rossby waves that make-up the response in setting the rectification strength. As it will be shown, a resonant-like response is achieved when the forcing length scale L, is well matched to the spectrum of free Rossby waves the forcing can excite (a function of the dispersion relation and hence β and the frequency ω). In particular, a maximal response is achieved when the forcing length scale corresponds to the wavelength associated with the wave at the origin of the Rossby wave dispersion circle at $k = -|l| = -B$ where $B = \frac{\beta}{2\omega}$ (Figure 2-7).
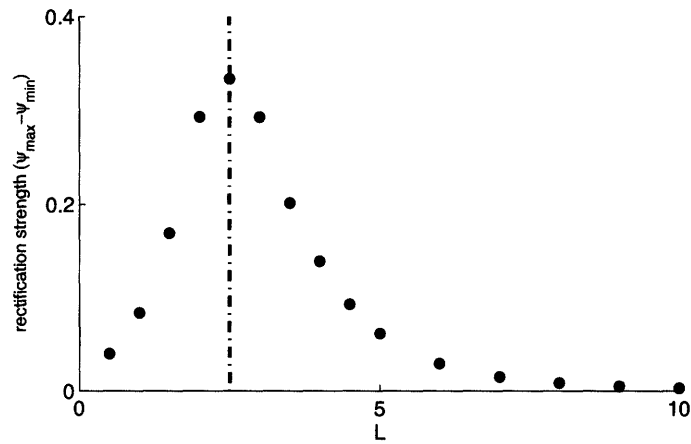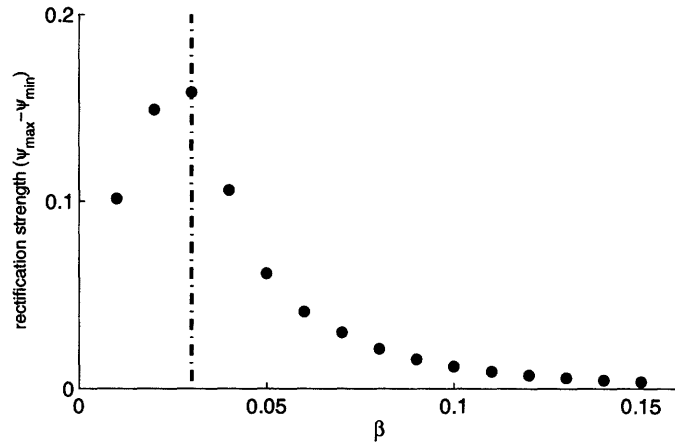
Figure 2-6: Dependence of mean rectified flow strength $(\overline{\psi}_{max} - \overline{\psi}_{min})$ ("rectification effectiveness") on select parameters of the problem: β (*top*) and forcing length scale L (*bottom*). Dashed lines indicate the parameter value corresponding to the peak or optimal response in the observed non-monotonic dependence of rectified flow strength on each of these parameters.
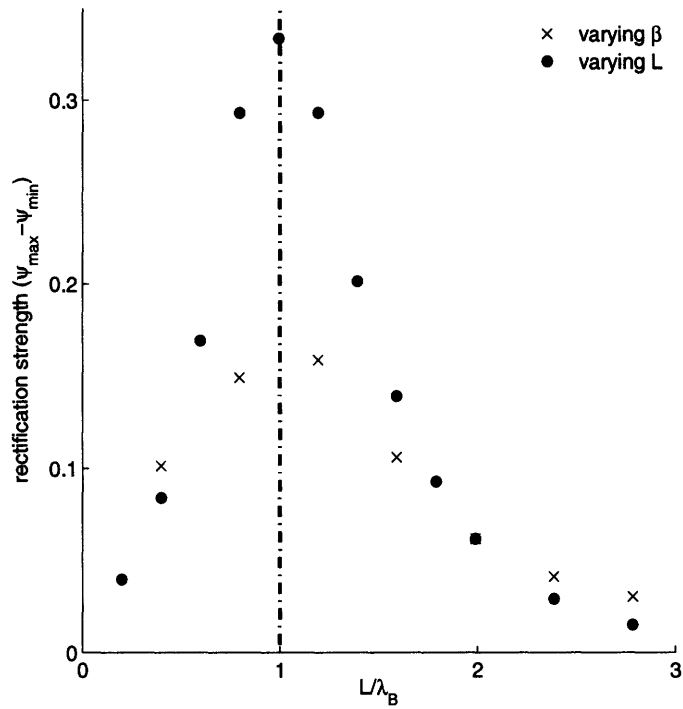
Figure 2-7: Demonstration that the "resonant" response occurs when the forcing length scale L is equal to the wavelength associated with the wave with wavenumbers $|k| = |l| = B$ (where $B = \frac{\beta}{2\omega}$), λ_B.

One can understand why this is the case based on the understanding of the rectification mechanism outlined in the previous section. In short, varying which waves on the dispersion circle that are excited (via the choice of forcing length scale and the dispersion circle) changes the rectified flow response because it changes the properties of wave energy radiation away from the forcing. This dictates the spatial distribution of wave activity which in turn impacts rectification because rectification depends directly on the spatial gradients of the wave or eddy terms. As it will be seen, the maximum response occurs when the forcing scale matches the wavenumber $k = -B$ because there are a number of properties of this particular wave's energy radiation that make it optimal for rectification. Specifically, by corresponding to the wave in the available Rossby wave spectrum with zero zonal group velocity and maximized meridional group velocity, it is the wave that is best suited to producing zonal asymmetry in zonal energy radiation and a large meridional component of energy radiation, both of which are necessary for effective rectification.

To illustrate, consider rectification from a fixed size plunger for three different values of β: one corresponding to that required for the zonal wavenumber preferentially excited by the plunger radius L_F, $k_F = -\frac{2\pi}{L_F}$ and the zonal wavenumber $k = -B$ to match ("$\beta_{optimal}$", $|k_F| = B$), one with $\beta < \beta_{optimal}$ ($|k_F| > B$) and one with $\beta > \beta_{optimal}$ ($|k_F| < B$) (see Figure 2-8). The effect of changing β changes the character of the waves that are excited by the forcing consistent with expectations based on the intersection of the forcing scale on the dispersion curve: for $\beta < \beta_{optimal}$ the wave field is dominated by waves with large meridional scale relative to their zonal scale ($k >> l$), while for $\beta > \beta_{optimal}$ the wave field is dominated by waves with comparable meridional and zonal wavelengths ($k \sim l$) (Figure 2-9 *top row*).

This change in the "population" of waves that are excited changes the pattern of the waves' energy radiation. In particular, as β is varied from sub-optimal to super-optimal, the wave population that is excited changes from one with waves with predominantly eastward zonal group velocity, c_{gx}, to one containing waves that have a predominantly westward c_{gx} component. Waves with a significant meridional group velocity, c_{gy}, are included in the excited spectrum when β is such to include waves
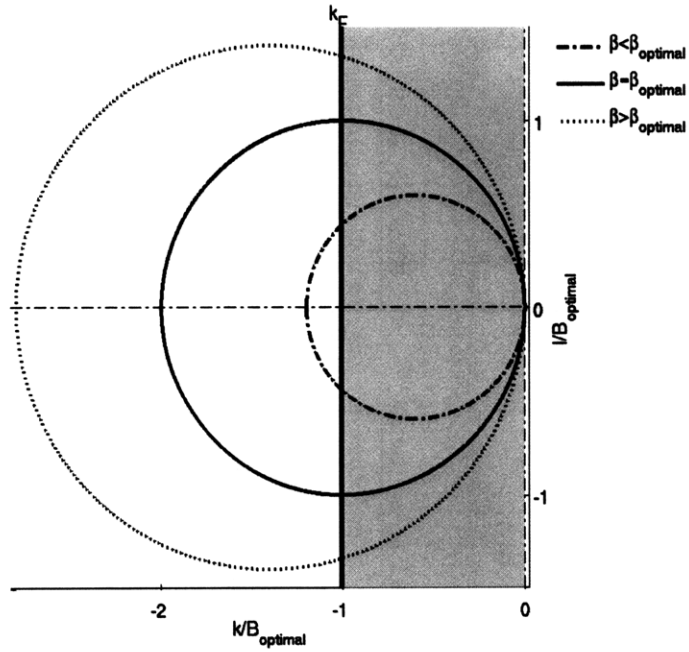
Figure 2-8: A visualization of the relation between the forcing scale $(k_F = \frac{2\pi}{L})$ and the free Rossby wave spectrum for the three values of non-dimensional β discussed in the text. Forcing excites Rossby waves with k wavenumbers $\leq k_F$ (shaded region) and l wavenumbers given by the dispersion relation (a function of β and forcing frequency ω) (circles). For $\beta < \beta_{optimal}$ the wave population contains waves with $|k| > B$ (with eastward zonal group velocity), waves with $|k| = B$ (with maximized meridional group velocity), and waves with $|k| < B$ (with westward zonal group velocity). For $\beta > \beta_{optimal}$, the spectrum of waves excited contains waves with $|k| < B$ (with westward zonal group velocity) only.
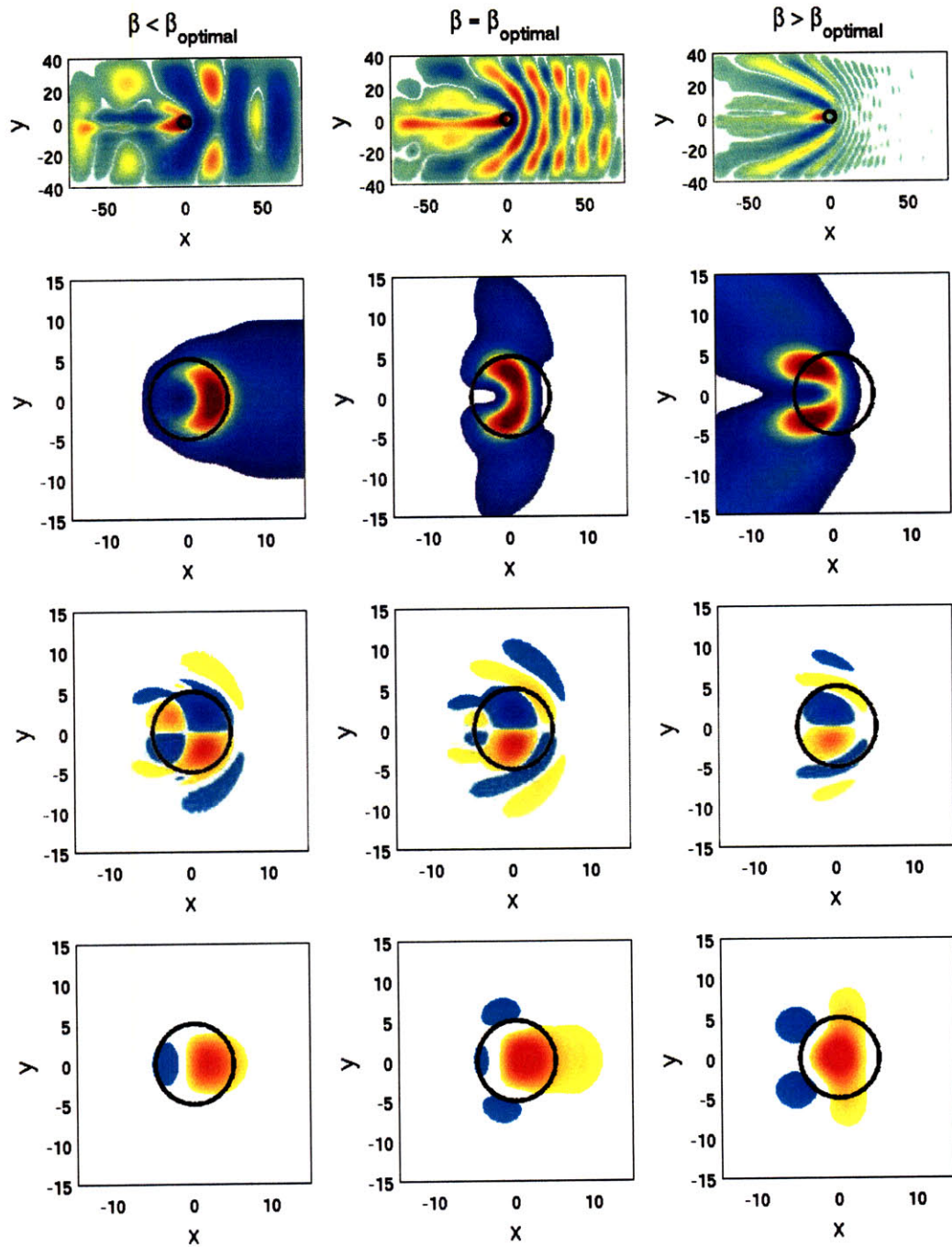
Figure 2-9: The effect of varying β from $\beta < \beta_{optimal}$ to $\beta > \beta_{optimal}$ on: *(a)* the population of waves excited *(1st row)*; *(b)* the orientation of energy radiation from the forcing *(2nd row)*; *(c)* the patterns of eddy relative vorticity flux divergence *(3rd row)*; *(d)* the patterns of eddy zonal momentum flux divergence *(4th row)*.
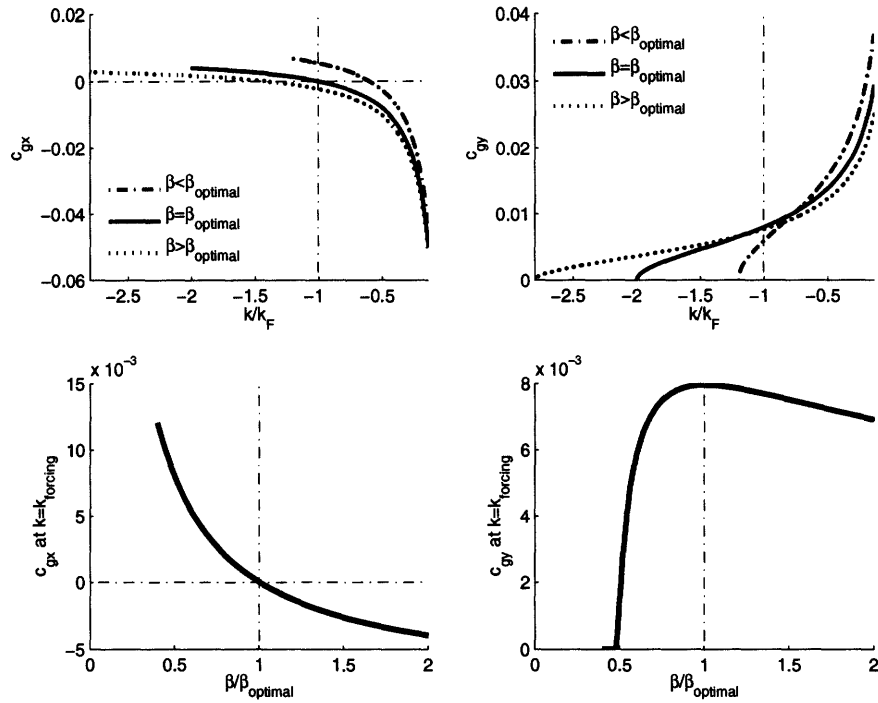
Figure 2-10: A visualization of the effect of changing the population of waves excited by the forcing on energy radiation from the plunger. As β is increased from $\beta < \beta_{optimal}$ to $\beta > \beta_{optimal}$, waves with eastward zonal group velocity ($c_{gx} > 0$) are included in the population of excited waves. $\beta_{optimal}$ is set by the conditions of $c_{gx} = 0$ and c_{gy} maximized at the forcing scale k_F.

near $|k| = B$ in the excited range (Figure 2-10). This is clearly seen in the differences in the time-mean eddy kinetic energy distributions for the three special cases (Figure 2-9 second row).

The changing properties of energy radiation impact rectification effectiveness through changing the spatial distributions of Reynolds stresses $\overline{u'u'}$, $\overline{u'v'}$ and $\overline{v'v'}$, for this results in changing patterns of Reynolds stress gradients which are what determine the eddy-mean flow interaction terms (the eddy flux divergences of vorticity and momentum) that produce the rectified flow. I find that both a zonal asymmetry and a significant meridional component of energy radiation are required for effective rectification, requirements that can be understood through consideration of the patterns of eddy vorticity flux divergence and eddy momentum flux divergence respectively:

(a) **Zonal energy radiation and the divergence of the eddy fluxes of vorticity**

45

As described above, shrinking β across the optimal threshold changes the population of waves excited by the forcing from one with strictly waves with a westward zonal component of their group velocity to one that includes waves with an eastward zonal component as well. As a consequence, the zonal radiation of energy becomes more and more zonally symmetric as β is decreased and more and more of the complete Rossby wave spectrum is excited. This is important to rectification effectiveness because it results in a significant change in the pattern of the eddy vorticity flux divergence, from the two-lobed pattern (that drives the counter-rotating gyres west of the forcing region) towards the zonally anti-symmetric four-lobed pattern (that results in no mean flow generation outside the forcing region) (Figure 2-9, *third row*).

This new understanding of the importance of zonal energy radiation asymmetry to rectification effectiveness provides another explanation for why the Green's function forcing fails to generate rectified flow. With a forcing length scale of essentially zero, the forcing excites all values of k and hence the entire Rossby wave spectrum regards of the Rossby wave parameters. With no asymmetry in the zonal energy radiation of the population of waves excited, rectification does not extend outside the forced region.

(b) Meridional energy radiation and the divergence of the eddy fluxes of momentum

Including waves near or at $|k| = B$ (*i.e.* waves with a significant meridional component to their group velocity) in the excited spectrum is also important to rectification effectiveness because of its impact on the patterns of eddy zonal momentum flux divergence. Comparing the patterns of this "zonal eddy force" for the three special cases (Figure 2-9, *bottom row*) one sees it is necessary to excite waves with a meridional component to their group velocity to separate (in latitude) the eddy momentum flux convergence in the forcing region (acting as an eastward force) from the eddy momentum flux divergences (acting as westward forces) to avoid their mutual cancellation. As the forcing scale and optimal wavenumber become mismatched, the direction of energy radiation becomes less meridional and more zonal, and the regions

of momentum flux convergence and divergence converge to the same latitude band. As a result of the cancellation that then results, rectification diminishes.

Rectification is optimized when the forcing scale preferentially excites the wave at $|k| = B$ for different reasons depending on if one considers the eddy vorticity flux divergence or eddy momentum flux divergence. Considering first the former, note that a forcing scale equal to the wavelength corresponding to $|k| = B$ excites Rossby waves with $|k| \leq B$ and hence all the waves in the Rossby wave spectrum with westward group velocity and none with eastward group velocity. Maximizing the zonal asymmetry in zonal energy radiation is optimal for producing the two-lobed eddy vorticity flux divergence pattern that drives the rectified flows. From the perspective of eddy momentum flux divergence, note that the Rossby wave at $|k| = B$ has zero zonal group velocity and maximized meridional group velocity. This is optimal for separating in latitude the zonal eddy momentum flux regions of convergence and divergence and results in minimal self-cancellation of the effective eddy eastward and westward forces. In summary, it is properties of both the zonal and the meridional energy radiation of the optimal wave at $|k| = B$ that make it best suited to produce rectified flows by the mechanism proposed. Together they provide a self-consistent explanation of why when the forcing scale is such to preferentially excite this part of the spectrum, the rectification response is enhanced.

2.5 Results: The Effect of Stratification

The effects of stratification on the problem can be considered by posing the problem for a $1\frac{1}{2}$ layer (reduced-gravity) fluid. Like the case of the barotropic problem, insights come from both an analytical and numerical consideration of the problem.

2.5.1 Effect on Rectification Effectiveness

I first make progress on the stratified problem by extending the analytical solution of HR83 to include a dependence on the inverse Burger Number, Bu^{-1}, as appropriate for the $1\frac{1}{2}$ layer problem. The inverse Burger number, $Bu^{-1} = \left(\frac{L}{R_D}\right)^2$ i.e. the ratio

of the horizontal length scale of the motion to the Rossby deformation radius, $R_D = \frac{ND}{f}$[1], represents a measure of the relative importance of rotation in the horizontal to stratification in the vertical, and increases as the effects of stratification become increasingly important.

With the addition of stratification in the reduced-gravity configuration, the Green's function problem becomes:

$$\frac{\partial}{\partial t}\nabla^2\psi - Bu^{-1}\frac{\partial}{\partial t}\psi + \beta\frac{\partial}{\partial x}\psi = \delta(\vec{x})e^{i\omega t} \qquad (2.4)$$

The solution has the same form as the barotropic problem ($\psi = Jo(\gamma r)cos(Bx + \omega t) + Yo(\gamma r)sin(Bx + \omega t)$) with a modification to γ, changing it from satisfying $\gamma^2 = B^2$ in the barotropic case to $\gamma^2 = B^2 - Bu^{-1}$ in the reduced-gravity case. This immediately informs us of two important effects of stratification on the problem. First, stratification reduces the wavenumber of the response shifting the excited wave field to longer wavelengths than in the absence of stratification. Second, it introduces a new cut-off: for sufficiently large values of the inverse Burger number (such that γ becomes imaginary) radiating solutions no longer exist and as such we expect rectification to cease.

I consider also the solution to the fully nonlinear problem using the numerical model and explore the effect of stratification on rectification through varying the Burger number and comparing properties of the wave field and its rectification effectiveness. I consider a range of inverse Burger numbers from 0 to 0.3, equivalent to varying the deformation radius from infinite (the barotropic case) to ~ 100 km.

The result of the numerical parameter study reveals that, as with other system parameters, rectification effectiveness has a non-monotonic dependence on stratification as is shown in Figure 2-11. The dependence however is different in character to that on β, ω and L_F, suggesting two distinct regimes of behavior as opposed to a resonant peak symmetric about an optimal value. For small values of inverse Burger

---

[1]Here N is the buoyancy frequency, D is the active layer depth in a reduced-gravity layered configuration, and f is the Coriolis frequency.
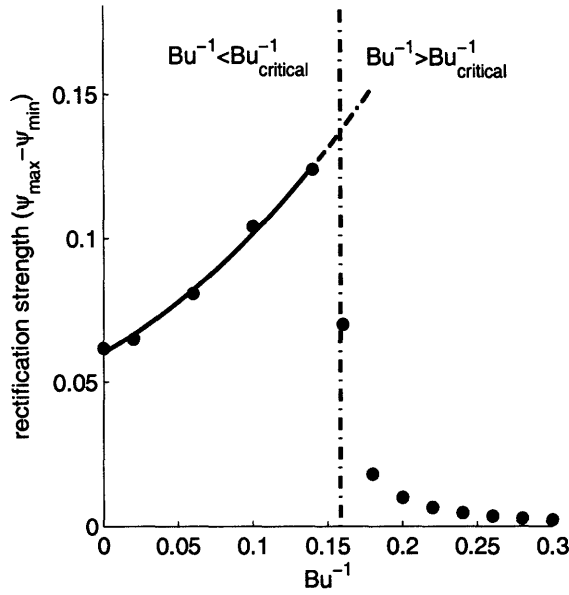
Figure 2-11: Dependence of mean rectified flow strength $(\overline{\psi}_{max} - \overline{\psi}_{min})$ ("rectification effectiveness") on the inverse Burger number, Bu^{-1}.

number, increasing the stratification causes the strength of the rectified flow to increase quadratically from the barotropic case. However at a critical value (here for $\beta = 0.05$, $\omega = 0.01$ and $L_F = 5$ at $Bu^{-1}_{critical} \approx 0.15$ corresponding to a deformation radius of order 130 km) the rectification response peaks and then drops off sharply to values less than that for a barotropic fluid as the inverse Burger number is further increased. This dependence raises several questions whose answers promise further insight into the rectification mechanism: Why does rectification effectiveness increase with stratification for small values of inverse Burger number? What sets the critical Burger number corresponding to the peak response? Why does rectification become ineffective for $Bu^{-1} > Bu^{-1}_{critical}$?

2.5.2 Interpretation via Wave Rectification

One can understand changes in rectification effectiveness with varying stratification as a result of both the effects revealed by the analytical solution and, as was the case with the earlier parameter studies discussed, changes in the population of waves that are selected to participate in the rectification process. In this case however, previous

49

resonant arguments will not be appropriate and as such, this study will teach us about additional requirements for effective rectification.

Stratification effects the Rossby wave dispersion relation by changing the radius of the dispersion circle (Figure 2-12). This has two important implications for the population of waves selected by the forcing. First, it reduces the spectrum of free wavenumbers available and hence concentrates the forcing amplitude into a narrower band of wavenumbers. Second, through the introduction of minimum zonal wavenumber, $k_{min} = -B + \frac{1}{2\omega}\sqrt{\beta^2 - 4\omega^2 Bu^{-1}}$, it eliminates the longest, fastest westward propagating waves from the available spectrum. Given it is only these waves that have a large enough group velocity to escape the forcing region radius in the critical time of half a forcing period, this increases the proportion of the forcing amplitude given to the shorter eastward propagating waves that remain inside the forcing region and participate in the rectification process (Figure 2-13). These effects can be seen in the snapshots of the excited wave fields and the orientation of their energy radiation for various values of Bu^{-1} in the upper two rows of Figure 2-14. As Bu^{-1} is increased towards the critical value, the wave field becomes less diverse in its population of waves, the waves become of larger amplitude, and there is an increasing dominance of eastward energy radiation.

Figure 2-14 suggests that this changing selection of waves enhances the rectification response for a few possible reasons. First, increased wave amplitudes (a consequence of concentrating the same forcing amplitude into a narrower spectrum of wavenumbers) results in larger values of the spatial gradients of the wave fluxes, and hence larger magnitudes of the eddy forcing terms, the eddy relative vorticity and zonal momentum flux divergences. Second, because increasing stratification tends to concentrate the wave response into a narrow band of wavenumbers centered around $k = B$, the waves selected as stratification is increased are the ones better suited to producing rectified flows on account of the significant meridional component to their group velocity and hence energy radiation. This results in a more effective separation in latitude of the regions of eddy zonal momentum convergence and divergence as is seen in the fourth row of Figure 2-14.
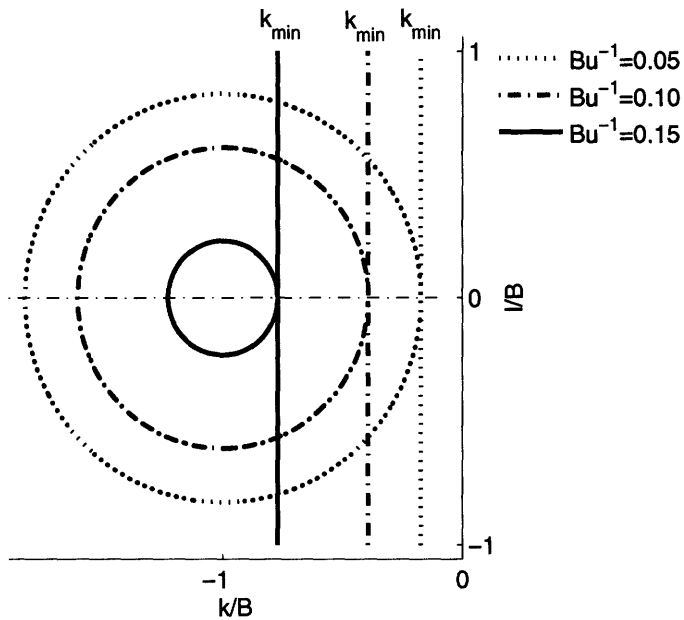
Figure 2-12: A visualization of the effect of stratification on the Rossby wave dispersion relation and therefore the wave population available to participate in rectification. Increasing Bu^{-1} shrinks the radius of the dispersion circle, reducing the range of k and l in the available spectrum. This eliminates the longest, fastest waves from the excited wave population by introducing a non-zero minimum k wavenumber, k_{min}, which increases with increasing inverse Burger number.
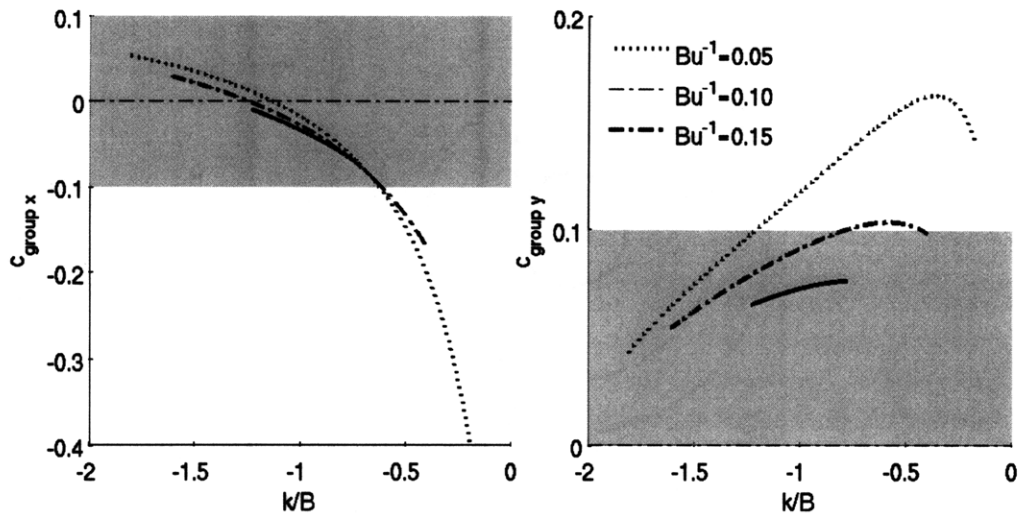
Figure 2-13: The energy radiation properties of the selected population of waves for various stratifications increasing towards the critical inverse Burger number. The zonal component (*left*) and the meridional component (*right*) of the wave's group velocity is shown as a function of zonal wavenumber for the range of wavenumbers in the available spectrum. The gray shading denotes the range of group velocities small enough such that the wave remains inside the forcing region in the critical time of half a forcing period and hence participates in rectification.
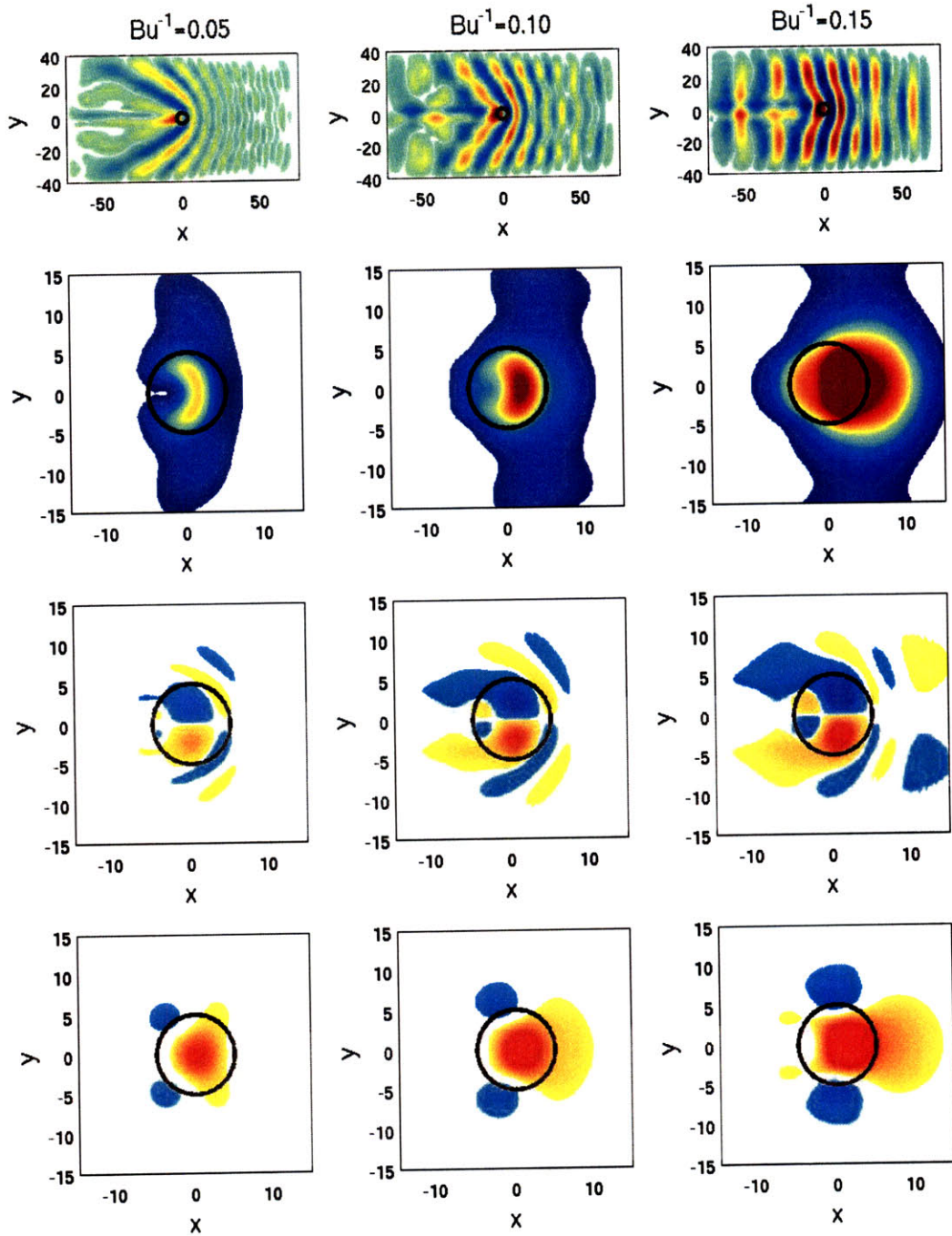
Figure 2-14: The effect of varying stratification by increasing Bu^{-1} towards the critical value on: (a) the population of waves excited (1st row); (b) the orientation of energy radiation from the forcing (2nd row); (c) the patterns of eddy relative vorticity flux divergence (3rd row); (d) the patterns of eddy zonal momentum flux divergence (4th row).
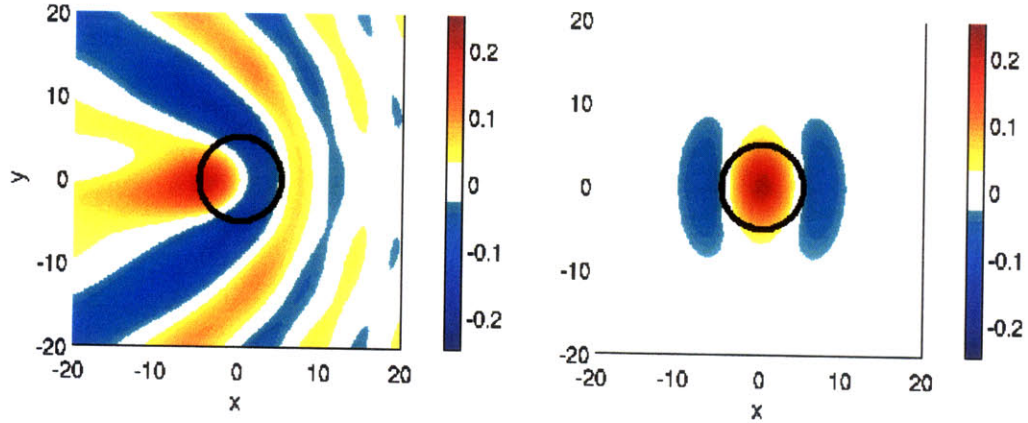
Figure 2-15: A comparison of the wave fields for the case $Bu^{-1} < Bu^{-1}_{critical}$ (*left*) *vs.* $Bu^{-1} > Bu^{-1}_{critical}$ (*right*). For sub-critical inverse Burger numbers, the plunger radiates waves outside the forcing region but for super-critical values, wave radiation ceases.

Hence it appears that rectification effectiveness increases with increasing stratification for small values of inverse Burger number as a result of concentrating the forcing amplitude into a narrow band of wavenumbers, exciting waves that both remain in the forcing region to participate in rectification, and that are also well suited to produce rectified flows on account of the orientation of their group velocity. But this enhancement does not continue indefinitely. Eventually, the stratification becomes large enough that the radius of the dispersion circle goes to zero and, as suggested by the analytical solution, the forcing fails to radiate waves. For the current set of parameters, this occurs at an inverse Burger number of $Bu^{-1} = B^2 = 0.16$. This condition defines the critical Burger number, and rectification effectiveness decays rapidly for larger stratifications. The failure of the forcing to radiate waves beyond this critical value in the numerical simulations is shown in Figure 2-15.

2.6 Results: The Effect of a Mean Background Flow

As a potentially useful model of localized wave radiation from an unstable jet, it is interesting to consider the plunger in the presence of a background flow and investigate its effect on the rectification process. To pose the simplest possible problem, I consider the same barotropic problem with the addition of a constant, uniform zonal background flow, U. The governing equation is modified to be:

$$\frac{\partial q}{\partial t} + J(\Psi + \psi, q) = F(x, y) - R\nabla^2\psi \qquad (2.5)$$

where Ψ is the stream function of the background flow given by $\Psi = -Uy$ in the case of a constant, uniform zonal flow as is considered here.

2.6.1 Effect on Rectification Effectiveness

The addition of the nonlinear term to the governing equation due to the background flow excludes a closed-form analytical Green's function solution in the previous form, so in this case I proceed directly to exploring the fully nonlinear problem with the numerical model. I explore the effect of a background zonal flow U on rectification through varying the magnitude and direction of U and comparing properties of the wave field and its rectification effectiveness. I find that the addition of even a small background flow has a significant effect on rectification effectiveness and hence consider non-dimensional Us in the range of -0.01 (westward) to +0.01 (eastward) which corresponds to dimensional flows of magnitudes on the order of 1 cm/s.

Again, similar to other system parameters, I find rectification effectiveness has a non-monotonic dependence on U in a physically relevant parameter range as is shown in Figure 2-16. In this case, the strength of the rectified flow increases with increasing U as it varies from large and westward towards eastward, peaks at a critical intermediate eastward speed (here for $\beta = 0.05$, $\omega = 0.01$ and $L = 5$ at non-dimensional $U_{optimal} = 0.004$ corresponding to a dimensional value on the order of 4 mm/s), be-
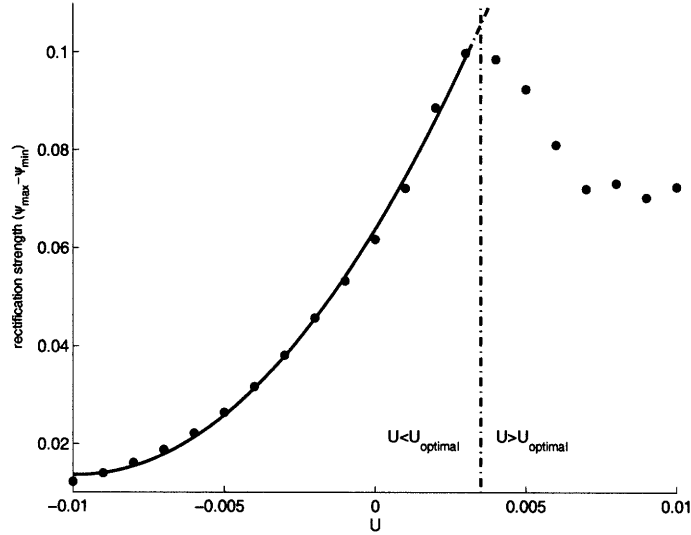
Figure 2-16: Dependence of mean rectified flow strength $(\overline{\psi}_{max} - \overline{\psi}_{min})$ ("rectification effectiveness") on the value of the constant zonal background flow U.

yond which it decreases again for large eastward values of U. Again, attempting to understand this dependence of rectification effectiveness on the value of the background flow, and in particular what sets the critical value for the maximum response, promises even more insight into the rectification mechanism.

2.6.2 Interpretation via Wave Rectification

In this case again I argue that the changing rectification response can be usefully understood by considering the rectification effectiveness of a given population of waves that are selected by the parameters of the problem, here the value of U. Similar to the case of stratification, where selection was achieved via changing the proportion of excited waves that remain in the forcing region based on a speed condition, here selection is via a condition on the net speed of the waves and whether they are (with the supplement or reduction provided by the background flow) sufficiently slow to remain in the localized vicinity of the forcing (in the critical time of a half period) to participate in the rectification that occurs there. Noting it is the net phase speed $(c_{phase} + U$ where c_{phase} is the intrinsic zonal wave speed) that matters, varying the magnitude of U is a means not only of varying the spectrum of excited waves (by

modifying the dispersion relation) but also of changing the fraction of the Rossby wave spectrum that meet this speed condition, and as such, changing the proportion of excited waves that rectify.

As a means of illustration, consider the fraction of the excited Rossby wave spectrum that meets the net phase speed requirement for three different values of U: $U < U_{optimal}$, $U \approx U_{optimal}$ (that producing the peak response) and $U > U_{optimal}$ (Figure 2-17) and the properties of the rectification in each of these three cases (Figure 2-18). For $U < U_{optimal}$ (in this case a large westward background flow), it is only the shortest, slowest waves (all with eastward group velocity) that aren't advected away from the plunger. Hence the waves that participate in rectification are limited to a narrow range of the available free Rossby wave spectrum $B << |k| < 2B$. The response is small because the waves with large meridional group velocity ($|k| \approx B$) are not included. As the magnitude of the westward flow is decreased however, the relative impact of the background advecting flow diminishes and faster waves corresponding to smaller values of $|k|$ now remain inside the forcing region in the critical time of a half period and so can now also participate in the rectification process. The effectiveness of the rectification increases. The response is large if the wave population that participates in the rectification includes the wave at $|k| = B$ with the maximum meridional group velocity while also maintaining asymmetry in zonal energy radiation. As U is increased further however, an even larger fraction of the spectrum is trapped, including now almost all the waves in the available spectrum with eastward group velocity. The response diminishes due to an increasing symmetry in the zonal radiation of energy to the east and west.

As seen in Figure 2-17, the peak response occurs when the background flow is such (through modification to the dispersion relation + selection based on the above speed criteria) to allow the optimal wave at $k = B$ to participate in rectification. Further insight is gained from the observation that $U_{optimal}$ is precisely the background flow required to arrest, through the condition $c_{phase} + U = 0$, the wave with the critical wavenumber $|k| = B$. As such, the wave that is optimized for rectification (that with maximum $|l|$, $|c_{gy}|$ and $|\overline{u'v'}|$), is rendered stationary to make the most significant
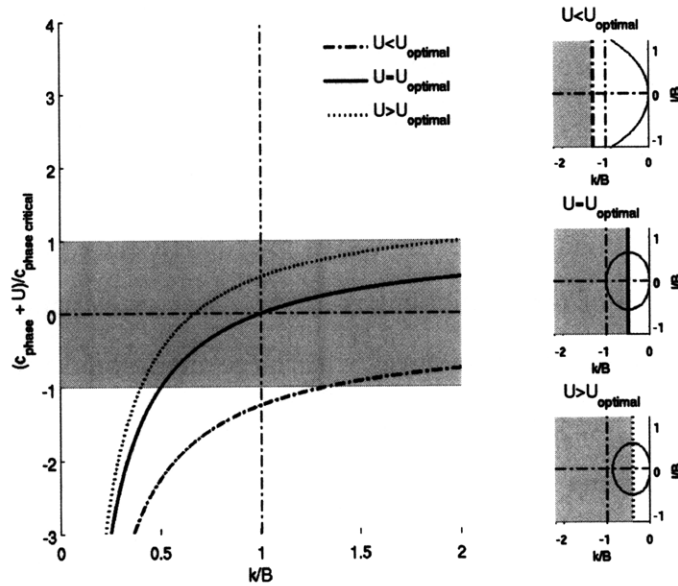
Figure 2-17: An illustration of the net wave speed condition that selects the population of waves that will participate in the rectification for a given mean background flow value. Curves show the net zonal phase speed (intrinsic zonal phase speed + the advecting background flow speed) as a function of zonal wavenumber k for three different characteristic values of U: sub-optimal (dashed), optimal (solid) and super-optimal (dotted), while the shaded region denotes the range of net speeds that are sufficiently slow such that the wave travels a distance less than a plunger radius in the time of one-half a forcing period (before the sign of the forcing changes sign) such that it remains "trapped" inside the forcing region. The intersection of the two delimit the range of k of the waves that participate in rectification, which is illustrated relative to the Rossby wave dispersion relation (altered by the addition of the given background flow) by the shaded region for each of the three cases on the right. Here it can be seen that for $U < U_{optimal}$ and $U > U_{optimal}$ participating waves do not include the optimum wave at $|k| = B$, while for $U = U_{optimal}$ the optimum wave is included.
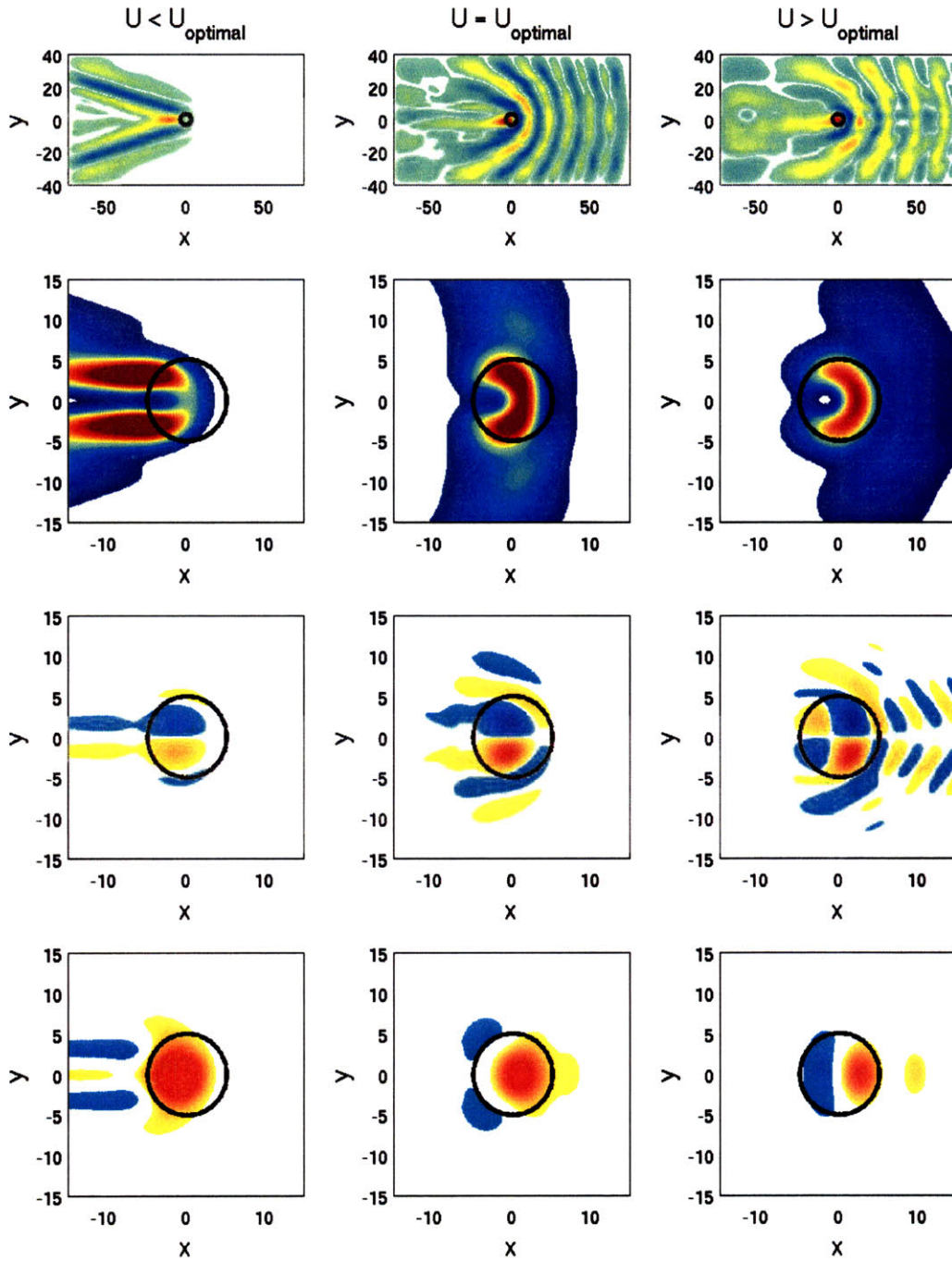
Figure 2-18: The effect of varying U from $U < U_{optimal}$ to $U > U_{optimal}$ on: *(a)* the population of waves excited *(top row)*; *(b)* the orientation of energy radiation from the forcing *(2nd panel)*; *(c)* the patterns of eddy relative vorticity flux divergence *(3rd row)*; *(d)* the patterns of eddy zonal momentum flux divergence *(4th row)*.
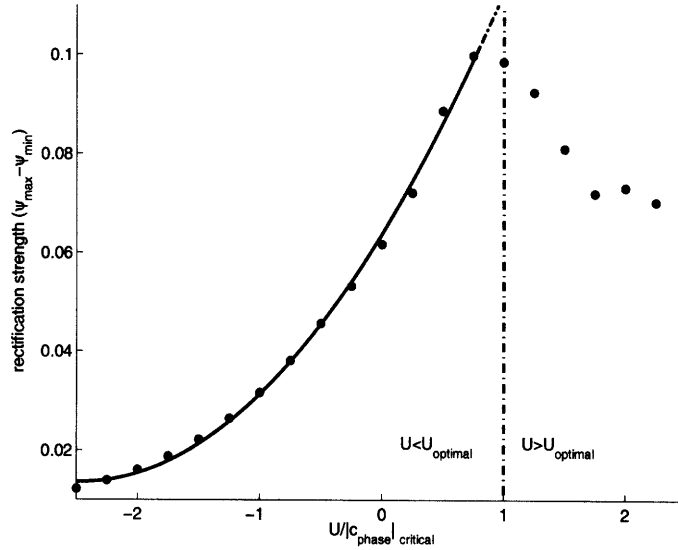
Figure 2-19: The dependence of mean rectified flow strength on the value of U as in Figure 2-16, but with the x axis normalized by the magnitude of the intrinsic zonal phase speed of the wave with the optimal zonal wavenumber $|k| = B$. The peak response occurs near where the background flow is equal and opposite to the phase speed of the wave with this optimal wavenumber, hence making the wave with the optimal characteristics for rectification stationary.

contribution to the rectification process. As seen in Figure 2-19, this condition of matching U to be equal and opposite to the zonal phase speed of the wave with the optimal wavenumber $|k| = B$ predicts the location of the peak response well.

Finally, thinking in terms of the rectification properties of the arrested wave is useful also in explaining the asymmetry observed in the rectification response for $U < U_{optimal}$ vs. $U > U_{optimal}$. As it has been shown, the rectification strength is directly related to the divergence of the eddy vorticity flux, which, as observed in the numerical simulations, depends critically on the magnitude of the Reynolds stress $\overline{u'v'}$ in the vicinity of the plunger. Now one expects, at least in a weakly nonlinear regime where the wave can be approximated as $\psi \propto e^{i(kx+ly-\omega t)}$, that $\overline{u'v'}$ will vary as kl (the product of the zonal and meridional wave numbers) and hence I examine how this quantity varies with U. Taking the k and l associated with the arrested wave as characterizing the population of rectifying waves, one sees that the Rossby wave dispersion relation is such that this product shows the same asymmetry: the relative size of $\overline{u'v'}$ approximated as kl increases rapidly for the waves arrested by $U < U_{optimal}$
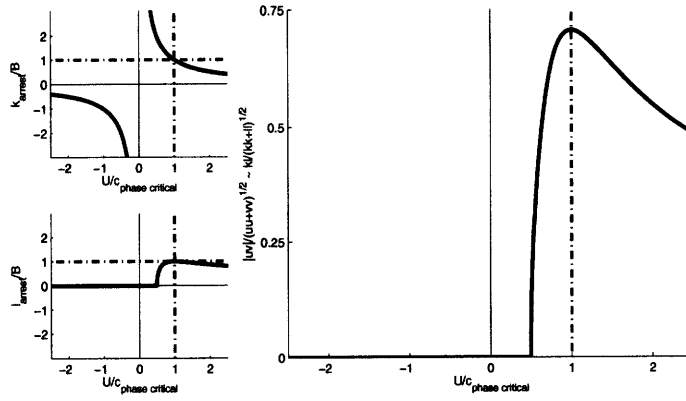
Figure 2-20: An explanation for the asymmetry in the rectification response for $U < U_{optimal}$ vs. $U > U_{optimal}$ based on the changing relation between k and l for a Rossby wave with $|k| > B$ vs. $|k| < B$. For $|k| > B$ (corresponding to $U < U_{optimal}$ if one takes k to be the arrested wavenumber), $k << l$, but near $|k| = B$, l increases rapidly to a comparable magnitude (*left*). This produces a rapid increase in the relative magnitude of kl (characteristic of the size of $\overline{u'v'}$) (*right*). For $|k| < B$ (corresponding to $U > U_{optimal}$ again if k is taken to be the arrested wavenumber) however, the change in both k and l is much slower, and hence they remain of comparable magnitude over a much larger range of k / U. This may account for the much slower change in rectification effectiveness observed.

and declines much more slowly showing signs of saturation for the waves arrested by $U > U_{optimal}$ (Figure 2-20). This suggests that it is this asymmetry between the magnitudes of k and l for a Rossby wave with $|k| > B$ vs. $|k| < B$ that is responsible for the asymmetry in rectification response observed.

2.7 Results: Extension to the Strongly Nonlinear Regime

A final parameter variation that is of interest is of course the forcing amplitude. As discussed in Section 2.3, in the limit of a small forcing amplitude, an analytical expansion solution predicts that the mean rectified flow will be given by the zonal integral of the relative vorticity flux divergence (the time-mean Jacobian) of the linear forced wave field, and be of the order of the square of the forcing amplitude. But what about rectification in a strongly nonlinear regime? Experiments varying system

61

parameters, stratification and the background flow discussed thus far have all been forced with a small forcing amplitude, and given the weak nonlinearity, interpretation in terms of the rectification effectiveness of a given population of linear Rossby waves has been appropriate. Where do the small-amplitude limit arguments break down and why? Do lessons learned in the weakly nonlinear regime discussed thus far have any use in understanding rectification in the strongly nonlinear regime?

2.7.1 Effect on Rectification Effectiveness

To examine the effect of forcing amplitude and the degree of nonlinearity on rectification effectiveness, I conduct a number of simulations varying the forcing amplitude. Results showing the dependence of rectification effectiveness on the forcing amplitude for the typical set of system parameters ($\beta = 0.05$, $\omega = 0.01$ and $L = 5.0$) are given in Figure 2-21. Note that for all "small amplitude" simulations discussed so far, the forcing amplitude was 0.001 (dimensionally equivalent to a wind stress of 0.1 N/ms^2 or equivalently an Ekman pumping velocity of 1x10^{-4} m/s), hence I now consider cases where the amplitude of the forcing is increased by more than an order of magnitude from these "wave-like" cases.

Figure 2-21 shows that the results from these tests confirm the analytical prediction of a quadratic dependence of mean flow strength on the forcing amplitude, A, for small values of A. This dependence however is observed to break down as the forcing amplitude / degree of nonlinearity of the flow is increased (for this set of parameters the critical amplitude is of the order $A = 0.005$). Beyond this critical value, in a regime where the degree of nonlinearity is large enough that the "weakly nonlinear" classification is no longer valid, the mean flow response shows signs of saturation, increasing much more slowly with an increase in forcing amplitude.

I am heartened however by the fact that despite this systematic change of behavior, examination of both the wave fields and the time-mean rectified flow for the "weakly nonlinear" and "strongly nonlinear" cases remain qualitatively very similar (Figure 2-22). This suggests that lessons learned about the rectification mechanism may still have some use in the strongly nonlinear regime. There are of course also some
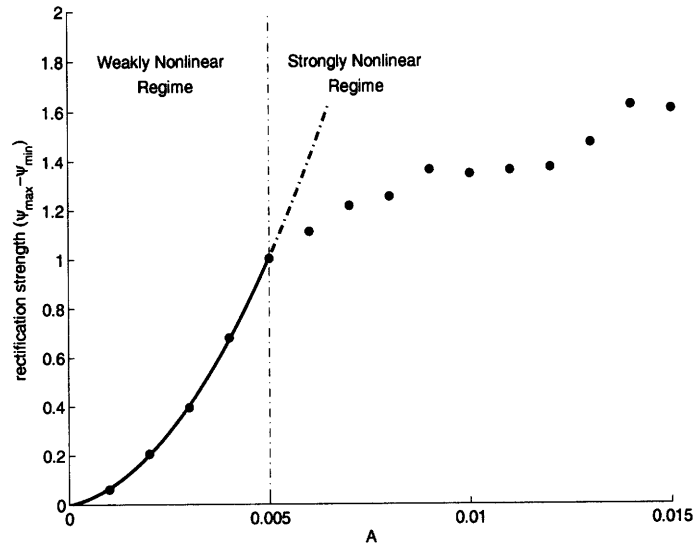
Figure 2-21: Dependence of mean rectified flow strength $(\overline{\psi}_{max} - \overline{\psi}_{min})$ ("rectification effectiveness") on the forcing amplitude for the standard case $\beta = 0.05$, $\omega = 0.01$, $L = 5.0$. The transition between a quadratic dependence of rectification strength on forcing amplitude to a much slower ($\sim$ linear?) rate of increase defines the transition between "weakly" and "strongly" nonlinear regimes.

important differences: when the system becomes strongly nonlinear, the wave field becomes more "circular" and the time-mean rectified flow becomes zonally "trapped" close to the forcing region while increasing its meridional extent. These changes hint at differences that may explain the cause of saturation in rectification effectiveness observed at large forcing amplitude.

2.7.2 Interpretation Via Wave Rectification Modified by Wave-Mean Flow Interactions

In previous sections, rectification and variations in its effectiveness due to variations in forcing and flow parameters have been interpreted via eddy momentum and vorticity transport, enstrophy balances, and the rectification effectiveness of a given population of linear Rossby waves selected by the parameters of the problem. As it will be shown, these same factors will be important in understanding rectification in the strongly nonlinear regime as well, but with an important modification due to the addition of mean-flow interaction now being important.
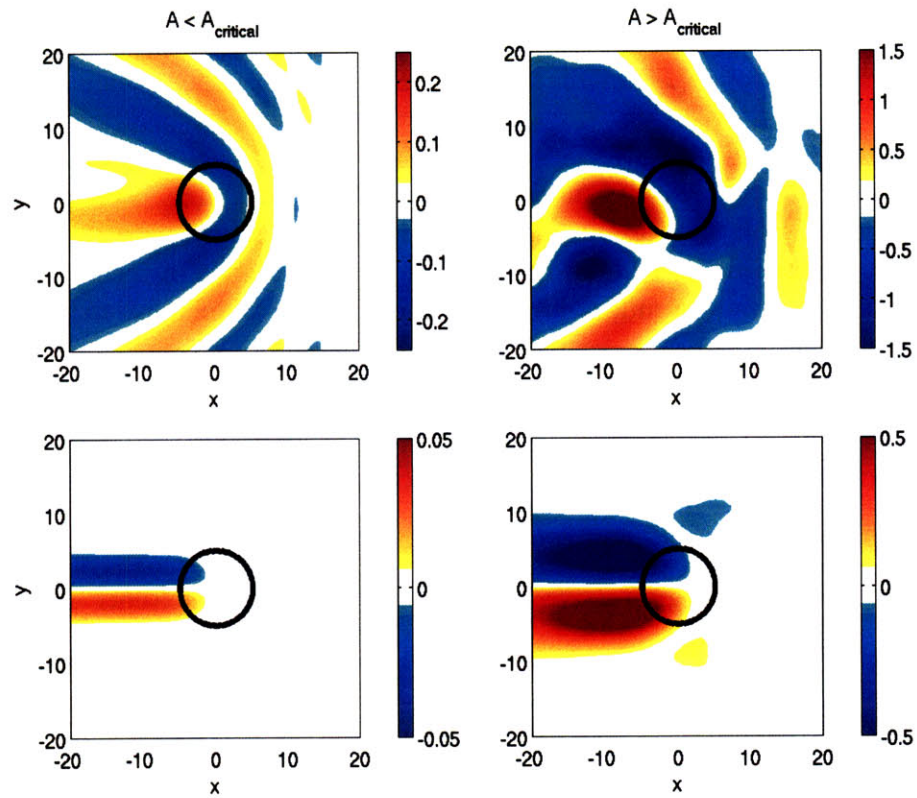
Figure 2-22: A comparison of wave fields (*top*) and their associated time-mean recti-fied flows (*bottom*) for the "weakly nonlinear" (*left*) *vs.* "strongly nonlinear" (*right*) case.

I propose that a useful way to understand rectification in the strongly nonlinear regime is via the same picture of the rectification mechanism developed in the weakly nonlinear case with the addition of a mean flow and its associated wave-mean flow interactions. This is a consequence of the rectified mean flow now being sufficiently strong that the interaction between the waves and the mean flow is significant. This interaction will be much more complicated than the case of a uniform mean background flow not only because the mean flow strength will be a direct function of the rectification effectiveness, but also because the feedback it will have on the waves' ability to rectify will have important spatial dependence, including, but not limited to, making, in certain locations, a significant contribution to the effective background PV gradient through which the waves are propagating. Despite this complexity however, as it will be shown, the net effect of its role will be to always counteract or reduce the ability of the waves/eddies to rectify. It is this counteracting effect that results in the saturation in the mean-flow strength at large forcing amplitude that is observed.

To see how the contribution of the presence of the rectified mean flow reduces rectification effectiveness at large forcing amplitudes I re-consider the dynamical quantities that were instructive in understanding rectification in the case of a small forcing amplitude and compare them for the weakly *vs.* strongly nonlinear regimes.

(a) Vorticity flux balances

First, I consider the time-mean vorticity flux balances for each case (Figure 2-23). In the weakly nonlinear case (Figure 2-23 *top row*), consistent with the simulations of HR83, the balance is predominantly a two term balance between the eddy PV flux divergence $(\overline{J(\psi\prime, \nabla^2\psi\prime)})$ and the planetary vorticity flux divergence $(\beta\overline{v})$ (a balance often referred to as the "eddy Sverdrup balance"). Mean meridional motions (northward north of the plunger and southward south of the plunger) are generated to produce the planetary flux divergence required to balance the eddy flux divergence, and it is these mean motions that are responsible for the homogenization of the mean PV and indirectly, driving the time-mean recirculations.
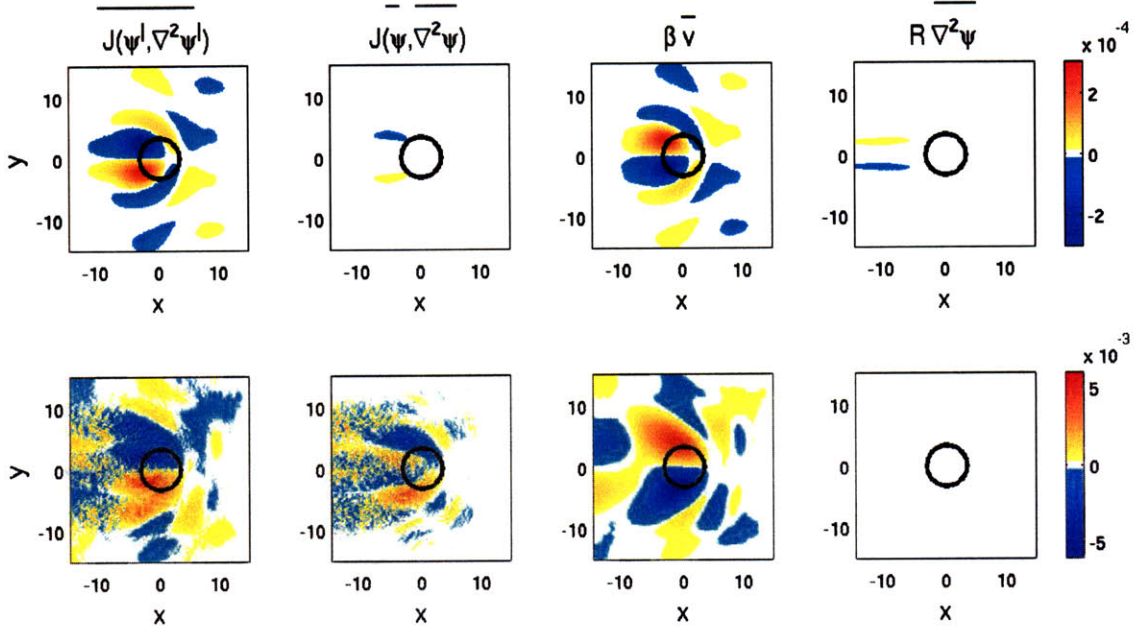
Figure 2-23: The time-mean vorticity balance: $\overline{J(\psi', \nabla^2\psi')} + J(\overline{\psi}, \overline{\nabla^2\psi}) + \beta\overline{v} = -R\overline{\nabla^2\psi}$ for the weakly nonlinear case (*top*) vs. the strongly nonlinear case (*bottom*).

In the strongly nonlinear case however (Figure 2-23 *bottom row*), as a result of the mean zonal flows generated by the rectification becoming sufficiently strong, this balance becomes three-way, as now the contribution of the mean relative vorticity flux ($J(\overline{\psi}, \overline{\nabla^2\psi})$ is also significant. Inside the time-mean jet, the mean relative vorticity flux divergence has the opposite sign to the eddy relative vorticity flux divergence and hence counteracts its effects. The mean meridional velocities required to balance the eddy flux divergence don't have to be as large, PV mixing is reduced and the strength of the recirculations grows less quickly.

(b) Enstrophy balances

This picture of the mean advection now becoming a player and resulting in decreased rectification effectiveness is further suggested by an examination of the terms in the enstrophy variance budget for the two cases. Recall that up-gradient eddy PV transport, and hence rectification, requires the eddy enstrophy destruction to be in some places positive, which in turn requires the sum of the other terms in the time-mean enstrophy variance budget (enstrophy variance advection by mean and

66

eddy velocities + dissipation) to be in some places negative. This could be achieved in different ways, but by keeping advection small relative to dissipation (which is always negative) this condition is guaranteed. This provides another explanation of the break-down in rectification effectiveness at large forcing amplitudes: when the mean rectified flows generated become sufficiently strong such that the mean enstrophy variance advection is no longer small (*i.e.* small relative to the eddy generation and dissipation), it becomes significant in the enstrophy variance budget and in doing so, acts to reduce the eddy up-gradient transport of PV responsible for the rectification. This can be seen in Figure 2-24, which shows that the dominant balance in the weakly nonlinear case (Figure 2-24 *top row*) is between eddy enstrophy destruction $(\overline{\mathbf{u}'\zeta'} \cdot \nabla\overline{\zeta})$ and dissipation $(-R\overline{\frac{\zeta'^2}{2}})$, whereas in the strongly nonlinear case (Figure 2-24 *bottom row*) all four terms in the budget are significant. The mean advection of enstrophy variance $(\nabla \cdot \overline{\mathbf{u}}\overline{\frac{\zeta'^2}{2}})$ acts in the opposite sense to the eddy enstrophy destruction inside the critical region of the forcing, and as such acts to reduce the rectification effectiveness from that which would be achieved in the absence of mean advection.

(c) Eddy zonal momentum fluxes

The importance of the mean flow interaction in the strongly nonlinear case can be seen also in the eddy zonal momentum flux divergence field (Figure 2-25). In the weakly nonlinear case (Figure 2-25 *left*), the regions of zonal momentum flux divergence occur north and south of the forcing latitude, and result from the waves radiating away from the forcing. As such, due to the separation in latitude of the regions of momentum divergence and convergence, the waves/eddies are effective at driving the westward recirculations. In the strongly nonlinear case (Figure 2-25 *right*) however, similar to the case of a strong eastward mean background flow, the main source of momentum flux divergence now lies on the jet axis west of the forcing, here resulting from the mean jet "running into" the westward propagating waves. The eddy momentum flux divergence acts now not to accelerate westward flows but instead to decelerate the mean eastward jet, and rectification effectiveness is reduced
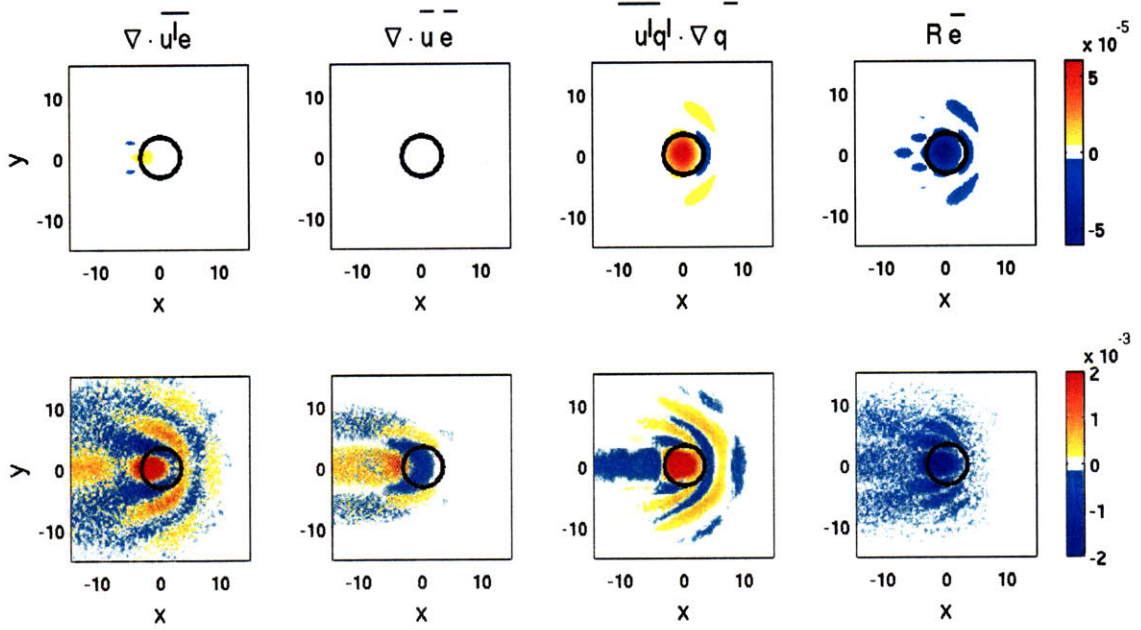
Figure 2-24: The time-mean enstrophy variance ($\frac{\zeta'^2}{2}$) budget: $\nabla \cdot \overline{\mathbf{u}'\frac{\zeta'^2}{2}} + \overline{\mathbf{u}} \cdot \nabla \overline{\frac{\zeta'^2}{2}} + \overline{\mathbf{u}'\zeta'} \cdot \nabla \overline{q} = -R\overline{\frac{\zeta'^2}{2}}$ for the weakly nonlinear case (*top*) *vs.* the strongly nonlinear case (*bottom*).

as a result.

2.8 Summary and Discussion

In summary, I have presented results from a study of eddy-driven mean flow in an idealized set-up, specifically the generation of two counter-rotating time-mean recirculation gyres west of a localized oscillatory forcing.

From both an analytical analysis in terms of an expansion solution in the forcing amplitude (valid in a weakly nonlinear regime) and the solution to the fully nonlinear problem obtained from numerical simulations, one understands that the mean flow is directly driven by the relative vorticity flux divergence of the forced wave or eddy field. Visualization of the eddy-mean flow interaction terms from the fully nonlinear numerical solutions show that rectified flow is produced because there is an up-gradient eddy PV flux inside the forcing region (a consequence of positive eddy
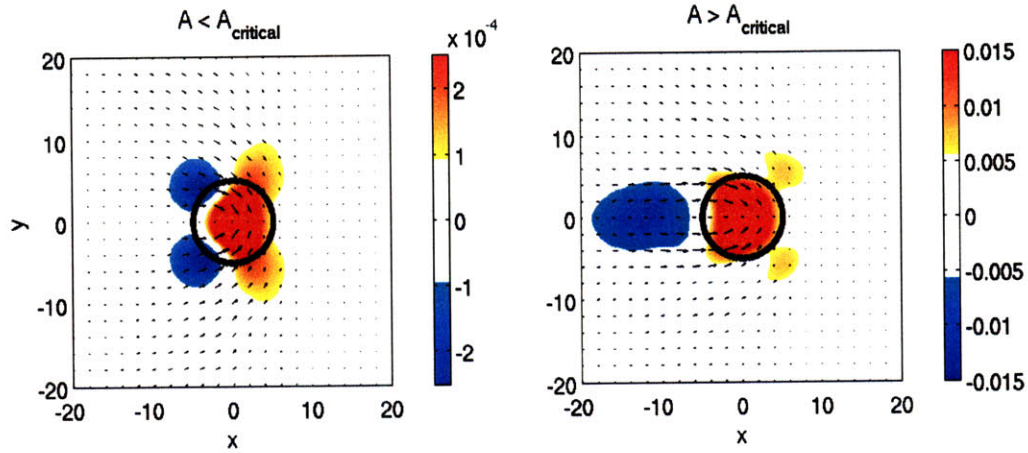
Figure 2-25: A comparison of the time-mean zonal "eddy force" (the negative of the time-mean eddy zonal momentum flux divergence, $\frac{\partial}{\partial x}\overline{u'u'} + \frac{\partial}{\partial y}\overline{u'v'}$) (color) with eddy momentum transport $(\overline{u'u'}\vec{i} + \overline{v'v'}\vec{j})$ (vectors) overlaid for the "weakly nonlinear" (*left*) *vs.* "strongly nonlinear" (*right*) case.

enstrophy destruction here) or equivalently because there is an eddy zonal momentum flux towards the forcing region (a consequence of eddy/wave energy radiation away from the forcing source). The existence of a forcing region (where enstrophy is destroyed and waves/eddies are permitted to flux PV up-gradient) is critical and highlighted by the fact that a Green's function solution (where the forcing region is reduced to a delta function in space) fails to produce rectified flows.

Numerical simulations show that the strength of the rectified flow that is generated is sensitive to system parameters and from this dependence one learns that the properties of the population of waves that participate in the rectification process determine how effective it is. Of particular importance is the nature of the energy radiation of the selected population of waves, as this determines the spatial distribution of wave activity and hence the spatial gradients of the wave/eddy terms. Rectification is most effective when there is a large asymmetry in zonal energy radiation east *vs.* west (as is achieved by exciting only a fraction of the Rossby wave spectrum) and when there is a significant component of meridional energy radiation (as is achieved if waves near $|k| = B$ are excited). This ensures that the pattern of eddy vorticity flux divergence is not perfectly asymmetric in x (and hence not self-canceling in the

zonal integral) and that the pattern of eddy zonal momentum flux divergence has its regions of convergence and divergence separated in latitude (again not self-canceling in the zonal integral). Varying either the forcing length scale or the spectrum of available free Rossby waves (by varying the dispersion relation through variation of β or forcing frequency) is a means to vary the population of waves that are excited, and as such vary the rectification effectiveness. The peak (resonant) response occurs when the forcing length scale matches the wavelength associated with the wave at the origin of the Rossby wave dispersion circle at $|k| = |l| = B$ so the wave with the optimal radiation properties is preferentially excited.

Stratification effects the rectification in a number of ways. As is seen in the modification to the analytical solution, stratification shifts the excited wave field to higher wavenumbers (shorter wavelengths) compared to the barotropic case and introduces a new cut-off such that for sufficiently large values of Bu^{-1}, the forcing can no longer radiate waves. Stratification also introduces a new way to change rectification effectiveness by eliminating the longest, fastest waves in the available free Rossby wave spectrum. This improves rectification effectiveness because it concentrates the forcing amplitude into a narrow band of wavenumbers, exciting waves that both remain in the forcing region to participate in rectification, and that are also well suited to produce rectified flows on account of the orientation of their group velocity. This enhancement to rectification effectiveness continues as increasing stratification concentrates the response into a narrower and narrower band of wavenumbers until the point that the stratification becomes large enough that the radius of the dispersion circle goes to zero and, as predicted by the analytical solution, the forcing fails to radiate waves. Rectification ceases as a result.

The presence of a mean background flow also has an important effect on rectification. It too is a means by which to select the waves that participate in the rectification, in this case via the condition that the net speed of the waves (given by the intrinsic zonal phase speed + the background flow) must be sufficiently slow to remain in the forcing region in one-half a forcing period. The maximum rectification occurs when the background flow is precisely that required to arrest the wave with the

critical wavenumber $|k| = B$, hence making the wave with the optimal characteristics for rectification stationary.

Finally, extending these results from a weakly nonlinear regime to a fully nonlinear one shows that the quadratic dependence of rectified flow strength on forcing amplitude, valid for the weakly-nonlinear regime, breaks down as the forcing amplitude / degree of nonlinearity of the flow is increased. In the strongly nonlinear regime, the increase in rectification effectiveness shows signs of saturation, increasing approximately linearly with forcing amplitude. Despite this change, qualitatively both the wave field and patterns of rectified flow are similar in both regimes, and a useful way to understand rectification in the strongly nonlinear case is via the same picture of the rectification mechanism developed in the weakly nonlinear case with the addition of the (rectified) mean flow and its associated wave-mean flow interactions. This is a consequence of the rectified mean flow becoming sufficiently strong at large forcing amplitudes such that the interaction between the waves and the mean flow becomes significant. The nature of this interaction has important spatial dependence given the spatial dependence of the mean rectified flow, but its net effect is to counteract or reduce the ability of the waves/eddies to rectify. This is achieved by the mean relative vorticity flux, acting in the opposite sense to the eddy flux divergence, becoming important in the forced latitude band, the mean advection of enstrophy variance, counteracting the eddy enstrophy destruction, becoming important inside the forcing region, and the mean-jet/wave interactions providing a source of eddy zonal momentum flux divergence that acts to decelerate the time-mean jet. As a result of these wave-mean flow interactions, a saturation in the rectified mean-flow strength in the strongly nonlinear regime results. This saturation phenomenon implies that efficient rectification reflects a quasi-linear resonance phenomenon that weakens for strong non-linearity, consistent with one's expectation that in a strongly nonlinear regime β and Rossby wave dynamics can be neglected.

To close, I try to consider the relevance of the results described here to oceanic applications. I note that the parameter values explored in this study are realistic and

relevant to synoptic scales of say a strong localized wind-stress or a localized concentration of eddy activity. I also note the the magnitude of the mean flow generated, on the order of the dimensional equivalent of a few centimeters per second for small amplitude forcing and up to the dimensional equivalent of tens of centimeters per second for large amplitude forcing, could be significant, especially below the thermocline where the mean velocities are small. However, it is important to also note that, as it has been shown, in order for the rectification to be effective, a very special relationship between the forcing and flow parameters must exist. Significant stratification or a background mean flow could also render the mechanism ineffective in practice. It appears that if this mechanism is important, it will be so only in particular cases where all the conditions are such to provide the required optimal conditions.

Nevertheless, it is my opinion that the rectification mechanism considered here could potentially be important especially in the driving of deep flows. If this were true, these mean flows would not be represented in a general circulation model with eddy effects parameterized simply as down-gradient diffusion. As is discussed in the next chapter, a study examining the downstream equilibration of an unstable jet (as say would be relevant to a separated western boundary current) suggests that this "plunger-like" mechanism of driving time-mean recirculations has application as a useful model for the effect of the eddies downstream of jet stabilization. Further exploration of the relevance of this process to the deep recirculation gyres in the Kuroshio Extension region, through the analysis of both direct observations and an eddy-resolving general circulation model, is on-going.

Chapter 3

Eddy-Mean Flow Interactions in the Downstream Evolution of an Idealized Western Boundary Current Jet

Abstract

I present results from a theoretical study on the role of eddy variability in the time-mean dynamics of a zonally-evolving, unstable, strongly inertial jet in a configuration and parameter regime that is relevant to oceanic western boundary current jets. Progress is made by diagnosing the eddy effect on the time-mean circulation, examining the mechanism that permits the eddies to drive the time-mean recirculation gyres, addressing the relative importance of eddy vs. steady state inertial terms, and contrasting barotropic, baroclinic, and mixed instability models.

I find that the nature of the eddy-mean flow interactions in this idealized western boundary current jet system is critically dependent on the downstream position relative to the evolving stability properties of the time-mean jet. Near the western boundary eddies act to stabilize the jet through down-gradient fluxes of potential vorticity (PV), but downstream of where the time-mean jet has (through the effect of the eddies) been stabilized, eddies act to drive the time-mean recirculations through the mechanism of an up-gradient PV flux. This up-gradient flux is permitted by an eddy enstrophy convergence downstream that results from the generation of eddies in the upstream region where the jet is unstable, the advection of that eddy activity downstream by the jet, and eddy enstrophy dissipation downstream of jet stabiliza-

tion. It is in this region of eddy decay that eddies drive the time-mean recirculations through the mechanism of nonlinear eddy rectification resulting from the radiation of waves from a localized region on a varying background PV field. I find that these same mechanisms operate in both the barotropic, baroclinic and mixed instability cases. In the two-layer case, the eddy-driving of the recirculations continues to be dominated by relative vorticity fluxes, and as such remains an essentially barotropic mechanism. Thickness fluxes act to equalize the eddy forcing in each layer, making the recirculations more barotropic.

In the relevant parameter regime, I find that eddy forcing and steady-state inertial terms are of equal importance in the downstream development of the time-mean jet-gyre system. Hence, including eddies in our description of the dynamics of these systems is essential. In the absence of eddy terms, the magnitude of the upper ocean jet transport would be significantly less, and the abyssal ocean recirculations (and their significant enhancement to the jet transport) would be missing altogether.

3.1 Introduction

3.1.1 Motivation

The Gulf Stream (GS) and the Kuroshio Extension (KE) current systems are among the most energetic current systems in the world ocean and are dominant features of the North Atlantic and North Pacific Oceans circulations respectively. After separating from their respective coasts at Cape Hatteras and the Boso peninsula, these western boundary currents (WBCs) turn eastward, and flow into the deep ocean. Here, they are no longer constrained by topography, and they become free, inertial, unstable jets, characterized by large amplitude meanders and pinched-off eddies. These WBC jets are of fundamental importance to the dynamics of steady basin-scale circulations, as regions of enhanced exchange of potential vorticity (PV) and energy, and by acting to restore global balances between forcing and dissipation. Understanding their dynamics is fundamental to improving our understanding of the ocean general circulation.

Observations of various types in all oceans indicate that eddy kinetic energy (EKE) is strongly (orders of magnitude) spatially inhomogeneous, reaching maxima in the vicinity of strong currents such as these WBC jets (Ducet and Le-Traon, 2001).

The GS and KE regions are prime examples of this, where the meandering of the streams results in an increase in the eddy kinetic and potential energies by orders of magnitude along the climatological mean path of the jet at all depths (Schmitz, 1984; Malanottte-Rizzoli, 1994; Hogg, 1988; Bower and Hogg, 1992). Given such high levels of eddy activity in these regions, our description of WBC jet dynamics clearly needs to include an understanding of the effects of this eddy variability.

An investigation into eddy-mean flow interactions in WBC jets is important because eddies potentially play an important role in the dynamics of these jet systems. Through their fluxes of momentum and vorticity, eddies can be important in determining the character of the mean jet (its mean strength, structure and stability properties), acting not only as a source of dissipation, but also as a driving force through nonlinear eddy-eddy and eddy-mean flow interactions (Thompson, 1977, 1978; Dewar and Bane, 1989; Hogg, 1992; Watts et al., 1995). Eddies also play a potential role in driving recirculations, the phenomenon through which the downstream transport of the separated jet is increased many-fold by the development of flanking, weakly depth-dependent gyres (Richardson, 1985; Schmitz and McCartney, 1993). In addition, eddy variability appears to also be important in coupling the strong motions in these baroclinic jets to deep abyssal circulations, driving the deep recirculation gyres (Hogg, 1983, 1985, 1993), and potentially acting back on the upper jet, influencing its speed and direction (Cronin and Watts, 1996; Cronin, 1996). Finally, eddies may also play a role in modulating the low-frequency variability in jet transport, the degree of meandering intensity / EKE, and the recirculation structure that these systems exhibit (Lee and Cornillon, 1995; Qui, 1995; Kelly et al., 1996). There are many possible explanations for the source of this variability ranging from external (e.g. atmospheric) forcing (Qui, 1995) to multiple state equilibria associated with highly inertial dynamics (McCalpin and Haidvogel, 1996; Berloff and Meacham, 1998; Primeau, 1998; Berloff and McWilliams, 1999; Meacham, 2000), but eddy effects may be important as well. For example, Spall (1996) and Qui (2000) have shown that the process of eddies fluxing PV away from the detached jet can lead to natural low-frequency oscillations (i.e. even without atmospheric coupling) in recirculation gyre

systems.

3.1.2 Past Work

Given the importance of WBC jets, work on the subject of their dynamics has had
a long history. Much has been learned about these systems, and their recirculation
gyres in particular, through idealized theoretical studies, *i.e.* via analytical analysis
or a numerical simulation of the solutions of various forms of the simplified equations
of motion in simplified configurations. Theoretical studies that lay the foundation
onto which the work described here will build can be thought of dividing into the
following three categories:

1. inertial theories in which time-mean recirculation gyres can arise from the
   steady state time-mean advection of PV alone (*e.g.* Fofonoff, 1954; Marshall
   and Nurser, 1986; Greatbatch, 1987; Cessi, 1990)

2. eddy-driven theories in which the effects of a directly prescribed vorticity forcing
   generates mean rectified flows through eddy-mean flow and eddy-eddy interac-
   tions (*e.g.* Starr, 1968; Whitehead, 1975; Haidvogel and Rhines, 1983; Cessi
   et al., 1987; Malanotte-Rizzoli et al., 1995; Berloff, 2005)

3. unstable jet studies in which the generation of mean recirculations arise from
   unstable jets in which eddy effects (arising from jet instabilities) and inertial
   effects can both play a role (*e.g.* Spall, 1994; Jayne et al., 1996; Beliakova, 1998;
   Jayne and Hogg, 1999)

Collectively these approaches demonstrate that recirculations can arise from the
steady-state inertial terms, or the rectification of eddy fluxes, or potentially both.
Steady-state inertial theories show that closed recirculation gyres are steady solutions
to the nonlinear equations of motion forced by a balance between the inertial term (the
mean advection of PV) and dissipation. At the same time, time-dependent numerical
simulations demonstrate that zonal flows and closed recirculations can be generated

solely from rectification effects through nonlinear eddy-mean flow and eddy-eddy interactions. Finally, rectified mean flows can also result from forcing by an unstable jet. In this case, mean recirculations to the north and south of the jet are produced by eddies, generated by the jet's instability, acting to smooth the PV anomalies associated with the jet, and in the process produce homogenized regions in which essentially inertial recirculations can develop. It is interesting that recirculations generated in this way in barotropic models are able to predict recirculation strength quite accurately in spite of their reliance on the barotropic instability mechanism.

Perhaps the most relevant precursory work to the study here is that of Beliakova (1998), who studied the problems of the generation and maintenance of recirculations by Gulf Stream instabilities. The problem of recirculation development was considered in the framework of the free spin-down of a $1\frac{1}{2}$ and 2-layer, zonally-symmetric, quasi-geostrophic jet via linear and nonlinear stability analysis, while questions related to the maintenance of the recirculations, with a specific focus on the low-frequency variability and multiple dynamical regimes of these jet-recirculation gyres systems, were examined in the context of a reduced gravity and 2-layer colliding jet model forced by inflows and outflows through a closed western boundary and an open eastern boundary. The work demonstrated that eddy-driven recirculations are robust features of the 2-layer model especially, with recirculation strength being a non-monotonic function of the baroclinic velocity parameter: strongest for strongly baroclinic basic flows, weakest for flows with intermediate baroclinic structure, and of medium strength for strongly barotropic flows. This non-monotonic dependence was a result of the two different processes responsible for the recirculation development: linear eddy-mean flow interactions for strongly baroclinic basic flows, and strongly nonlinear eddy-eddy and eddy-mean flow interactions for strongly barotropic flows. The work also showed that it was only when the mechanism of barotropic instability was present did the model have two energy states, and that the low frequency variability associated with the unique dynamical regime characterized by well-developed recirculations in both layers in physically relevant 2-layer model cases was relatively weak.

3.1.3 Present Work Objectives

Despite the highly variable, zonally evolving, strongly inertial and strongly baroclinic nature of WBC jet systems, thus far, configurations in which all of these components can interact and compete remain relatively unexplored. In previous work, theoretical studies of inertial effects in WBC jets have tended to be in steady (time-independent) frameworks, with eddies parameterized as a down-gradient diffusion of PV (Marshall and Nurser, 1986; Greatbatch, 1987; Cessi, 1990). Hence they fail to address the relative importance of inertial vs. eddy effects, both of which are likely to be important in the oceanic system. At the same time, studies on the role of eddies in these regimes have largely been devoid of the consideration of jet inertial effects (Haidvogel and Rhines, 1983; Cessi et al., 1987; Malanotte-Rizzoli et al., 1995; Berloff, 2005). Hence there is, in general, an inadequate connection between the prescribed forcing and the system's intrinsic dynamics. Exceptions are the work of Jayne et al. (1996), Beliakova (1998), and Jayne and Hogg (1999), studies which have addressed several of the issues related to the generation and maintenance of recirculations by a free inertial jet in barotropic, equivalently barotropic and baroclinic systems, but they are limited to zonally symmetric configurations and a focus on low-frequency variability and multiple dynamical regimes in the case of the work of Beliakova (1998), and to barotropic or equivalently barotropic dynamics without focus on the eddy-mean flow interaction mechanisms in the case of the studies of Jayne et al. (1996) and Jayne and Hogg (1999).

The work discussed here attempts to extend our theoretical understanding of the role of eddy variability in the time-mean dynamics of a zonally-evolving, strongly inertial, baroclinic, unstable jet in a configuration and parameter regime that is relevant to the GS and KE jet systems. It can be considered an extension of the work of Jayne et al. (1996) and Jayne and Hogg (1999) with a view to expand our understanding of the eddy-mean flow interaction mechanisms involved, to address the relative importance of eddy vs. inertial effects, and to include baroclinic dynamics (and baroclinic instability).

Questions guiding of the current study can be summarized as follows:

In an idealized model of a WBC jet:

1. what is the effect of eddies on the time-mean circulation, and what mechanism(s) permit that effect?

2. what is the importance of the eddy effect relative to steady state inertial terms?

3. how does this effect vary with system parameters, in particular the stability properties of the WBC that is the source of the eddy variability?

4. how does the addition of baroclinicity and baroclinic instability change our understanding of the eddy effects in a barotropic model?

These questions are examined through study of a numerical model of the downstream evolution of a barotropic jet subject to barotropic instability (the "barotropic case") and a baroclinic jet (in a two-layer framework) subject to a mixed (barotropic and baroclinic) instability mechanism (the "baroclinic case").

3.1.4 Chapter Outline

This chapter is organized as follows: In Section 3.2, I outline my approach. Here a description and justification of the model set-up are given. More technical details about the model equations, numerical method, and model parameters are supplied in Appendix C. In Sections 3.3 and 3.4 I present the results. Section 3.33 discusses results from my study of the barotropic case. It diagnoses the eddy effect on the time-mean circulation in a typical case appropriate to the GS and KE (Section 3.3.1), and explores the mechanisms that permit the eddies to drive the time-mean recirculation gyres (Section 3.3.2). From this emerges a two-regime conceptual picture of eddy-mean flow interactions in the downstream development of the time-mean jet-gyre system (Section 3.3.3). Having developed an understanding of the eddy effects and eddy-mean flow interaction mechanisms, next the importance of this eddy forcing (relative to steady-state inertial terms) in a WBC-like parameter regime is addressed

(Section 3.3.4), and the dependence of this eddy effect on system parameters is explored (Section 3.3.5). Section 3.4 presents similar results from my study of the baroclinic, mixed instability case, more relevant to actual WBC jet systems. Attention is focused on highlighting the significant commonalities with the barotropic case and describing the ways in which baroclinicity adds to or alters the barotropic eddy-mean flow interactions picture. In addition to topics outlined above, the relative impact and importance of eddy fluxes of relative vorticity *vs.* thickness is explored (Section 3.4.3). Finally, in Section 3.5 I summarize and discuss the results, evaluating their relevance to actual WBC jets by considering them in the context of past observational results, and also making a potentially useful analogy to atmospheric storm tracks.

3.2   Methodology

I study the role of eddy-mean flow interactions in the downstream evolution of an idealized WBC jet using a numerical model of an unstable, boundary forced jet in an open domain.

The model is quasi-geostrophic and fully nonlinear with x (zonal), y (meridional), and time dependence. It is run in one and two layer configurations. It is forced at the western boundary by imposing an unstable jet inflow directed eastward at $x = 0$. In the barotropic case, this inflowing jet is potentially barotropically unstable (*i.e.* it satisfies the Rayleigh necessary condition for instability requiring the potential vorticity gradient profile to change sign in the horizontal). In the two-layer case, it has the potential for both barotropic and baroclinic instability (*i.e.* it satisfies the two-layer model necessary condition for instability requiring the potential vorticity gradient profile to change sign somewhere in the domain, either in the horizontal or in the vertical (Pedlosky, 1963)). Heuristically, I consider this jet to be barotropically unstable if the potential vorticity gradient changes sign in the horizontal due to the jet's horizontal shear, and baroclinically unstable if the potential vorticity gradient changes sign in the vertical due to the jet's vertical shear, but note that in currents where both barotropic and baroclinic instability are possible, the type of instability

mechanism favored (and the accompanying energy transfer characteristics) are not strictly known *a priori*, and can be determined only by detailed calculation for the given velocity and potential vorticity distribution of the basic state.[1] Given that it is my intent to model the downstream development of a free inertial jet applicable to the WBC after it has separated from the coast and entered the open ocean, I allow the jet to evolve freely in the zonal direction from the western edge of the domain, and remove it at the eastern edge a long way downstream and in a manner that does not affect the upstream dynamics I study. I also put sponge layers on all the lateral boundaries to prevent wave reflection back into the interior to simulate open ocean conditions. Note that the presence of the sponge layer on the western boundary in particular has the effect of eliminating any feedback of the recirculation strength on the inflowing jet, and as such eliminates the potential for more complex behavior associated with the low-frequency variability and multiple dynamical regimes observed in these jet-gyre systems, a complicating feature I wished to eliminate from the system I studied. Note too that the sponge layer on the western boundary may have a significant influence on the partition of the eddy vorticity flux between relative vorticity and thickness components, although how the sponge layer controls the role of these fluxes in an analogous way to how no-slip and partial-slip boundary conditions on the western wall seem to control whether it is relative vorticity or thickness eddy fluxes that maintain the upper-ocean recirculations in double gyre models (see Berloff et al. (2007b) for a discussion), is at this time unknown. For full details about the model-set-up and the numerical method, please refer to Appendix C.

I pose the eddy-mean flow interaction problem in terms of a time-mean state and the variability about this mean state. I spin the system up to steady state (domain-integrated enstrophy constant with time), then accumulate turbulent statistics for a period long enough so that they are insensitive to the integration time (10, 000 non-dimensional time units). I use the model to diagnose dynamical quantities to gain insight into the dominant eddy-mean flow interaction mechanisms, and also to perform experiments that isolate the various instability types of the inflowing jet or

---

[1]See J. Pedlosky *Geophysical Fluid Dynamics* (1987) Section 7.15 for a detailed discussion.

vary parameters around GS and KE appropriate values. For full details about the experiments performed see Appendix C.

Finally, it is worthy of mention that although the model is highly simplified, there are several indications in past observations of the GS and in my analysis of new observations in the KE region that give some confidence that both the simplifications that the idealized model employs, and the physics that it retains, are appropriate to these WBCs. For example:

- Observations in the deep ocean in the KE indicate that the velocity structure below the thermocline has only a very weak depth dependence. As such, a model with simplified vertical structure should suffice.

- Point-wise energy balances in the GS system indicate that both baroclinic and barotropic mechanisms are active (Dewar and Bane, 1989). This also appears to be true in observations of the KE: both synoptic mean and instantaneous snapshots of the horizontal and vertical shears in the KE jet indicate that shears often far exceed the critical value for both barotropic and baroclinic instability based on Rayleigh and Phillips model criteria, and spectra of velocity records inside the time-mean jet indicate enhanced energy at a number of different mesoscale frequencies consistent with the timescales predicted by appropriate linear stability calculations. As such, a model with the capacity to support a mixed (barotropic + baroclinic) instability mechanism is necessary.

- It is now widely appreciated that the GS is a highly time-dependent current, which exhibits fluctuations in speed comparable to its mean speed (Fofonoff, 1981). There are several indications in KE observations that the KE system is similarly very nonlinear: perturbation velocities are on the order of the mean velocity, and observed wave phase speeds are on the order of (and often less than) individual particle speeds. As such fully nonlinear dynamics are essential.

For a more complete discussion of the relation of observations in the KE to the idealized dynamical model discussed here, please see Chapter 4.

3.3 Results: The Barotropic Case

I begin my investigation of eddy-mean flow interactions in idealized WBC jet systems by revisiting the barotropic model first discussed by Jayne et al. (1996). Given my interest in the role that eddies play in the driving of the time-mean recirculation gyres, and the demonstration by Jayne et al. (1996) that eddies in this configuration are capable of driving mean recirculations with barotropic dynamics only, this is an attractive starting point.

With the goals of understanding the eddy effect on the mean in this configuration, and, in particular, the mechanisms permitting this effect, I examine a typical case with barotropic dynamics only in a parameter regime that is relevant to a WBC extension jet (see Appendix C, Figure C-1). Properties of the forcing and the instantaneous and time-mean circulation of this test case are given in Figure 3-1. The inflowing jet profile satisfies the necessary condition for barotropic instability (the meridional PV gradient, Q_y, changes sign) (*upper left*), and the instantaneous circulation is characterized by large meanders, closed rings and waves that are radiated from the unstable jet. As was found in Jayne et al. (1996), the time-mean circulation is characterized by a pair of counter-rotating recirculation gyres that flank a time-mean zonal jet. The strength of these recirculation gyres increases with downstream distance to a local maximum and then decays.

3.3.1 The Effect of Eddies on the Time-Mean Circulation

There are a number of different budgets and frameworks to consider in diagnosing the eddy effect on the time-mean circulation. Here I present results from a few of the most illuminating:

(a) Eddy effect on the mean zonal momentum budget (the zonal "effective eddy force")

To view the effect of eddies on the mean zonal momentum budget, I consider the time-mean Reynolds decomposition of the zonal momentum equation, in which eddies appear as a time-mean eddy flux divergence of zonal momentum, $\frac{\partial}{\partial x}\overline{(u'u')} + \frac{\partial}{\partial y}\overline{(u'v')}$.
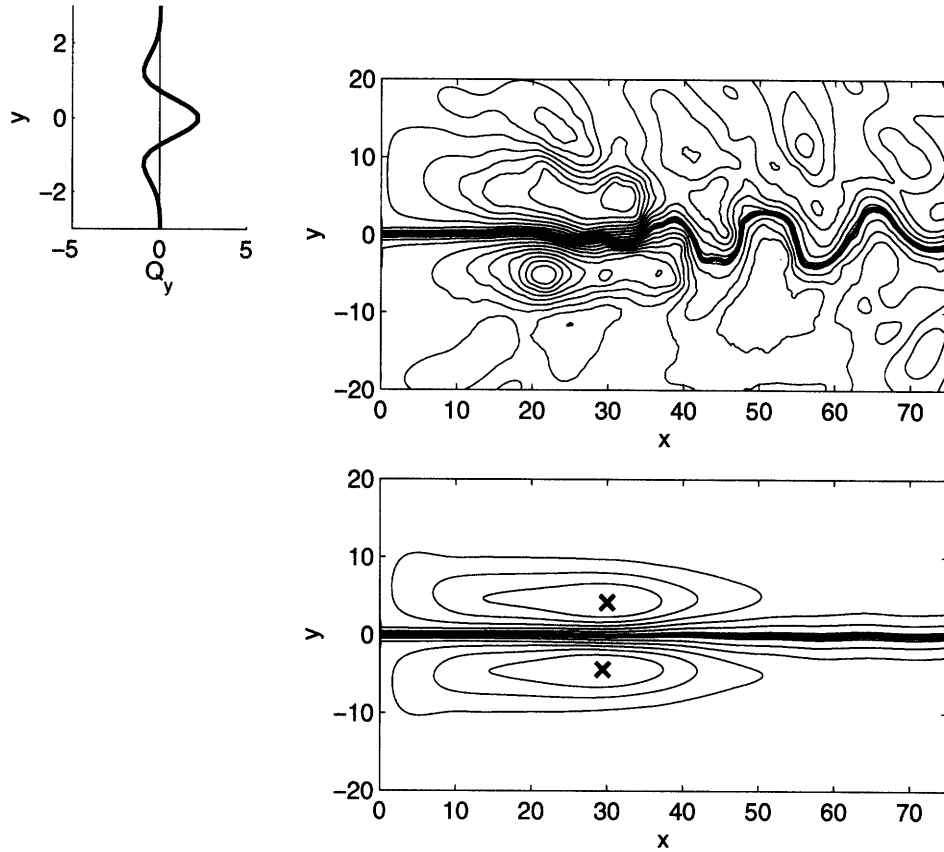
Figure 3-1: A snapshot of the instantaneous (*top*) and time-mean (*bottom*) circulation (streamfunctions) for a typical barotropic run relevant to a WBC jet extension ($A = -1.0, \ell = 1.0, \beta = 0.05$, see Appendix C for parameter definitions). The system is forced at the western boundary (at $x = 0$) by a jet whose profile satisfies the necessary condition for barotropic instability (the meridional gradient of its potential vorticity profile, Q_y, reverses sign, here becoming negative on the jet flanks) (*upper left*). The instantaneous circulation is characterized by large meanders, closed rings and waves that are radiated from the unstable jet. The time-mean circulation is characterized by a pair of counter-recirculating recirculation gyres that flank a time-mean zonal jet. The **xs** denote the locations of the maximum time-mean recirculation transport.

Here u and v are the zonal and meridional components of the velocity respectively, primes indicate an eddy quantity (a deviation from the time-mean), and the over bar denotes a time average. If placed on the right-hand side of the equation, this term looks equivalent to a steady zonal force on the time-mean flow, the origin of the label "effective eddy force" for this particular time-mean eddy flux divergence quantity. I consider this effective force in a Transformed Eulerian Mean (TEM) framework (Andrews and McIntyre, 1976, 1978), a transformation that amounts to a repartitioning of mean and eddy fluxes so that the transformed eddy fluxes include only non-skew (divergent) components (those components of the eddy flux that are skew, *i.e.* directed normal to the mean gradient and thus advective in nature, are incorporated into the "mean" flux - see Plumb and Ferrari (2005) for a full discussion). One particularly important result of this procedure is that the momentum budget becomes more readily understood in terms of basic eddy properties in the sense that the eddy forcing term in the transformed budget is directly dependent on the eddy fluxes of PV. In particular, in the case of a non-divergent flow, eddies appear in the transformed momentum budget as a force per unit mass equal in magnitude and normal to the eddy PV flux, hence the zonal effective eddy force, F_x, is given by the meridional eddy PV flux, $\overline{v'q'}$. It is often convenient to consider this quantity in terms of the gradients of the Reynolds stresses in one of the following equivalent forms:

$$F_x = \overline{v'q'} \;\; = \;\; \frac{\partial}{\partial x}(\overline{v'v'}) - \frac{\partial}{\partial x}\bar{\epsilon} - \frac{\partial}{\partial y}(\overline{u'v'}) \quad \text{where} \quad \bar{\epsilon} = \frac{1}{2}(\overline{u'u'} + \overline{v'v'}) \quad (3.1)$$

$$= \;\; \frac{\partial}{\partial x}\frac{(\overline{v'^2 - u'^2})}{2} - \frac{\partial}{\partial y}(\overline{u'v'}) \quad\quad\quad\quad (3.2)$$

Here q is the potential vorticity and ϵ is the eddy energy density. It is the "effective eddy force" in this form for the typical, WBC-relevant, barotropic case that is visualized in Figure 3-2. It is overlaid on contours of the time-mean streamfunction with the location of maximum time-mean recirculation transport indicated. The shaded region $0 < x < 10$ denotes the western sponge layer where dissipation is enhanced.

Now interpretation of the "effective eddy force" in the time-mean eddy-forcing problem is slightly less straightforward than its zonal-mean counterpart, and as such
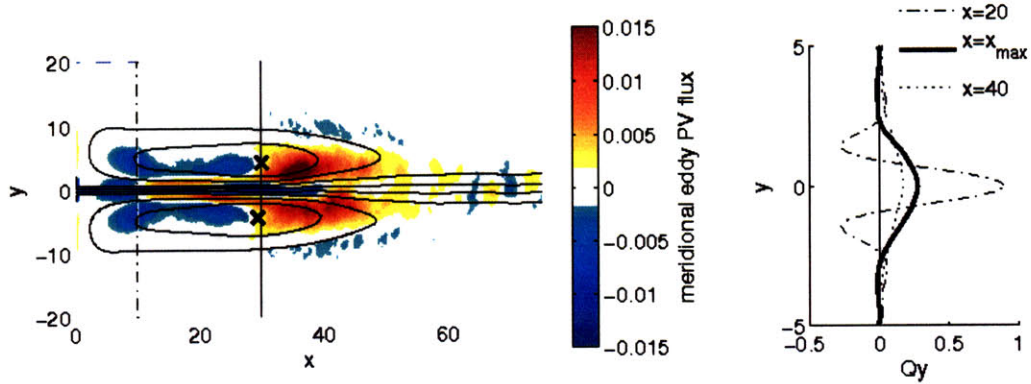
Figure 3-2: The "effective eddy force" in the TEM framework ($F_x = \overline{(v'q')} = \overline{(v'v')}_x - \overline{\epsilon_x} - \overline{(u'v')}_y$ where $\epsilon = \frac{1}{2}(\overline{(u'u')} + \overline{(v'v')})$) (color) overlaid on contours of the time-mean streamfunction with the location of maximum time-mean recirculation transport indicated (*left*). The xs denote the locations of the maximum time-mean recirculation transport, and the vertical line indicates the approximate downstream location corresponding to this maximum, x_{max}. The shaded region $0 < x < 10$ denotes the western sponge layer where dissipation is enhanced. An illustration of the downstream evolution of the meridional profile of the meridional PV gradient associated with the time-mean jet, used to assess its potential for barotropic instability (*right*).

deserves some words of explanation. The added complexity is a consequence of the fact that, as opposed to simply accelerating a mean zonal flow as in the zonal-mean problem, it, in combination with the zonal component of the eddy PV flux, drives a time-mean circulation via balancing a combination of the time-mean momentum flux divergence and the Coriolis torque of the time-mean residual (in this case ageostrophic) circulation. Intuition into the eddy forcing effect in the time-mean eddy-forcing problem however can be gained by considering the time-mean momentum balance in natural (*i.e.* aligned and normal to the mean geostrophic flow) coordinates (see Cronin (1996)), which then allows the interpretation of the component of the eddy PV flux normal to the mean flow as accelerating or decelerating the time-mean flow, while the component of the eddy PV flux tangential to the mean flow should be interpreted as turning the time-mean flow. Hence, F_x, the meridional component of the eddy PV flux visualized in Figure 3-2, can be thought of as an effective eddy zonal force accelerating or decelerating the time-mean flow when the mean flow is

zonal, and an effective eddy torque turning the time-mean flow towards zonal when the time-mean flow is oriented meridionally. With this in mind, Figure 3-2 shows that eddies play two important roles in the downstream evolution of the time-mean circulation: first, stabilizing the jet to its horizontal shear, and second, forcing the time-mean recirculation gyres. They achieve the former effect by fluxing PV meridionally inside the time-mean jet. Since the mean flow is zonal here, the meridional eddy PV flux here acts to accelerate or decelerate the time-mean zonal flow, and in this case decelerates the time-mean jet at its axis by exerting an effective westward force ($F_x < 0$) and accelerates the jet at its flanks by exerting effective eastward forces ($F_x > 0$), having the overall effect of reducing the jet's large-scale horizontal shear and stabilizing it to its barotropic instability. Eddies achieve the latter effect by fluxing PV meridionally outside the time-mean jet, in particular at the zonal edges of the time-mean recirculation gyres. Since the mean flow is oriented meridionally here, the meridional eddy PV flux here acts to turn the time-mean flow zonally, in this case turning the flow eastwards at the western edge of the recirculation gyres and westwards at the eastern edge of the recirculation gyres. In this way, eddies are playing an important role in the driving of the closed circulations flanking the jet.

One feature of the picture of the effective eddy force in Figure 3-2 that is outstanding and worthy of note is the switch in sign of the eddy forcing on the flanks of the jet that is observed at a given distance downstream (here at $x \approx 30$), a switch in sign that determines the downstream location of the maximum in time-mean recirculation transport. What determines this downstream location will be explored in time, but for now, useful to the purpose of understanding the effect of eddies on the time-mean circulation and the mechanism that permits that effect, it is helpful to note that this switch in forcing sign is observed to correspond to the downstream location where the mean meridional PV gradient, $\overline{q_y}$, on the flanks of the jet first ceases to be negative, or more precisely where the mean jet profile first ceases to satisfy the necessary condition for barotropic instability (Figure 3-2 *right*). In short, the effect of the eddies on the mean circulation is observed to undergo a fundamental change across the boundary between where the mean jet is unstable upstream and

where it has been stabilized (by the effect of the eddies) downstream.

(b) Eddy effect on the mean vorticity budget

A second way to view the effect of the eddies on the mean circulation is through their contribution to the time-mean vorticity budget. Here again eddies appear in the mean budget as a forcing term given by the negative of the divergence of their flux, this time as the negative of the divergence of the eddy vorticity flux, $\overline{(\mathbf{u}'q')}$:

$$-\nabla \cdot \overline{(\mathbf{u}'q')} = -\frac{\partial^2}{\partial x \partial y}(\overline{u'u'}) + \frac{\partial^2}{\partial x \partial y}(\overline{v'v'}) + \frac{\partial^2}{\partial^2 x}(\overline{u'v'}) - \frac{\partial^2}{\partial^2 y}(\overline{u'v'}) \qquad (3.3)$$

This term acts as a driver of the mean-flow through the time-mean vorticity balance. This "eddy vorticity forcing" is visualized in Figure 3-3 (*left*). It is again overlaid on contours of the time-mean streamfunction with the location of maximum time-mean recirculation transport / time-mean jet stabilization indicated. The time-mean circulation driven by this forcing, computed as the solution to the linear vorticity equation forced statically by this eddy flux divergence field, is shown in Figure 3-3 in the right panel.

Like the picture of the effective eddy force, again there is a systematic switch in forcing sign across the time-mean jet's unstable - stable boundary. It is also significant to note that the dominant contribution to the eddy vorticity forcing comes from the region downstream of jet stabilization. From the mean circulation driven by this eddy forcing field (Figure 3-3 *right panel*), one sees directly the eddies' responsibility in driving the pair of time-mean recirculation gyres.
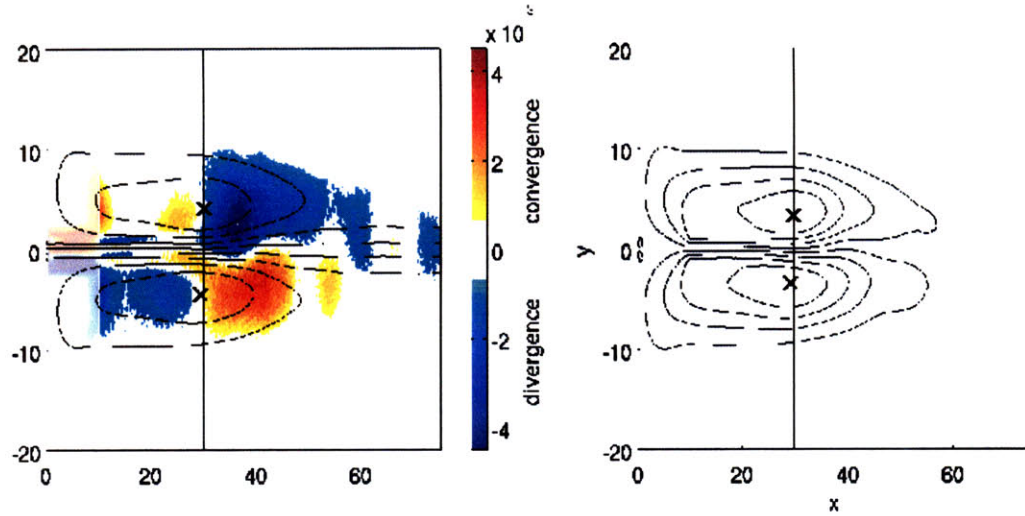
Figure 3-3: The eddy vorticity forcing (the negative of the divergence of the eddy vorticity flux $(-\nabla \cdot \overline{(\mathbf{u}'q')} = -\overline{(u'u')}_{xy} + \overline{(v'v')}_{xy} + \overline{(u'v')}_{xx} - \overline{(u'v')}_{yy})$ (color) overlaid on the properties of the time-mean streamfunction (*left*). The time-mean circulation driven by the eddy vorticity forcing, computed as the solution to the linear vorticity equation forced statically by the above eddy vorticity forcing field (*right*).

(c) Eddy effect on the mean kinetic energy budget

A third way to view the effect of eddies on the time-mean circulation is via energetic considerations. The effect of eddies in the budget for the kinetic energy of the mean flow appears as a production term in the equation for conservation of mean kinetic energy, $\overline{KE}$:

$$\frac{\partial}{\partial t}\overline{KE} = -\left(\overline{u}\left(\frac{\partial}{\partial x}\overline{u'u'} + \frac{\partial}{\partial y}\overline{u'v'}\right) + \overline{v}\left(\frac{\partial}{\partial x}\overline{u'v'} + \frac{\partial}{\partial y}\overline{v'v'}\right)\right) + ... \qquad (3.4)$$

When negative, this represents eddies extracting kinetic energy from the mean flow, and when positive, it represents a production of mean flows by eddy rectification. This quantity is visualized in Figure 3-4. Again the contours of the time-mean streamfunction with the location of maximum time-mean recirculation transport / time-mean jet stabilization is indicated.

Here again is seen a systematic switch in eddy forcing sign across this important unstable - stable jet boundary, with eddies primarily extracting kinetic energy from the mean upstream of where the time-mean jet is stabilized, and producing mean
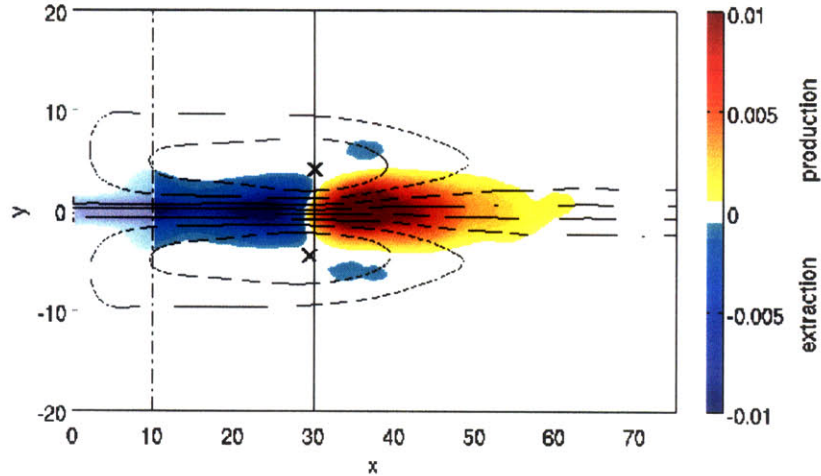
Figure 3-4: The production of mean kinetic energy by the eddies $\left(-\left(\overline{u}\left(\overline{(u'u')}_x + \overline{(u'v')}_y\right) + \overline{v}\left(\overline{(u'v')}_x + \overline{(v'v')}_y\right)\right)\right)$ (color) again overlaid on contours of the time-mean streamfunction with the location of maximum recirculation transport / time-mean jet stabilization indicated.

kinetic energy downstream of this location. Like the dominance of the eddy vorticity forcing downstream of jet-stabilization, this picture again suggests the importance of the downstream region in the eddy-driving of the mean recirculation gyres.

To summarize, from the diagnosis of the eddy effect on the time-mean budgets of zonal momentum, vorticity, and kinetic energy, a picture has emerged of eddies playing two distinctive roles in the downstream development of the time-mean jet: first stabilizing the jet to its horizontal shear, and second driving the time-mean recirculations. What has also emerged is a sense of the importance of zonal variation: in particular the role of eddies undergoes a fundamental change upstream *vs.* downstream of the location where the time-mean jet profile is stabilized. Finally, there are several indications that implicate the region downstream of jet-stabilization as being important to the eddy-driving of the recirculation gyres. But what mechanism permits the eddies to drive mean flows in this region? As it will be seen, insights lie in consideration of eddy enstrophy and wave radiation from a localized region downstream.

90
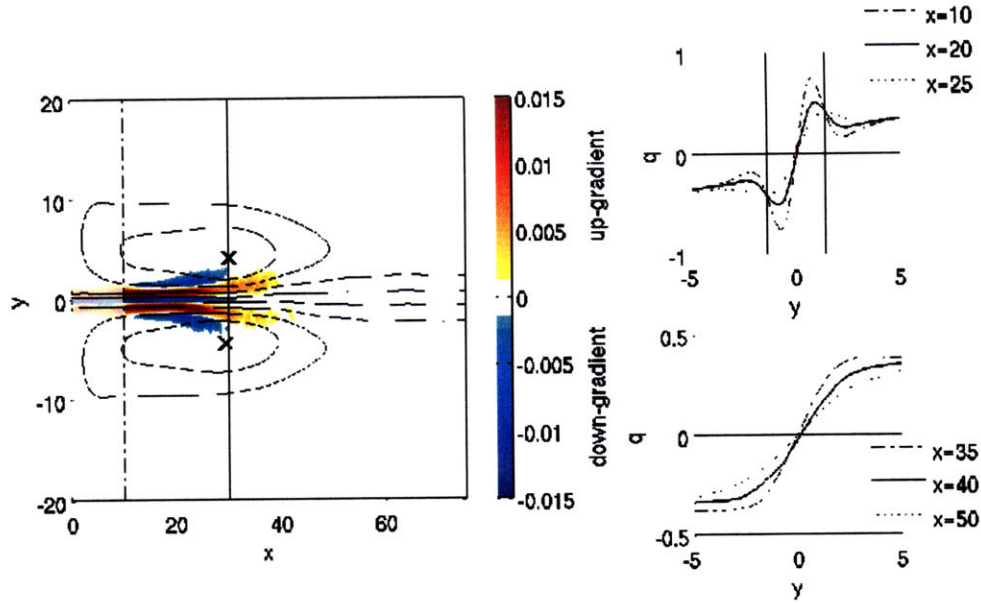
Figure 3-5: The negative of the eddy enstrophy generation term (eddy enstrophy destruction) in the enstrophy variance budget ($\overline{(\mathbf{u}'q')} \cdot \nabla \overline{q}$) which indicates the sense of the eddy vorticity transport relative to the mean PV gradient (color) overlaid on properties of the time-mean streamfunction (*left*). The zonal evolution of the mean PV meridional profile ($\overline{q}$) (*right*).

3.3.2 Insights into the Eddy-Driving Mechanism

(a) Insights from eddy enstrophy destruction

For eddies to accelerate time-mean flows, an eddy PV flux up the mean gradient is required (Rhines and Holland, 1979). Hence to gain insight into the mechanism that permits the eddies to drive the time-mean recirculations, I first consider the sense of the eddy PV flux relative to the mean PV gradient. This is captured in the eddy enstrophy generation term in the enstrophy variance budget, $-\overline{(\mathbf{u}'q')} \cdot \nabla \overline{q}$, which, as the product of the eddy flux of PV and the mean PV gradient, has a sign that indicates the sense of the eddy vorticity transport relative to the time-mean gradient. I visualize the negative of this quantity, in essence eddy enstrophy destruction, $\overline{(\mathbf{u}'q')} \cdot \nabla \overline{q}$, in Figure 3-5 so positive values (red colors) indicate regions of up-gradient eddy PV fluxes.

This picture reveals that there are two important regions of up-gradient eddy fluxes in the jet's downstream evolution permitting the eddy-driving of time-mean

flows: first on the flanks of the time-mean jet upstream of jet stabilization (where eddies act to stabilize the jet by driving flows to broaden it) and second, just downstream of jet stabilization (where eddies act to drive the time-mean recirculations). Yet again, the importance of the region downstream of jet stabilization in the eddy-driving of the recirculation gyres is highlighted. From this picture it is confirmed that the time-mean recirculations result from an eddy flux of PV up the mean-gradient that occurs just downstream of the mean jet's stabilization.

Investigation into the individual terms that contribute to the eddy enstrophy generation term $\left(\overline{u'q'}\frac{\partial \overline{q}}{\partial x}\ vs.\ \overline{v'q'}\frac{\partial \overline{q}}{\partial y}\right)$ reveal that this pattern of downstream evolution mirrors the pattern of the downstream evolution of the zonal gradient of the mean PV field $(\frac{\partial}{\partial x}\overline{q})$. In particular, up-gradient fluxes downstream of jet stabilization results from the change from a four-lobed pattern of $\frac{\partial}{\partial x}\overline{q}$ associated with the downstream evolution of a barotropically unstable jet profile, to a two-lobed pattern of $\frac{\partial}{\partial x}\overline{q}$ associated with the downstream evolution of a barotropically stable jet profile (Figure 3-5 *right*). Here again is the suggestion that the fundamentally different effect of eddies on the mean circulation in the upstream *vs.* downstream regions is a result of differences in the mean background PV gradient.

(b) Up-gradient eddy fluxes permitted by eddy enstrophy advection

Further insight into what allows this up-gradient eddy PV flux comes from consideration of the other terms in the enstrophy variance budget. In the **zonal**-mean eddy-mean flow interaction problem, a much more commonly studied problem given its relevance to the atmosphere, the enstrophy variance budget (assuming eddy enstrophy advection, a triple correlation term, is small) reduces to a two-term balance between eddy enstrophy destruction and dissipation, $\overline{(\mathbf{u'}q')} \cdot \nabla\overline{q} = -D$ where D represents the dissipation of eddy enstrophy. This two-term balance guarantees that, given dissipation is always positive, eddy enstrophy destruction is negative, and hence that the eddy PV flux is always down the mean gradient. This argument is the basis of down-gradient turbulence closures. In the problem with zonal dependence however, convergences and divergences of the advection of eddy enstrophy, $\overline{\nabla \cdot \mathbf{u}\frac{q'^2}{2}}$, now also

92
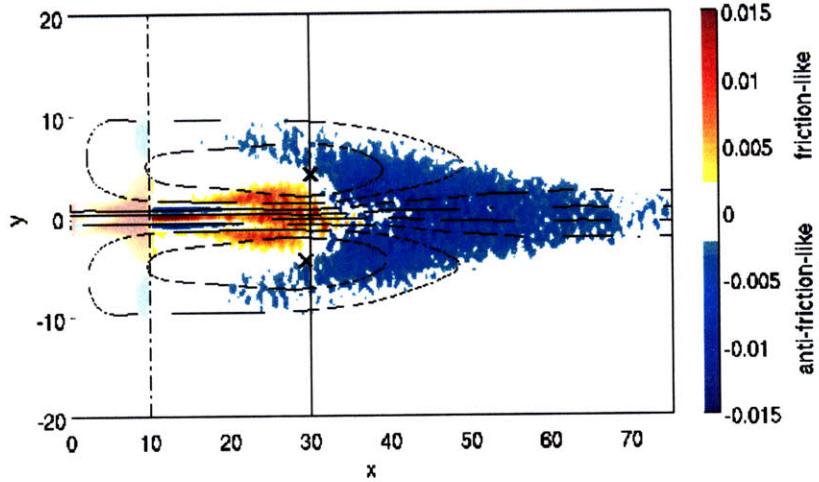
Figure 3-6: The divergence of the advection of eddy enstrophy $(\overline{\nabla \cdot \mathbf{u}\frac{q'^2}{2}})$, the additional term in the eddy-mean flow interaction problem with zonal dependence that can potentially balance the eddy enstrophy destruction term and hence permit up-gradient eddy PV fluxes (color) overlaid on properties of the time-mean streamfunction.

may play a role, providing an additional term to potentially balance the eddy enstrophy destruction term, and hence permit up-gradient eddy PV fluxes (the time-mean enstrophy variance budget is now $\overline{(\mathbf{u}'q')} \cdot \nabla\overline{q} = -D - \overline{\nabla \cdot \mathbf{u}\frac{q'^2}{2}}$). This new additional term, the divergence of eddy enstrophy advection, for the WBC-typical barotropic jet is visualized in Figure 3-6.

Consideration of the divergence of eddy enstrophy advection illustrates the important role that zonal variation, and in particular the phenomenon of eddies being created in one region and being advected by the jet to another region where they dissipate (a phenomenon which results in regions of significant eddy enstrophy flux convergence and divergence) plays in this problem. Now it can be seen that inside the time-mean jet up until jet stabilization, there is an eddy enstrophy flux divergence (acting in the same sense as dissipation and hence requiring a down-gradient eddy PV flux to form a local balance), but on the flanks of the time-mean jet and downstream of jet stabilization are regions of eddy enstrophy flux convergence (acting in the opposite sense as dissipation). This convergence is significant enough to overcome dissipation and allow up-gradient eddy fluxes in these regions as seen in Figure 3-5.

In short, it is the separation in space between regions of eddy enstrophy generation by the unstable jet and eddy enstrophy dissipation downstream of jet stabilization that is key. Advection of eddy enstrophy results in eddy enstrophy convergence that permits an up-gradient eddy PV flux, and ultimately the eddy driving of the time-mean recirculation gyres.

(c) A localized wave-radiator model downstream of jet stabilization

The eddy vorticity forcing field (Figure 3-3) shows us the importance of the region downstream of jet stabilization to the eddy forcing of the time-mean circulation, and the eddy enstrophy destruction field (Figure 3-5) implicates that it is here that eddies flux PV up the mean-gradient and drive the mean recirculation gyres. A potentially useful model for understanding how eddies drive the mean flow in this downstream region is suggested by the similarity of the downstream region eddy vorticity forcing pattern to that of the simple model of a localized wave-maker on a beta plane discussed in Chapter 2. This conceptual model is potentially useful in understanding the eddy driving mechanism because, as it was shown, the fluxes associated with the waves or eddies generated by a localized wave-maker can drive time-mean recirculation gyres through the process of nonlinear eddy rectification.

This comparison between the eddy vorticity forcing field (the eddy flux divergence of relative vorticity, $-\nabla \cdot \overline{(\mathbf{u}'q')}$) in the downstream region of the jet and in the localized wave-maker model is illustrated in Figure 3-7. The black circle in the latter denotes the region where a localized oscillatory vorticity forcing is applied. Both are charactered by a dipole pattern consisting of a vorticity flux divergence in the southern half of the forced region, and a vorticity flux convergence in the northern half of the forced region. In the lower panels of Figure 3-7 is illustrated the time-mean circulation that results from the above eddy vorticity forcing, computed as the solution to the linear vorticity equation forced statically by the above eddy vorticity forcing field. Consistently, both are characterized by a pair of counter-rotating time-mean recirculation gyres west of the forcing. This result is significant for the jet, as it confirms that eddy forcing in the region downstream of jet stabilization is responsible,

at least in part, for driving the time-mean recirculations observed.

Similarities between the dynamics of the region downstream of jet stabilization and the dynamics of the localized wave-maker are further seen in the energetics. If one examines the spatial distribution of eddy energy associated with the downstream evolution of the time-mean jet (Figure 3-8 *upper left*), one sees that the growing instability of the jet in time followed by the subsequent dissipation of those eddies after the jet has been stabilized, combined with jet's advection, results in a localized maximum of eddy energy located just downstream of jet stabilization. This "bullet" of eddy energy is not unlike the localized source of eddy activity generated by the localized wave-maker (Figure 3-8 *upper right*), and the similarity makes the relation of the recirculation driving in the jet and by the wave-maker seem plausible. Examination of the mean to eddy kinetic energy conversion rate in the jet in this region $\left(\overline{u'}^2\frac{\partial}{\partial x}\overline{u} + \overline{u'v'}\left(\frac{\partial}{\partial y}\overline{u} + \frac{\partial}{\partial x}\overline{v}\right) + \overline{v'}^2\frac{\partial}{\partial y}\overline{v}\right)$ (Figure 3-8 *lower left*) also shows similarities, in particular a region of significant eddy to mean energy conversion that is similar to that inside the forced region of the wave-maker (Figure 3-8 *lower right*). This region of negative mean to eddy energy conversion is observed in the jet to be slightly downstream of the "effective wave-maker" location based on the eddy energy distribution, potentially explained by the effect of a large mean zonal advection associated with the presence of the jet.

In summary, there exist many similarities in the pattern of the eddy energy distribution, the eddy vorticity forcing, and in energetic conversions between mean and eddy kinetic energies in the jet model downstream of jet-stabilization and in the recirculation-driving localized wave-maker model. This, in combination with the suggestion that the source of the recirculation driving in the jet occurs downstream of jet stabilization, leads us to the picture that the mechanism by which the eddies drive the recirculations in the time-mean jet system is via the radiation of waves from a localized region downstream of where the jet instability has been stabilized. In this case, the localized wave forcing is being supplied by a localized concentration of eddy activity that results from the process of the jet stabilizing itself as it evolves downstream. Lessons learned about the rectification mechanism and how its effectiveness

95
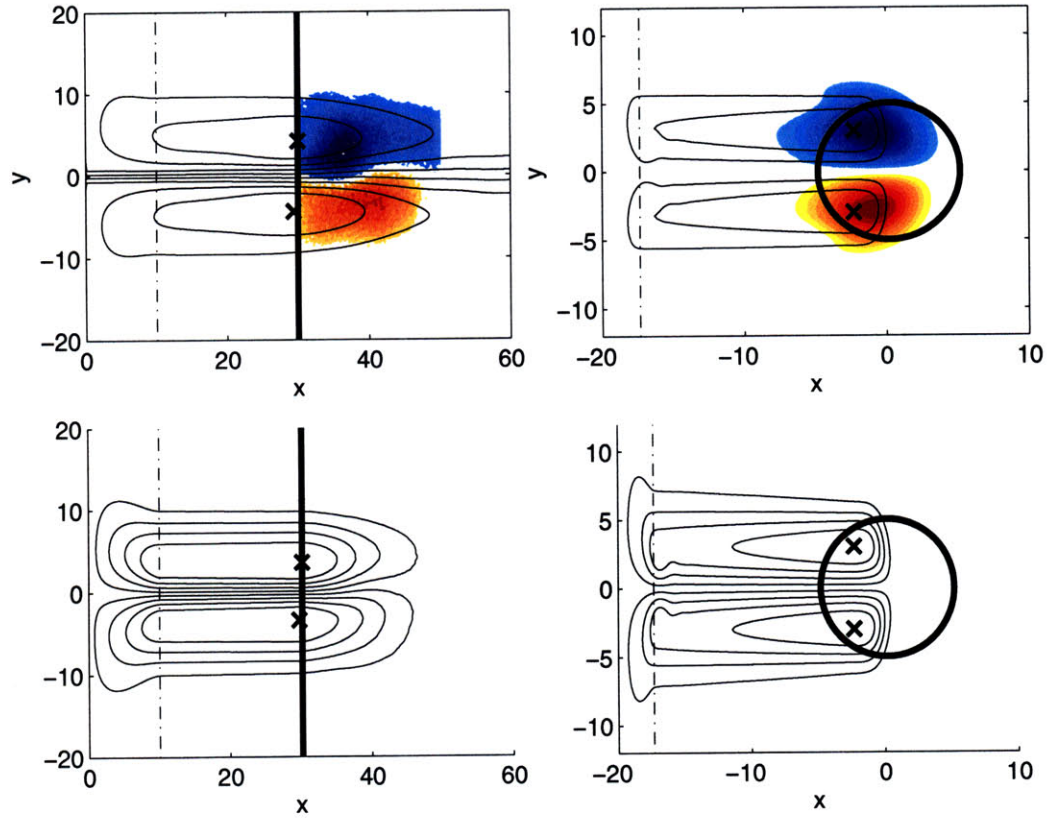
Figure 3-7: The eddy vorticity forcing (the negative of the eddy flux divergence of relative vorticity, $-\nabla \cdot \overline{(\mathbf{u}'q')}$) for the region downstream of jet stabilization in the barotropic jet model (*left*) *vs.* that for the wave-maker model (*right*) (*top*). The black line in the former denotes the unstable jet / wave-radiator regime boundary, and only forcing downstream of this boundary is applied. The circle in the latter denotes the region where a localized oscillatory vorticity forcing is applied. Contours are of the time-mean streamfunction from the fully nonlinear solution showing the recirculation gyres in each case. The time-mean circulation that results from the above eddy vorticity forcing, computed as the solution to the linear vorticity equation forced statically by the above eddy vorticity forcing field (*bottom*).
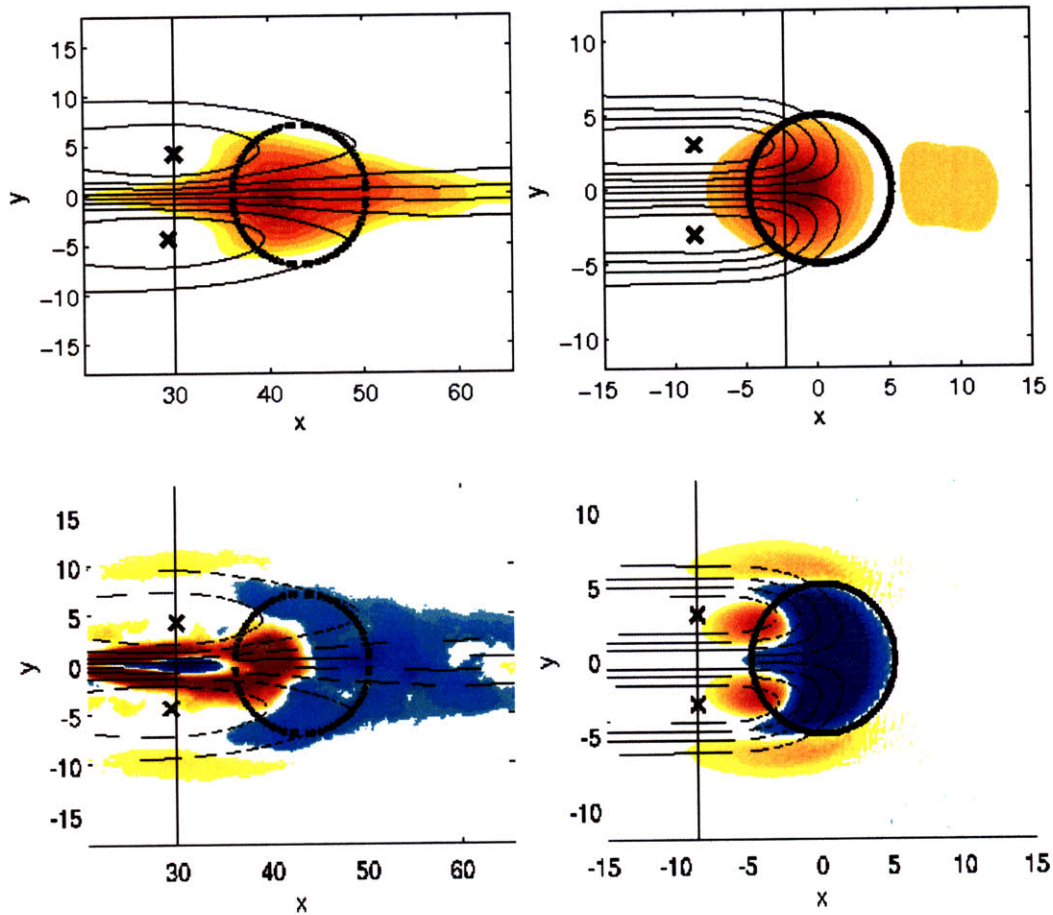
Figure 3-8: A comparison of the downstream region of the jet (*left*) and the localized wave-maker model (*right*) in terms of the spatial distribution of eddy energy (as visualized by the time-mean variance of the streamfunction, $\overline{\psi'\psi'}$) (*top*), and the mean to eddy kinetic energy conversion rate (as defined in Figure 3-4) (*bottom*). The black circle indicates the forced region in the wave-maker model in the right panels, and where one could consider an effective wave-maker was located based on the eddy energy distribution in the jet model in the left panels.

is influenced by the variation of forcing parameters, stratification, and the presence of a mean background flow discussed in Chapter 2 should equally apply to this WBC jet application.

3.3.3 A Conceptual Description of Eddy-Mean Flow Interactions

To characterize the role that eddies play in the downstream evolution of the time-mean WBC jet-gyre system, I have considered the eddy contribution to the budgets of mean momentum, vorticity, and kinetic energy. Consideration of the time-mean enstrophy variance budget has provided insight into the mechanism that permits their mean-circulation driving effects. Throughout, the discussion has featured a fundamental switch in properties of the eddy effect across the mean jet's unstable *vs.* stable boundary, a consequence of the important change in the background PV gradient that occurs there.

As a consequence, I argue that the role of eddies in this system is usefully understood as two distinct downstream regions based on the time-mean jet's stability properties: an upstream one where the time-mean jet is still unstable based on the necessary condition for barotropic instability ($\frac{\partial}{\partial y}\bar{q}$ changes sign implying $\frac{\partial}{\partial y}\bar{q}_{min} < 0$) and a downstream one where the time-mean jet is stabilized to the necessary condition ($\frac{\partial}{\partial y}\bar{q}$ is single-signed implying $\frac{\partial}{\partial y}\bar{q}_{min} > 0$) (Figure 3-9 *upper left*). In each of these regions, eddies interact with the time-mean circulation in a fundamentally different way, a consequence of them acting on a fundamentally different background PV gradient with a sign reversal associated with the unstable time-mean jet in the upstream region, and with no sign reversal in the downstream region. The switch in sign of the eddy effect across this boundary results in the downstream location of the maximum in eddy-driven time-mean recirculation transport being located at this location.

Given this division of regions based on mean jet stability/the downstream location of maximum time-mean recirculation transport, the role of eddies in the downstream

development of the time-mean jet/gyre system can then be summarized as follows (Figure 3-9):

In the unstable jet regime (upstream of the maximum in time-mean recirculation transport):

- the effective eddy force inside the time-mean jet is westward, acting to decelerate the time-mean jet (*upper right*)

- the production of mean kinetic energy by the eddies is negative, indicating that mean kinetic energy is being converted to eddy kinetic energy through the instability process (*middle left*)

- the eddy vorticity forcing is in the sense to drive "anti-recirculation gyres" (recirculation gyres with the opposite sense of circulation), acting to decelerate the time-mean jet (*middle right*)

- the eddy enstrophy destruction inside the time-mean jet is negative, indicating a down-gradient eddy PV flux (*lower left*)

- the eddy enstrophy advection is divergent, acting in the same sense as friction (*lower right*)

In contrast, in the stable jet regime (downstream of the maximum in time-mean recirculation transport) the sign of these eddy effects reverses:

- the effective eddy force inside the time-mean jet is eastward, acting to accelerate the time-mean jet (*upper right*)

- the production of mean kinetic energy by the eddies is positive, indicating that eddies drive time-mean flows (*middle left*)

- the eddy vorticity forcing is in the sense to drive the time-mean recirculation gyres (*middle right*)

- the eddy enstrophy destruction inside the time-mean jet is positive, indicating an up-gradient eddy PV flux (*lower left*)
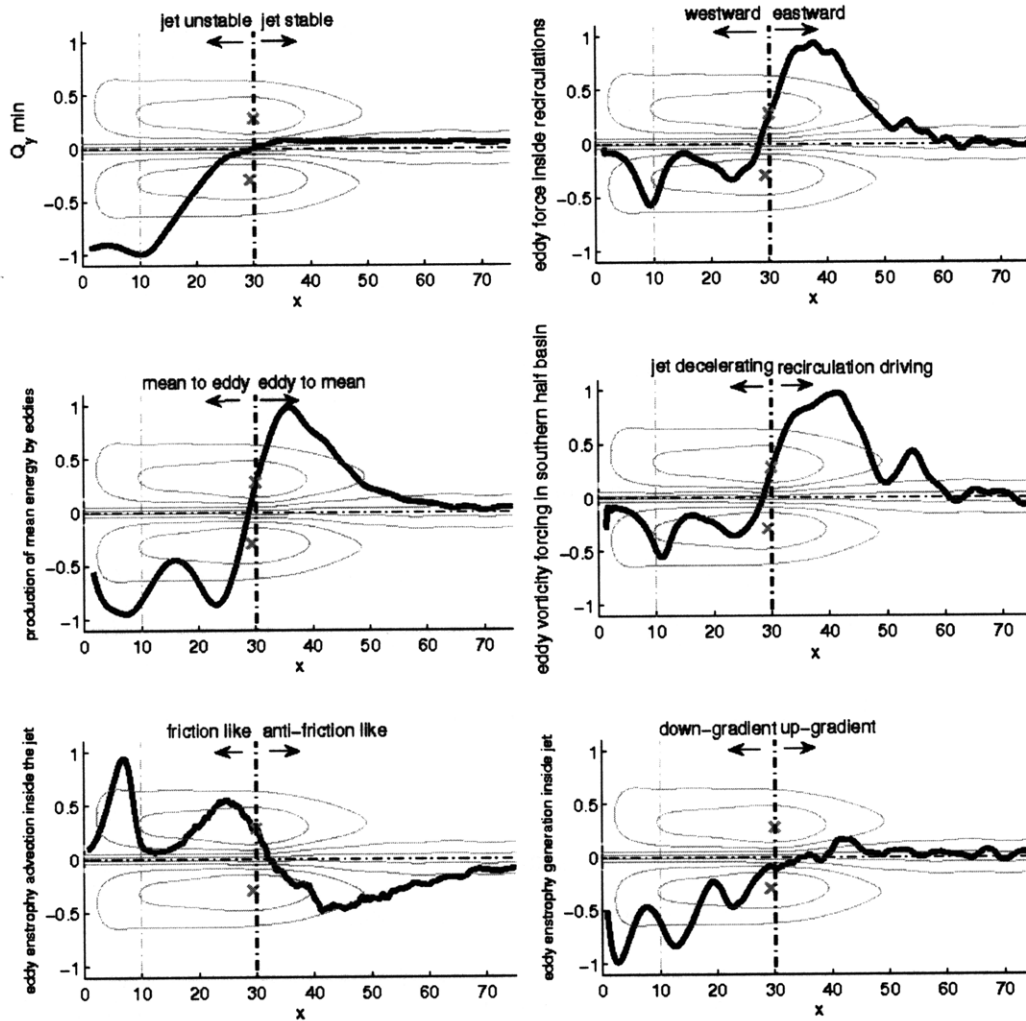
Figure 3-9: The downstream evolution of (a) the time-mean jet's stability properties (*upper left*) (b) the effective eddy force (*upper right*) (c) the production of mean kinetic energy by the eddies (*middle left*) (d) the sense of the eddy vorticity forcing (*middle right*) (e) the eddy enstrophy destruction inside the time-mean jet (*lower left*) and (f) the sign of the eddy enstrophy advection (*lower right*).

- the eddy enstrophy advection is convergent, acting in the opposite sense as friction and permitting an up-gradient eddy PV flux (*lower right*)

In summary therefore, in the upstream region close to the western boundary eddies interact with the time-mean flow in a way consistent with what one would expect in an unstable jet regime: they tend to decelerate and broaden the jet, extract energy from the mean, and mix PV down the mean-gradient. Further downstream however, their effort to stabilize the mean jet as it evolves downstream is successful, and when it is, their role undergoes a fundamental switch in sign, a consequence of the fundamentally changed background PV gradient they now act on. Downstream of where the jet is stabilized, eddies now act to drive the time-mean recirculation gyres, converting eddy kinetic energy to mean kinetic energy and fluxing PV up the mean gradient. I label the upstream region as the "unstable jet" regime, where eddy-mean flow interactions are dominated by stabilizing the jet, and the downstream region as the "wave radiator" regime, where, based on its similarities to the localized wave-maker model, the dynamics are dominated by the radiation of waves from a localized source of eddy energy.

3.3.4   The Relative Importance of Eddy Forcing

As discussed in the introduction, past work has demonstrated that time-mean recirculation gyres can arise from the steady state inertial terms alone, the rectification of eddy fluxes alone, and, in the case of an unstable jet, potentially both. Here I ask the question what is the relative importance of eddy forcing compared to steady state inertial terms in the forcing of the time-mean recirculations in this configuration and parameter regime appropriate to WBC jets?

Figure 3-10 compares the eddy *vs.* mean zonal momentum flux divergences for the typical WBC relevant barotropic run. At first glance, the common color scale indicates that the size of the eddy term is comparable to the size of the mean term, making them of roughly equal importance in the momentum budget of the jet/gyre system.
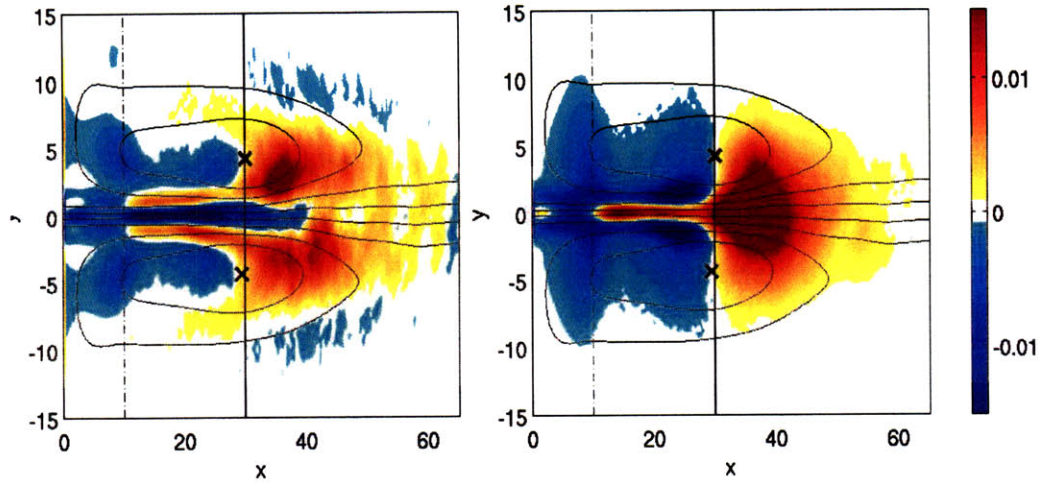
Figure 3-10: The divergence of the eddy flux of zonal momentum $\left(\frac{\partial}{\partial x}\left(\overline{u'u'}\right) + \frac{\partial}{\partial y}\left(\overline{u'v'}\right)\right)_{TEM}$ (the "effective eddy force") (*left*) *vs.* the divergence of zonal momentum advection by time-mean velocities $\left(\overline{u}\frac{\partial \overline{u}}{\partial x} + \overline{v}\frac{\partial \overline{u}}{\partial y}\right)$ (the mean inertial term) (*right*).

Closer inspection reveals other features of note. Inside the time-mean jet upstream of jet stabilization, the sense of the eddy term and mean term oppose each other: as is expected, in the unstable jet regime the effect of the eddies is to oppose the inertial acceleration of the jet and act to decelerate it. Outside the time-mean jet and downstream of jet stabilization however, the sense of the eddy term tends to act in the same sense as the mean inertial term, augmenting the effects one would see in the absence of time-dependent terms. Here both eddy and mean terms make roughly equal contributions to providing the torque on the time-mean flow needed to force the closed recirculations. This implies that although time-mean recirculations will feature in the time-mean circulation of the system if eddy terms are not included, they will be significantly weaker than in the case with eddy effects properly resolved.

Figure 3-11 compares the eddy *vs.* mean vorticity flux divergences for the same typical WBC relevant barotropic run. As in the case of the momentum budget, the common color scale indicates that the size of the eddy term is comparable to the size of the mean term. In the time-mean vorticity balance however, mean and eddy terms are each important in different regions. The mean flux divergence dominates
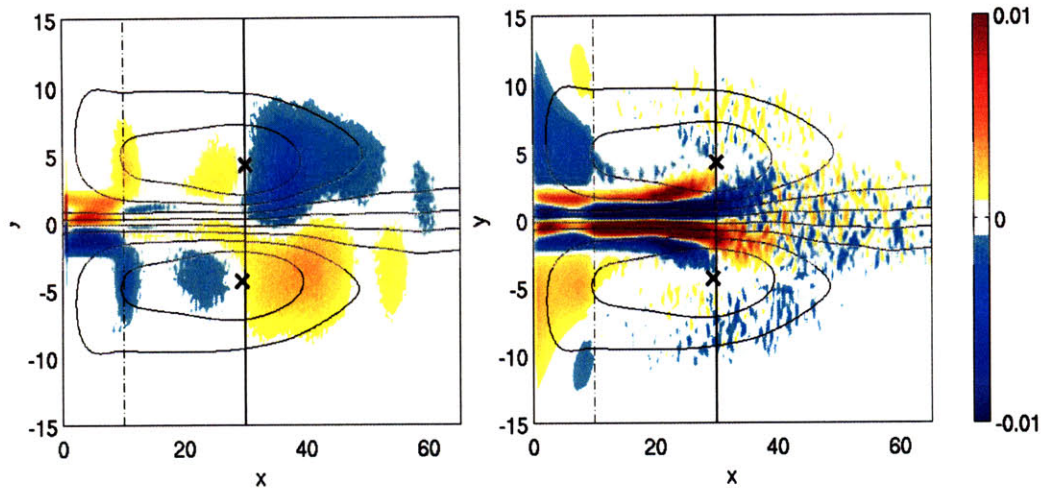
Figure 3-11: The divergence of the eddy flux of vorticity $\left(\overline{J(\psi', \nabla^2 \psi')}\right)$ (*left*) *vs.* the divergence of vorticity advection by mean velocities $\left(J(\overline{\psi}, \overline{\nabla^2 \psi})\right)$ (*right*).

inside the time-mean jet in the region upstream of jet stabilization. Here the eddy flux divergence is insignificant by comparison. Downstream of jet stabilization and outside the time-mean jet however, the eddy flux divergence dominates with large regions of eddy flux divergence south of the jet and eddy flux convergence north of the jet, the characteristic dipole pattern associated with wave radiation away from a localized source, and capable of driving the time-mean recirculation gyres. The mean flux divergence is significant downstream of jet stabilization as well, although it tends to be more localized to the time-mean jet. Interesting, it acts in the same sense as the eddy flux divergence there. Hence the mean *vs.* eddy vorticity forcing confirms the conclusion of the comparison between mean *vs.* eddy momentum forcing, that is that recirculations will feature in the time-mean circulation of the system if eddy terms are not included, however eddies are significant in increasing their strength and also, as can be seen here, increasing their meridional extent by radiating energy (and eddy flux divergences) away from the jet.

3.3.5 Dependence on System Parameters

A second goal of this study was to understand the time-mean state property dependence on system parameters. To examine this I performed a series of parameter studies that varied parameters around GS and KE-like values. In the case of the barotropic jet, the variation of interest was the supercriticality, or the degree of barotropic instability, of the inflowing jet, achieved via the variation of the non-dimensional β parameter, $\beta = \frac{\beta_{dim}L^2}{U}$ where β_{dim} is the meridional gradient of the planetary vorticity, and L and U are typical length and velocity scales of the flow. Decreasing this parameter can be thought of as equivalent to making the jet stronger and/or sharper, hence having greater horizontal shear and being more barotropically unstable.

Results of the barotropic parameter studies are summarized in Figure 3-12. Here it is seen that the properties of the time-mean circulation, in particular of the time-mean recirculations (their strength and their meridional and zonal extent), are sensitive to the supercriticality of the inflowing jet that is the source of the eddy variability that drives them. In particular, as the WBC jet becomes more unstable, the recirculations become stronger (Figure 3-12 *left panel*), and shrink in their zonal extent while expanding in their meridional extent (Figure 3-12 *right panels*). Note that the observed linear dependence of the eddy-forced, time-mean flow on the supercriticality of the entering jet is expected in a weakly nonlinear regime, and hence this result suggests that weakly nonlinear theory is potentially applicable for jets with KE-like scales, as well as for those that are more unstable than the KE throughout the full-range of physically realistic supercriticalities considered.

To make a connection with the localized wave-maker mechanism of driving the time-mean recirculations discussed in the previous chapter, I also consider the dependence of the time-mean recirculation strength on a measure of the PV forcing imposed by the inflowing unstable jet intended to be analogous to the PV forcing amplitude of the wave-maker. I take this measure of forcing amplitude to be the magnitude of the net (inflow-outflow) PV anomaly associated with the inflowing jet profile inte-
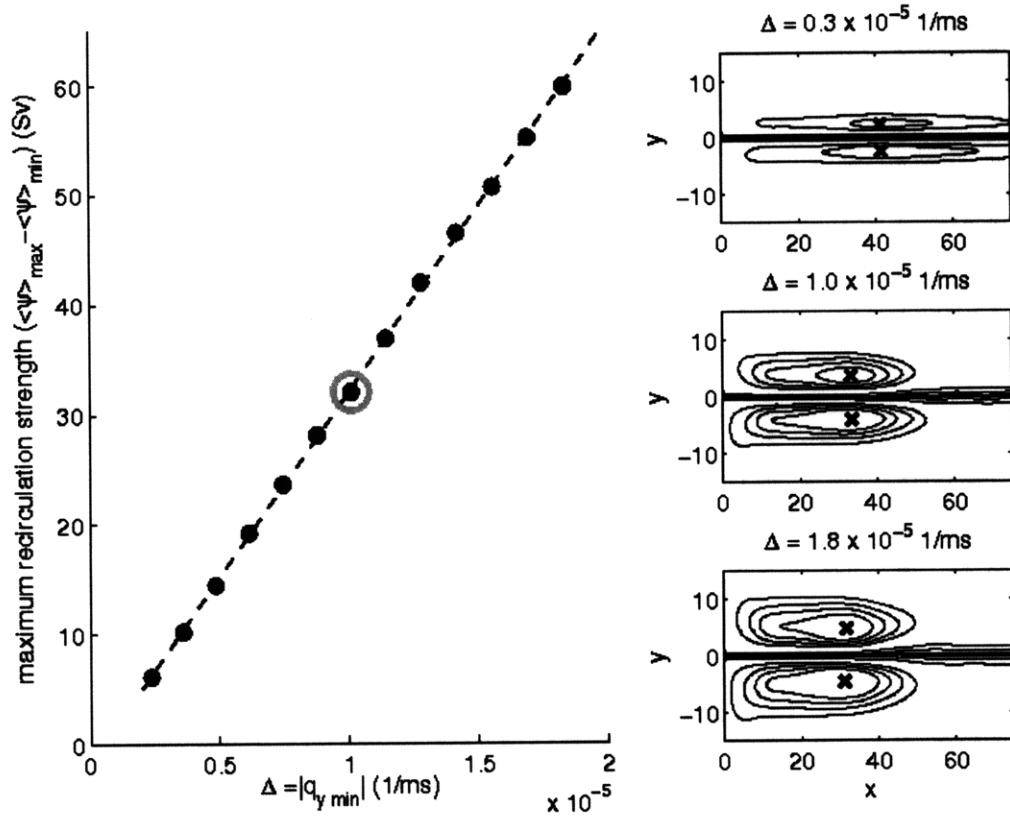
Figure 3-12: The dependence of the mean recirculation strength (as measured by the maximum time-mean recirculation transport, $\overline{\psi}_{max} - \overline{\psi}_{min}$) on the supercriticality of the inflowing jet, Δ (as measured by the depth of the negative region in the jet's meridional PV gradient profile, $|q_{ymin}|$) in a physically relevant range of parameters ($0.04 \leq \beta \leq 0.4$) (*left*). An estimate for the supercriticality of the KE, determined from the synoptic mean velocity profile of the Kuroshio jet at the point of separation from the coast derived from satellite altimetry data (see Figure C-1), is indicated by the gray circle. The time-mean circulation (streamfunctions) for small (*top*), moderate (*middle*), and large (*bottom*) inflowing jet supercriticalities showing the changing nature of the recirculation gyres as the entering jet becomes increasingly unstable (*right*).

grated over the jet's half width, a measure of the total PV anomaly associated with the imposed jet that must be mixed by the eddies between inflow and outflow. This relationship between forcing amplitude and mean circulation response in the jet configuration is shown in Figure 3-13, to be compared with the analogous dependence of recirculation strength on forcing amplitude in the wave-maker configuration in Figure 2-21. Here it is seen that for weakly unstable jets, like for the wave-maker in a weakly nonlinear regime, recirculation strength grows quadratically with forcing amplitude, while for strongly unstable jets, the rate of increase in the mean flow response slows to a linear dependence, similar to the behavior of the wave-maker in a strongly nonlinear regime. It is noteworthy that when viewed in this way, results from the jet parameter studies suggest that the parameter range considered spans a transition between weakly nonlinear and strongly nonlinear regimes, while these same results viewed in the context of the traditional definition of supercriticality instead suggest that weakly nonlinear theory is valid for all values of the parameters considered.

Finally, in attempts to better understand the observed dependence of recirculation extent on the supercriticality of the inflowing jet, I also consider the parameter study results in the context of linear stability calculations. As the right panels of Figure 3-12 demonstrate, in addition to becoming stronger as the inflowing jet's supercriticality increases, the time mean recirculations also are observed to shrink in their zonal extent, with the downstream location of maximum recirculation transport (and jet stabilization) moving upstream. The dependence of this key downstream location on forcing amplitude is shown explicitly in the left panel of Figure 3-14. For small forcing amplitudes, the downstream location of maximum time-mean recirculation transport is located far downstream. This location however moves rapidly upstream as jet supercriticality is increased in the weakly nonlinear regime, until a saturation is achieved in the strongly nonlinear regime. Note that partial insight into this dependence is suggested by the results of the linear stability calculation for the inflowing jet profiles considered, and specifically the result that the inverse growth rate shows a very similar dependence, decreasing as the jet profile becomes more unstable (Figure 3-14 *right*). The correspondence of these results is encouraging,
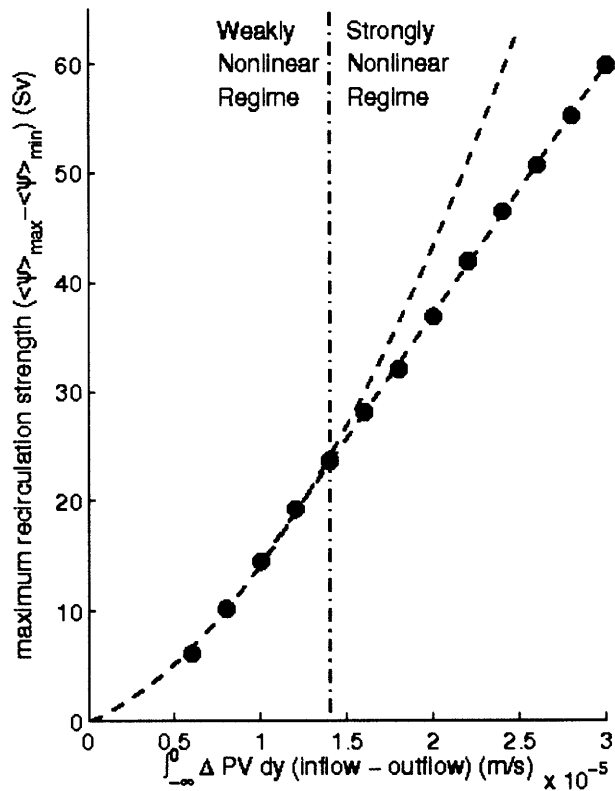
Figure 3-13: As in Figure 3-12, but with the mean circulation response now plotted as a function of a measure of the PV forcing amplitude supplied by the inflowing unstable jet, ΔPV (as measured by the magnitude of the net (inflow-outflow) PV anomaly associated with the imposed jet profiles) integrated over the jet's half width, intended to be analogous to the PV forcing amplitude of the wave-maker discussed in Chapter 2. The dashed vertical line indicates a transition from a weakly nonlinear to strongly nonlinear regime based on the observed change in the mean flow response from quadratic to linear in the forcing amplitude.
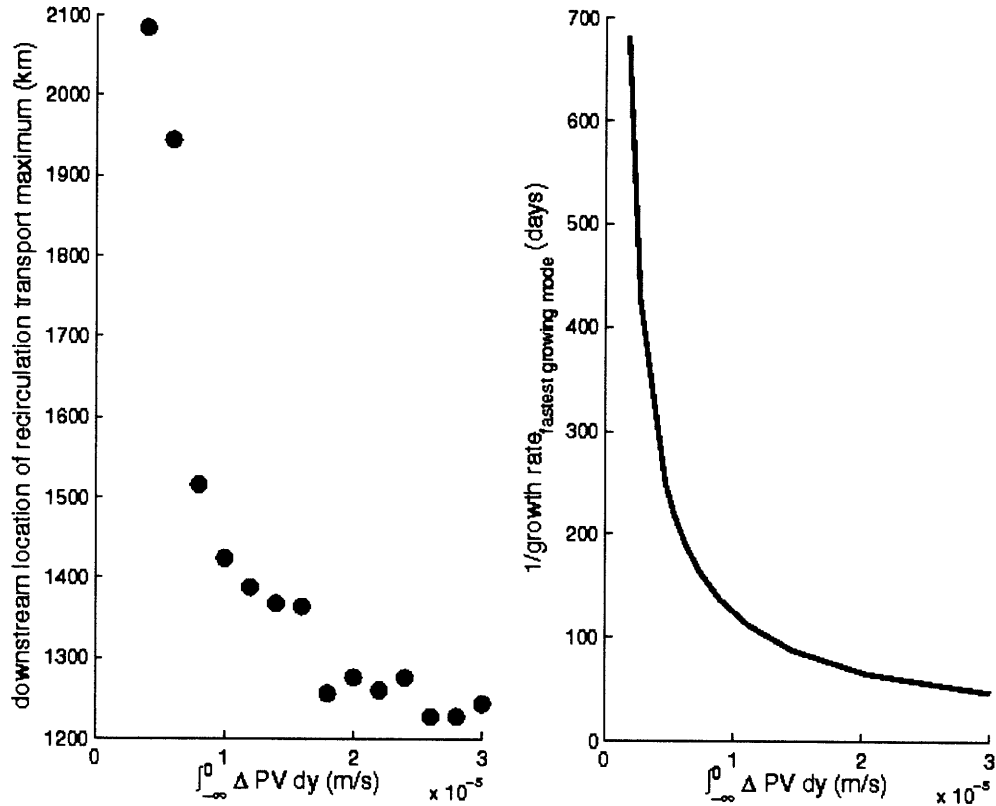
Figure 3-14: The dependence of recirculation zonal extent (as measured by the downstream location of maximum time-mean recirculation transport, $\overline{\psi}_{max} - \overline{\psi}_{min}$) (*left*) vs. inverse growth rate (from the linear stability calculation for the inflowing jet profile) (*right*) on forcing amplitude.

and suggests that the linear stability calculation predictions for the properties of the fastest growing mode have some utility in predicting the properties of the fully nonlinear solution, and further supports the claim that weakly nonlinear dynamics have validity in a WBC-appropriate parameter regime. The similarity in the behavior of these two quantities leads to the hypothesis that the downstream location of maximum recirculation transport (and jet stabilization) is related to the distance the jet advects the growing instability in the time it takes for the eddies to grow to sufficient size such that their fluxes are effective at stabilizing the mean-jet profile. The growth rate is faster for more unstable jets, but the magnitude of the PV anomaly associated with that jet is also larger, so distance to stabilization is not a simple direct function of inverse growth rate and jet speed alone.

This brings me to the end of my analysis of the barotropic case. It has resulted in an expanded picture of the nature and importance of the eddy effect on the time-mean circulation, the mechanisms that permit that effect, and the dependence of that effect on system parameters in an idealized WBC-like jet. These results however are limited in their applicability to WBC jets by the fact that they are all derived from a system with barotropic dynamics only. The GS and KE jets are, on the other hand, of course strongly baroclinic, and one expects baroclinic instability to also play a role. How does baroclinic dynamics change our understanding of the eddy effects in the barotropic model? The extension of these results to a two-layer case, more applicable to an unstable WBC jet separating form the coast and entering the open ocean, is considered next.

3.4   Results: The Baroclinic Case

In a two-layer, baroclinic configuration, the inflowing jet can be barotropically unstable, baroclinically unstable, or both. Given my interest in the dynamics of separated WBC jets, I restrict my attention to cases where there is an inflowing jet at the western boundary of the upper layer, but zero inflow at the western boundary of the lower layer. This is appropriate to the WBC at the point of separation from the coast when it turns to enter the deep, relatively quiescent, open ocean.

In this configuration, I consider both the case where I expect the system to be unstable to baroclinic instability only, and the case where I expect the system to be subject to a mixed (barotropic and baroclinic) instability mechanism. In the former case, the imposed upper layer jet is weak enough and broad enough (β is large enough) such that it is stable to the necessary condition for barotropic instability, but the lower layer is shallow enough (the lower layer inverse Burger number, $\frac{1}{S_2}$, is large enough) such that the thickness contribution to the lower layer PV gradient causes a reversal in sign of the PV gradient in the vertical at the jet axis, thus satisfying the necessary condition for instability (Figure 3-15 *upper left*). In the mixed instability case, I impose a strong, sharp upper layer jet such that there is a sign reversal in the

meridional PV gradient in both the horizontal in the upper layer and in the vertical (Figure 3-16 *upper left*).

The instantaneous and time-mean circulations for both cases are shown in Figures 3-15 and 3-16 respectively. Note that in both cases, the time-mean circulation is characterized by time-mean recirculation gyres in both layers that flank the time-mean jet.

I have studied both cases in detail, but will restrict discussion here to the mixed instability case. The reason for this is that to achieve the baroclinically unstable only case, one requires a choice of parameters (in particular the choice of a very large β and a large lower layer Burger number) that are unphysical for the WBC jet application. As such, discussion of the baroclinic instability only case is academic. In any case, it so happens that, through eddy fluxes associated with the stabilization of the vertical shear, the baroclinically unstable case evolves to a mixed instability case downstream, and shares similar dynamics to the mixed instability case that will be discussed.

3.4.1 The Effect of Eddies on the Time-Mean Circulation

As in the barotropic case, I consider the effect of eddies on the time-mean circulation by considering their contribution to the time-mean budgets of momentum, vorticity and kinetic energy. Here I summarize these effects, highlighting the commonalities with the barotropic case where they exist, and the new features that result from the addition of baroclinic dynamics.

(a) Eddy effect on the mean zonal momentum budget (the zonal "effective eddy force")

In the two-layer case, the TEM framework involves the definition of a residual circulation with the aim of removing skew buoyancy flux from the buoyancy budget, then rewriting the momentum budget to replace ageostrophic velocities with the residual velocity. This removes explicit eddy terms from the buoyancy budget, and the eddies appear in the momentum budget, like in the barotropic case, as a force per unit mass equal in magnitude and normal to the eddy PV flux, which now includes
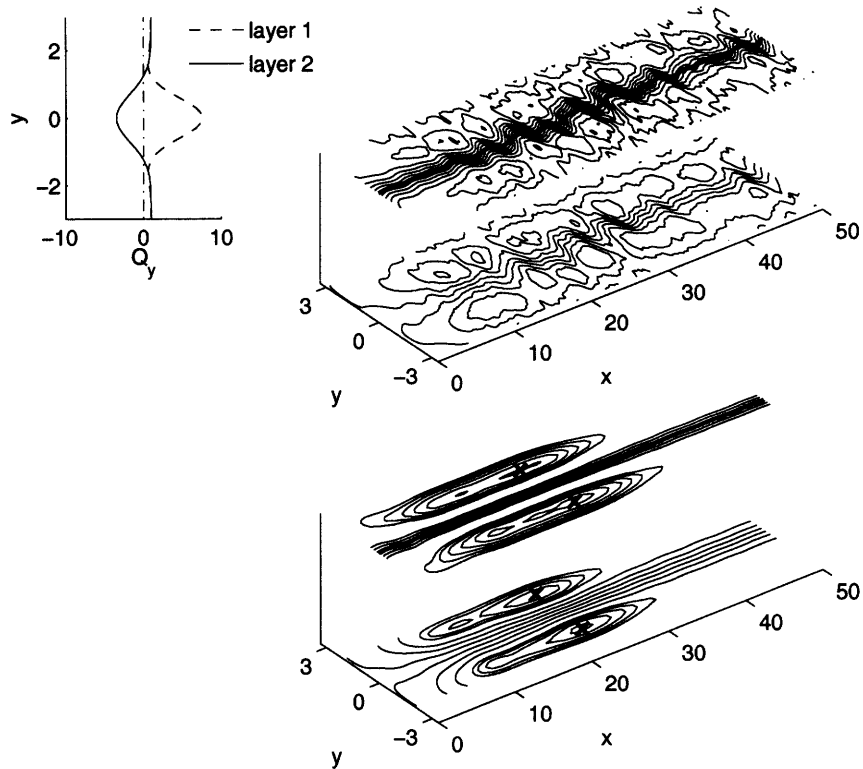
Figure 3-15: A snapshot of the instantaneous (*top*) and time-mean (*bottom*) circulation (streamfunctions) for a typical baroclinically unstable two-layer run ($A = -1.0$, $\ell = 1.0$, $\beta = 1.0$, $S_1 = S_2 = 4.0$, see Appendix C for definitions). The model is forced at the western boundary ($x = 0$) in the upper layer by a jet whose vorticity gradient profile does not change sign in the horizontal ($Q_{1y} > 0$ everywhere) (*upper left*), and as such we expect (heuristically) it to be stable to barotropic instability. There is no inflow in the lower layer. The vertical shear between the upper layer jet and the quiescent lower layer at the the western boundary is such that the vorticity gradient profile does change sign in the vertical ($\frac{Q_{1y}}{Q_{2y}} < 0$ at the jet axis) (*upper left*), and as such we expect (heuristically) the system to be unstable to baroclinic instability. The instantaneous picture is characterized by waves that are radiated from the jet in both layers. The time-mean circulation is characterized by a pair of weakly depth-dependent counter-recirculating gyres that flank a time-mean zonal jet. The xs denote the locations of the maximum time-mean recirculation transport in each layer.
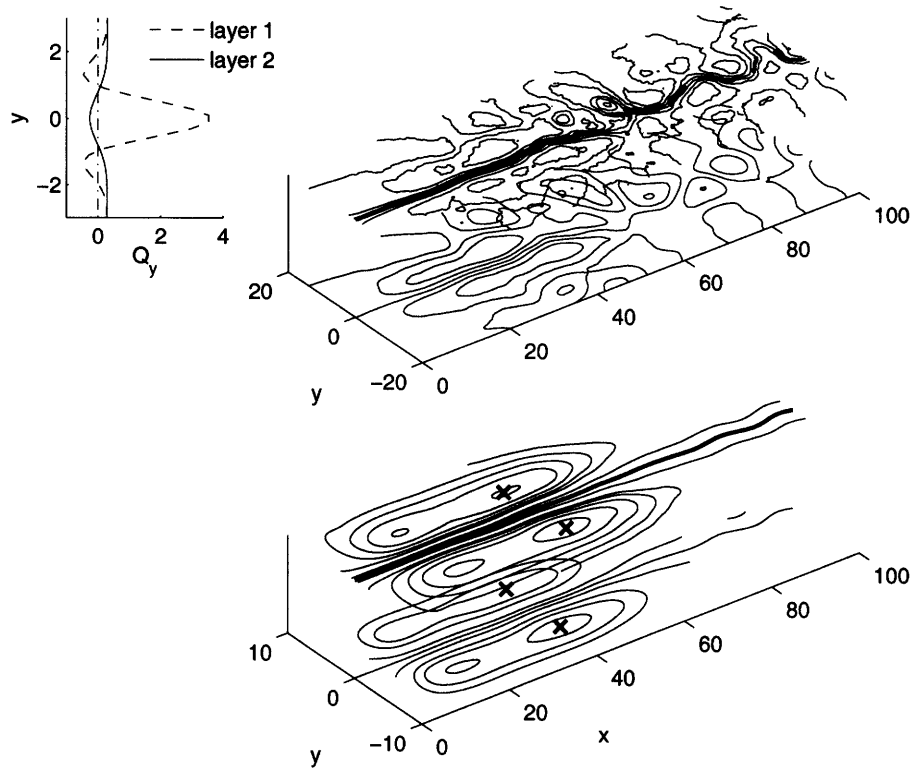
Figure 3-16: A snapshot of the instantaneous (*top*) and time-mean (*bottom*) circulation (streamfunctions) in the upper and lower layers of a typical two-layer case relevant to a WBC jet extension ($A = -1.0$, $\ell = 1.0$, $\beta = 0.03$, $S_1 = 1.0$, $S_2 = 0.25$). The system is forced at the western boundary ($x = 0$) in the upper layer by a jet whose vorticity gradient profile, Q_{1y}, changes sign in the horizontal (*upper left*). There is no inflow in the lower layer. The vertical shear between the upper layer jet and the quiescent lower layer at the western boundary is such that the vorticity gradient profile also changes sign in the vertical ($\frac{Q_{1y}}{Q_{2y}} < 0$) (*upper left*). As such, we expect the inflowing jet to be potentially subject to a mixed (both barotropic and baroclinic) instability mechanism. The instantaneous circulation is characterized by waves radiated from the upper layer jet and intense upper layer jet meandering downstream. In the lower layer, it is characterized by deep recirculations upstream and an intense eddy field downstream. The time-mean circulation is characterized by weakly depth-dependent recirculations and the development of a lower-layer time-mean zonal jet.

both relative and thickness contributions. The zonal component of this "effective eddy force", F_{xn} is thus given by:

$$F_{x1} = \overline{v_1' q_1'} = \frac{\partial}{\partial x}(\overline{v_1' v_1'}) - \frac{\partial}{\partial x}\overline{\epsilon_1} - \frac{\partial}{\partial y}(\overline{u_1' v_1'}) + \frac{1}{S_1}(\overline{v_1'(\psi_1' - \psi_2')} - \overline{v_2'(\psi_1' - \psi_2')}) \quad (3.5)$$

$$\text{where} \quad \overline{\epsilon_1} = \frac{1}{2}(\overline{(u_1' u_1')} + \overline{(v_1' v_1')} + \overline{((\psi_1' - \psi_2')(\psi_1' - \psi_2'))}) \quad (3.6)$$

Here numerical subscripts indicate the layer. S_1 is the upper layer Burger number, $S_1 = \frac{ND_1}{fL}$, where N is the buoyancy frequency, D is the upper layer depth, f is the Coriolis frequency and L is a typical horizontal length scale of the flow (the Burger number can be thought of as a representation of the relative importance of stratification in the vertical to rotation in the horizontal). The lower layer zonal effective eddy force, F_{x2}, is analogous. These forces are visualized in the left panels of Figure 3-17 in the upper layer (*top*) and in the lower layer (*bottom*). The black contours are of the time-mean streamfunction to indicate the position of the mean zonal jet and recirculation gyres, again with the xs denoting the location of maximum time-mean recirculation transport in each layer. The shaded region $0 < x < 10$ denotes the western sponge layer where dissipation is enhanced.

As described in Section 3.3.1a, it is helpful to interpret this quantity as acting in the sense of accelerating or decelerating the time-mean flow when the mean flow is zonal, and turning the time-mean flow when the mean flow is oriented meridionally. Viewed in this way, Figure 3-17 shows that the zonal effective eddy force in the two-layer configuration acts in analogous ways as in the barotropic jet, namely (heuristically) stabilizing the (now upper layer) jet to its barotropic instability, and providing torques on the mean flow to close the recirculation gyres (now in the lower layer). Like the barotropic case, the former effect is achieved via a meridional eddy PV flux in the upper layer inside the time-mean jet that is in the sense to exert an effective westward force at the jet axis and effective eastward forces on the jet flanks up until the approximate downstream location where the jet has been (heuristically) stabilized to its barotropic instability in the time-mean (*i.e.* $\overline{q}_{1y}$ becomes single signed
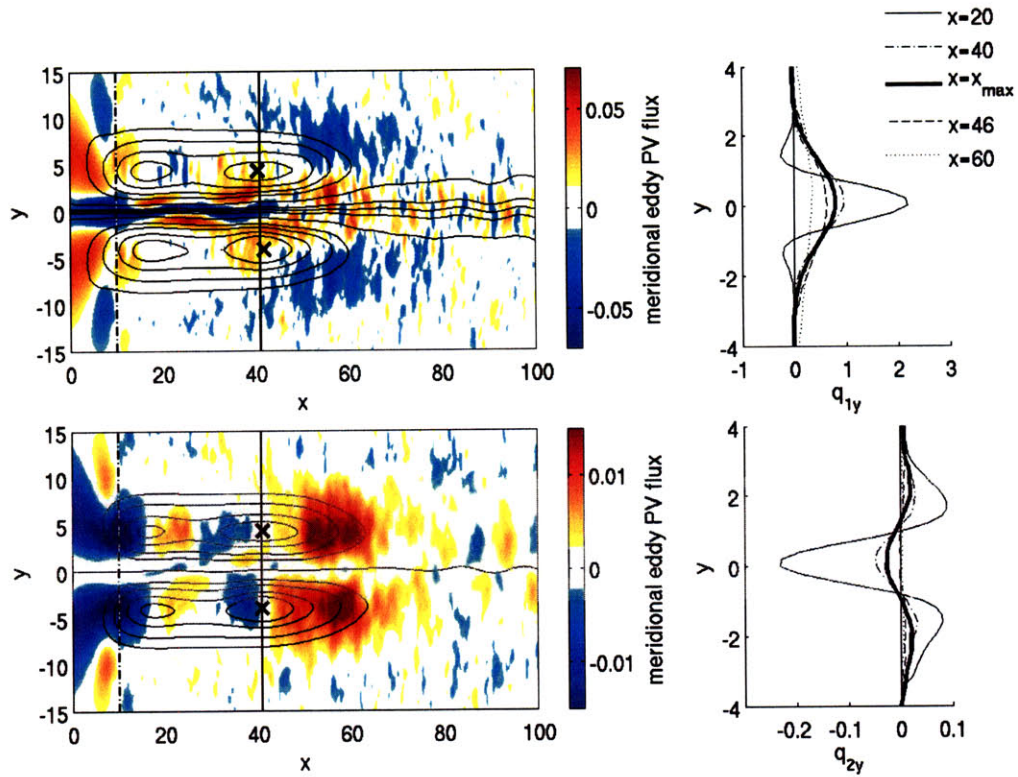
Figure 3-17: The zonal "effective eddy force" in the two-layer case (defined in the text) (color) for the upper layer (*top*) and the lower layer (*bottom*) (*left*). The black contours are of the time-mean streamfunction to indicate the position of the mean zonal jet and recirculation gyres, with xs denoting the location of maximum time-mean recirculation transport. The shaded region $0 < x < 10$ denotes the western sponge layer where dissipation is enhanced. The downstream evolution of the meridional profiles of the meridional PV gradient associated with the time-mean jet in the upper (*top*) and lower (*bottom*) layers (*right*).

(Figure 3-17 *upper right*)). Also like the barotropic case, the latter effect is achieved via a meridional eddy PV flux inside the time-mean recirculations, here in the lower layer, that is in the sense to introduce anti-cyclonic curvature to the time-mean flow north of the jet axis and cyclonic curvature to the time-mean flow south of the jet axis at the western boundary, and cyclonic curvature north of the jet axis and anti-cyclonic curvature south of the jet axis at the eastern extent of the recirculation gyres.

There are differences between the effective eddy force picture in the barotropic and two-layer cases as well. Most notable is the addition of a secondary local maxima in recirculation transport upstream of stabilization, and additional lower layer eddy forces in the sense to force the divergence and convergence of the lower layer jet consistent with it. I hypothesize that this new feature may be related to the addition of the baroclinic instability mechanism to the problem, and an interplay between the counteracting efforts of eddies acting to reduce the horizontal shear in the upper layer jet while also acting to reduce the vertical shear (and in the process flux momentum into the upper-layer jet). As it will be seen, other diagnostics will help to build on this idea. A second new feature is that the eddy torque responsible for closing the recirculation gyres, dominant in the lower layer, is now absent from the upper layer picture. This, as it will be seen, is a consequence of the fact that the eddy effect inside the time-mean recirculations is derived primary from eddy thickness fluxes in the two-layer case, and hence if "recirculation-driving" in the lower layer is, by necessity, "anti-recirculation driving" (*i.e.* driving a circulation clockwise to the north of the jet and anti-clockwise to the south of the jet) in the upper layer, although this effect is dwarfed by the effect of eddy relative vorticity fluxes which dominate the upper layer eddy PV flux. Further insights into how the eddy thickness flux acts in this way to make the recirculation strength less depth-dependent than it would otherwise be in the absence of these fluxes will also be elaborated on in further discussions.

Finally, it is useful to note that, again similar to the barotropic case, an interesting relation between the stability of the time-mean jet and the sense of the eddy effect in the two-layer case is observed. With the addition of baroclinic instability in the two-layer problem, there are now both horizontal and vertical shears that the eddies act to

reduce. From an examination of the downstream evolution of the meridional profiles of the mean meridional PV gradient in both the upper and lower layers (Figure 3-17 *right*) it can be seen that, similar to the barotropic case, the switch in the sign of the eddy forcing inside the time-mean recirculations (determining the downstream location of maximum recirculation transport) is related to the stability properties of the time-mean jet. In particular, this maximum is located (at $x \sim 42$ in this case) in between where the upper layer time-mean jet profile is first likely "stabilized" to barotropic stability (*i.e.* where $\bar{q}_{1y}$ is first single signed everywhere, at $x \sim 40$ in this case) and the system is first likely "stabilized" to baroclinic instability (*i.e.* where $\frac{\bar{q}_{1y}}{\bar{q}_{2y}}$ is first single signed everywhere, at $x \sim 48$ in this case). Understanding the role of the jet's stability properties in determining the eddy effect and its evolution downstream will also be developed further in subsequent discussions.

(b) Eddy effect on the mean vorticity budget

In the two-layer system, the eddy QGPV flux is $\overline{u'_{ni}q'_n} = \overline{u'_{ni}\left(\frac{\partial}{\partial x}v'_n - \frac{\partial}{\partial y}u'_n \pm \frac{1}{S_n}(\psi'_n - \psi'_{n\pm 1})\right)}$. The divergence of this flux is the eddy-forcing term in the time-mean vorticity balance, given by (in non-dimensional form and in the 2-layer framework in the upper and lower layers respectively):

$$
\begin{aligned}
\overline{\partial_i u'_{1i}q'_1} &= \frac{\partial^2}{\partial x \partial y}(\overline{v'_1 v'_1}) - \frac{\partial^2}{\partial x \partial y}(\overline{u'_1 u'_1}) + \frac{\partial^2}{\partial^2 x}(\overline{u'_1 v'_1}) - \frac{\partial^2}{\partial^2 y}(\overline{u'_1 v'_1}) \\
&+ \frac{1}{S_1}\left(\frac{\partial}{\partial x}(\overline{u'_1 b'_1}) - \frac{\partial}{\partial x}(\overline{u'_2 b'_2}) + \frac{\partial}{\partial y}(\overline{v'_1 b'_1}) - \frac{\partial}{\partial y}(\overline{v'_2 b'_2})\right)
\end{aligned}
\tag{3.7}
$$

$$
\begin{aligned}
\overline{\partial_i u'_{2i}q'_2} &= \frac{\partial^2}{\partial x \partial y}(\overline{v'_2 v'_2}) - \frac{\partial^2}{\partial x \partial y}(\overline{u'_2 u'_2}) + \frac{\partial^2}{\partial^2 x}(\overline{u'_2 v'_2}) - \frac{\partial^2}{\partial^2 y}(\overline{u'_2 v'_2}) \\
&+ \frac{1}{S_2}\left(\frac{\partial}{\partial x}(\overline{u'_2 b'_2}) - \frac{\partial}{\partial x}(\overline{u'_1 b'_1}) + \frac{\partial}{\partial y}(\overline{v'_2 b'_2}) - \frac{\partial}{\partial y}(\overline{v'_1 b'_1})\right)
\end{aligned}
\tag{3.8}
$$

Here $b'_1 = \psi'_1 - \psi'_2$ and $b'_2 = \psi'_2 - \psi'_1$. This quantity is visualized in the left panels of Figure 3-18, the upper layer on top and the lower layer on bottom. Again the time-mean streamfunction is indicated by the black contours, and the **xs** denote the downstream location of maximum time-mean recirculation transport.
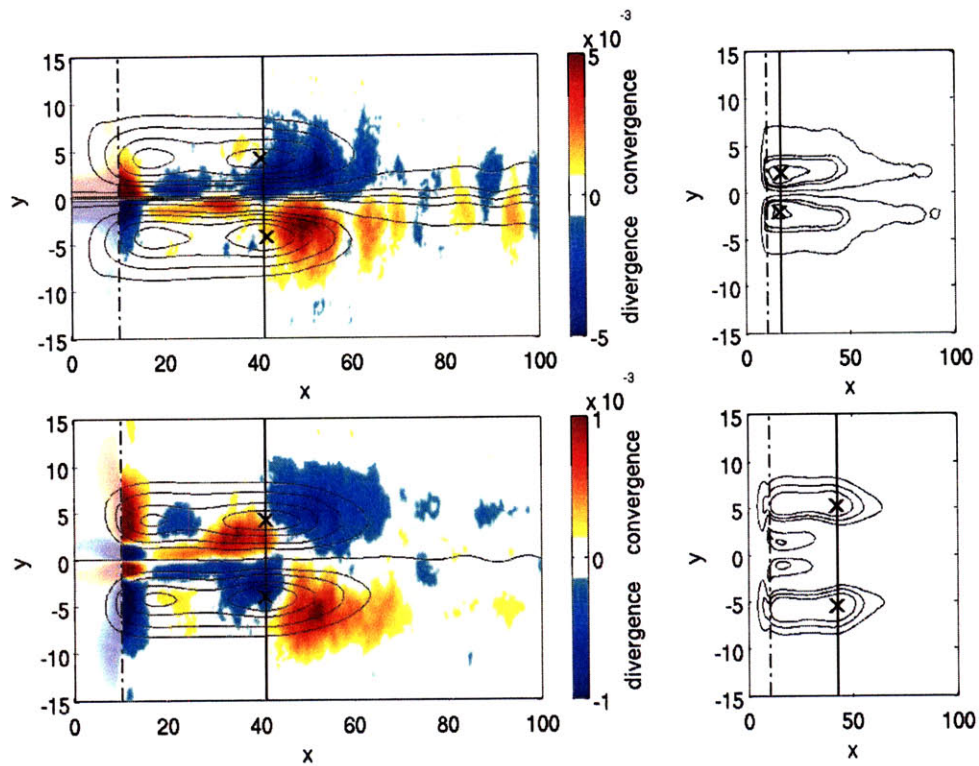
Figure 3-18: The eddy vorticity forcing (defined in the text) (color) for the upper layer (*top*) and the lower layer (*bottom*) (*left*). The time-mean circulation driven by this eddy forcing, computed as the solution to the linear vorticity equation forced statically by the eddy vorticity forcing field (*right*).

Like the case of the effective eddy force, the eddy vorticity forcing in the two-layer case shows both important similarities and new features to the barotropic picture.

Most notable is the dominant, recirculation-driving, dipole pattern of eddy vorticity flux convergence and divergence north and south of the jet axis downstream of jet stabilization, familiar from the barotropic case. This is the dominant feature of both the upper and lower layer fields. It suggests relevance of the barotropic eddy-driving mechanism to each layer of the baroclinic case. The upstream "anti-recirculation gyre"-driving dipole pattern, responsible for limiting the westward extent of the strongest recirculation velocities, is also featured, although it is seen prominently only in the lower layer.

There are new features as well. Here most notable is the new contribution localized to inside the time-mean jet upstream of jet stabilization / the location of maximum recirculation transport. Its opposite sense in each layer indicates that it is likely a consequence of thickness fluxes. As it will be seen, the effect of this eddy forcing is to drive (in part) the lower layer zonal jet that develops downstream beneath the upper layer forced jet, a result of the eddies acting to reduce the jet's vertical shear.

The time-mean circulation driven by this eddy forcing, again computed as the solution to the linear vorticity equation forced statically by the eddy vorticity forcing field, is shown in the right-hand panels of Figure 3-18. Here again it can be seen that the eddies in the baroclinic case are responsible for driving time-mean recirculation gyres in both layers, although there are differences between these gyres driven directly by linear dynamics forced by the eddy vorticity forcing alone, and those in the fully nonlinear solution (for example the downstream location of the maximum time-mean recirculation transport in the upper layer, and the circulation inside the time-mean zonal jet that develops in the lower layer). The role of the new contribution upstream of jet stabilization is explored by computing the time-mean circulation (Figure 3-19 *right*) driven by linear dynamics forced this time only by the eddy vorticity forcing field upstream of jet stabilization (Figure 3-19 *left*). As mentioned, here it can be seen that this new eddy forcing is responsible for driving (in part) the lower layer zonal jet that develops downstream beneath the upper layer forced jet, while forcing a narrow
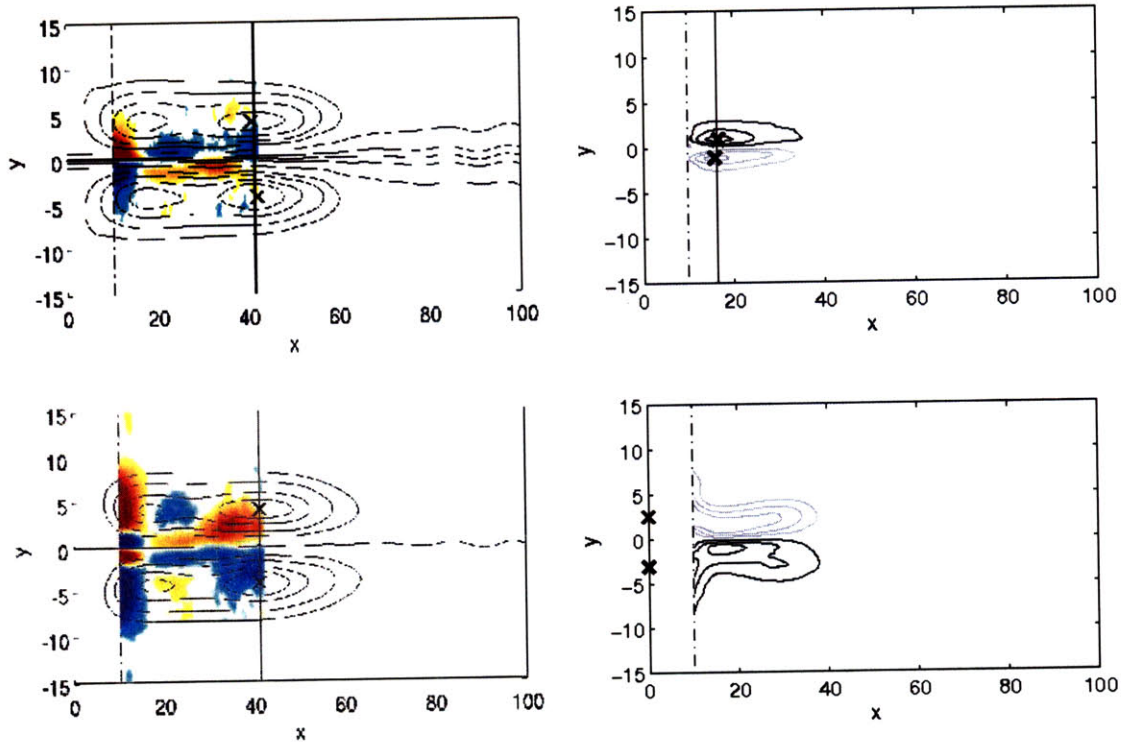
Figure 3-19: The time-mean circulation (*right*) driven by linear dynamics forced by only the eddy-vorticity forcing field upstream of the location of jet stabilization (*left*) for the upper layer (*top*) and lower layer (*bottom*) respectively. Black contours indicate positive values of the eddy-driven time-mean streamfunction while gray contours indicate negative values.

pair of "anti-recirculation gyres" (clockwise circulation to the north, anti-clockwise circulation to the south) in the upper layer which have the effect of decelerating the upper layer jet at its axis. By accelerating a lower layer jet and decelerating the upper layer jet, this new eddy forcing contributes to reducing the jet's large-scale vertical shear, and stabilizes it to its baroclinic instability.

(c) Eddy effect on the mean kinetic energy budget

As in the barotropic case, eddies produce and extract kinetic energy from the mean according to the production term in the equation for conservation of mean
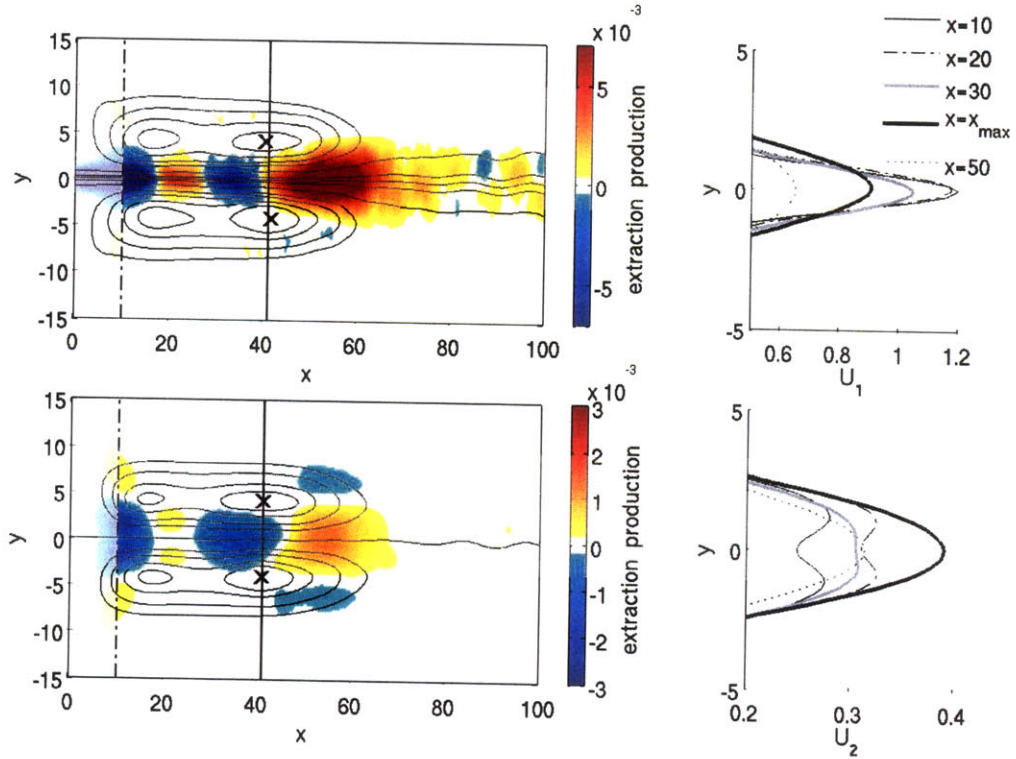
Figure 3-20: The production term in the equation for conservation of mean kinetic energy in each layer (defined in the text) (color) for the upper layer (*top*) and the lower layer (*bottom*) (*left*). The downstream evolution of the meridional profiles of the time-mean zonal velocity associated with the time-mean jet in the upper layer (*top*) and lower layer (*bottom*) (*right*).

kinetic energy in each layer:

$$\frac{\partial}{\partial t}\overline{KE_i} = -\left(\overline{u_i}\left(\frac{\partial}{\partial x}\overline{u_i'u_i'} + \frac{\partial}{\partial y}\overline{u_i'v_i'}\right) + \overline{v_i}\left(\frac{\partial}{\partial x}\overline{u_i'v_i'} + \frac{\partial}{\partial y}\overline{v_i'v_i'}\right)\right) + ... \quad (3.9)$$

This mean energy production term is visualized for this typical mixed instability case in Figure 3-20 for the upper layer (*top*) and lower layer (*bottom*) (Figure 3-20 *left*) respectively.

Here it can be seen that both layers exhibit a similar pattern in eddy and mean kinetic energy conversions as in the barotropic case in the vicinity of jet stabilization / maximum recirculation transport, with eddies extracting kinetic energy from the mean upstream of where the time-mean jet is stabilized, and producing mean kinetic

energy downstream of this location. Again, the commonality with the barotropic case suggests the dominance of barotropic mechanisms in the eddy and mean energy conversions. The significant production of mean kinetic energy by the eddies downstream of jet stabilization again indicates the importance of this region in the eddy-driving of the mean recirculations.

Like the cases of the effective eddy force and the eddy vorticity forcing however, there is also additional upstream structure: here an extraction - production pattern associated with the first local maxima in recirculation transport. The lower layer jet is seen to strengthen, weaken, strengthen and weaken again consistent with this picture (Figure 3-20 *lower right*). Again it is suggestive of an interplay between the two instability mechanisms in the problem, and the counteracting effects of eddies in the lower layer acting to reduce vertical and horizontal shears.

To summarize, diagnosis of the eddy effect on the time-mean budgets of zonal momentum, vorticity, and kinetic energy in the baroclinic case has produced a picture of an eddy effect on the time-mean circulation that shares many significant similarities to the barotropic case: eddies continue to act to stabilize the upper layer jet to its barotropic instability, and drive the recirculations via an eddy flux convergence / divergence pattern downstream of jet stabilization. The picture however is modified by the addition of baroclinic dynamics: lower layer dynamics especially exhibit differences stemming from the lack of influence of a strong jet in the background PV field and from forcing by thickness fluxes. Differences also arise from the additional instability mechanism in the problem, resulting in an additional eddy effect upstream of jet stabilization that acts to stabilize the system to its baroclinic instability, and new structure in both the time-mean circulation and the eddy effect there, a consequence of the interplay of counteracting eddy effects to reduce the jet's horizontal and vertical shears. Like the barotropic case, the zonal coordinate is important in defining the regime of eddy-mean flow interaction behavior (jet-stabilizing *vs.* recirculation-driving) however now the regime boundary is defined by some average of where the time-mean jet is stabilized to it barotropic-like and baroclinic-like instabilities, which

occur at different distances downstream.

3.4.2 Insights into the Eddy-Driving Mechanism

(a) Eddy enstrophy considerations

As in the barotropic case, the eddy enstrophy generation and eddy enstrophy advection terms in the enstrophy variance budget, $-\overline{(\mathbf{u}'q')} \cdot \nabla \bar{q}$ and $\overline{\nabla \cdot \mathbf{u}\frac{q'^2}{2}}$ respectively where now $q_n = \left(\frac{\partial}{\partial x}v_n - \frac{\partial}{\partial y}u_n \pm \frac{1}{S_n}(\psi_n - \psi_{n\pm 1})\right)$, give insight into the eddy-driving mechanism. These terms are visualized in Figure 3-21, with the negative of the eddy enstrophy generation term (eddy enstrophy destruction) on the left, and the divergence of the eddy enstrophy advection on the right. Red colors in the right panels indicate eddy enstrophy destruction (regions of up-gradient eddy PV flux) and blue colors in the left panels indicate advection convergence in a sense counter to dissipation (potentially permitting regions of up-gradient eddy fluxes). Again there are many similarities and also new features compared to the barotropic case.

It is interesting that the upper layer picture looks essentially identical to that of the barotropic case, with up-gradient fluxes on the flanks of the time-mean jet upstream of jet stabilization (associated with the action of the eddies to reduce the jet's horizontal shear), and also just downstream of jet stabilization (associated with the action of the eddies to drive the time-mean recirculation gyres). In both cases, this pattern is a result of the downstream evolution of the PV gradient associated with a barotropically unstable jet being stabilized as it evolves downstream.

The picture of eddy enstrophy destruction / up-gradient eddy fluxes in the lower layer however is new, a function of the fundamentally different dynamics in the lower layer due to the absence of a strong jet signature in the background mean PV gradient. Here is seen a pattern of up- and down- gradient fluxes localized to the flanks of the time-mean jet that develops as part of the lower layer recirculations, that proceed the pattern of lower layer jet strengthening and weakening as the barotropic and baroclinic instability mechanisms inter-play. Like the upper layer, there is a second region of important up-gradient flux just downstream of jet stabilization / the maximum in time-mean recirculation transport associated with the driving of the lower layer time-
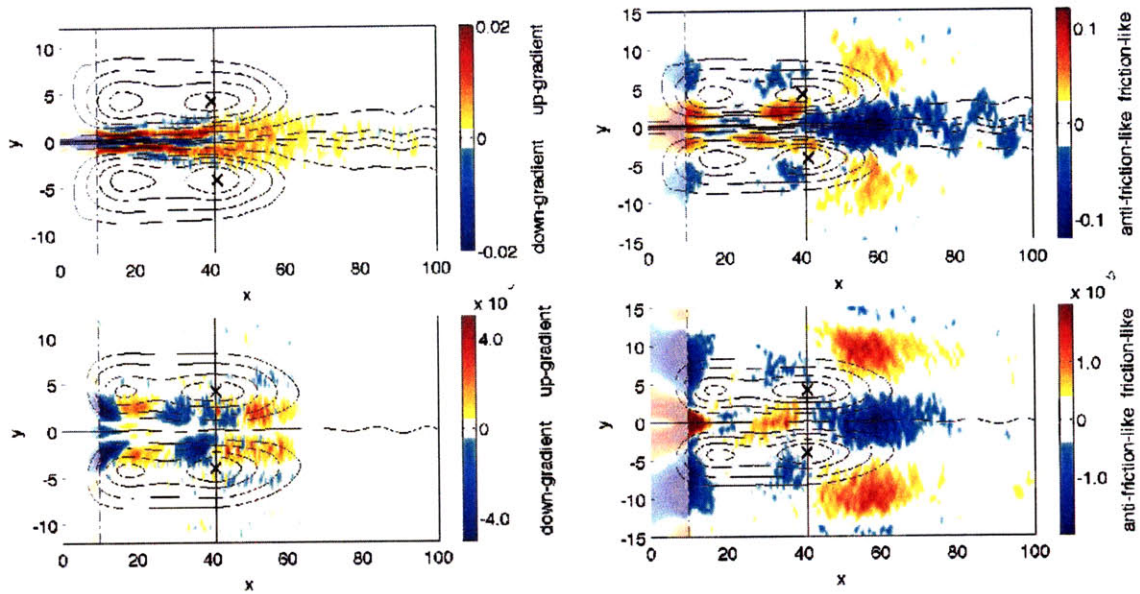
Figure 3-21: The eddy enstrophy destruction (*left*) and eddy enstrophy advection divergence (*right*) in the enstrophy variance budget of the two-layer, mixed instability case (defined in the text) (color) for the upper layer (*top*) and the lower layer (*bottom*) respectively. Red colors on the right indicate positive eddy enstrophy destruction (regions of up-gradient eddy PV flux) and blue colors on the left indicate an eddy enstrophy convergence in the sense counter to dissipation (potentially permitting regions of up-gradient eddy fluxes).

mean recirculation gyres.

The picture of the divergence of eddy enstrophy advection (Figure 3-21 *right*) confirms that these critical regions of up-gradient fluxes are permitted by significant eddy enstrophy advection convergence. Similar to the barotropic case, one sees a picture of eddy enstrophy divergence co-incident with regions of down-gradient eddy PV fluxes in regions where barotropically unstable dynamics dominate, and eddy enstrophy convergence co-incident with regions of up-gradient eddy PV fluxes in regions where baroclinically unstable or wave-radiator dynamics dominate. The dominance of the enstrophy convergence downstream of jet stabilization again implicates this downstream region as the source of the eddy-driven recirculations.

(b) A localized wave-radiator model for the eddy-driving mechanism: the two layer analogue

The similarity in the eddy vorticity forcing field downstream of jet stabilization in both the upper and lower layers of the two-layer system to the barotropic case, and the importance of this region to the eddy-driving of the recirculations suggested by the above eddy enstrophy considerations, suggest that the localized wave-radiator mechanism for the eddy-driving of the time-mean recirculations has application to the two-layer case as well. I test this hypothesis and investigate the role of the eddy-forcing downstream of jet stabilization by computing the time-mean circulation in each layer (Figure 3-22 *right*) driven by linear dynamics forced by the eddy vorticity forcing field in the wave-radiator regime only (Figure 3-22 *left*). Here both layers are forced by the time-mean eddy vorticity forcing in that layer. This experiment confirms that the action of the eddy forcing downstream of jet stabilization is indeed to drive time-mean recirculations in both layers.

3.4.3 A Conceptual Description of Eddy-Mean Flow Interactions

In previous sections it has been shown that the role of eddies in the downstream evolution of a two-layer, mixed instability jet shares many features in common with
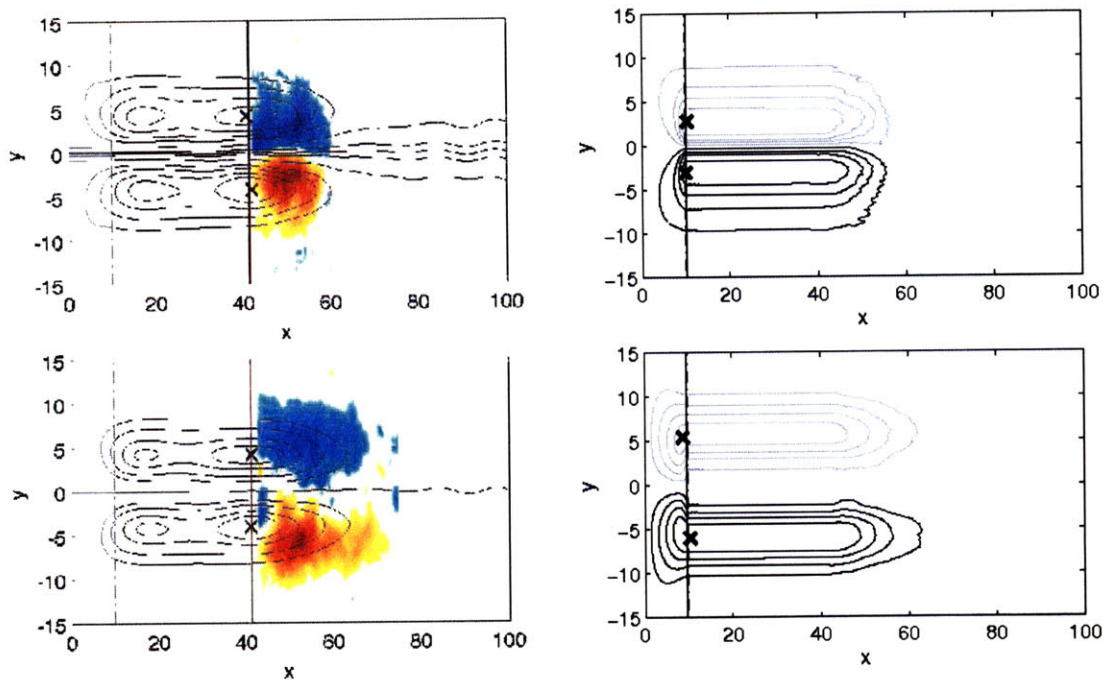
Figure 3-22: The time-mean circulation in each layer (*right*) driven by linear dynamics forced by the eddy-vorticity forcing field downstream of jet stabilization (*left*), computed to test the relevance of the localized wave-radiator model in the mixed instability case. Black contours indicate positive values of the eddy-driven time-mean streamfunction while gray contours indicate negative values.

the barotropic case. So, like the barotropic case, I argue that the role of eddies in the baroclinic case is also usefully understood (grossly) as dividing into two downstream regions based on the time-mean jet's stability properties: one where the time-mean jet is unstable essentially between the inflow and the downstream location of maximum time-mean recirculation transport (the "unstable jet regime"), and a second downstream of this location, when the time mean jet has been stabilized (the "wave-radiator" regime). In general, in the unstable jet regime, eddies act to decelerate and broaden the jet, extract energy from the mean, and mix PV down the mean-gradient, while downstream of jet stabilization, in the wave-radiator regime, they act to drive the time-mean recirculation gyres, convert eddy kinetic energy to mean kinetic energy, and flux PV up the mean gradient, similar to the barotropic case previously discussed.

But the baroclinic dynamics adds additional details to the story. First, the criterion for dividing these two downstream regions in the two-layer case is made more complicated by the fact that there are now two meridional PV gradients to consider: that of the upper layer and that of the lower layer, and two instability mechanisms to consider: that of barotropic instability and that of baroclinic instability. Second, there are now regions where one effect of the eddies is always in opposite senses in each layer (for example the "effective eddy force" is always of opposite signs in the two layers) while another eddy effect is in the same sense in each layer (for example the eddy enstrophy divergence is always the same sign in the two layers). Reconciling how and why eddies act in opposite senses in each layer for one dynamic quantity while acting in the same sense for another, also needs to be part of the modified baroclinic story.

Based on these additional details, the two regime description of eddy-mean flow interactions in the downstream evolution of a baroclinic WBC jet is modified from the barotropic case as follows (Figure 3-23): In a mixed instability jet in a parameter regime appropriate to the GS and KE, the regime of eddy-mean flow interaction behavior (jet stabilizing *vs.* recirculation driving) continues to be defined by the jet's stability properties. In the upper layer, the relevant stability criterion appears to be

the barotropic instability of the upper layer jet *i.e.* the variation of the upper layer PV gradient in the horizontal. In the lower layer too, the eddy-mean flow interaction behavior appears to be a function of the variation of that layer's PV gradient in the horizontal, here negative on the jet axis due to the jet's vertical shear. In short, it appears that insight into the eddy-mean flow interaction regime in each layer can be gleamed from whether that layer's PV gradient changes sign in the horizontal, regardless of whether that change in sign arises from horizontal or vertical shear. This stability criterion defines the sign of the eddy vorticity forcing (jet decelerating *vs.* recirculation driving) (*lower left*), the nature of eddy enstrophy advection inside the jet (divergent and friction-like *vs.* convergent and anti-friction-like) (*upper right*), the sign of the eddy enstrophy generation and hence the sense of the eddy PV flux relative to the mean gradient (down-gradient *vs.* up-gradient) (*middle right*), and the direction of conversion between mean and eddy kinetic energy (mean to eddy *vs.* eddy to mean) (*lower right*). In this typical example, the upper layer's PV gradient is stabilized ($\overline{q}_{1y\,min} > 0$) slightly upstream of where the lower layer's PV gradient is stabilized ($\overline{q}_{2y\,min} > 0$) (*upper left*), so the switch of sign of eddy effect in the quantities above tends to occur slightly upstream in the upper layer compared to the lower layer.

The exception to this rule of the sign of the eddy effect being determined by the variation of the PV gradient in the horizontal in that layer alone, and critical to the barotropic nature of the recirculation gyres, is the effective eddy force (*middle left*). The effective eddy force behaves differently because inside the recirculations, as it will be seen, it is dominated by thickness over relative vorticity fluxes in both layers, and as such, its sign is determined by an integrated effect of the sense of the eddy effect in each. It is this integrated effect that places the maximum in recirculation transport somewhere in between where the upper layer jet and lower layer jet are stabilized, its relative position between these two stabilization points being a function of the relative sizes of the layer Burger numbers.

Finally, comment should be made about the additional structure in the fields upstream of jet stabilization, in particular the region in between $x \sim 18$ and $x \sim 28$
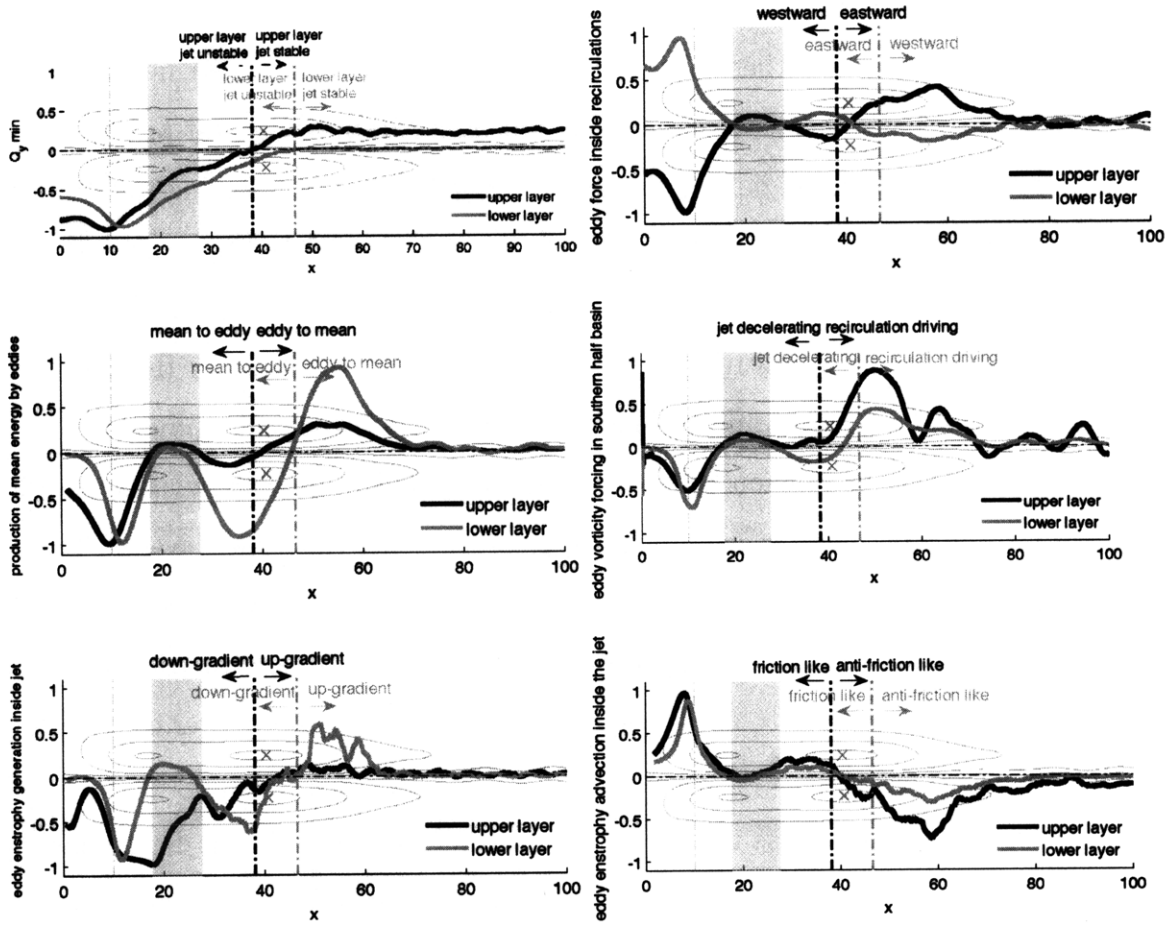
Figure 3-23: As in Figure 3-9, the downstream evolution of (a) the time-mean jet's stability properties ($\overline{q}_{ny\,min}$) (*upper left*) (b) the effective eddy force (*upper right*) (c) the production of mean kinetic energy by the eddies (*middle left*) (d) the sense of the eddy vorticity forcing (*middle right*) (e) the eddy enstrophy destruction inside the time-mean jet (*lower left*) and (f) the sign of the eddy enstrophy advection (*lower right*). Properties of the upper layer are plotted in black and properties of the lower layer are in gray. The background contours are that of the barotropic streamfunction ($\psi_{BT} = \frac{1}{S_2}\psi_1 + \frac{1}{S_1}\psi_2$). The shaded region denotes the boundaries of a new upstream region that is a feature of the mixed instability case. See the text for a full discussion.

128

non-dimensional units in this example (shaded in Figure 3-23). In this region, many of the generalizations about the sign and sense of the eddy effect in the "unstable jet regime" discussed above temporarily do not apply. This additional upstream region is a feature unique to the baroclinic case, as is the first local maximum in time-mean recirculation transport that results from it. Examination of the jet and jet stability properties in search of what makes this region unique relative to the rest of the "unstable jet regime" implicates the lower layer jet: in this region the lower layer eddy-driven jet that has been strengthening downstream starts to temporarily weaken and broaden, as if reacting, for the first time, to its own horizontal shear. This continues for a time until it becomes weak enough that baroclinic instability seems to dominate again, and it begins to strengthen again as it evolves downstream, so as to reduce the vertical shear with the upper layer jet. This phenomenon of non-monotonic changes in structure with downstream distance is unique to the deep eddy-driven jet as for it, the effects of eddies acting to stabilize it to its horizontal *vs.* vertical shears are counteracting, whereas the action of eddies to weaken and broaden the upper layer jet acts to stabilize it to both.

3.4.4 The Roles and Relative Importance of Relative Vorticity vs. Thickness Fluxes in the Eddy Forcing

The addition of baroclinic dynamics results in an additional mechanism by which eddy fluxes can influence the dynamics, that of thickness or stretching fluxes of PV. Here I decompose the eddy effects discussed thus far into their relative vorticity and thickness components, and ask what roles each play and what is their relative importance in a GS or KE-like regime. This decomposition for each of the eddy terms in the major dynamical budgets is shown in Figures 3-24 and 3-25 for the upper and lower layer respectively.

Figure 3-24 shows us that in the upper layer, in general, the contribution of the eddy relative vorticity flux dominates over the thickness flux contribution. This is perhaps expected given the presence of the upper layer jet and the significant

contribution it makes to the background PV gradient via its large mean gradient of relative vorticity. In the eddy vorticity forcing (Figure 3-24 *middle*), the thickness contribution is roughly an order of magnitude smaller than the relative vorticity contribution. The same dominance of eddy relative over thickness vorticity fluxes is also seen in the eddy enstrophy divergence (Figure 3-24 *bottom*). In contrast however, in the effective eddy force (Figure 3-24 *top*), relative and thickness fluxes each play order one roles. It is the eddy relative vorticity flux that acts to stabilize the upper layer jet. It also acts to drive the recirculations. In contrast, upper layer thickness fluxes act in a sense counter to the recirculation-driving tendency of the upper layer relative fluxes. This same opposing sense is seen in the vorticity forcing, however here the effect is relatively small. Hence it is as a consequence of thickness fluxes that the upper layer recirculation strength in the two-layer configuration is weaker than the equivalent barotropic case.

In the lower layer (Figure 3-25) this dominance of relative vorticity over thickness fluxes is not observed. This again is expected given the lack of a significant relative vorticity contribution to the background PV gradient in the lower layer given the absence of a lower layer jet. In the case of the effective eddy force (Figure 3-25 *top*), the thickness contribution dominates and is responsible for providing the torque on the mean flow needed to close the lower layer recirculations. The exception however is in the eddy vorticity forcing (Figure 3-25 *middle*), in which relative vorticity fluxes continue to play the dominant role. Note that this dominant forcing role played by the relative vorticity flux divergence in the lower layer resembles the vorticity forcing in the barotropic case, suggesting that the mechanism responsible for the eddy-driving of the recirculations in this two-layer case remains a barotropic one. Also note that, in contrast to the upper layer, the role of thickness fluxes in the lower layer are in the sense to add to the effect of the relative fluxes, thus augmenting the strength of the eddy-driven circulation relative to the barotropic case. Given that the relative vorticity fluxes feeding off the background PV gradient associated with the upper layer jet are much larger in the upper layer compared to the lower layer, in this way thickness fluxes act in the sense to equalize the eddy vorticity forcing in the two
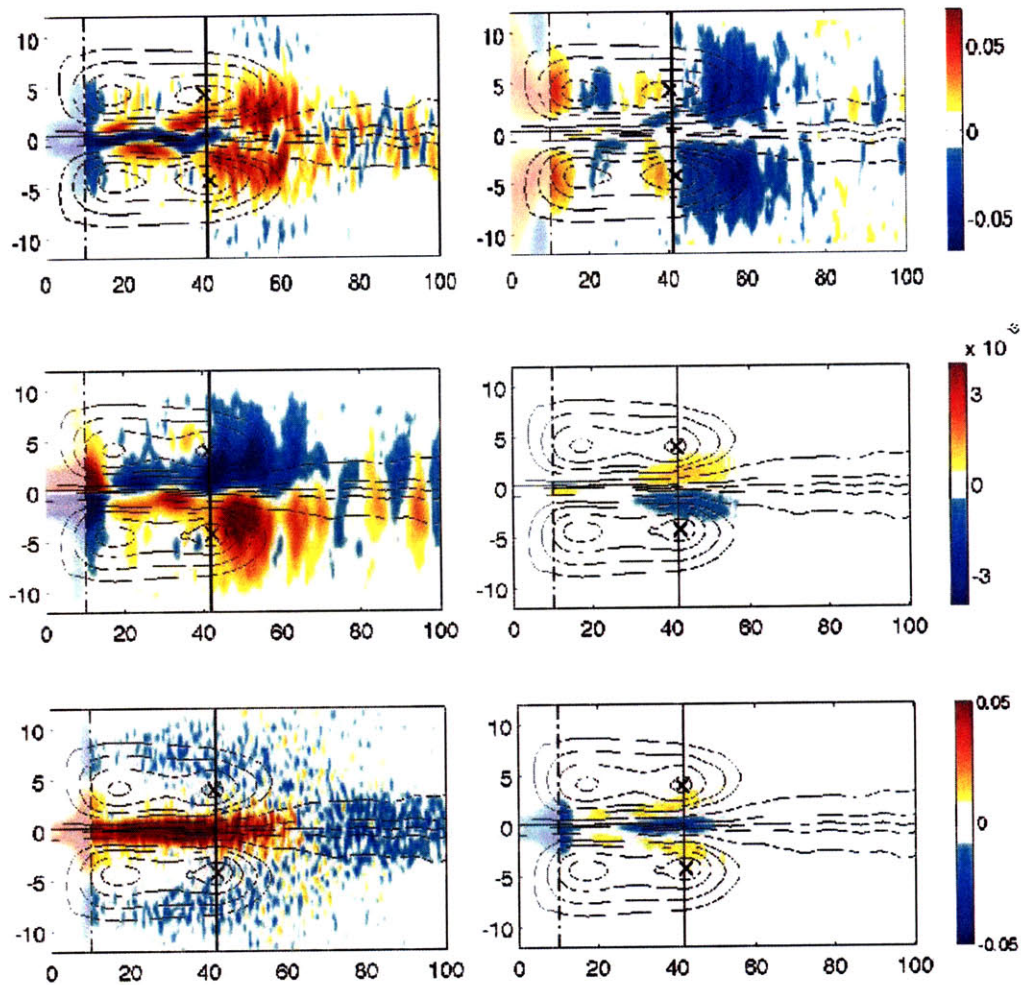
Figure 3-24: Contributions of the relative vorticity (*left*) and thickness (*right*) flux components to the upper layer "effective eddy force" (*top*), upper layer eddy vorticity forcing (*middle*), and the upper layer divergence of eddy enstrophy advection (*bottom*), each on a common color scale to determine their relative importance.

131
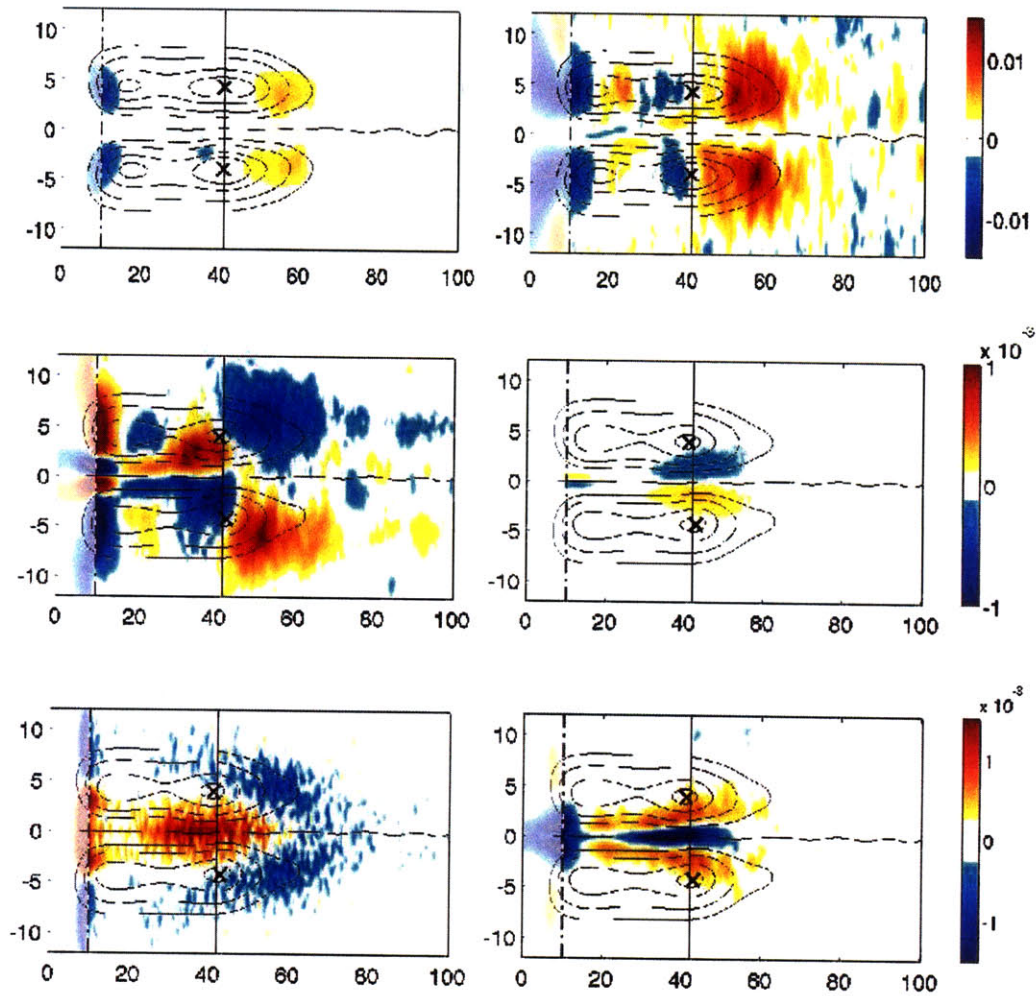
Figure 3-25: As in Figure 3-24 but for the lower layer.

layers, making the recirculation strength less depth-dependent than in the absence of these fluxes (Figure 3-26).

This comparison between the relative importance of relative vorticity *vs.* thickness fluxes in the eddy forcing highlights an important difference between the eddy momentum *vs.* vorticity forcing. Regardless of layer, the thickness flux dominates the eddy momentum forcing inside the recirculations and the relative flux dominates the eddy vorticity forcing, despite the general dominance of relative fluxes in the upper layer and thickness fluxes in the lower layer. This is significant as it helps one to understand first that it is a result of the general dominance of the relative vorticity flux in the eddy vorticity forcing that makes the vorticity dynamics responsible for the
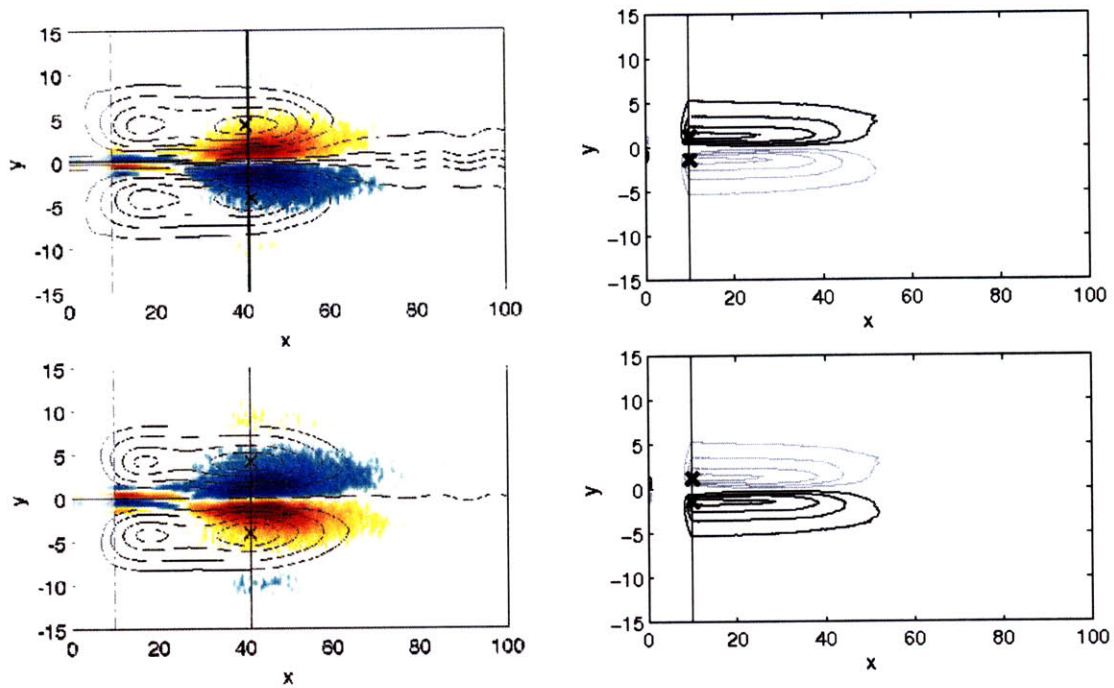
Figure 3-26: The eddy vorticity forcing resulting from the eddy flux divergence of thickness fluxes only (*left*) and the time-mean circulation it drives (*right*) for the upper layer (*top*) and lower layer (*bottom*) respectively. Black contours indicate positive values of the eddy-driven time-mean streamfunction while gray contours indicate negative values. The effect of the thickness fluxes in the upper layer is in the sense to counter the forcing of the recirculations driven by relative fluxes by driving a pair of "anti-recirculation gyres" (clockwise circulation to the north, anti-clockwise circulation to the south). In the lower layer, the effect of the thickness fluxes is in the sense to add to the forcing of the recirculation gyres driven by the relative fluxes.

eddy-driving of the recirculation gyres remain barotropic in this baroclinic case, and second that it is a result of the general dominance of the thickness flux in the eddy momentum forcing that makes the recirculation gyres only weakly depth dependent, with a downstream location of maximum transport at an integrated position where the jet is stabilized to its barotropic and baroclinic instability mechanisms.

3.4.5 The Relative Importance of Eddy Forcing

I examine the relative importance of steady state inertial terms *vs.* eddy flux terms in this more WBC jet representative two-layer case by comparing the nature and relative size of the eddy *vs.* mean (inertial) nonlinear forcing terms in both the time-mean zonal momentum budget and the time-mean vorticity budget.

Figure 3-27 contrasts the divergence of the eddy *vs.* time-mean flux of zonal momentum, $\left(\frac{\partial}{\partial x} \left(\overline{u'u'} \right) + \frac{\partial}{\partial y} \left(\overline{u'v'} \right) \right)_{TEM}$ *vs.* $\overline{u} \frac{\partial}{\partial x} \overline{u} + \overline{v} \frac{\partial}{\partial y} \overline{v}$, in each layer. As in the barotropic case, one sees that in both layers the eddy forcing term is of the same order as the mean inertial term, hence it plays at least an order one role in the mean momentum budget. Unlike the barotropic case however, the mean and eddy terms in the upper layer now act in opposing senses downstream of jet stabilization. Conversely, in the lower layer, mean and eddy terms tend to act in reinforcing senses. The absence of the strong inertial jet in the lower layer makes its dynamics fundamentally different to the upper layer in this respect.

Figure 3-28 contrasts the divergence of the eddy *vs.* time-mean flux of potential vorticity, $\left(\frac{\partial}{\partial x} \left(\overline{u'q'} \right) + \frac{\partial}{\partial y} \left(\overline{v'q'} \right) \right)$ *vs.* $\overline{u} \frac{\partial}{\partial x} \overline{q} + \overline{v} \frac{\partial}{\partial y} \overline{q}$ where $q_n = \nabla^2 \psi_n + \beta y \mp \frac{1}{S_n} (\psi_1 - \psi_2)$, $n = 1, 2$, in each layer. Like the barotropic case, the mean flux divergence dominates inside the time-mean jet upstream of time-mean jet stabilization, but eddy and mean terms are of comparable magnitude downstream of jet stabilization. In the lower layer, where there is no forced time-mean jet imposed, eddy and mean terms are of comparable importance everywhere. In general, eddy and mean terms act in the same sense, hence the eddy contribution enhances the mean inertial effects, making the recirculations significantly stronger than they would be in the absence of eddy effects.
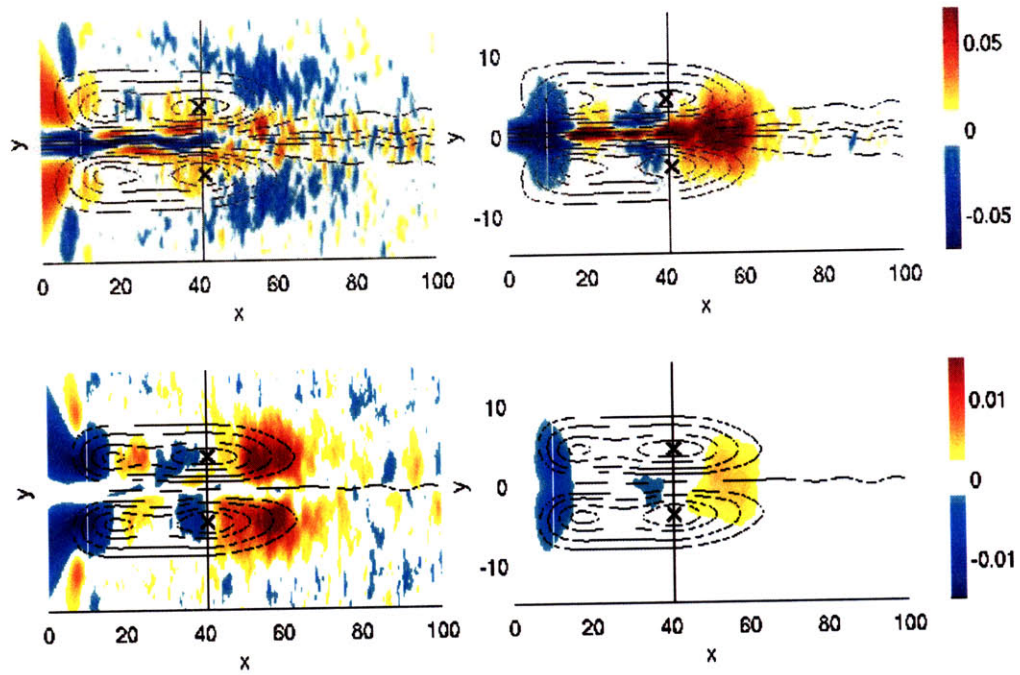
Figure 3-27: The divergence of the eddy flux of zonal momentum $\left(\frac{\partial}{\partial x}\left(\overline{u'u'}\right) + \frac{\partial}{\partial y}\left(\overline{u'v'}\right)\right)_{TEM}$ (*left*) *vs.* the divergence of zonal momentum advection by mean velocities $\left(\overline{u}\frac{\partial \overline{u}}{\partial x} + \overline{v}\frac{\partial \overline{u}}{\partial y}\right)$ (*right*) in the upper layer (*top*) and lower layer (*bottom*).
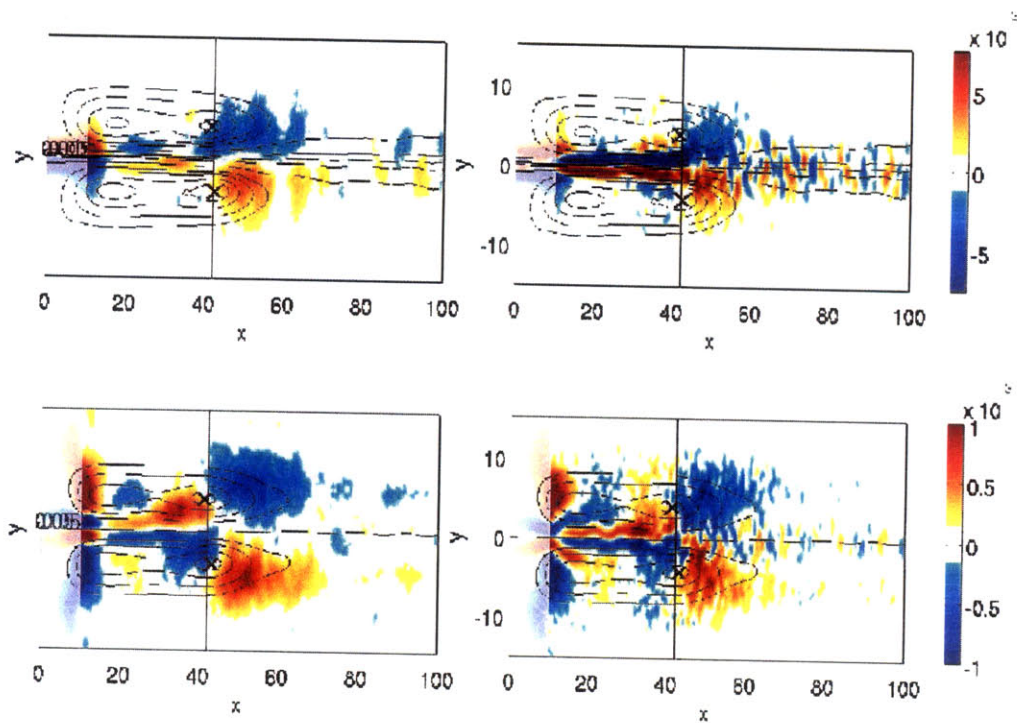
Figure 3-28: The divergence of the eddy flux of PV $\left(\frac{\partial}{\partial x}\left(\overline{u'q'}\right) + \frac{\partial}{\partial y}\left(\overline{v'q'}\right)\right)$ (*left*) *vs.* the divergence of PV advection by mean velocities $\left(\overline{u}\frac{\partial \overline{q}}{\partial x} + \overline{v}\frac{\partial \overline{q}}{\partial y}\right)$ (*right*) in the upper layer (*top*) and lower layer (*bottom*).

3.4.6 Dependence on System Parameters

As in the barotropic case, I explore the dependence of properties of the time-mean, eddy-driven circulation on forcing parameters by varying the supercriticality, or the degree of instability, of the inflowing jet. In the two-layer case, the variation of the non-dimensional β parameter now varies both the criticality of the upper layer jet to barotropic instability and the criticality of the system to baroclinic instability. Decreasing this parameter can be thought of as equivalent to making the upper layer jet stronger, increasing both the horizontal shear in the upper layer and the vertical shear between layers.

Results of these parameter studies as a function of the supercriticality of the upper layer inflowing jet are summarized in Figure 3-29. As in the barotropic case, as the supercriticality of the inflowing jet increases, the time-mean recirculation strength increases approximately linearly as is predicted by weakly nonlinear theory, with upper layer recirculation strength growing slightly more rapidly than lower layer recirculation strength. An exception to this rule exists however for the lower layer recirculation strength in the case of weak forcing, and it appears that the forcing must exceed some critical minimum amplitude to drive the lower layer recirculations at all. Examination of the time-mean streamfunctions (Figure 3-29 *right*) shows that, again similar to the barotropic case, the time-mean recirculations in both layers tend to shrink in their zonal extent and expand in their meridional extent as the inflowing jet becomes more unstable.

I also consider the two-layer parameter study results as a function of forcing amplitude as described in section 3.3.5 (Figure 3-30). I find that the functional dependence of mean recirculation strength on the forcing amplitude is simplified in the two-layer case if the modal (barotropic and baroclinic) streamfunctions ($\psi_{BT} = \frac{1}{S_2}\psi_1 + \frac{1}{S_1}\psi_2$ and $\psi_{BC} = \psi_1 - \psi_2$ where S_1 and S_2 are the upper and lower layer Burger numbers respectively) are considered in place of the layer versions, hence results are here presented in terms of the barotropic and baroclinic mean circulations. I observe that the strength of the barotropic and baroclinic components of the eddy-driven circulation

137
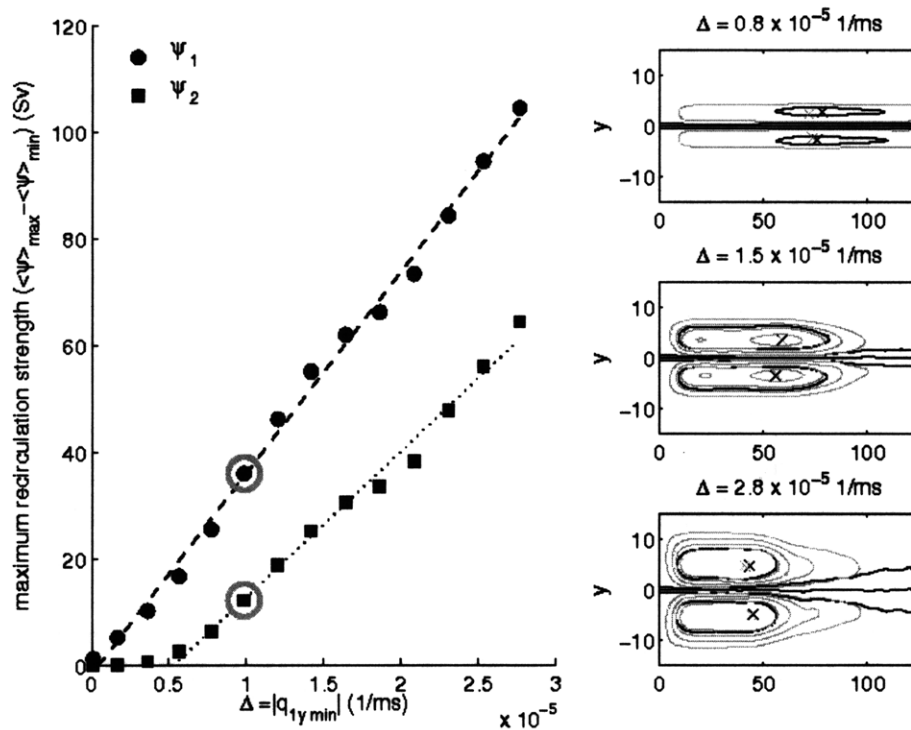
Figure 3-29: The dependence of the mean recirculation strength in each layer on the supercriticality of the inflowing upper layer jet, Δ (as defined in Figure 3-12) in a physically relevant range of parameters ($0.02 \leq \beta \leq 0.9$) (*left*). Upper layer recirculation strength is shown by circles, lower layer recirculation strength by squares. An estimate for the supercriticality of the KE, determined from the synoptic mean velocity profile of the Kuroshio jet at the point of separation from the coast derived from satellite altimetry data (see Figure C-1), is indicated by the gray circle. The time-mean circulation for select runs given by contours of the time-mean streamfunction (*right*). Upper layer circulation is in black and lower layer circulation is in gray. Contour intervals are the same for all cases to allow comparison.
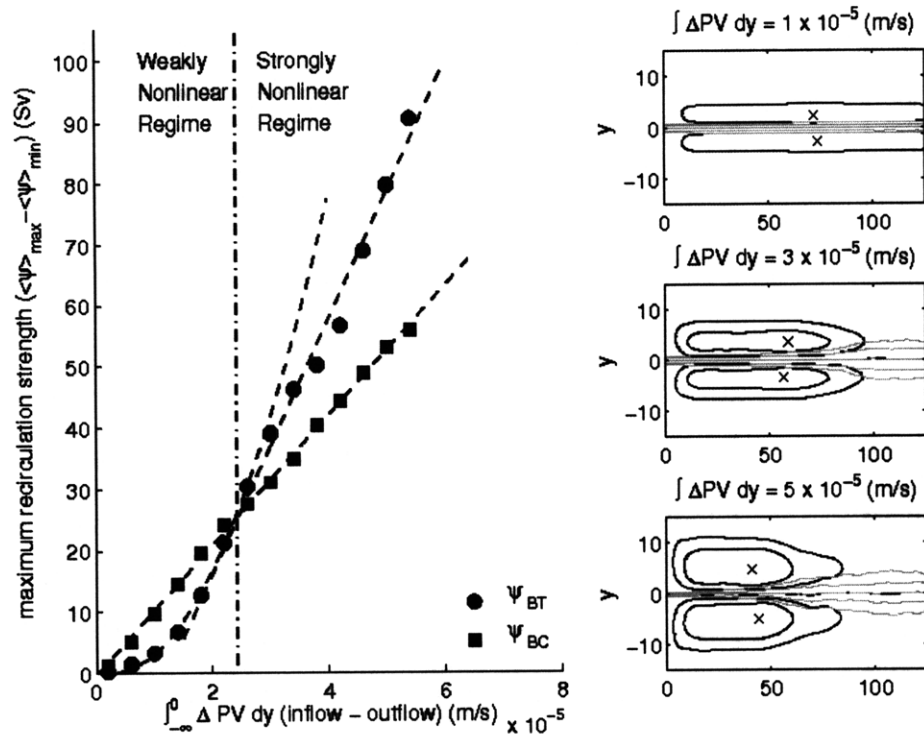
Figure 3-30: As in Figure 3-29 but now considering the modal (barotropic and baroclinic) streamfunctions ($\psi_{BT} = \frac{1}{S_2}\psi_1 + \frac{1}{S_1}\psi_2$ and $\psi_{BC} = \psi_1 - \psi_2$) in place of the layer versions, and plotted as a function of a measure of the PV forcing amplitude supplied by the inflowing upper layer unstable jet as described in Section 3.3.5. The dashed vertical line indicates a transition from a weakly nonlinear regime to a strongly nonlinear regime based on the observed change in the dependence of barotropic recirculation strength on forcing amplitude from quadratic in the weakly nonlinear regime to linear in the strongly nonlinear regime.

each have a distinct dependence on forcing amplitude: the barotropic transport grows quickly with forcing amplitude (quadratically for small forcing amplitude and slightly slower in the strongly nonlinear regime), while the baroclinic transport grows linearly with forcing amplitude for both weak and strong forcing. This observation clarifies why the upper layer recirculations tend to grow in strength faster in the weakly nonlinear regime: ψ_1 is influenced more strongly by the barotropic streamfunction due to its shallower depth.

Comparison of the barotropic *vs.* baroclinic time-mean streamfunctions for various jet forcing strengths (Figure 3-30 *right*) shows that the recirculations are a feature of the barotropic streamfunction, exhibiting the same trend of decreased zonal extent

and increased meridional extent with increasing jet supercriticality. The sharpening of the time-mean jet upstream of jet stabilization and the widening of the time-mean jet downstream of jet stabilization / maximum recirculation transport is contained in the baroclinic streamfunction.

It is interesting to note that the transition from a weakly nonlinear regime (where barotropic recirculation strength increases quadratically with forcing amplitude) to a strongly nonlinear regime (where the rate of increase of barotropic recirculation strength slows) corresponds approximately to where the contribution of the time-mean barotropic streamfunction first exceeds that of the baroclinic streamfunction. There are other qualitative changes in the nature of the baroclinic circulation around this forcing strength as well. Further investigation into the differences between the weakly nonlinear and strongly nonlinear regimes in the two-layer case and the cause for this transition in behavior is on-going.

Finally, as in the barotropic case, the time-mean recirculations in the two-layer case shrink in their zonal extent with the downstream location of maximum recirculation transport (and jet stabilization) moving upstream as the inflowing jet becomes more unstable in a way that is consistent with the linear stability calculation's prediction for the inverse growth rate associated with the fastest growing mode (Figure 3-31). Similarities suggest that, as in the barotropic case, the distance downstream where the mean jet profile becomes stabilized and the time-mean recirculation transport becomes maximized, is again related to the time it takes the eddies associated with the fastest growing mode to grow to sufficient amplitude. Comparing these results to the barotropic case (Figure 3-14), it can be seen that in the two-layer case the downstream location of mean jet stabilization / maximum recirculation transport tends to be further downstream for an equivalent forcing amplitude, while the inverse growth rate tends to be shorter. This suggests that the eddies must grow to larger amplitude in the baroclinic case compared to the barotropic one for their fluxes to be capable of stabilizing the mean jet profile, a consequence perhaps of the fact that they must stabilize the jet both to its horizontal **and** vertical shear in this mixed instability case.
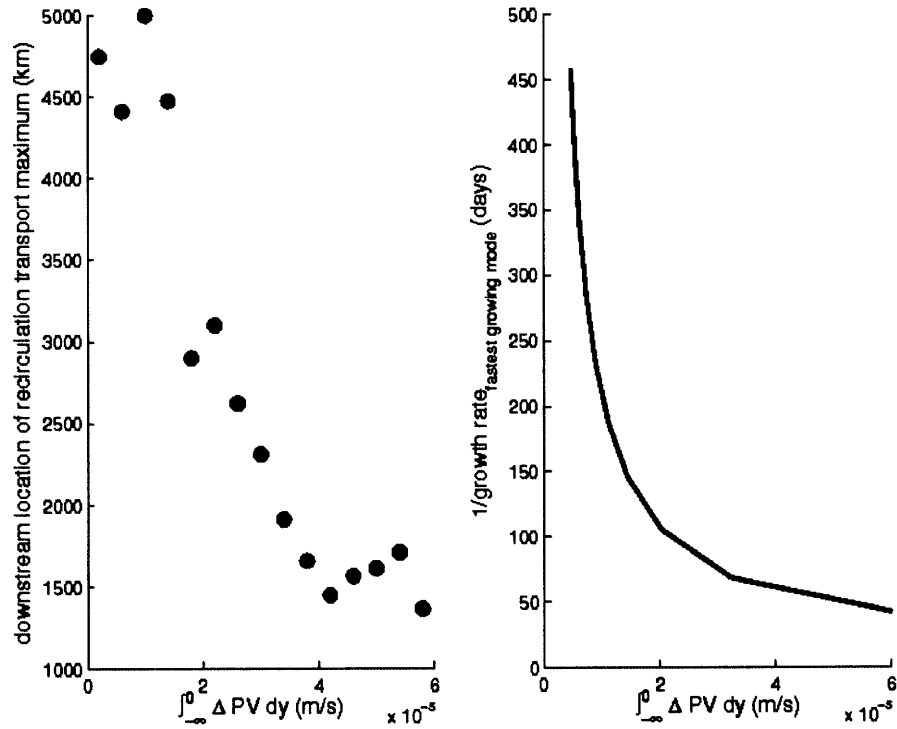
Figure 3-31: The dependence of the zonal extent of the recirculations (as measured by the downstream location of maximum time-mean barotropic recirculation transport) (*left*) vs. that of the inverse growth rate from the linear stability calculation for the inflowing jet profile (*right*) on forcing amplitude for the two-layer jet configuration.

3.5 Summary and Discussion

3.5.1 The Barotropic Case: A summary

A revisit of the barotropic model of Jayne et al. (1996), with the view of understanding the nature and importance of the eddy effect on the mean, the mechanisms that permit that effect, and the dependence of that effect on system parameters, has resulted in a picture of eddy-mean flow interactions in this idealized WBC jet system that is critically dependent on zonal position relative to the evolving stability properties of the time-mean jet. Upstream of jet stabilization, eddies act to stabilize the jet through down-gradient fluxes of PV. Downstream of where the time-mean jet has (through the effect of the eddies) been stabilized, eddies act to drive the time-mean recirculations through the mechanism of an up-gradient PV flux. This up-gradient flux is permitted by an eddy enstrophy convergence downstream that results from the generation of eddy enstrophy in the unstable jet regime, the advection of that eddy activity downstream by the mean jet, and the dissipation of that eddy enstrophy downstream of jet stabilization. In this picture, eddies drive the time-mean recirculations in this downstream region through the mechanism of nonlinear eddy rectification, made possible by a localized source of eddy activity generated by the unstable jet stabilizing itself as the instability is advected downstream, acting on a PV gradient that is in essence, just a modified β-plane, given the now stabilized time-mean jet no longer causes a reversal of sign in the mean meridional PV gradient. These eddy effects are important to the overall dynamics of the system, and are of comparable importance to the mean inertial terms in the dynamical budgets in a parameter space appropriate to the GS and KE. Finally, the properties of the time-mean recirculations that the eddies drive are strongly dependent on the stability properties of the jet that generated them: recirculation strength increases linearly with the supercriticality associated with the WBC at the western boundary, and zonal extent is empirically related to the inverse growth rate of the fastest growing mode as predicted by the linear stability calculation for the inflowing jet profile.

3.5.2 The Two Layer Case: A summary

In a configuration where a zonal jet is imposed at the western boundary in the upper layer of a two-layer system, as is relevant to a WBC at the point of separation from the coast, I find that the eddy-mean flow interactions remain essentially barotropic, with the added baroclinicity and the baroclinic instability mechanism adding new details to the barotropic story.

Like the barotropic case, the role of eddies in the downstream evolution of the time-mean circulation continues to be usefully characterized as dividing into two downstream regions: an upstream region where the time-mean jet is unstable and eddies act to stabilize the jet profile, extract energy from the mean, and mix PV down the mean gradient, and a downstream region where the time-mean jet is stable and eddies act to drive time-mean recirculations. In the two-layer configuration these eddy-driven recirculations occur in both layers, and are weakly depth-dependent relative to the baroclinic jet. The eddy-driving mechanism also continues to be essentially the same as the barotropic case: eddies drive the time-mean recirculations via a dipole pattern of eddy vorticity flux convergence and divergence north and south of the jet downstream of where the time-mean jet has been stabilized. The eddy-driving is via a mechanism that is analogous to the driving of time-mean recirculation gyres from the rectification of eddy fluxes generated in a localized region on a background PV gradient that is monotonically varying. The eddy-driving of the mean circulation is permitted by an up-gradient eddy PV flux in this downstream region which results from a significant eddy enstrophy convergence resulting from the dissipation of eddies generated upstream and advected eastward by jet. Given that this gross picture is valid for both the upper and lower layers, I conclude that even in this baroclinic case, the eddy-driving of the recirculations is essentially a barotropic mechanism. This is also supported by the observation that the effect of the eddies on the time-mean circulation (jet stabilizing *vs.* recirculation-driving as determined by the sense of the eddy vorticity forcing) is defined in each layer by the properties of that layer's PV gradient (and specifically its variation in the horizontal), and by the dominance of the rela-

143

tive vorticity flux divergence over the thickness flux divergence in the eddy vorticity forcing in both layers. The result that the barotropic transport grows quadratically with forcing amplitude in a weakly nonlinear regime and more slowly in a strongly nonlinear regime, as in the barotropic case, further suggests the barotropic nature of the eddy-driving mechanism in this two-layer configuration.

New details in this description resulting from the baroclinic dynamics come from the addition of the baroclinic instability mechanism, the addition of thickness fluxes as an alternative means by which eddies can impact the mean circulation, and the potential for different lower layer vorticity dynamics given the absence of a strong jet contributing to the background PV gradient. As mentioned, the eddy effect in each layer is determined by the horizontal variation of that layer's PV gradient, but given that it is the system's vertical shear that determine the lower layer's PV gradient, baroclinic instability also plays a key role. First, the interplay between the two instability types can result in additional structure in the downstream evolution of the mean jet-gyre system. In the WBC-typical example discussed, two local maxima in time-mean recirculation transport associated with multiple strengthening and weakening cycles of the lower layer eddy-driven jet are observed, resulting from a cycling of which instability mechanism is dominant at that point in the jet system's downstream development. Second, given the rates at which the eddies act to stabilize the jet to its barotropic *vs.* baroclinic instability differ, hence the downstream evolution of eddy effect (and in particular the downstream location of the switch in sign of eddy forcing from unstable jet regime to wave radiator regime) will differ in the upper *vs.* lower layer. The barotropic nature of the recirculation gyres arises despite this as a result of the dominance of the thickness fluxes in the effective eddy force inside the time-mean recirculation gyres in both layers. In this way, eddies contribute to the forcing of the recirculation gyres with a sign that is an integrated effect of the sense of the eddy effect in the upper and lower layer, and the location of maximum recirculation transport is somewhere in between the stabilization to the two instability types. Recirculation strength is diminished in the upper layer and strengthened in the lower layer relative to the barotropic case as a consequence of the action of these thickness

fluxes, which results in the barotropic nature of the recirculations. Finally, although a correspondence between the inverse growth rate of the fastest growing mode and the downstream location of maximum recirculation transport and jet stabilization remains, the addition of baroclinic instability results in larger downstream distances to stabilization, despite faster eddy growth rates. This suggests that eddies must grow to larger amplitude for their fluxes to stabilize the system in the baroclinic case.

Finally, it is important to note that as in the barotropic case, in the WBC relevant baroclinic case, eddy forcing and time-mean inertial terms are of relatively equal magnitude. Hence, including eddies in our description of the dynamics of WBC jet systems is essential. This is especially true for the lower layer, where eddy and mean terms are of opposing senses, and the recirculations are solely eddy-driven. In the absence of eddy terms, upper layer recirculations would be significantly weaker and the lower layer recirculations (and their significant enhancement to the jet transport) would be missing altogether.

3.5.3 Some Caveats

One of the major results of this study is that the nature of the eddy-mean flow interactions in the idealized WBC jet systems studied is critically dependent on zonal position relative to the evolving stability properties of the **time-mean** jet. Despite its heuristic value in this case however, it is important to recognize that the use of the time-averaged distribution of the PV gradient to evaluate the stability of the jet and the nature of the eddy-mean flow interactions **cannot** be justified on first principles (as formally stability involes the instantaneous flow and the spatial pattern of the perturbation field). Some other caveats that should be made include:

- While the temporal interpretation of the results seem to have heuristic value in explaining the observed eddy-mean flow interaction behavior, the relevance of spatial instabilities (*i.e.* disturbances with real frequency and complex zonal wavenumber coresponding to a system forced in a local region at constant frequency) also needs to be recognized. In papers on the temporal instabilities

of the GS for instance, many authors (e.g. Johns, 1988; Xue, 1991) agree that spatial instability is probably more relevant than the temporal variant in this application.

- In addition to normal mode instabilities (both temporal and spatial), the relevance of pulse instabilities (*i.e.* the linear solution that represents the asymptotic solution to the evolution of a localized disturbance, as an approximation to the full initial value problem as time goes to infinity) should be considered. In particular, convective instabilities, a category of pulse instabilities where the disturbance "propagates" along the system as it grows in time, may be especially appropriate. If a system is convectively unstable and forced continuously with constant frequency at a local region, spatial instability is likely to occur. This scenario likely has relevance to the problem considered here.

- There is no local relation between "local" stability characteristics (based on "local" cross-sectional profiles) and the disturbance intensity or its interaction with the mean in currents whose cross-stream structure varies in the downstream direction. And in cases where the advective time-scale of the current is much less than the dissipation time, as in WBC jets, disturbances may propagate from unstable regions into stable regions and continue to extract energy from the mean and grow in amplitude (see Pedlosky (1976) for a full discussion). This scenario provides a likely explanation for why the downstream location of maximum eddy kinetic energy in these idealized WBC jet studies is found downstream of the location where the time-mean jet is first stabilized (and the recirculation strength is maximized), however it calls into question the conclusion that the downstream boundary for the change in the nature of the eddy-mean flow interactions (and for the up-gradient eddy PV flux) is located at the jet's stabilization point, as oppposed to at the location of maximum EKE further downstream. In general, the relation between the downstream locations where the time-mean jet is first stabilized to its temporal instability, the instanteous jet is first stabilized to its temporal instability, the jet is first stabilized

to its spatial instability, EKE is maximized, and the recirculation strength is maximized, needs to be examined more carefully.

- Finally, an understanding of time-dependence in the downstream location of instantaneous jet stabilization, and how this relates to the nature of eddy-mean flow interactions, is still required. The utility of our understanding of the long-period oscillation that exists in the finite-amplitude state of a baroclinic wave or packet of waves as discused in Pedlosky (1970, 1972), and how this may translate to downstream variation in the jet's stabilization point, also need to be assessed. An evalution of a time series of the model jets' behavior, currently underway, will hopefully provide some insight into these matters.

3.5.4 Relevance to Actual Oceanic WBC Jet Systems

It is worth reiterating that the theoretical study discussed here was designed and carried out with priority placed on maintaining relevance to actual oceanic WBC jet systems. As mentioned in the discussion of the model set-up, although the model is highly simplified, there are several indications in past observations of the GS and the analysis of new observations in the KE region that indicate that aspects of the simplifications that the model employs and the physics it retains in its idealized set-up are appropriate to these systems (see Chapter 4 for a full discussion). In this way, I agrue that the theoretical results presented here have potential relevance to the dynamics of the GS and KE jet systems.

Ideally, the relevance of these theoretical results would be tested by looking for consistencies between model signatures and ocean observations. Unfortunately, due to the challenge of obtaining enough observational data to accurately calculate various eddy statistics, diagnostic studies of the relation between the mean or low frequency state and eddies using direct observations have been rare. Some attempts have been made with limited data on regional scales which provide tidbits for comparison however, and many of these provide partial pictures of WBC jet dynamics that are consistent with the model dynamics observed. For example, current meter records

analyzed by Dewar and Bane (1989) in the GS system at 73°W (250 km downstream of Cape Hatteras in what should be the "unstable jet regime" if defined relative to the downstream evolution of along-stream EKE), provide evidence of GS eddies acting to accelerate flows at abyssal levels while decelerating the mean jet at thermocline depths, consistent with the picture of the eddy force seen in "unstable jet" regime in the baroclinic model. With respect to eddy vorticity forcing, measurements in the abyssal GS suggest that the eddy relative vorticity and thickness fluxes are of comparable strength there, with the eddy relative flux divergence being of the right sign and order of magnitude to drive a recirculation of the observed strength, while the thickness flux acts to make the recirculation more barotropic (Hogg, 1993), again consistent with the model findings. Of particular interest to this study is observational evidence of a changing role of eddy effects in the downstream evolution of the WBC jet system. By compiling various data sources at 73°W and 68°W, Dewar and Bane (1989) conclude that the eddy-field at 73°W, upstream of the EKE maximum (Reverdin et al., 2003), is significantly different in its effects on the GS than at 68°W (near the EKE maximum), transitioning from a state dominated by baroclinic instability upstream to barotropic instability near the downstream location of maximum EKE. This evolution is also in agreement with the downstream development of the WBC-representative mixed instability case.

Motivation for this study came from a recent observational program in the KE called the Kuroshio Extension System Study (KESS), designed, in part, to investigate the processes that govern the jet's variability and the role of eddy fluxes in forcing the jet's recirculation gyres. As such, KESS provides a unique observational data set to examine the jet, its eddy variability, and their interactions that is unprecedented in both its spatial and temporal resolution, and affords us a unique opportunity to understand how these theoretical ideas about eddy-mean flow interactions in unstable jets apply to the actual ocean. Addressing the question of the relevance of these theoretical results to the KESS observations is treated in Chapter 4. In short, consistences in the signatures of dynamically significant properties between model predictions and observations in the KE region, give confidence in the model's potential ability to

capture the essential physics of the KE jet system.

3.5.5 A Barotropic Ocean Storm Track?

In this study of eddy-mean flow interactions in WBC jets, the eddy-mean flow interaction dynamics discussed result from the zonal evolution of the system from a region of eddy growth (the "unstable jet regime") to a region of eddy decay (the "wave-radiator regime"). This importance of zonal variation is reminiscent of eddy-mean flow interaction dynamics seen in atmospheric storm tracks, regions of enhanced eddy activity where eddies preferentially grow through baroclinic instability through the storm track and decay downstream (Chang et al., 2002; Hoskins and Hodges, 2002). As a consequence of this life cycle, at the entrance and over the core of the storm track, eddies provide a down-gradient heat flux and accelerate the mean jet eastward; at the exit and downstream they force a westward mean flow (Hoskins et al., 1983). In this way, storm tracks "self-maintain", the tendency for cyclonic (anticyclonic) circulation on the poleward (equatorward) flanks resulting from the Eliassen-Palm flux divergence from the track, serves to force the mean westerly flow which counteracts the destructive effects of the eddy heat fluxes on the baroclinicity.

Atmospheric storm track eddy-mean flow interactions described above certainly operate in this way in the baroclinic case of the WBC model I studied. However, in addition, in this WBC model an analogous evolution of eddy-mean flow interaction dynamics operate resulting from the life cycle of eddy growth through **barotropic** instability. As a consequence of this eddy life cycle, at the entrance and over the core of the barotropic "storm track", eddies still provide a down-gradient PV flux, but now it is in the sense to decelerate the mean jet; at the exit and downstream they now provide an eastward force. In this barotropic version, the simpler of the covariance terms in the eddy PV flux, $\overline{u'v'}$, has the same well-known effect as its baroclinic counterpart, intensifying the anticyclonic (cyclonic) tendencies on the southern (northern) side of the jet, thereby driving recirculations and producing an increase in the barotropic component of the zonal jet. The other term however, $\overline{v'^2} - \overline{u'^2}$, the term producing the quadrupole pattern that is responsible in baroclinic storm tracks

for anticyclonic tendencies to the northeast and southwest and cyclonic tendencies to the northwest and southeast (see Orlanski, 1998) is reversed in sign. In the barotropic version, this term now acts to restrict the westward extent of the strongest recirculation velocities upstream of the $\overline{v'^2} - \overline{u'^2}$ maximum, and to add to the recirculation strength downstream of the $\overline{v'^2} - \overline{u'^2}$ maximum.

In the barotropic case, barotropic storm track dynamics is the only mechanism at play. In the baroclinic, mixed instability case however, the atmospheric-like baroclinic storm track and the barotropic storm track dynamics compete, interchanging dominance as the jet evolves downstream and resulting in non-monotonically increasing recirculation strength. Ultimately it is the barotropic dynamics that come to dominate. The importance of barotropic instability in WBC jet systems is a potential explanation for why, despite finding localized regions in the Southern Ocean where ocean eddies provide statistically significant vorticity forcing, Williams et al. (2007) find that the contribution of eddy vorticity forcing along the extensions of the GS and KS is relatively small. Their diagnostic is a measure of susceptibility to baroclinic instability only and may be much larger if barotropic instability was also taken into account.

As Williams et al. (2007) note, thinking of ocean storm tracks (of both the baroclinic and barotropic type) might be useful since the existence of localized storm tracks is directly related to a characteristic life cycle for the eddies. When eddies are growing, they provide down-gradient tracer fluxes, and when eddies decay they provide up-gradient tracer fluxes. This temporal (or in the case of a time-varying instability mechanism being advected by an inertial jet, spatial) variation in how eddies behave may be critical for understanding their effect on the background state and in developing realistic parameterization schemes.

Chapter 4

Eddy-Mean Flow Interactions in the Kuroshio Extension and their Relation to a Simplified Dynamical Model

Abstract

Using new observations in the Kuroshio Extension (KE) at the downstream location of maximum eddy kinetic energy, I address the nature of eddy-mean flow interactions in the KE jet. I describe the state of the time-mean jet and its recirculations during the observational period, characterize the system's eddy variability in terms of jet meandering, ring interaction, wave activity, and jet instability, and examine indicators of the nature of the eddy-mean flow interactions. The analysis provides the first clear evidence of a northern recirculation gyre in the KE, as well as support for the hypothesis that the recirculations are, at least partially, eddy-driven. The observations also suggest that the KE jet is potentially both barotropically and baroclinically unstable at the location observed, making jet instability a likely source of at least some of the eddy variability of the system.

I also use the observations to evaluate the relevance of the idealized western boundary current jet model study to the oceanic system by considering both the model set-up and its results relative to observations of the KE jet. I show that the idealized model's simplified vertical structure and source of eddy variability (the mixed instability of the inflowing jet), as well as nonlinear dynamics, are appropriate to the observed system. Further, I demonstrate various consistencies between model predictions and

observational results in the downstream development of both time-mean and eddy properties. These consistencies suggest of the idealized model's potential success in capturing aspects of the essential physics of the KE jet system.

4.1 Introduction

4.1.1 Motivation

Beginning in 2004, a major, multi-institutional, international collaborative investigation of the Kuroshio Extension (KE) was undertaken. Known as KESS, the Kuroshio Extension System Study was an ambitious deployment of modern instruments with the goals of understanding the processes governing the intense meandering and eddy variability of the KE jet, and the nature of the interaction of the jet and its recirculation gyres. Making use of new advances in instrumentation, KESS provided new observations of the KE jet, its eddy variability and their interactions that are unprecedented in both their spatial and temporal resolution. As such, KESS affords us a unique and exciting opportunity to improve our understanding of the nature and importance of eddy-mean flow interactions in western boundary current (WBC) jet systems from an observational perspective. It is this opportunity that motivates the study presented here.

In addition to promising new insights from observations alone, the KESS data set provides a unique and exciting opportunity to test theoretical ideas of how eddy-mean flow interactions in unstable jets apply to the actual ocean. The theoretical study of eddy-mean flow interactions in an idealized WBC jet, reported on in Chapter 3, was motivated by the KESS observational program, and now in turn, motivates this study of eddy-mean flow interactions in the KE jet using KESS observations. Analysis of observational data is essential to understanding the relevance of the theoretical model to the dynamics of the real oceanic system. Making this reality check is also a major motivation of the work presented here.

Finally, this new look at the KE jet, its variability and eddy-mean flow interactions is important because eddy variability likely plays a critical role in WBC jet dynamics.

WBC jets like the KE are of fundamental importance to the dynamics of basin-scale circulations as they are regions of enhanced exchange of potential vorticity (PV) and energy, and because they act to restore global balances between forcing and dissipation. They play important roles in subtropical-subpolar exchange, the formation of mode water, and the steering and intensification of extra-tropical storms. Of particular relevance to eddy-mean flow interactions given the potential role of eddies in their forcing, is the importance of their recirculation gyres. Recirculations which flank WBC jets can significantly alter the structure and enhance the transport of the jet, and act as sites for deep wintertime convection, mode water formation, and reservoirs of heat and PV. Eddy variability in these systems is significant, and we expect eddy-eddy and eddy-mean flow interactions to play an important role in system dynamics. In particular, we expect eddies and their nonlinear interactions to impact mean jet-gyre strength, structure and stability (Thompson, 1977, 1978; Dewar and Bane, 1989; Hogg, 1992; Watts et al., 1995), play a role in driving the jet's flanking recirculations (Richardson, 1985; Schmitz and McCartney, 1993; Hogg, 1983, 1985, 1993), couple strong upper ocean motions to deep abyssal motions (Shay et al., 1995; Howden, 2000; Watts et al., 2001), and potentially act as a source of the low frequency variability observed in these jet-gyre systems (Spall, 1996; Qui, 2000). Improving our understanding of the nature and importance of eddy-mean flow interactions in WBC jet systems hence is of fundamental importance to our overall understanding of WBC jet dynamics, and in turn our overall understanding of the large-scale circulation.

4.1.2 Past Work

Over the past few decades, a number of substantial programs focused on different parts of WBCs have been undertaken, with a bias towards the Atlantic Ocean. These include studies of the Brazil-Malvinas Confluence, the Western tropical Atlantic Studies, the Subtropical Atlantic Climate Study, and the North Atlantic Current Study. Most closely related to the goals here and, arguably the most ambitious, was the Synoptic Ocean Predication Experiment (SYNOP) in the late 1980s (see Hogg, 1992;

Watts et al., 1995; Johns et al., 1995; Shay et al., 1995; Bower and Hogg, 1996). This study focused on the Gulf Stream (GS) Extension region. The existence of strong northern and southern recirculations gyres flanking the GS was previously known (Worthington, 1976; Richardson, 1985). SYNOP however resulted in important new insights into the workings of the meandering jet and its relationship to the surrounding ocean, and this resulted in a fundamental change in the scientific community's understanding of the interconnected system of currents, recirculations and eddies. In particular, the association of strong velocities under the GS with an organized deep flow that was dynamically connected to the upper baroclinic jet (Savidge and Bane, 1999a,b; Howden, 2000), and the importance of eddy-mean flow interactions whereby the GS generates eddies which in turn act back on the mean flow (Cronin, 1996) was first recognized. This shallow-deep coupling is thought to happen through baroclinic instability, a belief supported by a number of other studies (Dewar and Bane, 1989; Rossby, 1987; Cronin and Watts, 1996), however this is not a universal conclusion (e.g. Hall, 1986), and numerical models generally implicate the barotropic energy conversion process (e.g. Haidvogel and Holland, 1978; Holland and Haidvogel, 1980). Outside of SYNOP, diagnostic studies of the relation between the mean or low frequency state and eddies using direct observations have been rare, although some attempts have been made with limited data on regional scales. For example, Thompson (1977, 1978) attempted to infer crude properties of the eddy-mean flow interactions in the vicinity of the GS through the analysis of current meter data by attempting to evaluate the sign of the eddy momentum flux gradients. His observations suggested that eddies may be playing a role in the net driving of the mean jet by transferring momentum between the jet and the nearby inshore counter-current via cross-stream momentum flux convergences and divergences, making "eddy-driving" a possible source for the excess momentum needed to drive the mass transport in the GS above the expected Sverdrup value.

Relative to the GS, the KE jet and its eddy-mean flow interactions are much less explored, at least by the western scientific community. With respect to the KE jet-gyre structure, prior to KESS, the existence of a tight recirculation gyre to the

south of the jet with structure and transport analogous to the GS was recognized. By some accounts, a recirculation gyre also exists to the north of the KE jet, but its existence had not been decisively demonstrated: it is absent from the regional mean circulation derived from hydrography (Teague et al., 1990) and a careful compilation of deep current meter records by Owens and Warren (2001). With respect to the KE's eddy variability, the region is recognized to be one of especially high eddy kinetic energy (EKE) (*e.g.* Wyrtki et al., 1976; Qui, 2002), and although the KE represents a dynamically simpler regime than the GS (*e.g.* with no deep WBC and flatter topography), there were indications of the existence of an energetic abyssal eddy field (Schmitz, 1987, 1988; Hallock and Teague, 1996). Finally, with respect to jet stability, in contrast to the GS, Hall (1989, 1991) found that in the KE, baroclinic processes dominate with significant mean-to-eddy potential eddy conversion, although her analysis was restricted by the availability of just one mooring (at 35°N, 152S°E). Both she and Qui (1995) and Adamec (1998), who worked with sea surface height data, showed that the barotropic conversion process feeds energy from the mean flow to eddies on the south side of the current, but in the opposite direction on the north side.

4.1.3 Present Work Objectives

What is missing from these studies in the KE is more complete vertical and lateral information to characterize the jet and its eddy-mean flow interactions. In addition, open questions remain both specific to the KE jet itself (*e.g.* Is there a northern recirculation gyre? What is the relative importance of barotropic *vs.* baroclinic instability?), and also about the similarities and differences between the KE and GS with respect to their jets, eddy variability and eddy-mean flow dynamics. Despite its obvious similarities to the GS, the KE is fundamentally different in many ways: it has a distinct orientation, topography, influence from thermohaline circulation, and modes of variability. As a consequence, it may experience different instability mechanisms, and potentially dissimilar physics governing its variability and recirculation gyres. Finally, a revisit of eddy-mean flow interactions in WBC jets is timely as to-

day's fundamentally improved remote-sensing, *in situ* observational, and computing abilities relative to the days of SYNOP enable us to address these questions in a comprehensive manner. It is these needs, questions and opportunities that guide KESS generally and the present study in particular.

The specific goals of the work presented here are to use the KESS data set to learn more about the nature and importance of eddy-mean flow interactions in the KE. As mentioned above, there is opportunity to do this both through an analysis of the KESS observations alone, and in using them to test the relevance of the theoretical model and its findings I have studied to the dynamics of the real oceanic system. As such, my study is guided by two main objectives:

1. To characterize the state of the mean KE jet and its recirculation gyre(s), its eddy variability, and the nature of their interactions within the KESS time frame at the KESS location.

2. To evaluate the relevance of the idealized WBC jet model to the KE system both in terms of the model design and its findings.

To achieve the latter, I require a broader view of the KE jet system, and this will require me to draw on other observations in the KE region. In this way, I hope to address not only a detailed look into KE eddy-mean flow interactions provided by the KESS window, but also at the nature of eddy-mean flow interactions in the KE region more generally.

4.1.4   Chapter Outline

This chapter is organized as follows: In Section 4.2, I describe the observational data. I describe the KESS program generally, the KESS data I use in this study in particular, the other sources of observational data in the KE region that I employ, and the data processing methods. In Sections 4.3 and 4.4 I present the results. Section 4.3 focuses on the first goal, that of characterizing eddy-mean flow interactions in the KE jet based on observations of the KESS mooring array. I characterize the structure

of the mean jet-gyre system within the KESS time frame in both geographical and stream-coordinates, discuss the source and nature of the eddy variability observed during KESS in terms of jet meandering, ring interactions, wave radiation, and jet instability, and finally comment on what the observations imply for eddy-mean flow interactions at this location. Section 4.4 relates to the second goal, that of testing the relevance of the theoretical study of an idealized WBC jet to the KE system. Here I discuss how the observations relate to the model's simplified configuration in terms of vertical structure, nonlinearity, and forcing, as well as give examples of various consistencies between model predictions and observational results in the downstream development of mean and eddy properties. The latter is critical in giving confidence in the idealized model's potential ability to teach us about aspects of the essential physics of the oceanic system. Finally, in Section 4.5, I summarize and discuss the results, as well as providing ideas for future work.

4.2   Data and Processing

4.2.1   The Kuroshio Extension System Study

As described in the introduction, KESS was a large observational program investigating the KE with the goal of understanding the processes governing the variability of the KE jet and the interaction between the jet and its recirculation gyres. It deployed a four-dimensional, mesoscale-resolving *in situ* array located at the downstream location of the maximum in EKE of the KE (Figure 4-1 *upper left*). The observational period spanned a total of 704 days, from spring 2004 until spring 2006.

Instrumentation (Figure 4-1) was centered around a mooring array consisting of seven full depth moorings deployed along a north-south tending line coincident with a Jason satellite altimeter repeat track. This line extended across the axis of the KE jet, spanning its north-south excursions (Figure 4-1 *upper right*) and extending into the recirculation gyres. The moorings measured the mean surface velocity field with upward looking acoustic Doppler current profilers (ADCPs) at 250 m depth, velocity,
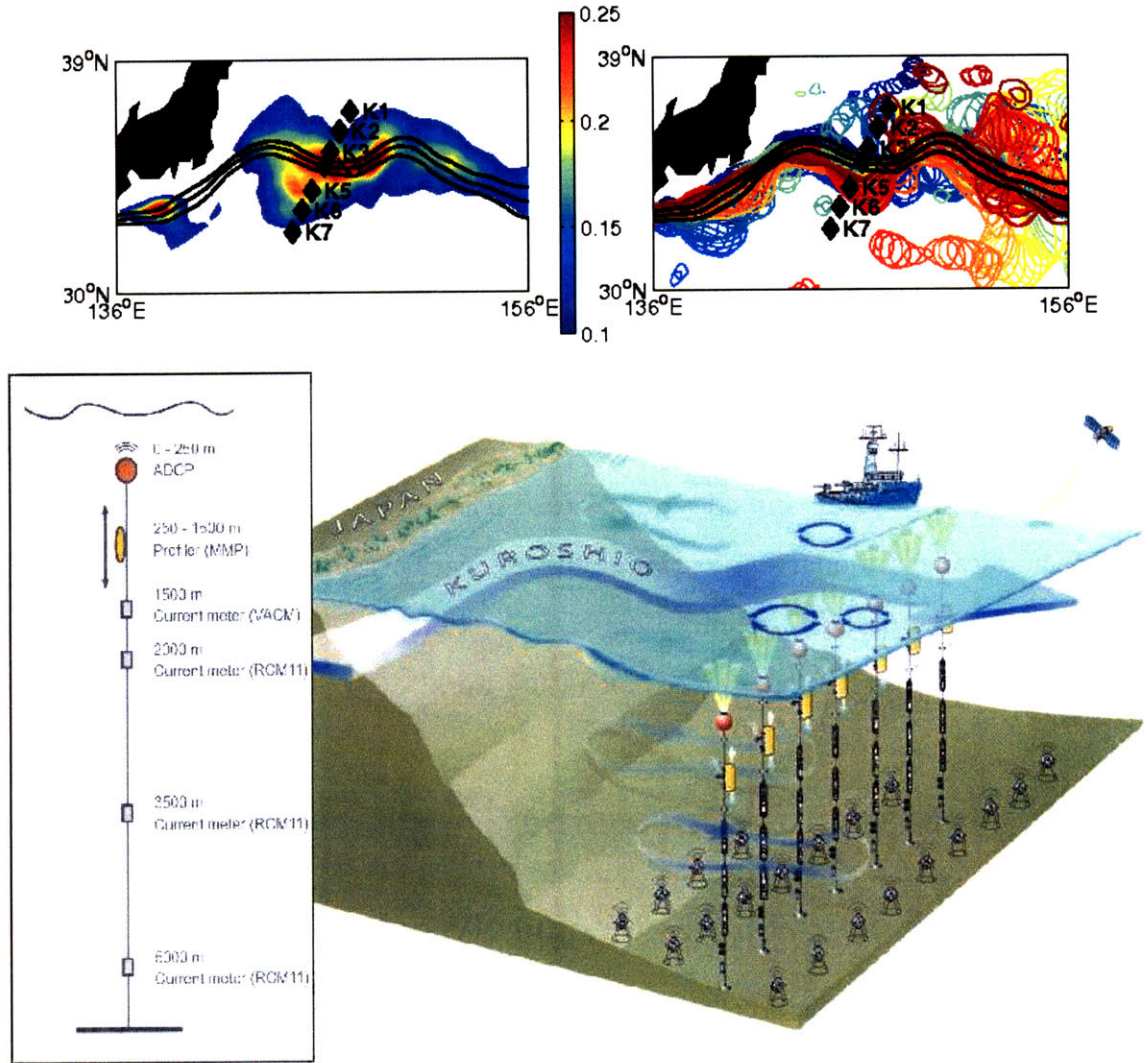
Figure 4-1: A graphical description of the Kuroshio Extension System Study (KESS). The location of the KESS mooring array (black diamonds) relative to the time-mean EKE distribution in $m^2 s^{-2}$ (color) and the time-mean jet axis position (black contours indicating the time-mean 1.9, 2.0 and 2.1 m SSH contours) computed from the 14-year satellite altimetry record (*upper left*). A description of the jet meandering and ring interaction during the KESS period (spring 2004 - spring 2006) as indicated by a superposition of weekly snapshots of the 2.1 m SSH contour (used as a proxy for the jet's position) as measured by altimetry (*upper right*). A schematic of the KESS instrumentation (*bottom*) which included a line of seven full depth moorings, an array of inverted echo sounders, floats (not shown), shipboard surveys and satellite remote sensing. A schematic of the mooring instrumentation (*bottom left*) displays how the moorings measured fluctuations in the density and velocity fields through most of the water column. (Illustration credit: Paul Oberlander and Luc Rainville)

temperature and salinity between 250 m and 1500 m with McLane Moored Profilers (MMPs) that took a profile once every fifteen hours, velocity at 1500 m depth with vector-averaging current meters (VACMs), and finally temperature and velocity at three additional levels beneath the thermocline (2000 m, 3500 m and 5000 m depth) at 15 minute intervals with Aanderaa RCM-11 acoustic current meters. As such, the moorings resolved the fluctuations in the density and velocity fields through most of the water column for timescales from hours to seasons. They provided measurements of the flow and temperature fields across the axis of the KE jet with sufficient duration and resolution in the cross-jet distance to consider eddy-mean flow interactions. As such, they will provide the primary source of data for this study.

In addition, KESS instrumentation included an array of fifty inverted echo sounders equipped with bottom pressure gauges and current meters (CPIES) centered around the mooring line. The CPIES array mapped the time-varying velocity and density structure above both in the vertical and the horizontal in two dimensions. A total of 48 profiling APEX floats were deployed on two occasions within the recirculation gyres, providing drift velocity estimates at their parking depth of 1500 m and profiles of temperature and salinity from 1500 m depth to the near surface every 5 days with 5 m vertical resolution. Shipboard surveys performed high resolution feature studies on three cruises. Finally, satellite measurements of sea surface height (SSH) and sea surface temperature provided a larger context for the array.

The KESS collaboration involves a large number of investigators using different aspects of the data to address various questions related to mesoscale processes in the jet-gyre system, air-sea fluxes, subtropical mode water formation, and high frequency variability. The study here focuses on the state of the KE jet, the KE's eddy variability, and eddy-mean flow interactions using the mooring and satellite data. Other studies using the KESS observations are reported on the KESS website at http://www.uskess.org.

4.2.2 Other Sources of Observational Data in the KE Region

KESS provided data with high resolution locally, but given the importance of the downstream evolution of the jet that was found in the theoretical study discussed in Chapter 3, it is important also to look upstream and downstream of KESS. To do this, I exploit additional sources of observational data in the KE region. First, I make use of *in situ* measurements from past programs in the region: namely from the WESTPAC program, located downstream of KESS conducted in the early 1980s (see Schmitz et al., 1982), and also from the KERE program, located upstream of KESS conducted in the early 1990s (see Hallock and Teague, 1995) (Figure 4-2). Both programs consisted of tall mooring arrays with measurements of velocity and density both above and below the thermocline for a duration of two years. Second, I make use of the satellite altimetry record in the region, as it provides both a more continuous picture of downstream development, and also a much longer time series to better characterize the time-mean and eddy statistics. The altimeter products used were produced by Ssalto/Duacs and distributed by Aviso. The 14-year record I refer to is from the beginning of the AVISO altimetric data set (1992) until the end of the KESS period (spring 2006).

4.2.3 Data Processing

As described above, this study focuses on the KESS mooring array observations. To characterize the system as a function of cross-jet distance and depth, time series of velocity at each mooring were constructed at six depth levels. Surface geostrophic velocity from satellite altimetry and velocity at a nominal depth of 250 m from the ADCP record were used to characterize the upper ocean velocity structure. Velocity at the four instrumented subthermocline depths (1500 m, 2000 m, 3500 m, and 5000 m) were used to characterize the deep ocean. Note that the MMP measurements were not used in this study due to the low and biased data return, see Appendix D for details.

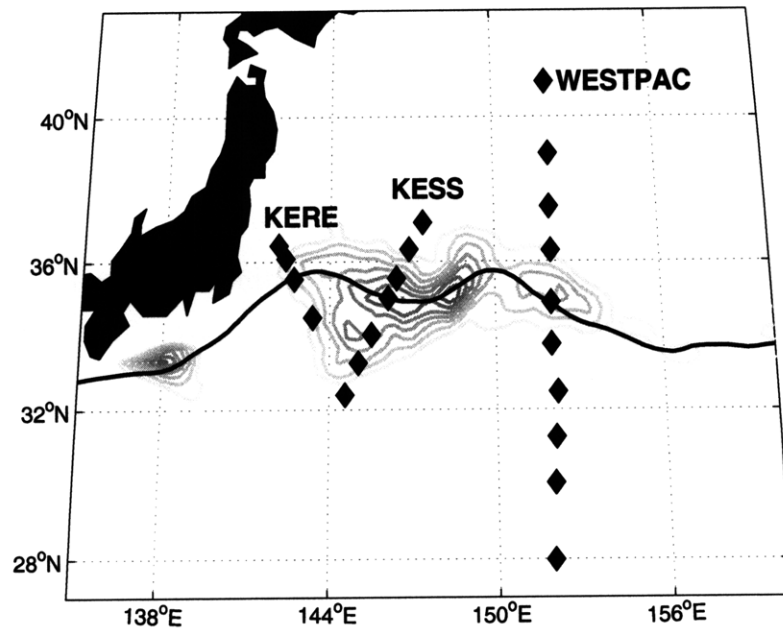The velocity records were corrected for mooring motion, low-pass filtered and

Figure 4-2: The location of the KERE and WESTPAC mooring arrays relative to the KESS array and the mean EKE distribution in the KE region. Grey contours are of the 14-year mean EKE distribution derived from the satellite altimetry record. The black contour is the 14-year mean position of the 2.1 SSH contour, which is used as a proxy for the jet axis.

subsampled at one day. Gaps were filled either by the record mean in the case of the ADCP measurements, or by a gap filling procedure that exploited records at other subthermocline depths and the observed structure of the flow beneath the thermocline in the case of the deep ocean records. Again see Appendix D for further details.

In addition to a geographical picture provided by the mooring observations, it was useful to compute a stream-coordinate frame for the jet. This frame was defined by a time-varying origin and downstream and cross-stream axes orientation based on the instantaneous position and orientation of the jet axis in the vicinity of the array. This frame gave important information on the nature of the jet meandering at the array location, and also permitted the calculation of a stream-coordinate mean picture of jet structure that consists of time-mean downstream velocity as a function of distance from the jet axis, essentially a picture of the time-mean jet structure with the effects of jet meandering removed. The stream-coordinate calculation was done using three different independent proxies for the jet axis location using altimetry, CPIES and temperature information. See Appendix D for a full description.

Finally, as evidenced from altimetry measurements (Figure 4-1 *upper right*), there were several times during the KESS observational period when warm and cold-core rings were interacting with the mooring array. It was useful to identify these times, and this was achieved by defining a temperature criterion at 250 m depth to identify the presence of warm or cold core rings on the flanks of the jet. Times when rings were interacting with the array were removed from the record for some of the analysis. See Appendix D for more details.

4.3 Results: Eddy-Mean Flow Interactions in KESS

4.3.1 Mean Jet Structure

As a first step in characterizing eddy-mean flow interactions during KESS, I characterize the mean state. Here I describe the time-mean jet structure using the mean computed over the 704 day KESS period (15 June 2004 until 19 May 2006).

(a) Geographical description

Computing the mean value of the velocity time series measured by the KESS mooring array allows characterization of the time-mean KE jet structure as a function of latitude and depth at the KESS location. The picture revealed is of a strong, surface-intensified jet oriented to the southeast (Figure 4-3). Satellite altimetry measurements indicate a mean (geostrophic) jet at the surface at this location with a strength of ~ 0.6 m/s and a width of $\sim 2.3°$ latitude (~ 200 km)[1]. KESS subsurface measurements in the upper ocean indicate a sharp decay in jet strength with depth (the time-mean peak velocity is reduced to 0.3 m/s at 250 m depth and 0.02 m/s at 1500 m depth) (Figure 4-4), as well as a shift of the jet axis to the south, consistent with thermal wind balance. In contrast, in the deep ocean, the jet strength and structure show very little depth dependence (Figure 4-4 *upper right*, Figure 4-5). Here is observed weakly depth-dependent westward flanking flows to both the north and south of the time-mean jet with velocities of magnitudes comparable to that of the deep jet itself, making these recirculations a significant feature of the time-mean deep jet structure. In contrast, flanking flows are weak and disorganized in the upper ocean (there exists no clear evidence of westward recirculations), with weak westward flows observed to the north of the jet but not to the south (Figure 4-6).

(b) Stream-coordinate description

The stream-coordinate view of mean jet structure (as described in Section 4.2.3) is summarized in Figures 4-7 – 4-10. Like in the geographical mean picture, the stream-coordinate mean jet is a strong, sharp, surface-intensified jet that extends throughout the water column oriented to the southeast (Figure 4-7). As one would expect, it is stronger (the time-mean peak surface velocity is ~ 1.2 m/s) and sharper (the time-mean surface width is ~ 180 km) than its geographical mean counterpart (Figure 4-8). The mean subsurface upper ocean jet is also significantly stronger (with a strength of 0.9 m/s at 250 m depth and ~ 0.1 m/s at 1500 m depth), and its deep subthermocline structure is more vertically aligned with a baroclinic structure that

---

[1]Note that altimetry gives a smoothed description of the jet because of the ~ 300 km length scale used in the objective mapping.
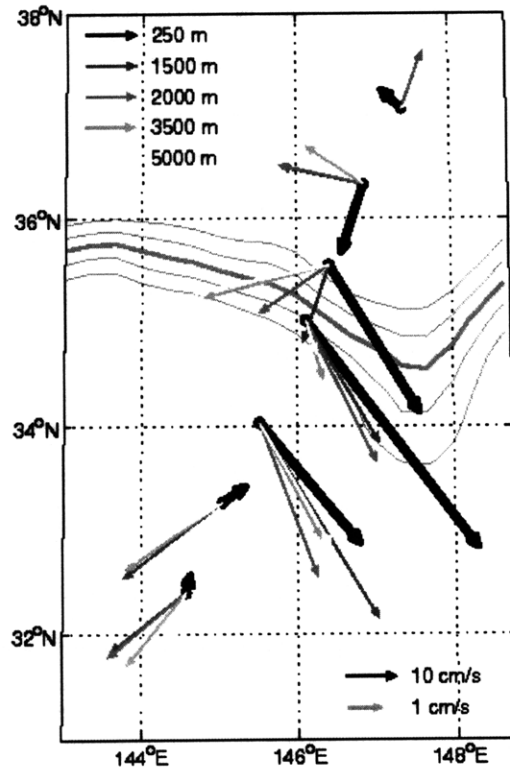
Figure 4-3: The KESS period mean velocity vectors at five vertical levels as measured by the KESS mooring array. Note that upper ocean (250 m depth) vectors are scaled differently than abyssal ocean (1500 m - 5000 m depth) vectors to permit visualization on a single plot, and hence the difference between the magnitude of upper ocean velocities relative to abyssal ocean velocities is greater than it appears. Gray contours are of the time-mean SSH from satellite altimetry measurements during the KESS period showing the 1.9 - 2.3 m contours in 0.1 m contour intervals. The heavy line is the time-mean 2.1 SSH contour used as proxy for the jet axis position.
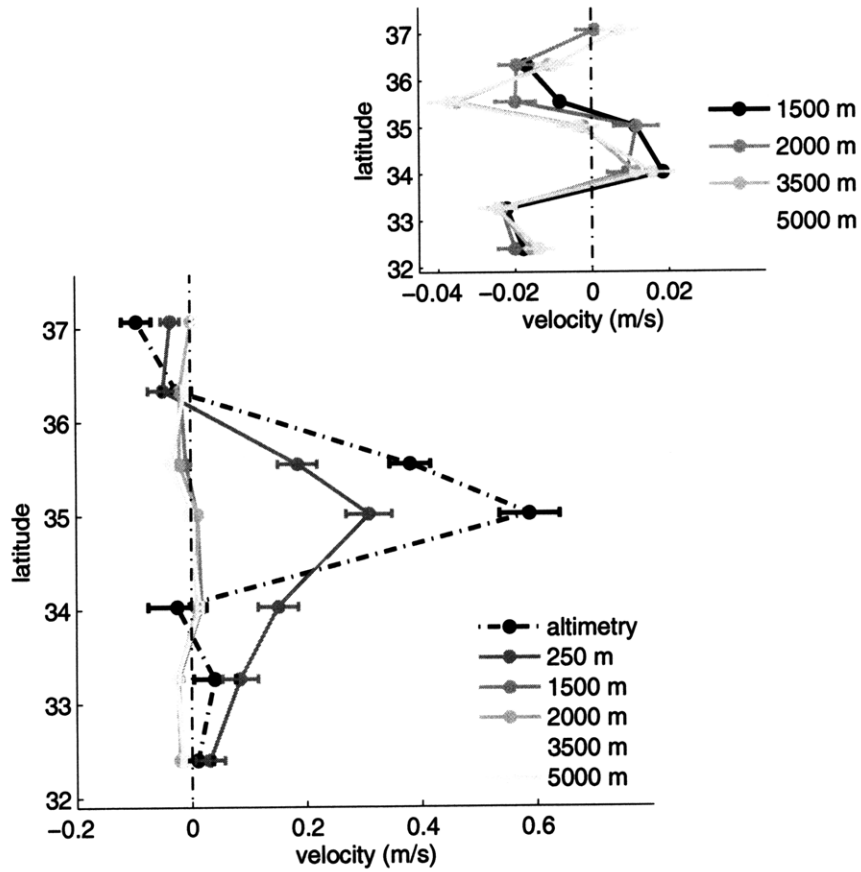
Figure 4-4: Cross-jet profiles of time-mean zonal velocity at five vertical levels as measured by the KESS mooring array. The KESS period mean surface geostrophic zonal velocity, computed from the gradients of the altimetric SSH field at the mooring locations, is also included. Error bars indicate the standard error in the mean using a number of degrees of freedom given by the number of decorrelation time scales contained in the record length.
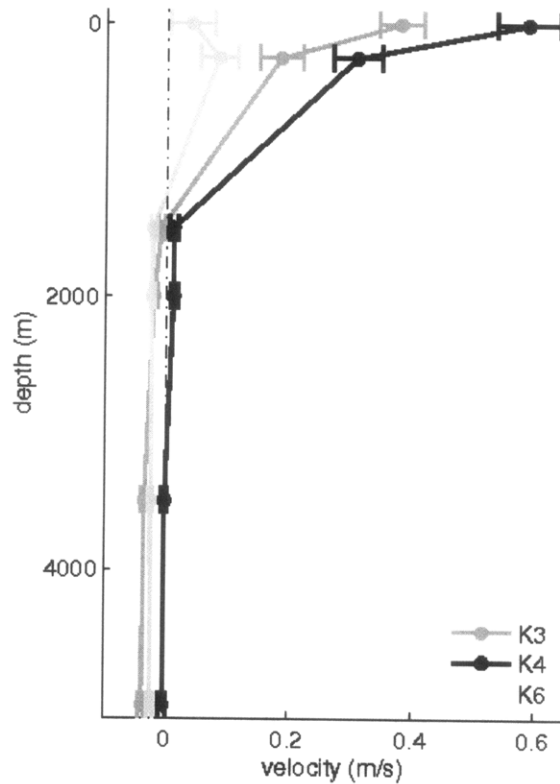
Figure 4-5: Vertical profiles of the KESS period time-mean zonal velocity measured by three different moorings: near the time-mean jet axis (K4) (*black*) and flanking the time-mean jet to the north (K3) (*gray*) and south (K6) (*light gray*). SSH altimetry at the KESS mooring locations is used to define the surface velocity. Error bars indicate the standard error in the mean as described in Figure 4-4.
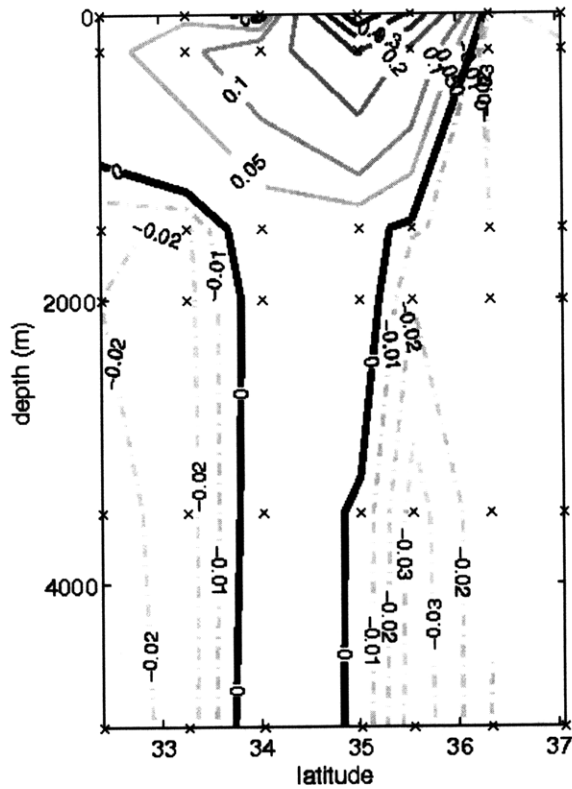
Figure 4-6: A contour plot of time-mean zonal velocity (in m/s) as a function of lat-itude and depth summarizing the geographical description of the KESS period time-mean jet structure. Solid contours indicate positive (eastward) values and dashed contours indicate negative (westward) values. **xs** denote locations where data is avail-able: an array of seven moorings each with measurements at six levels in the vertical (including SSH altimetry at the surface).
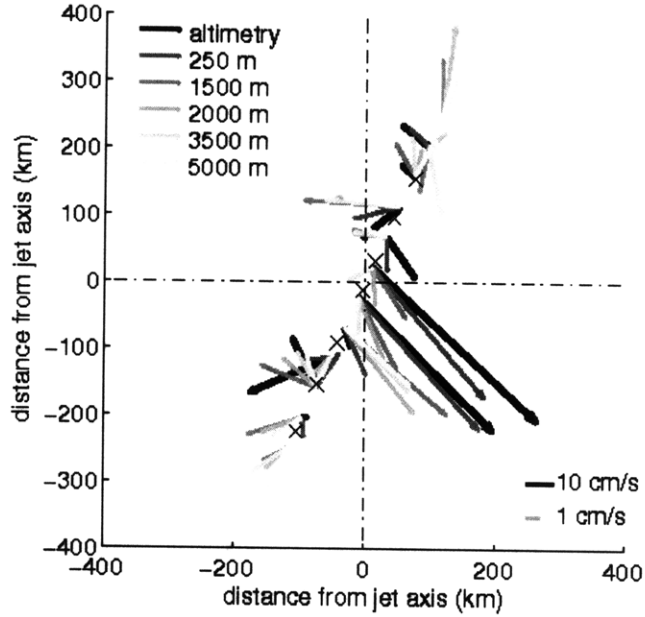
Figure 4-7: The cross-jet distribution of KESS period mean velocity vectors from the stream-coordinate description of time-mean jet structure. As in Figure 4-3, mean velocity vectors as measured by the KESS mooring array are shown at five levels in the vertical, but now as a function of distance from the jet axis. An estimate of the surface geostrophic velocity from satellite altimetry is also included. Note upper ocean (surface and 250 m depth) vectors are scaled differently from abyssal ocean vectors, which results in the difference in the magnitude of the vectors in the upper ocean *vs.* the deep ocean appearing less pronounced.

is more pronounced (Figure 4-8). As such, in this view, the stream-coordinate mean jet is much more strongly sheared in both the horizontal and vertical than suggested by the geographical mean picture. This has important implications for its stability properties, see Section 4.3.2d for a more detailed discussion.

The stream-coordinate view of mean jet structure is important to the question of whether time-mean recirculations exist in the KE because it shows westward flanking flows to both the north and south of the time-mean jet in the upper ocean as well as in the deep ocean, suggesting the existence of barotropic recirculations that exist throughout the water column (Figure 4-9, Figure 4-10). These recirculations are observed to be much more barotropic than the strongly baroclinic jet, with velocities of the same order in both the upper and deep ocean. Their existence in the stream-
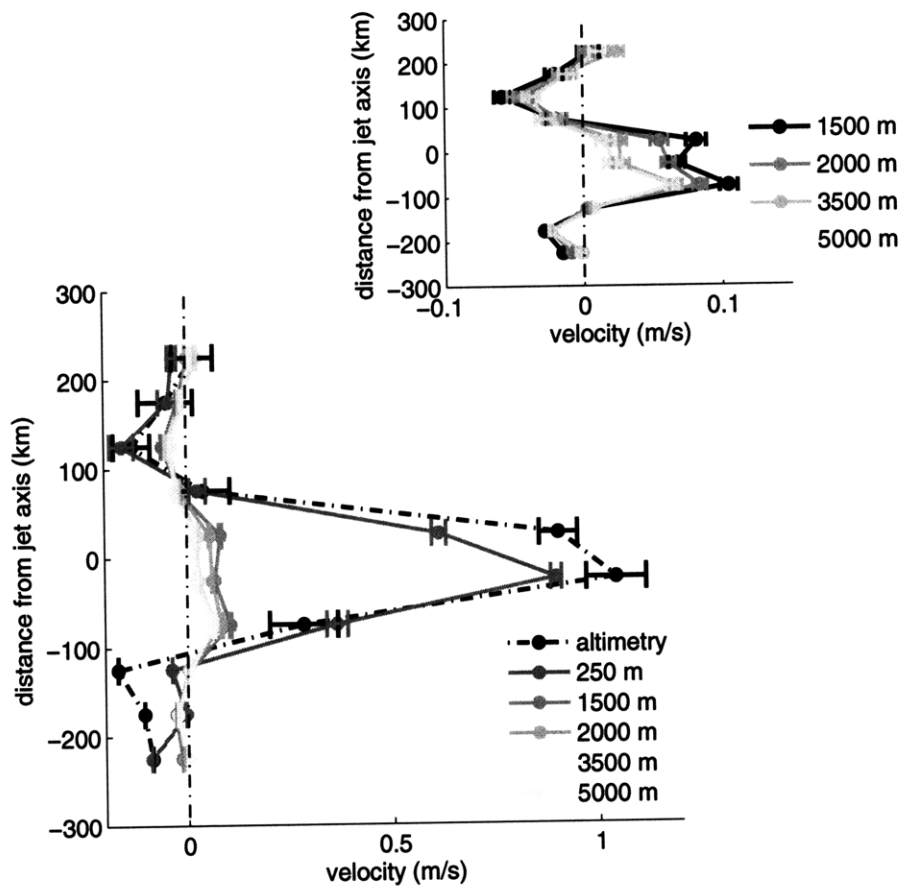
Figure 4-8: Cross-jet profiles of the time-mean downstream component of velocity at six levels in the vertical (one from altimetry and five levels from KESS mooring measurements). Error bars indicate the standard error in the mean
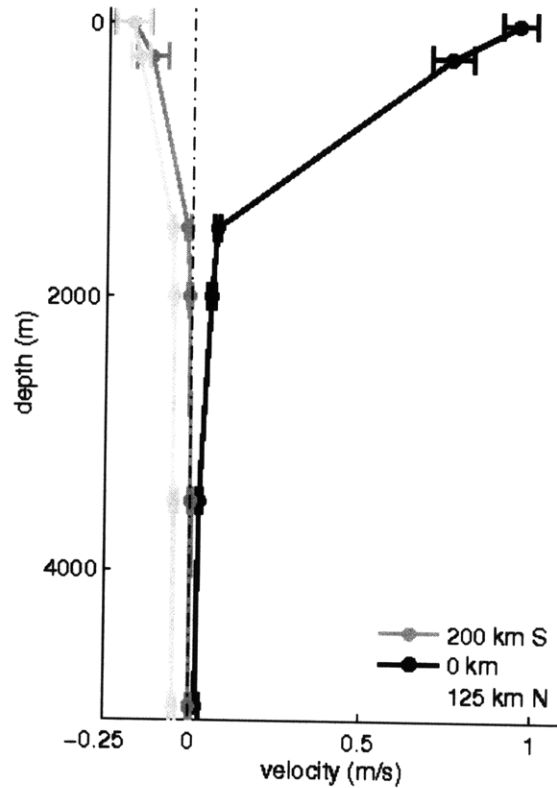
Figure 4-9: Vertical profiles of KESS period time-mean downstream velocity at the jet axis (0 km) (*black*), and flanking the jet to the north (125 km from the jet axis) (*light gray*) and south (200 km from the jet axis) (*gray*). Again error bars indicate the standard error in the mean.

coordinate frame, suggests that their absence in the upper ocean in the geographical mean picture is a result of the meandering of the strong upper ocean jet "smearing" out the relatively weak westward flanking flows in the time-mean calculation. Note that prior to KESS, although the existence of a recirculation gyre to the south of the jet had been demonstrated, the existence of a northern recirculation gyre was in question. Hence KESS has provided the first clear observational evidence of a northern recirculation gyre in the KE, seen here in the KESS mooring data and observed in other KESS measurements as well. See Jayne et al. (2008) for a full discussion.
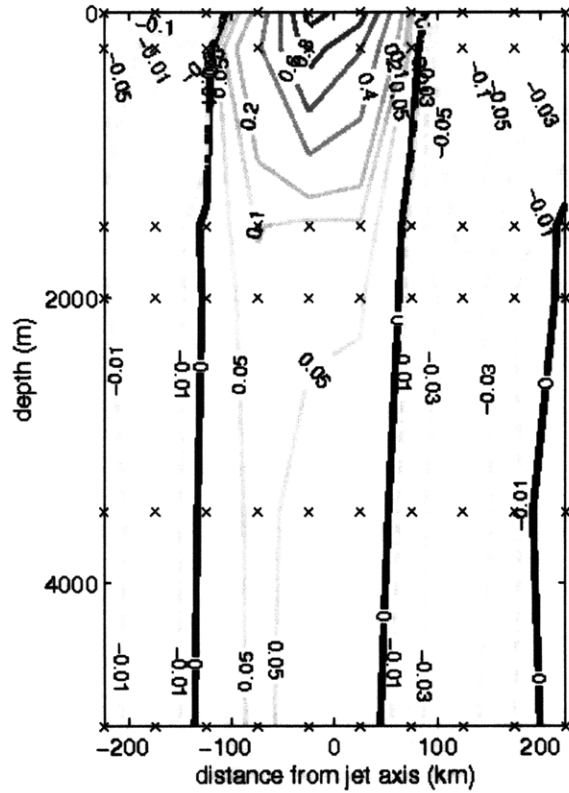
Figure 4-10: A contour plot of time-mean downstream velocity (in m/s) as a function of depth and distance from the jet axis summarizing the stream-coordinate description of the KESS period time-mean jet structure. Solid contours indicate positive (downstream) values while dashed contours indicate negative (upstream) values. Data locations are indicated by **xs**: an array of ten 50 km wide bins of distance from the jet axis in the horizontal, and six levels in the vertical (including velocity derived from satellite altimetry at the surface).

4.3.2 Eddy Variability

As the second ingredient in characterizing eddy-mean flow interactions, I consider the nature of the eddy (*i.e.* temporal) variability observed during KESS. Here I characterize properties of the observed eddy variability by describing it in relation to some of its various sources: jet meandering, ring interaction, wave radiation/interaction, and jet instability.

(a) Jet meandering

As discussed in Appendix D, the KESS data set provides various proxies for the jet axis position, both measured *in situ* and sensed remotely, and these data give information about the nature and the extent of the meandering of the jet at the KESS location. A superposition of snapshots of the jet path during the KESS period (Figure 4-11) illustrates that the extent of the jet's north-south meandering at the KESS location spans several degrees of latitude, and that during the KESS period, the jet crossed the axis of the mooring array as far south as south of the southernmost mooring (K7) and as far north as the K2 mooring. The time series of jet axis position (Figure 4-12) gives quantitative information about the meandering: during the KESS period, the jet axis location varied about is mean position with a standard deviation on the order of 60 km and a maximum range on the order of 300 km. Spectra (Figure 4-13) indicate enhanced energy at 50 day period and in a broader band centered around 23 day period. This second frequency is consistent with the timescales predicted by appropriate linear stability calculations which are on the order of 20-30 days for the fastest growing modes. See Appendix D for details.

Comparing the geographical *vs.* stream-coordinate descriptions of mean velocity and EKE distributions give indications of the effect of jet meandering on the time-mean jet structure and its variability (Figure 4-14). The comparison of time-mean jet structure (Figure 4-14 *left*) shows that jet meandering has the effect of reducing the peak jet speed (by $\sim 50\%$ in the upper ocean and $\sim 75\%$ in the deep ocean) and eliminating the westward recirculations in the upper layer in the geographical mean. Hence (as expected) jet meandering "smears" out peak jet velocities, but it
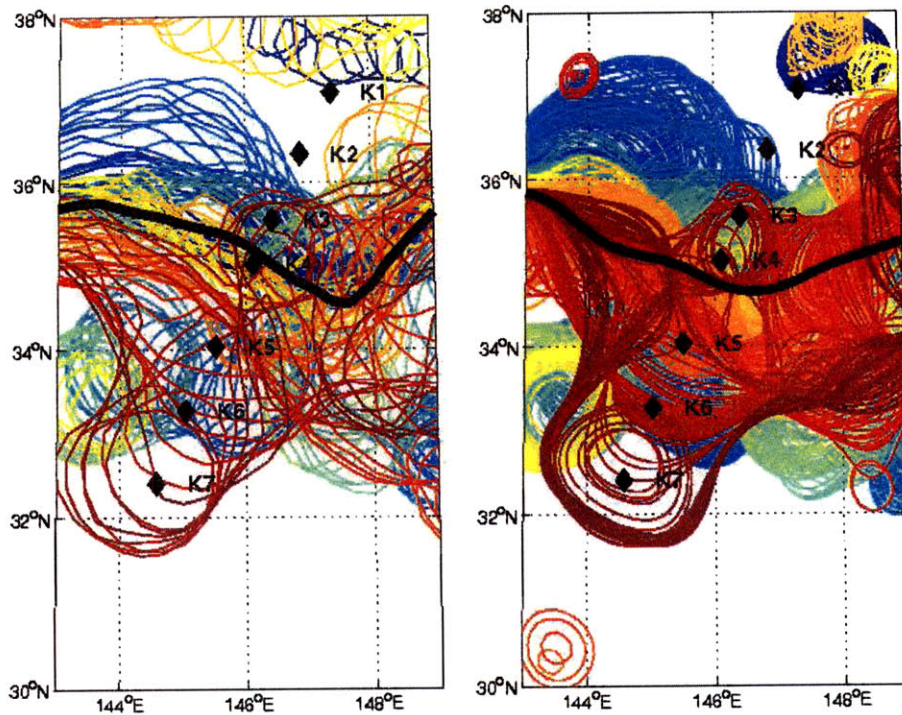
Figure 4-11: Weekly snapshots of the 2.1 m SSH contour measured by satellite altimetry (*left*) and daily snapshots of the thermocline depth (specifically the 350 m depth contour of the 12° C isotherm) from KESS CPIES data (*right*), each serving as a proxy for the jet axis position. The location of the KESS moorings are indicated. Blue colors indicate times close to the beginning of the observational period, and red colors indicate times near the end of the KESS period. The heavy dark line is the KESS period mean jet axis location.
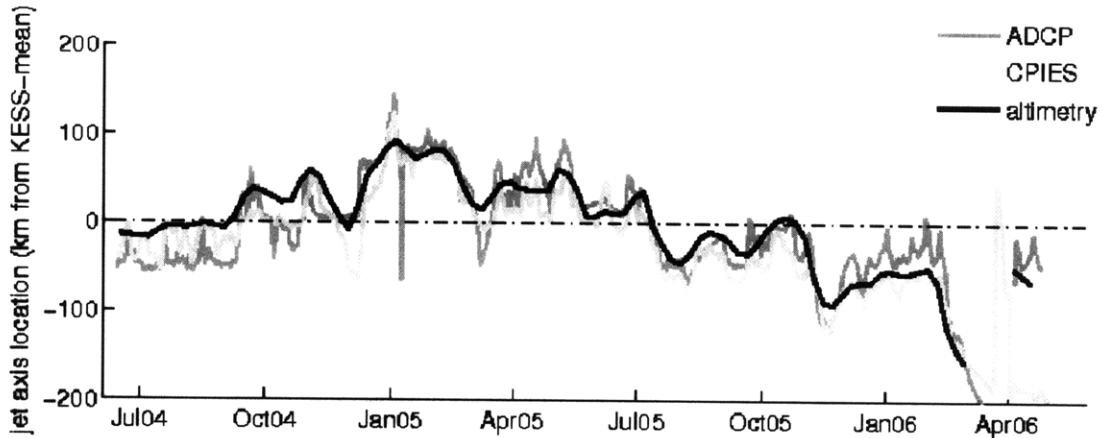
Figure 4-12: The timeseries of jet axis location along the KESS mooring line for each of the three proxies for jet path considered in the definition of the stream-coordinate system. The good correspondence between the time series based on different proxies for jet axis position gives confidence that each is a consistent measure of the jet axis location.

also eliminates upper ocean recirculations in the time-mean picture, a consequence presumably of occasional strong eastward velocities associated with the meandering jet dominating over weak flanking westward flows in the computation of the time average. Note that the differences in the geographical *vs.* stream-coordinate mean structures, particularly with respect to the existence of time-mean westward recirculations, are much less significant in the deep ocean compared to the upper ocean, consistent with the fact that the jet is much stronger in the upper ocean relative to the deep. The comparison of the time-mean cross-jet EKE distributions (Figure 4-14, *right*) reveal new structure in the stream-coordinate description that is hidden by the meandering in the geographical mean picture. In particular, in the upper ocean the stream-coordinate EKE distribution is sharply peaked at the jet axis, and has local minimums inside the recirculations. This structure is not seen in the geographical distribution, which is much more broadly distributed as a consequence of the jet meandering. It is interesting to note that in the deep ocean (Figure 4-14, *lower right*), EKE levels are approximately two times larger in the geographical frame compared to the stream-coordinate frame. This suggests that jet meandering is a much larger
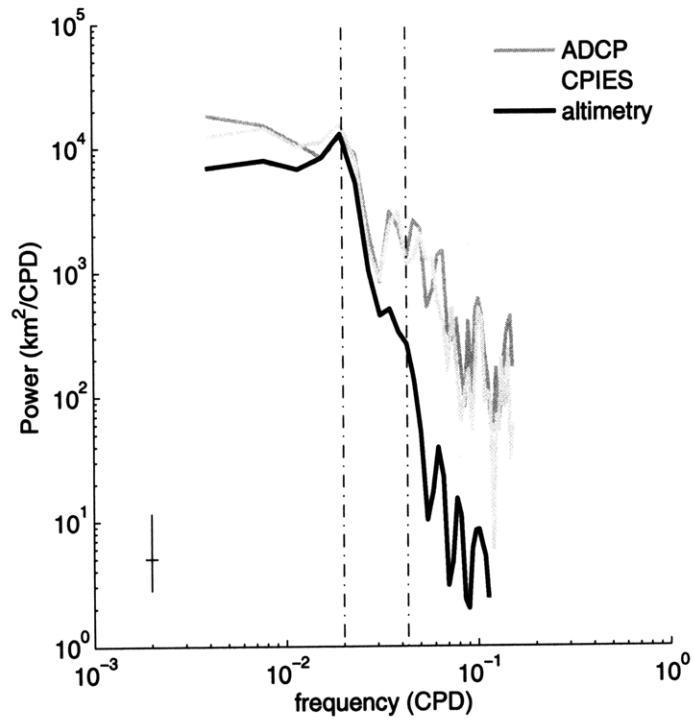
Figure 4-13: An estimate of the power spectral density computed from the time series of jet axis position (Figure 4-12) for each of the three proxies for jet axis location. The spectra is computed using Welch's averaged periodogram method using a total of three sections each with a length of 256 days. The 95% confidence interval is indicated in the lower left. Dashed vertical lines denote a period of 50 and 23 days.
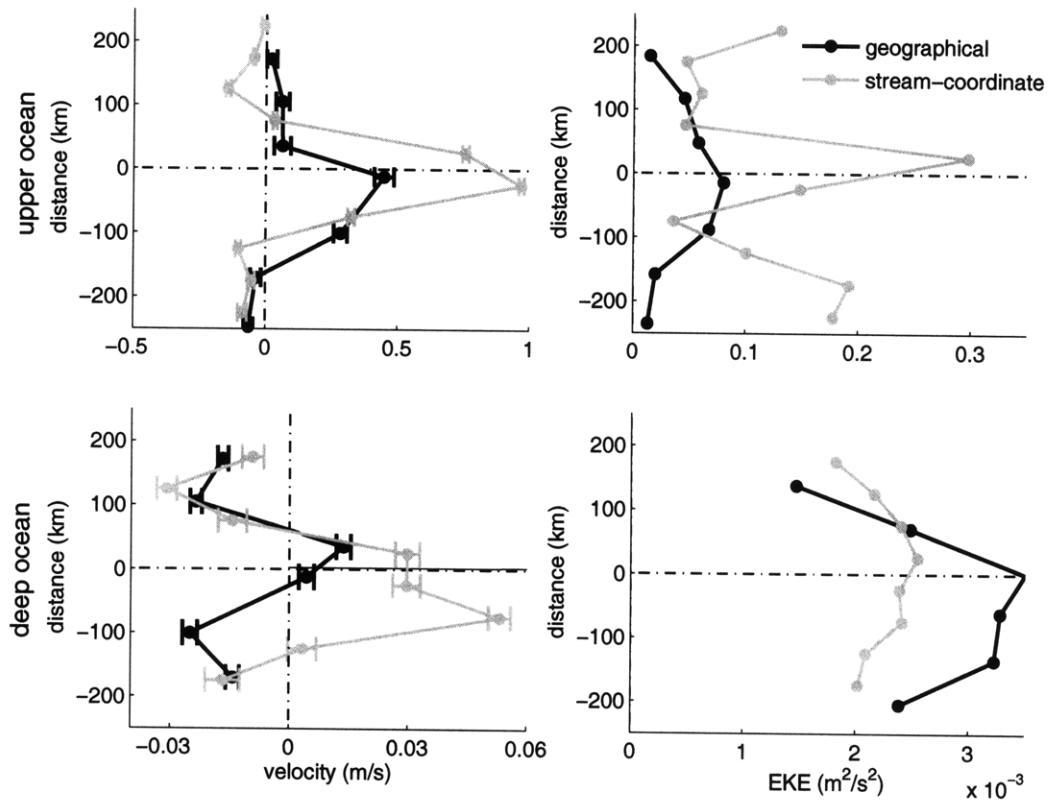
Figure 4-14: The cross-jet distributions of time-mean zonal/downstream velocity (*left*) and time-mean EKE ($\frac{1}{2}\left(\overline{u'u'} + \overline{v'v'}\right)$) (*right*) for the geographical (*black*) and stream-coordinate (*gray*) frames. The upper ocean structure (the average of altimetry surface values and mooring measurements at 250 m depth) and the deep ocean structure (the average of the four deep current meter measurements at 1500 m, 2000 m, 3500 m and 5000 m depth) are given in the upper and lower panels respectively. Error bars on the mean velocity indicate the depth-averaged standard error in the mean.

contributer to the eddy variability there compared to the upper ocean, where rings, wind, and other sources of variability likely also play a significant role.

(b) Ring interactions

As described in Appendix D, the interaction of warm and cold core rings with the KESS moorings were identified by a temperature criterion at 250 m depth. Identification and removal of rings from the time series give us information on the nature of ring interactions and their effects on the jet and its variability.

Using this temperature criterion, I find that rings interacted with the KESS array

(at at least one mooring site) for a total of 187 days out of a 704 day long record (*i.e.* $\sim$ 25% of the time). The distribution of ring interactions in time (Figure 4-15, *left*) shows ring interactions are not uniformly distributed, but rather are frequent in localized concentrations, specifically in the winter of 2005 and in the winter/spring of 2006. To say whether elevated levels of ring activity in winter is typical, would require examination of a longer time series, possible with the altimetry record. The distribution of ring interactions in space (Figure 4-15, *right*) shows that ring interactions with the array occurred at all moorings and hence to both the north and south of the jet. The largest number of ring interactions occurred at the moorings K5 and K6 (almost always south of the jet), where the largest and strongest rings (as seen in the altimetry record) tend to pass.

Comparing the mean jet structure and EKE distributions computed from the full timeseries *vs.* the timeseries with ring events removed (Figure 4-16) gives indication of the effect of rings on the time-mean jet structure and its variability. The comparison of time-mean jet structure (Figure 4-16 *left*) shows the interesting result that the effect of rings on the flanking mean jet structure is negligible. In particular, the westward recirculations seen in the time-mean jet remain a feature in the mean structure whether or not ring events are included. This is important as it implies that the existence of the time-mean recirculations is not simply a function of the time-averaging of rings propagating westward on the flanks of the jet. In contrast, the comparison of the EKE distributions shows a significant effect of rings on the structure of the eddy variability on the jet flanks. Here including ring interactions increases the peak values in EKE on the outer edges of the recirculations ($\pm$ 200 km from the time-mean jet axis) by approximately 50%. In short, ring interactions contribute significantly to the variance structure on the flanks of the jet, but they do not have a significant effect on the mean jet structure there, at least if it is assumed that their effect has influence only during the times when they are present. (Rings influencing the structure of the jet in such a way that dynamical changes result from their passage afterwards is of course plausible and not taken into account by this test.) Most importantly, with or without ring interactions included, the time-mean recirculations remain.
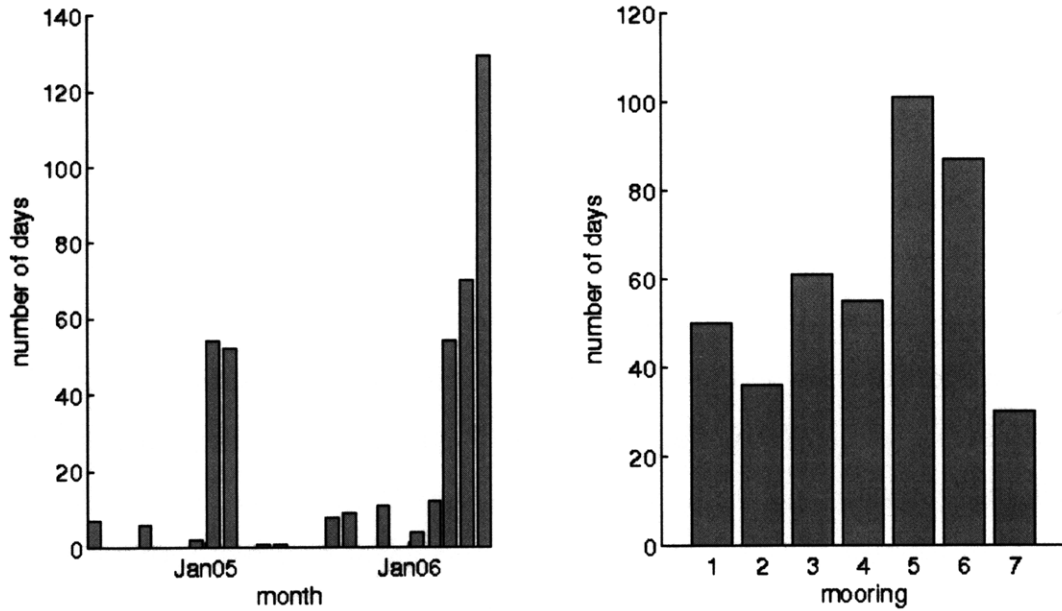
Figure 4-15: Histograms showing the distribution of "ring events" (days when a ring was present at a mooring location based on the temperature criterion described in Appendix D) in time (*left*) and space (*right*). Bins are months and moorings respectively, with "1" denoting the mooring K1 (the northern-most mooring in the array) and "7" denoting the mooring K7 (the southern-most mooring in the array). Note that if a ring was present at more than one mooring on a given day, it is counted as more than one day, resulting in counts in some months that exceed the number of days in that month.
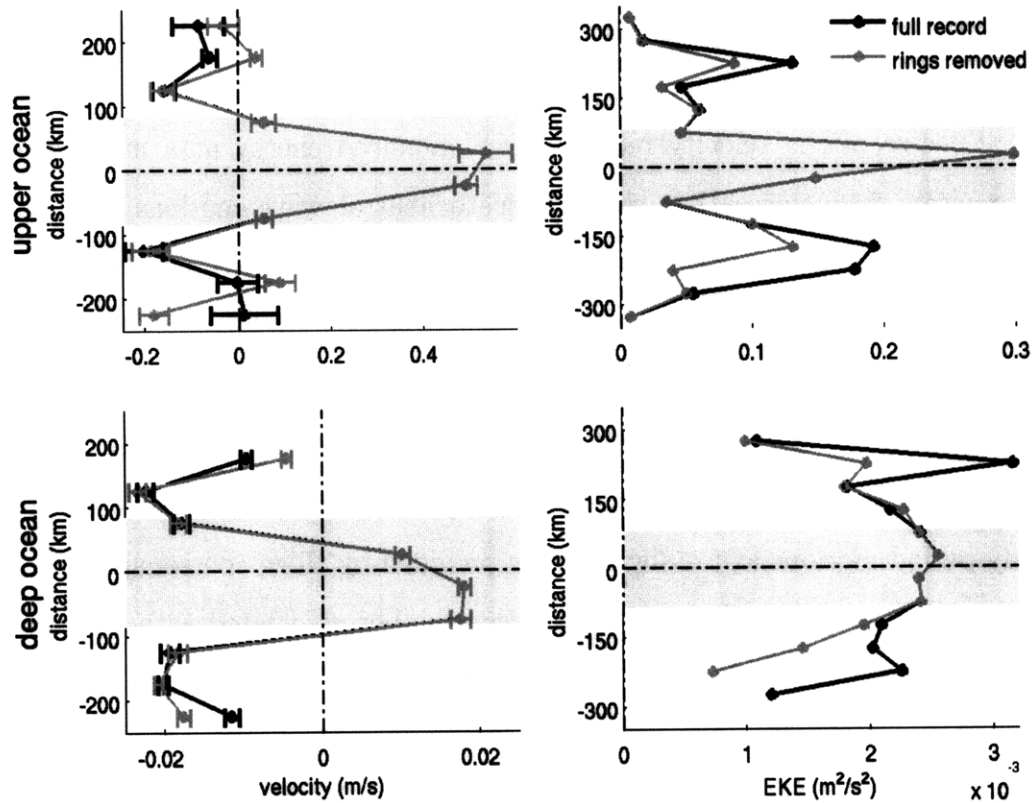
Figure 4-16: A comparison of the cross-jet distributions of time-mean zonal velocity (*left*) and time-mean EKE (*right*) computed from the full timeseries (*black*) *vs.* the timeseries with times corresponding to ring interactions with the mooring array removed (*gray*). As in Figure 4-14, the upper ocean structure (average of surface and 250 m depth values) and the deep ocean structure (average of the four deep current meter records ranging from 1500 m - 5000 m depth) are shown in the upper and lower panels respectively. Error bars on the mean velocity indicate the depth-averaged standard error in the mean. Grey boxes indicate the width of the time-mean jet, inside which rings are not identified by the criterion, and hence where no difference in the two timeseries being compared exists.

179

(c) Wave radiation and interaction

There exists the potential for waves in the system, either being radiated from the jet, generated by jet instability, or generated remotely and interacting with the jet-gyre system. Indeed a striking feature seen in animations of the instantaneous velocity vectors measured by the KESS mooring array is the periodic rotation of the velocity vectors on the flanks of the jet, suggestive of wave activity there.

Spectra of the velocity records show enhanced energy at a number of different mesoscale frequencies that could indicate neutral wave motions or jet instability. In general, peaks in power are seen near the 100-day period (most predominantly in the deep ocean), the 40-day period, and in the 10-20 day period range. The highest of these frequencies is suggestive of a jet instability timescale (see Appendix E), but energy at lower frequencies may be associated with Rossby waves either radiated from the jet or generated remotely. Support for the classification of the 40-day period motions as Rossby waves is provided by Hogg (personal communication), who demonstrates that the observed wavenumber associated with this wave activity is consistent with the barotropic Rossby wave dispersion relation (Figure 4-18).

Finally, Hovmöller diagrams formed from the velocity timeseries show two periods of distinct wave propagation (Figure 4-19): in the winter of 2005 and in the spring of 2006. It is interesting to note that these times correspond to times of elevated ring activity in the upper ocean (Figure 4-15). These propagating signals are seen at all depths but are most distinct at the abyssal levels, likely due to the less noisy character of the fields there which make the wave signals easier to see.

(d) Jet instability

One expects jet instability (both barotropic and baroclinic) to be a potentially important source of eddy variability in the system. To gain some insight into the KE jet's stability properties at the KESS location, I look for enhanced energy at expected jet instability timescales and consider observed velocity shears in the context of stability criteria.

As discussed in Section 4.3.2c, spectra of the velocity records show enhanced
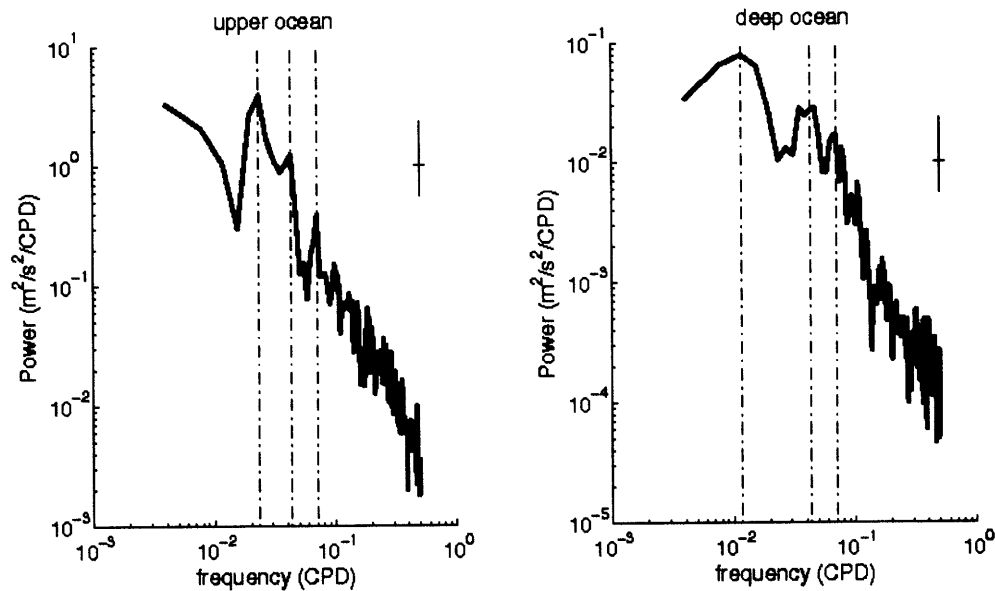
Figure 4-17: Estimate of the power spectral density computed from the time series of downstream velocity near the time-mean jet axis in the upper ocean (at 250 m depth) (*left*) and in the deep ocean (average of 1500 m, 2000 m, 3500 m and 5000 m depths) (*right*). As in Figure 4-13, the spectra is computed using Welch's averaged periodogram method using a total of 3 sections each with a length of 256 days. The degrees of freedom in the estimate are increased by averaging the records from three moorings near the time-mean jet axis (K3, K4 and K5), although due to the horizontal coherence in these records, these are not strictly independent. The 95% confidence level assuming record independence (hence it is conservative) is indicated in the upper right. Peaks are highlighted at 42, 23 and 16 days (*left*) and 125, 23 and 16 days (*right*) by the dashed vertical lines.

181
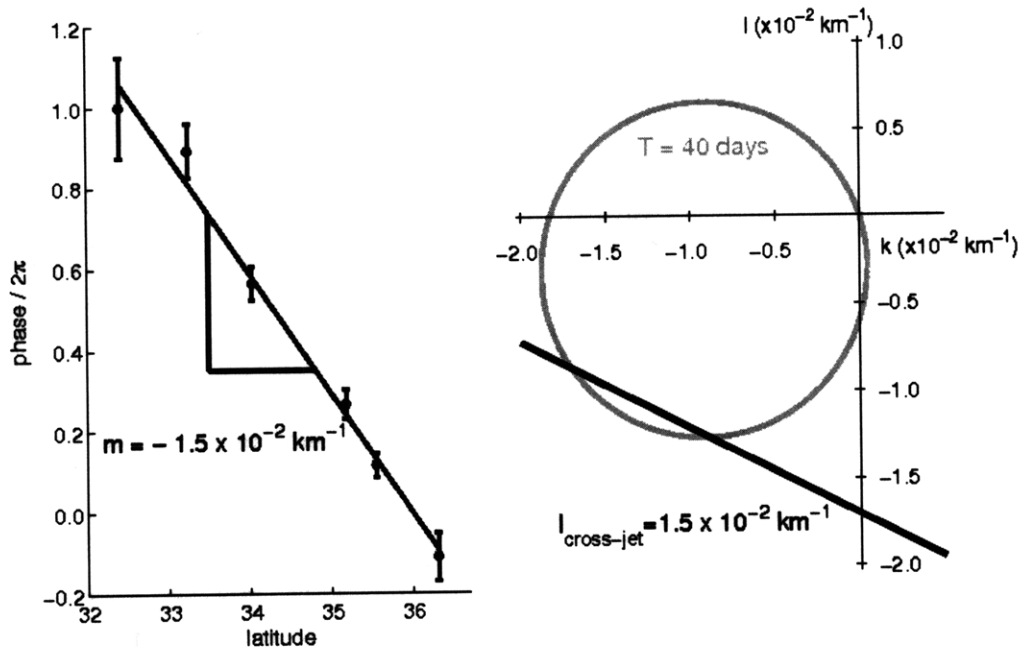
Figure 4-18: Phase *vs.* latitude of the 1st EOF mode (accounting for 51% of the total variance) at 40 day period (*left*). The linear variation of phase with latitude implies a constant cross-jet wave number given by the slope. A test of the barotropic Rossby wave dispersion relation for the observed wavenumber (*right*). The intersection of the circle (representing all possible pairs of k-l wavenumbers for a barotropic Rossby wave of 40 day period) and the line (corresponding to pairs of k-l wavenumbers consistent with the observed cross jet wavenumber) implies the observed phase variation with latitude is consistent with a barotropic Rossby wave. (Adapted from Hogg (personal communication)).
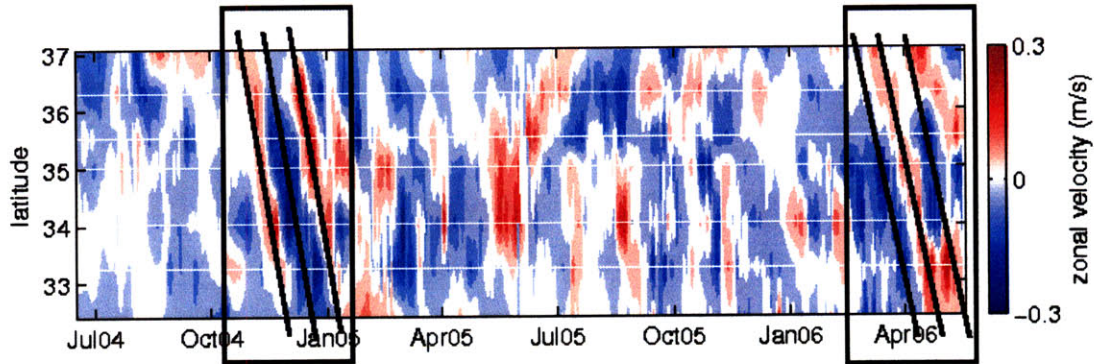
Figure 4-19: A Hovmöller plot (contours of velocity as a function of latitude and time) for zonal velocity at 5000 m depth as measured by the KESS mooring array. Tilted alternating bands of positive and negative values indicate wave propagation with a meridional phase speed given by the slope of the band (here 0.1-0.2 m/s). Periods of distinctive wave propagation, in the winter of 2005 and in the spring of 2006, are highlighted (*boxes*).

energy at a number of different mesoscale frequencies (Figure 4-17). One such frequency band (that corresponding to periods on the order of 20 days) is suggestive of the timescale of a barotropic instability of the KE jet, as predicted by an appropriate linear stability calculation (see Appendix E for details). Enhanced energy at timescales consistent with those of the linear stability calculations provide support for the hypothesis that some of the variability in the KE originates from the instability of the KE jet.

Insight into the potential stability properties of the jet is further gained by considering the observed velocity shears in the context of necessary conditions for instability. Here the relevant shears to consider are not those associated with the time-mean jet, but rather the instantaneous jet structure. Hence to more accurately evaluate the stability properties of the jet, I examine both the shears associated with the stream-coordinate mean jet structure (to be thought of as a "mean" or typical snapshot of instantaneous jet structure hereafter termed the synoptic mean) and extreme instantaneous values in the time series. These horizontal and vertical shears and their

183

associated implications for the stability properties of the jet are given in Figures 4-20 and 4-21.

One way to get an indication of the jet's potential for barotropic and baroclinic instability is to apply the idealized Rayleigh and Phillips model necessary conditions for instability to the observed horizontal and vertical shears respectively. Note that strictly one cannot isolate these instability criteria, the necessary condition for instability of a flow with both horizontal and vertical shear is defined by a change of sign of its total potential vorticity gradient. Nevertheless, there is potential heuristic value in considering the potential for barotropic instability in the jet and for baroclinic instability of the vertical shear independently, as is considered in Figure 4-20. To evaluate the magnitude of the horizontal shear in the context of its potential for barotropic instability, I compute the cross-jet distribution of the meridional gradient of the barotropic PV, $Q_y = \beta - U_{yy}$. Here β is the meridional gradient of the planetary vorticity and U_{yy} is the meridional gradient of the jet's meridional shear U_y, which approximates the jet's relative vorticity. The Rayleigh necessary condition for barotropic instability requires this quantity to change sign in the horizontal, which, as is shown, is satisfied in both the synoptic mean and extreme snapshot, it having negative values on the jet flanks. To evaluate the magnitude of the vertical shear in the context of its potential for baroclinic instability, I approximate the vertical structure of the system as consisting of two layers, and consider the vertical shear between them, $\Delta U = U_1 - U_2$, relative to the critical value given by the Phillips model, $\Delta U_{critical} = \frac{\beta}{F_2}$ [2]. For layer velocities I take the upper ocean mean (the average of surface and 250 m depth values) and the deep ocean mean (the average of 1500 m, 2000 m, 3500 m and 5000 m depth values) of the peak jet velocity at the jet axis, but note that this is an approximation, the stability criterion is derived for layer velocities that are independent of latitude. Here again the observed vertical shears ($\Delta U =$

---

[2]Here U is the zonal velocity, β is the non-dimensional β parameter, $\beta = \frac{\beta_{dim} L^2}{U}$, with L and U being typical length and velocity scales, and F_2 is the lower layer Froude number, $F_2 = \frac{f_0^2}{g' H_2}$, where f_0 is the Coriolis parameter, g' is reduced gravity, $g' = g\frac{\rho_1 - \rho_2}{\rho_0}$ (g is the gravitational acceleration and ρ_1, ρ_2, ρ_0 are the density in the upper and lower layers and the reference density respectively), and H_2 is the lower layer depth.

0.82 m/s (synoptic mean) and $\Delta U = 1.02$ m/s (extreme snapshot)) both exceed the critical value ($\Delta U_{critical} \sim 0.2$ m/s taking $\beta = 0.05$ and $F_2 = 0.25$) [3]. Taken together with the Rayleigh condition test, it suggests that the KE is potentially subject to a mixed instability at this location.

A similar conclusion about the jet's stability properties is reached taking a different tactic, that of considering the stability properties of the KE jet by making a two-layer approximation and applying the two-layer model necessary condition for instability (Pedlosky, 1963). The barotropic structure of the KE system below the thermocline suggests that making a two-layer approximation to evaluate its dynamics may be appropriate. Making this approximation, one can then evaluate the system's stability properties by examining the layered version of the meridional PV gradients (and whether a change of sign is observed in either the horizontal or the vertical). This is explored in Figure 4-21. Here again both the synoptic mean and extreme snapshot show that the layered versions of the vorticity gradient change sign in the vertical at the jet axis, again confirming that the observed shears are large enough to satisfy the necessary condition for instability. Note that this is consistent with the results of Howe (2008), who determined the PV gradient associated with the mean stream-coordinate structure of the KE from the CPIES data for a subsection of the KESS period, and found it to change sign in both the horizontal and the vertical.

In short, both the synoptic mean and instantaneous snapshots of the horizontal and vertical shears observed during KESS indicate that shears can far exceed the critical values for both barotropic and baroclinic instability based on idealized Rayleigh and Phillips model criteria, and for instability based on the meridional gradients of approximations to the layered PV gradients. This combined with the observation of enhanced energy at timescales consistent with those predicted by appropriate linear stability calculations, suggest that, even as far downstream as the KESS array location, the KE jet is potentially subject to a mixed instability mechanism that is a likely source of some of its eddy variability.

---

[3]To compute appropriate non-dimensional numbers, I take U to be 1 m/s and L to be 50 km as typical scales of the horizontal jet structure. F_2 assumes a thermocline depth of 750 m in a 5000 m depth ocean.
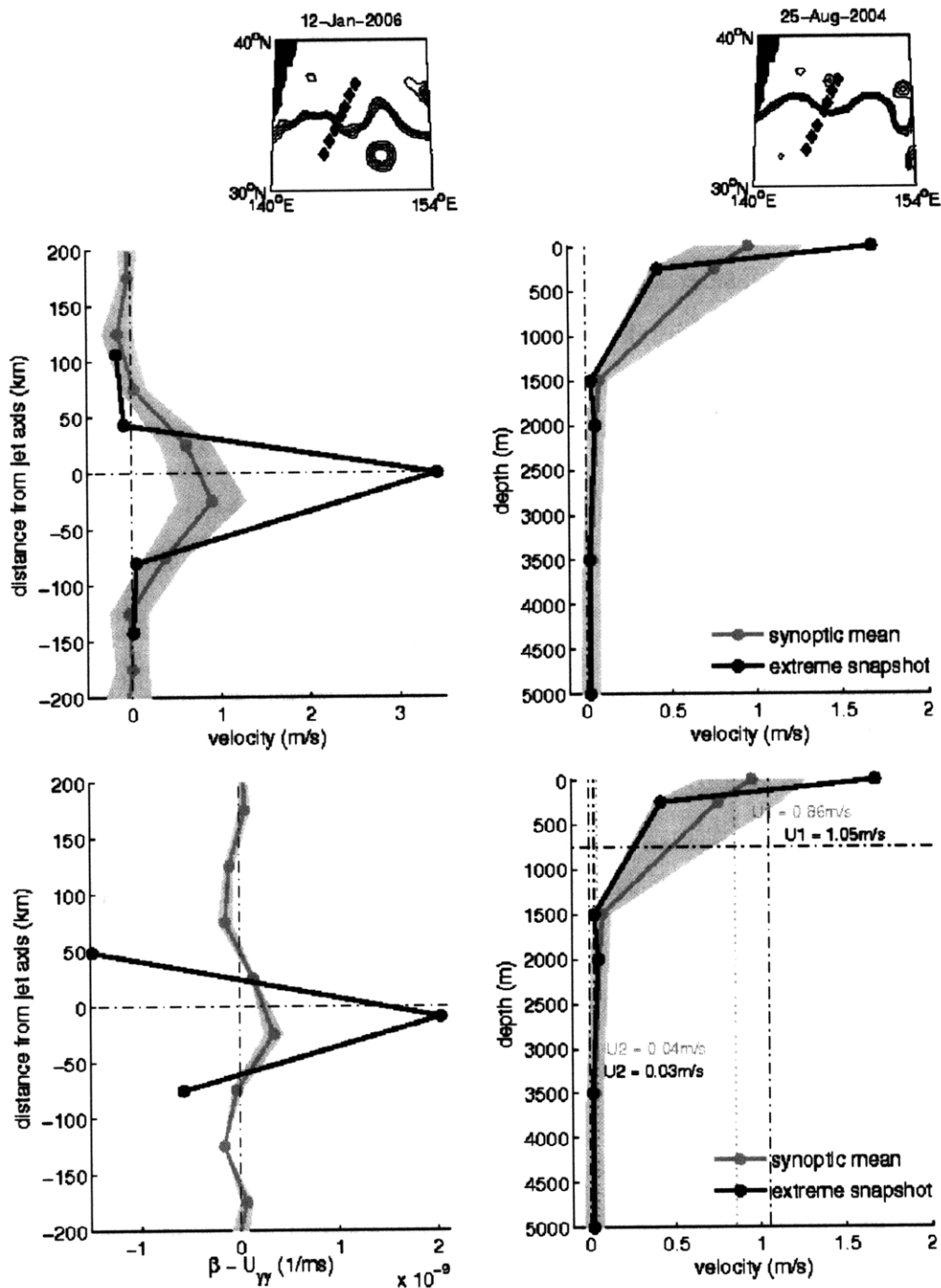
Figure 4-20: Synoptic mean (*gray*) and an extreme snapshot (*black*) of the horizontal jet structure at 250 m depth (*upper left*) and the vertical jet structure at the jet axis (*upper right*) to illustrate typical and extreme velocity shears observed during KESS. The gray shading in the synoptic mean is the mean ± one standard deviation. Map inserts are snapshots of the jet structure (contours of SSH from altimetry in the range of 1.9 to 2.3 m with a 0.1 m contour interval) corresponding to the time of the extreme snapshot. The implications of these shear magnitudes on the barotropic (*lower left*) and baroclinic (*lower right*) stability properties of the jet based on Rayleigh and Phillips model criteria. See the text for a discussion.
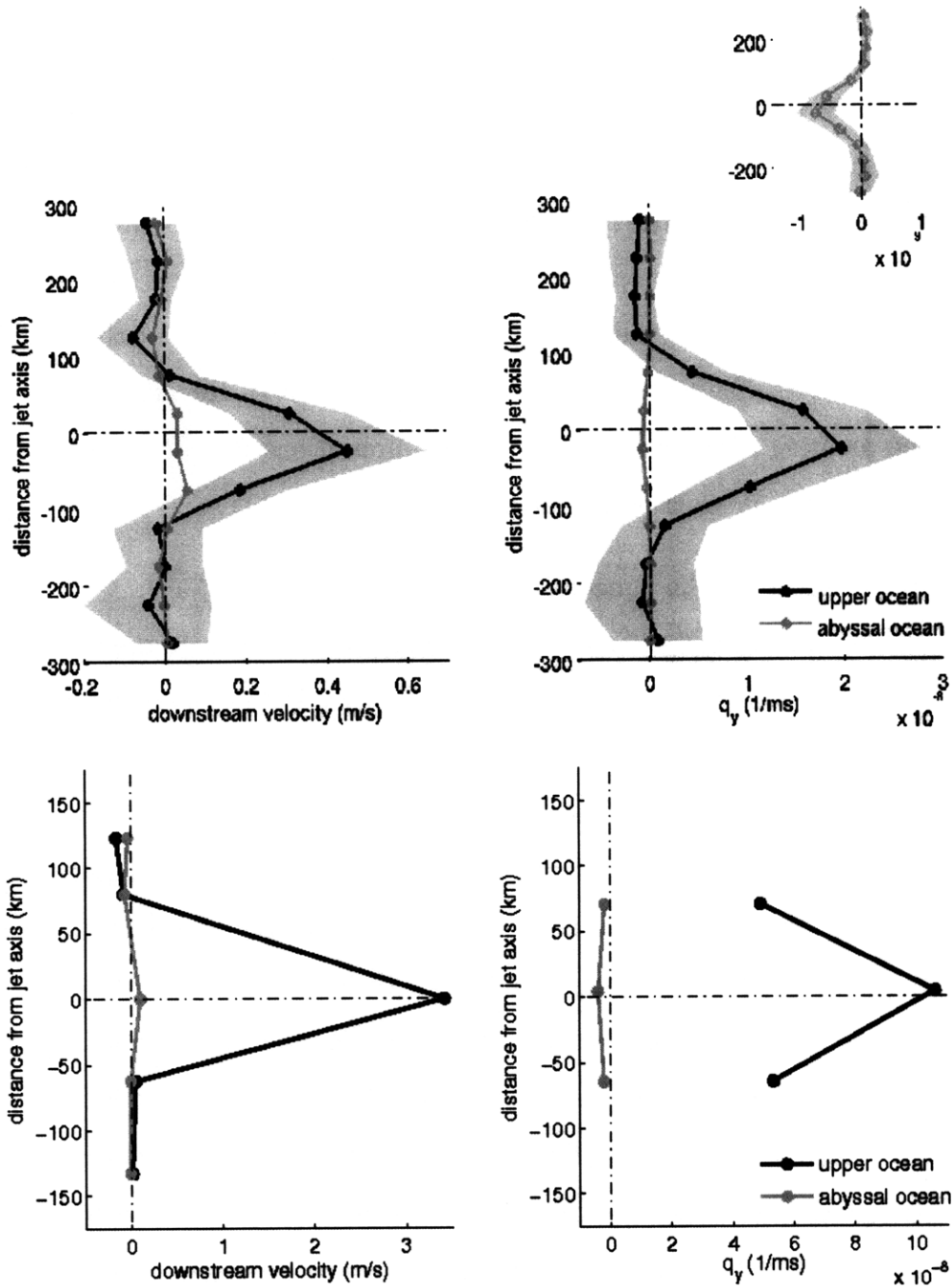
Figure 4-21: An approximate "upper layer" (*black*) and "lower layer" (*gray*) jet profile (*left*) formed by the velocity at 250 m depth and an average of the velocities at the abyssal depths respectively as measured by the KESS mooring array for the synoptic mean (*top*) and an extreme snapshot (*bottom*). Again shading in the synoptic mean indicates the mean ± one standard deviation. The corresponding layered versions of the meridional PV gradient ($q_{1y} = -U_{1yy} + \beta + \frac{f^2}{N^2 D_1^2}(U1 - U2)$ and $q_{2y} = -U_{2yy} + \beta + \frac{f^2}{N^2 D_2^2}(U2 - U1)$) using the above jet profiles and layer depths of 800 and 4000 m for D_1 and D_2 respectively (*right*). Here N is the buoyancy frequency, taken to be $0.005 \frac{1}{s}$. All other symbols have been defined previously in the text.

187

4.3.3 Eddy-Mean Flow Interactions

As the final ingredient, I attempt to gain some insight into how the mean flow and eddy variability interact, with particular interest in evaluating the eddy effect on the mean. Even with the relatively high spatial and temporal resolution of the KESS array, evaluating eddy forcing terms, which require computing a large number of spatial derivatives of the variability fields, is difficult. Although not the complete story, I make do with evaluating the cross-jet distributions of Reynolds stresses observed by the mooring array, and consider their implications for eddy forcing and various eddy-mean flow interaction scenarios.

(a) Eddy effect on the time-mean jet as diagnosed by $\frac{\partial}{\partial y}\overline{u'v'}$:

To consider the eddy effect on the time-mean jet, I evaluate the cross-jet distribution of the time-mean Reynolds stress $\overline{u'v'}$ (Figure 4-22). The meridional gradient of this quantity has implications for the effective "eddy force" on the time-mean flow, which follows from the Reynolds decomposition of the time-mean zonal momentum equation in which the effect of the eddies appears as a flux divergence of zonal momentum, $\frac{\partial}{\partial x}\overline{u'u'} + \frac{\partial}{\partial y}\overline{u'v'}$. Here I can evaluate only the second term in this eddy forcing quantity. The argument is often made that along-jet variations are small relative to cross-jet variations making terms involving zonal gradients negligible relative to those involving meridional gradients, however the validity of this assumption in a WBC jet that is evolving in strength and structure downstream should be questioned[4]. In the KESS mooring array measurements, a similar pattern of $\overline{u'v'}$ across the jet in both the upper and deep ocean is seen, with $\frac{\partial}{\partial y}\overline{u'v'} > 0$ (implying a westward effective eddy force if one neglects the zonal gradient contribution) on the jet flanks and $\frac{\partial}{\partial y}\overline{u'v'} < 0$ (implying an eastward effective eddy force) at the jet axis (Figure 4-22). This is in the sense to accelerate the jet at its axis and accelerate the time-mean westward recirculations on the jet flanks, consistent with the hypothesis that the recirculations are, at least partially, eddy-driven.

Note that this pattern of $\overline{u'v'}$ is **not** consistent with the scenario of a barotropically

---

[4]The idealized WBC model results discussed in Chapter 3 suggest that $\frac{\partial}{\partial x}\overline{u'u'}$ and $\frac{\partial}{\partial y}\overline{u'v'}$ make roughly equal contributions to the eddy momentum flux divergence.
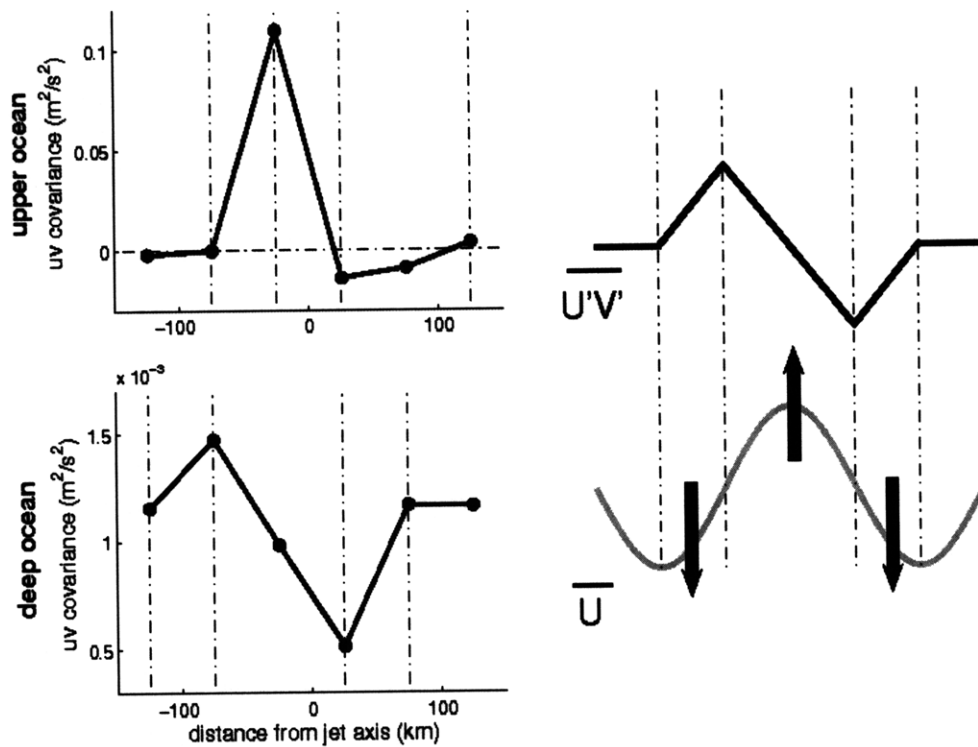
Figure 4-22: The cross-jet distribution of the time-mean covariance $\overline{u'v'}$ as measured by the KESS mooring array (*left*) for the upper ocean (average of the surface and 250 m depth values) (*top*) and the deep ocean (average of values at 1500 m, 2000 m, 3500 m and 5000 m depths) (*bottom*). Dotted lines denote boundaries between regions where the meridional gradient, $\frac{\partial}{\partial y}\overline{u'v'}$, and the associated effective eddy force derived from it, changes sign. A schematic illustrating the sense of the effective eddy force (denoted by the black arrows) derived from this $\overline{u'v'}$ pattern (*right*).
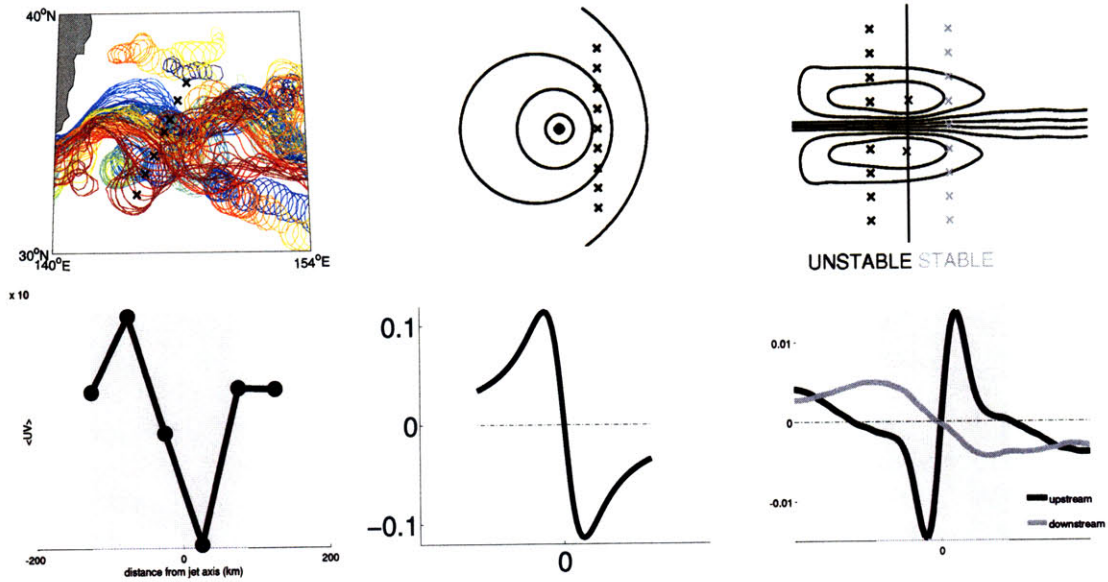
Figure 4-23: The cross-jet distribution of $\overline{u'v'}$ observed in the deep ocean by the KESS mooring array (*left*) compared to that of two idealized models: a localized wave radiator as discussed in Chapter 2 (here the analytical solution for Rossby wave radiation from a point source) (*middle*), and the downstream development of an idealized WBC jet as discussed in Chapter 3 (*right*). Grey shading denotes the width of the time-mean jet where applicable.

unstable jet, in which eddies flux momentum away from the jet and act to reduce its large-scale horizontal shear. Instead, this pattern mirrors that of a localized wave radiator, which as discussed in Chapter 2, results from energy radiation from a localized forcing. It is also consistent, as discussed in Chapter 3, with the "wave radiator" regime in the downstream development of an idealized WBC jet, which in the model is found downstream of mean jet stabilization (Figure 4-23). Important to an eddy-mean flow interaction perspective, as mentioned above, this is a pattern associated with eddy-driving of the time-mean recirculations.

In short, the cross-jet $\overline{u'v'}$ pattern observed supports the hypothesis that at the KESS location, eddies act in the sense to drive the time-mean recirculations. This pattern is consistent with a localized wave radiator model, which has been found to exist in the downstream development of an idealized WBC jet downstream of mean jet stabilization. The location of the KESS array near the downstream location of

190

maximum EKE (which in the idealized WBC model occurs close to the downstream location of mean jet stabilization) makes the idea that the KESS array belongs to the "wave radiator" regime of the KE jet plausible.

(b) Plausible eddy-mean flow interaction scenarios

I next consider the cross-jet distributions of all of the time-mean Reynolds stresses $\overline{u'u'}$, $\overline{u'v'}$ and $\overline{v'v'}$ as well as the time-mean EKE structure observed at the KESS mooring array, and compare them to those of various idealized models potentially relevant to the KE jet system. In this way, by looking for consistencies and discrepancies in the patterns, I hope to determine plausible eddy-mean flow interaction scenarios for the KE jet at this location that are at least consistent with the observed Reynolds stress distributions. A comparison of the observed distributions and those of select idealized models is summarized in Figure 4-24. Idealized models include (from simplest to most complex) (1) a simple meandering jet (a basic flow cosine jet with north and south walls in phase (the "sinuous mode") meandering past a line of fixed moorings) (2) waves radiated from the "rigid corrugation model" (Hogg, 1994) (the neutral Rossby wave field forced by a zonally oriented propagating boundary with sinusoidal corrugations) and (3) a barotropically unstable jet (Kamenkovich and Pedlosky, 1996) (a basic state jet plus the perturbation field that arises from the linear stability of a steady, barotropically unstable jet profile, see Appendix E for details).

The comparison shows that it is challenging to differentiate between different eddy-mean flow interaction scenarios because features of the Reynolds stress distributions of the various idealized models are either not unique or require fine cross jet resolution to discern structure inside the width of the time-mean jet. Nevertheless, some general comments can be made:

- the single peaked structure of $\overline{u'u'}$ and double peaked structure of $\overline{v'v'}$ observed in the upper ocean is consistent with the barotropically unstable jet model

- the double peaked structure of $\overline{u'u'}$ and $\overline{v'v'}$ observed in the deep ocean is consistent with the rigid corrugation model (waves radiated from a meandering jet)

- the observed non-zero $\overline{u'v'}$ distribution indicates a scenario more complex than simply a meandering jet or the waves radiated from it. Jet instability or Rossby wave radiation from a localized source are consistent with the observation of a non-zero $\overline{u'v'}$ correlation

In short, although the comparison of the observed cross-jet Reynolds stress distributions with those of idealized models of eddy-mean flow interaction scenarios does not offer conclusive results, it is suggestive of a scenario of a barotropically unstable jet in the upper ocean and wave radiation from the deep meandering jet. This seems plausible given the much weaker shears at deep levels relative to the upper ocean.

4.4 Results: Relation to a Simplified Dynamical Model

A second goal of the observational analysis was to test the relevance of the idealized studies, particularly of the WBC jet in Chapter 3, to the oceanic system. GS and KE observations were considered in the parameter choice of that theoretical study. Here I connect the theoretical study to observational results more directly, evaluating the relevance of its idealized set-up and its theoretical results to the observed system.

4.4.1 Relevance of Model Design

The theoretical model of Chapter 3 is, by design, idealized in many respects. For example, it has highly simplified vertical structure and the source of its eddy variability is restricted to the intrinsic variability of the unstable jet. Despite its simplicity however, there are several indications in the analysis of the KESS observations, as well as other observations in the KE region, that suggest both that some of the simplifications that the model employs and some aspects of the physics that it retains in this idealized configuration are appropriate to the KE jet. Three such examples are discussed here.
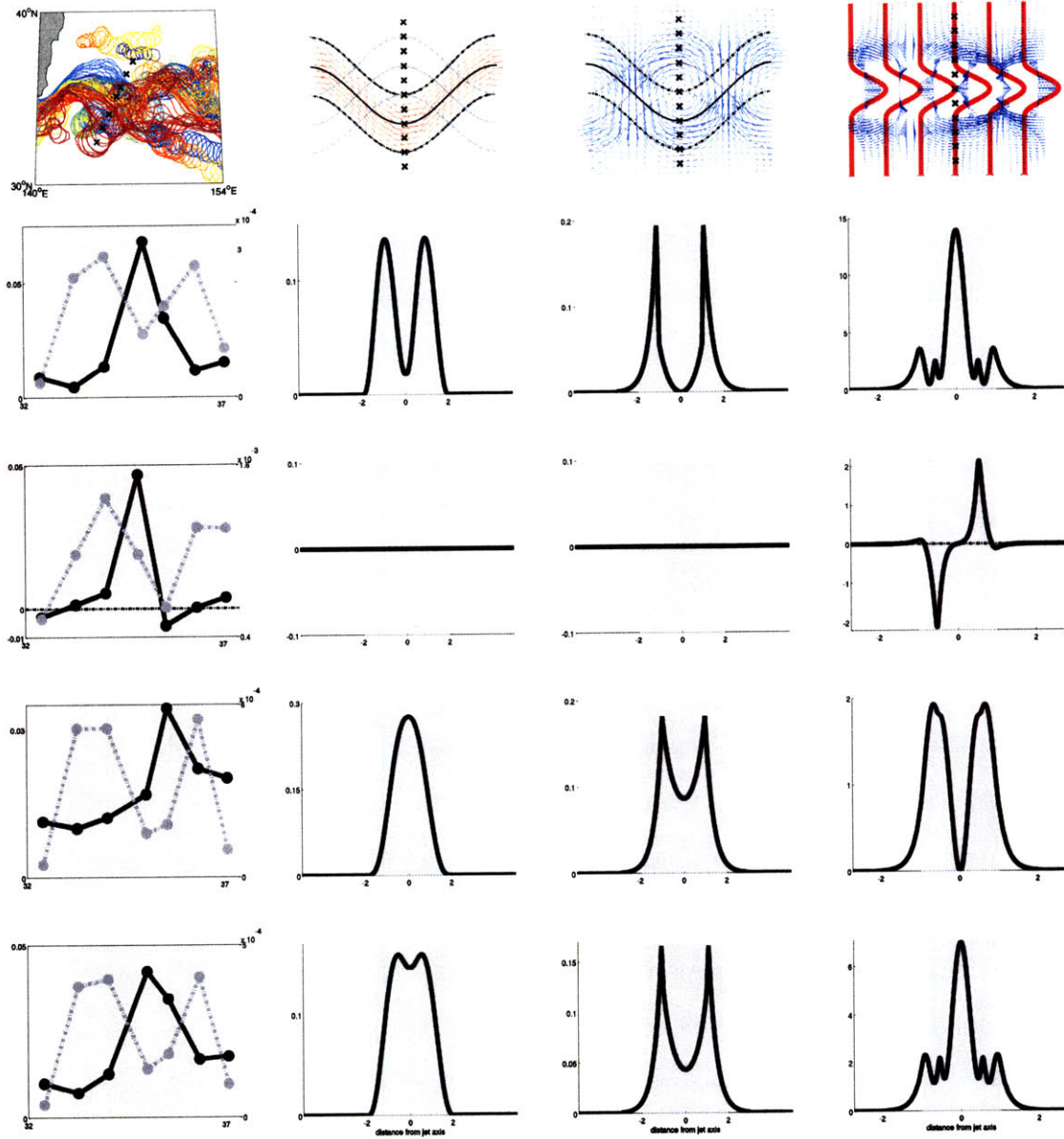
Figure 4-24: The cross-jet distributions of $\overline{u'u'}$ (2nd row), $\overline{u'v'}$ (3rd row), $\overline{v'v'}$ (4th row) and $\overline{EKE} = \frac{1}{2}\left(\overline{u'u'} + \overline{v'v'}\right)$ (5th row) observed at the KESS mooring array (1st column) compared to those of various idealized models: 1. a meandering jet (2nd column) 2. the Rossby wave field generated by a meandering jet (3rd column) and 3. a barotropically unstable jet (4th column). The KESS observations are shown for the upper ocean (at 250 m depth) in black scaled by the left-hand axes, and the deep ocean (averaged over 1500 m, 2000 m, 3500 m and 5000 m depth) in gray scaled by the right-hand axes. Velocity fields were band-passed filtered in the mesoscale range (periods of 10 - 100 days) before the variances and covariances were computed to clarify the cross-jet variations. The gray shading indicates the width of the time-mean jet in all columns.

193

(a) Vertical structure

First, KESS observations suggest that a dynamical model of the KE system with simplified vertical structure may suffice. KESS mooring observations indicate that, in general, the velocity structure at the KESS location has only a very weak depth dependence. This is especially true flanking the jet and below the thermocline, where motions tend to be in phase with very little amplitude variation with depth. An example is illustrated in Figure 4-25, which displays the full water column time series of zonal velocity as measured by the K2 mooring, situated north of the time-mean jet. Here it is seen that the variations in velocity extend throughout the water column. Motions in the deep ocean (below ~ 1500 m) especially appear essentially depth-independent, showing amplitude variation with depth only for the very largest events in the record.

If one evaluates the vertical coherence between velocity at various depths, one finds that the velocities at all depths are significantly coherent for a range of mesoscale frequencies (Figure 4-26). Quantifying the vertical coherence between velocity in the upper ocean (above the thermocline) and deep ocean (below the thermocline), for example between 250 m and 5000 m depth (Figure 4-26 *top*), shows that at this particular mooring, the records are significantly coherent in the frequency range corresponding to periods between approximately 20 and 60 days. In contrast, quantifying the vertical coherence between velocity at different depths below the thermocline, for example between 1500 m and 5000 m depth (Figure 4-26 *bottom*), shows that the records are significantly coherent for a much larger frequency range, here for all periods greater than about 5 days. The zero phase relationship between velocity at 1500 m and 5000 m depth indicates motions are in phase below the thermocline. The results presented use the velocity records from the mooring K4, but they are typical of all moorings. They are also consistent with the observations by Schmitz (1984) in the KE at 152°E, which showed that the normalized kinetic energy frequency distributions were independent of depth as a good first approximation, and that the lowest frequencies were strongly vertically coherent from 350 to 6000 m depths. All of these observations suggest it may be appropriate to at least treat the system below the
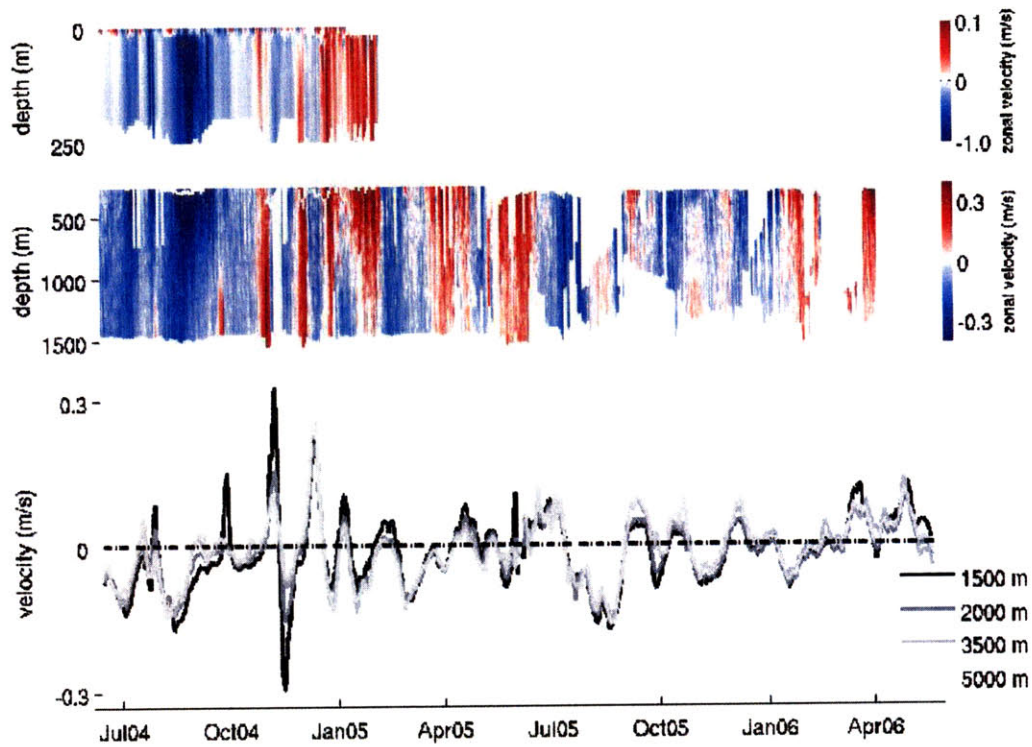
Figure 4-25: A sample full water column time series of zonal velocity measured by the mooring K2, situated north of the time-mean jet. It illustrates the vertical coherence of the velocity field that is typical at the KESS location, especially below the thermocline (*lower panel*), where the variations in velocity are in phase and only weakly depth-dependent in their amplitude.
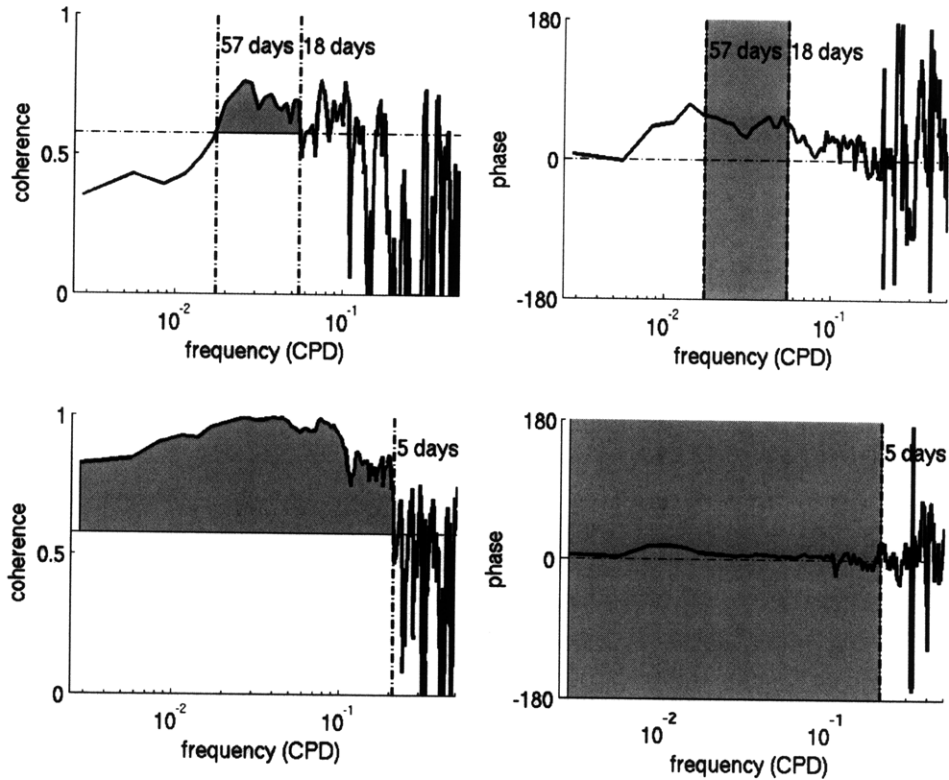
Figure 4-26: Vertical coherence amplitude (*left*) and phase (*right*) as a function of frequency in the zonal velocity between the upper ocean and deep ocean (250 m depth and 5000 depth) (*top*) and below the thermocline (1500 m depth and 5000 m depth) (*bottom*). Here velocity records are from the mooring K4, but results are typical of all moorings. In each, the level of 95% significance is indicated by the dashed horizontal line, and the range of frequencies for which the records are significantly coherent are shaded gray.

thermocline as a single dynamical layer.

(b) Degree of nonlinearity

Second, there are several indications that the system is very nonlinear, and hence a dynamical model with full nonlinearity is essential. Time series of velocity measured by the KESS moorings show a high degree of variability, with perturbation velocities, u' where $u' = u - \bar{u}$ (u is the instantaneous velocity and $\bar{u}$ is the time-mean velocity), typically on the order of 1 m/s in the upper ocean and 0.1 m/s in the deep ocean, often exceeding the mean value, $\bar{u}$, typically on the order of 0.1 m/s in the upper ocean and 0.01 m/s in the deep ocean, by an order of magnitude. Standard deviations of
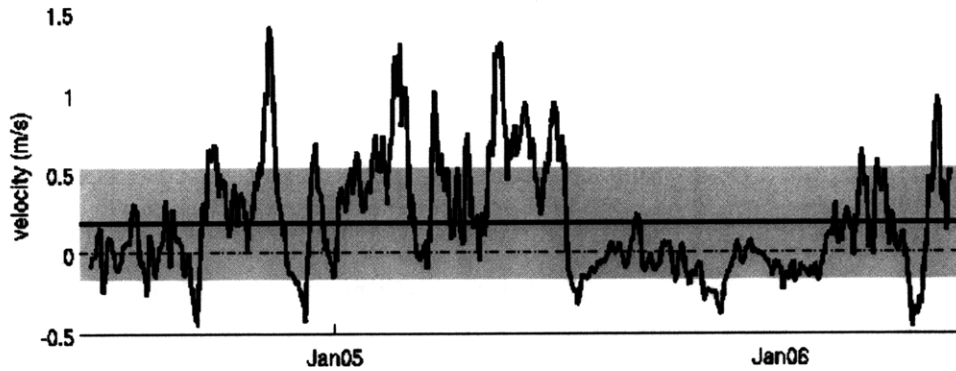
Figure 4-27: A sample time series of velocity measured by the KESS mooring array (here zonal velocity at 1500 m depth at the mooring K3, *i.e.* north of the time-mean jet) to illustrate the high degree of nonlinearity observed in the velocity fields during KESS. The mean (0.18 m/s) is indicated by the thick black line and the gray shading indicates the mean $\pm$ one standard deviation (0.35 m/s). The maximum velocity is 1.40 m/s which corresponding to a maximum perturbation velocity of 1.22 m/s. The instantaneous velocity exceeds the mean value $\pm$ the standard deviation approximately 30% of the time.

these time series, a measure of the average or characteristic perturbation velocity, are also large, and typically comparable to the magnitude of the mean. An example is given in Figure 4-27, which illustrates a degree of variability that is typical. In this particular time series (zonal velocity at 1500 m depth at the K3 mooring just north of the time-mean jet), the mean value is 0.18 m/s, the standard deviation is 0.35 m/s, the maximum excursion from the mean is 1.22 m/s, and the instantaneous velocity exceeds the mean value $\pm$ the standard deviation approximately 30% of the time. These frequent large perturbation velocities suggest strongly nonlinear system dynamics at play.

Meandering of the jet past the fixed moorings is a very strong contributer to variability observed at nearly all the moorings, so to isolate meandering effects from other sources of nonlinearity intrinsic to the jet, I consider also measures of variability and nonlinearity in the stream-coordinate frame, which effectively removes the effects of jet meandering. A summary of the mean, standard deviation and maximum values at each instrumented depth both inside the jet (within $\pm$ 25 km of jet axis) and inside

the recirculation gyres (at 125 km and 200 km from the jet axis for the northern and southern recirculation gyres respectively) is given in Table 4.1. The statistics indicate that except inside the time-mean jet in the upper ocean (where the strong mean jet is located), standard deviations are either comparable to or exceed the mean value, by up to an order of magnitude in some cases. Maximum values also tend to be an order of magnitude larger than the mean value, making the magnitude of the perturbation velocities large relative to the magnitude of the mean flow. This is especially true below the thermocline and inside the recirculation gyres. A high degree of variability in the stream coordinate frame indicates that there is also significant variability and nonlinearity intrinsic to the jet itself.

| | | depth | | | | | |
		0 m	250 m	1500 m	2000 m	3500 m	5000 m
	mean	0.95	0.76	0.07	0.06	0.03	0.02
jet	max	1.53	1.90	0.24	0.24	0.22	0.19
	std	0.32	0.37	0.05	0.05	0.05	0.05
	mean	-0.18	-0.16	-0.06	-0.05	-0.05	-0.05
northern RG	max	-0.90	-0.87	-0.15	-0.15	-0.18	-0.21
	std	0.31	0.18	0.05	0.05	0.05	0.06
	mean	-0.07	-0.03	-0.01	-0.01	-0.00	-0.00
southern RG	max	-0.52	-0.46	-0.17	-0.21	-0.15	-0.17
	std	0.29	0.26	0.05	0.04	0.04	0.04

Table 4.1: Various statistics of the timeseries of downstream velocity for each of the instrumented depths inside the jet (within ± 25 km of jet axis) and inside the recirculation gyres (RGs) (at 125 km and 200 km from the jet axis for the northern and southern recirculation gyres respectively). All values are in units of m/s.

A high degree of nonlinearity in the KE system is also suggested by the relative magnitudes of wave phase speeds *vs.* individual particle speeds observed. Wave phase speeds determined from Hovmöller plots of the mooring measurements of velocity are typically on the order of 0.1 m/s (Figure 4-19)), and are frequently also on the order of (and often less than) individual particle speeds, which are typically on the order of 0.1 - 1.0 m/s. We expect nonlinearity to be important when individual particle speeds approach and exceed wave speeds in the system. Hence this observation provides another indication that nonlinearities in the dynamics are important, and that a fully

198

nonlinear model of the dynamics is essential.

Finally, the degree of nonlinearity can be estimated by the non-dimensional β parameter, $\frac{\beta_{dim}L^2}{U}$, for the observed length, L, and velocity scales, U, a measure of the relative importance of the relative vorticity of the flow to the planetary vorticity. Taking observed scales from the stream-coordinate picture of the time-mean jet (representative of synoptic scales) of $L = 85$ km (the half-width of the jet) and $U = 1$ m/s (the surface peak velocity), and β_{dim} as simply the gradient of the planetary vorticity, implies a non-dimensional β parameter of 0.1. This is comparable to the GS, which has a value for non-dimensional β in the range of 0.02-0.13 (Flierl et al., 1987).

(c) Stability properties of the inflowing jet

As discussed in Section 4.3.2d, there is the suggestion in the KESS observations that the KE jet is potentially subject to both barotropic and baroclinic instability at the KESS location. Relevant to evaluating the design of the theoretical model however is the stability properties of the upstream jet, that at the point of WBC separation from the coast, as this serves as the forcing profile for the jet's downstream development in the open ocean. I attempt to gain some insight into the properties of the "boundary-forced" jet in the KE system by using a combination of altimetry at 141.3°E and information from the KERE mooring array, located at approximately 142.6°E. I use the former to evaluate the typical (synoptic mean) and extreme horizontal shears of the KE jet near the point of its separation from the coast (the longitude was selected to correspond to approximately where the KE jet enters the deep ocean, as is illustrated in the upper snapshots in Figure 4-28 which show 141.3°E (labeled $x = 0$) relative to the bathymetry which is indicated by the gray contours). I use the latter to evaluate its typical and extreme vertical shears at this approximate location (Figure 4-28, *top*). As in Figure 4-20, consideration of the implications of these shears for the barotropic and baroclinic stability properties of the jet at this location are also computed (Figure 4-28, *bottom*). They show that, like at the KESS location, both the horizontal and vertical shears in both the synoptic

mean and in the extreme snapshots are sufficient to satisfy the necessary conditions for both barotropic and baroclinic instability based on idealized Rayleigh and Phillips model criteria. The meridional barotropic PV gradient associated with the surface jet profile, $Q_y = \beta - U_{yy}$, changes sign in the horizontal by becoming negative on the jet flanks, and the crude approximations to the vertical shear, $\Delta U = U_1 - U_2$ (0.48 m/s in the synoptic mean and 0.95 m/s in the extreme snapshot), exceed the Phillips model critical value for the jet scales at this location (~ 0.2 m/s). As was noted in Section 4.3.2d, isolating the horizontal and vertical shears and applying these two conditions separately is not strictly valid, however it does provide the heuristic conclusion that like at the KESS location, the KE jet is potentially both barotropically and baroclinically unstable. This suggests that a jet subject to mixed instability is a plausible source for at least some of the variability of the KE jet system and is a realistic model forcing.

4.4.2 Model - Observations Consistencies

In addition to using observations to test the relevance of the model design and set-up, I can evaluate the relevance of the theoretical results of Chapter 3 to the dynamics of the KE system by looking for consistencies and discrepancies between model predictions and observational results. Given the importance of zonal variation found in the theoretical study, the most useful tests are those that check the consistency in downstream development of properties in the model *vs.* the observed KE jet-gyre system. Here I make such comparisons for both mean jet-gyre properties, as well as properties of the eddy variability and their associated signatures of eddy-mean flow interactions.

(a) Downstream evolution of the mean jet-gyre system

Both the altimetry record and the KESS observations in combination with past mooring deployments up and downstream give us views of the downstream development of the time-mean KE jet-gyre system which can then be compared to the downstream development of the time-mean jet in the idealized model. These com-
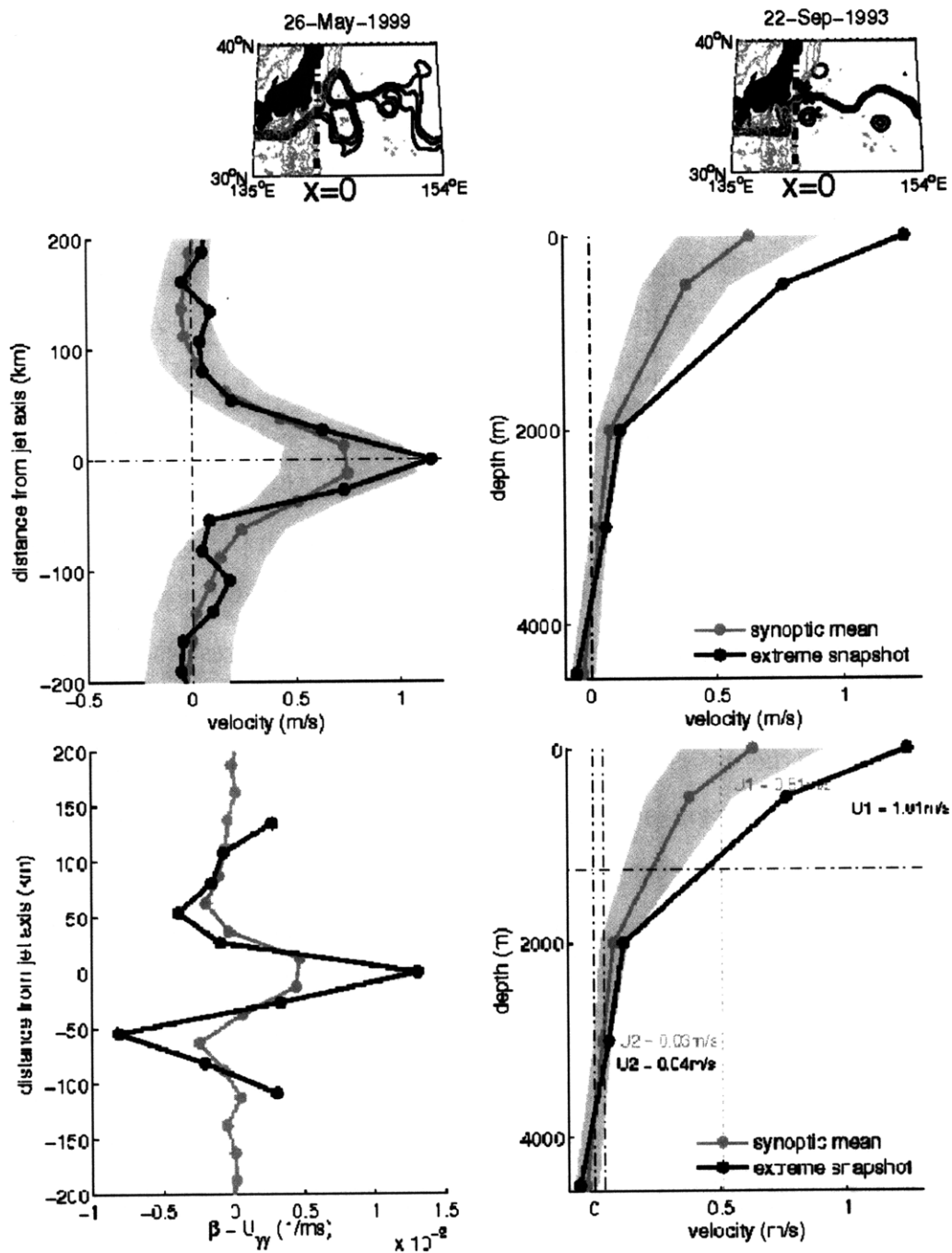
Figure 4-28: Synoptic (stream-coordinate) mean (*gray*) and an extreme snapshot (*black*) of the horizontal jet structure at 141.3°E (evaluated from the surface geostrophic velocity derived from the 14-year altimetry record) (*upper left*) and the vertical jet structure at the same approximate location (evaluated from the KERE mooring array) (*upper right*). Grey shading denotes the synoptic mean ± one standard deviation. Snapshots of the KE jet state visualized via SSH (as in Figure 4-20) at the times corresponding to the extreme snapshots are above. Region bathymetry is shown in these snapshots by the gray contours (contours are at 2000, 4000, 6000 and 8000 m respectively), and the location of the KERE moorings is shown in the upper right by the **xs**. The implication of these shear magnitudes on the barotropic (*lower left*) and baroclinic (*lower right*) stability properties of the jet as in Figure 4-20 are shown in the lower panels.

201

parisons are presented in Figures 4-29 through 4-31.

Using the mooring observations, I compare the downstream evolution of the time-mean KE jet profile in both the upper and deep ocean to that of the time-mean jet in the upper and lower layers of the two-layer model run in a KE-like parameter regime and dimensionalized using the scales of the inflowing KE jet derived from satellite altimetry data as described in Section 4.4.1c (Figure 4-29). Downstream locations in the model for the comparison are selected to be similar to the mooring array locations relative to the time-mean EKE distribution (Figure 4-29 *upper inserts*). Note that the mean jet structure in the observational data is viewed in the stream-coordinate frame, which was found to be critical in revealing the details in the downstream development of the jet/gyre structure given the intense meandering of the KE jet and the course cross-jet resolution of the moorings. Conversely, model results are presented in the geographical frame, as the calculation of the stream-coordinate description of the model jet structure is still underway. Despite this frame difference however, there are several important similarities between the model and the observations in the downstream development of mean jet and gyre properties that are encouraging and worthy of mention. These include a strengthening and sharpening of the jet and the development of westward recirculations up until the downstream location of maximum EKE, followed by a weakening and broadening of the jet and a weakening of the recirculation strength past the downstream location of maximum EKE. This same downstream development pattern is seen in the stream-coordinate mean profiles of the jet derived from the 14-year altimetry record (Figure 4-30). Here again evidence of the jet sharpening and the westward recirculations developing upstream of the EKE maximum is seen, both of which then weaken downstream of the EKE maximum consistent with the model's behavior. Note that the KE jet appears to evolve in the downstream coordinate more slowly than the idealized model (a point to be revisited), so the furthest-most downstream location for the altimetry comparison was selected to be a disproportionate distance downstream from the EKE maximum to more clearly demonstrate the trend of decreasing jet and recirculation strength.

One is able to look at the downstream development of mean jet-gyre properties in
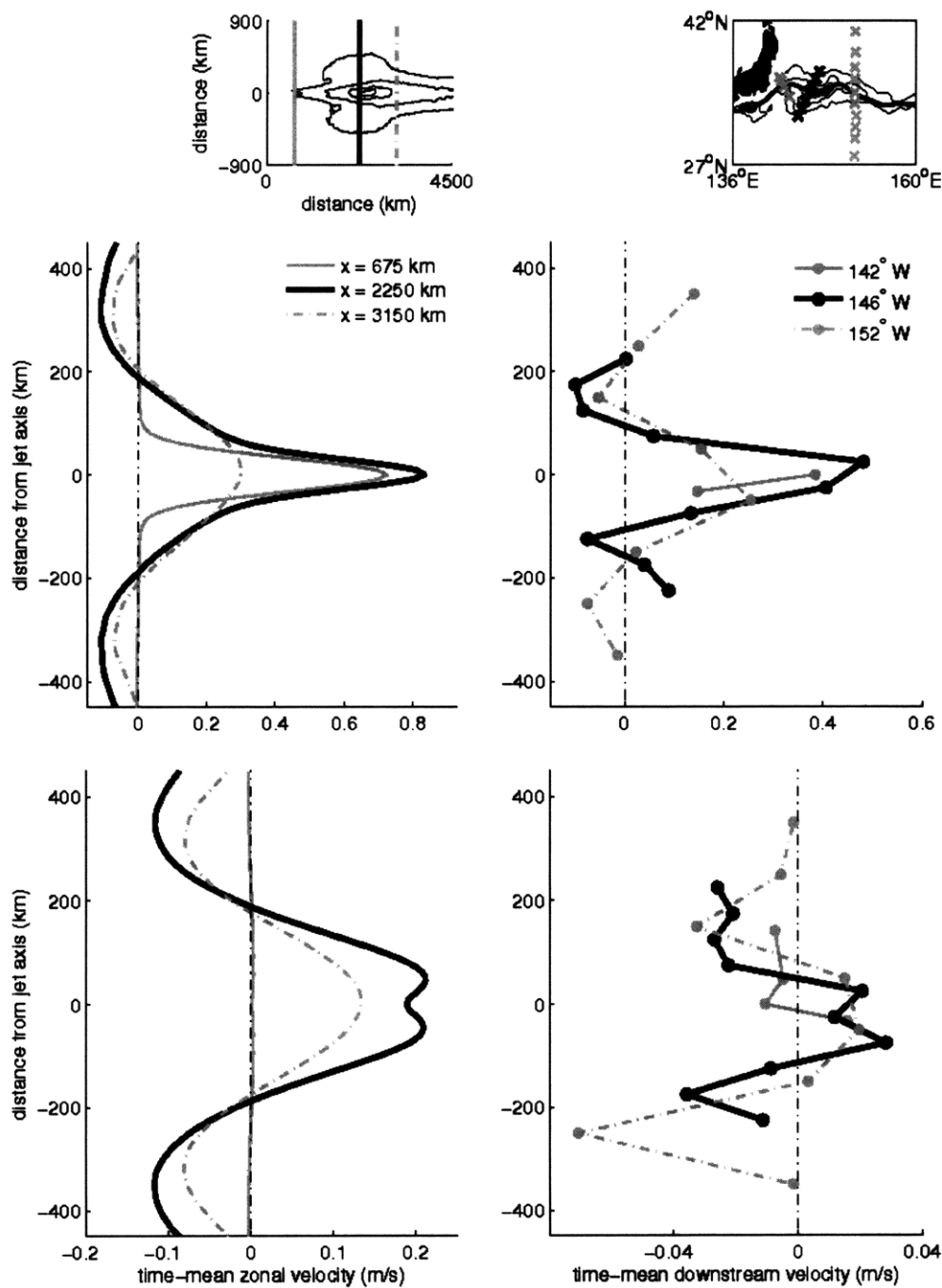
Figure 4-29: A comparison of the downstream evolution of the time-mean jet profile from the idealized model in a KE-like regime (*left*) *vs.* that of the KE jet derived from mooring observations (*right*) at three locations downstream. Downstream locations for the comparison in the model are selected to be similar to the mooring array locations relative to the time-mean EKE distribution (*upper inserts*). The upper layer and upper ocean (at 500 m depth with a linear interpolation used to estimate the velocity at this depth if measurements were not available) are shown in the upper panels, the lower layer and deep ocean (at 4000 m depth again linearly interpolated if necessary) are shown in the lower panels.
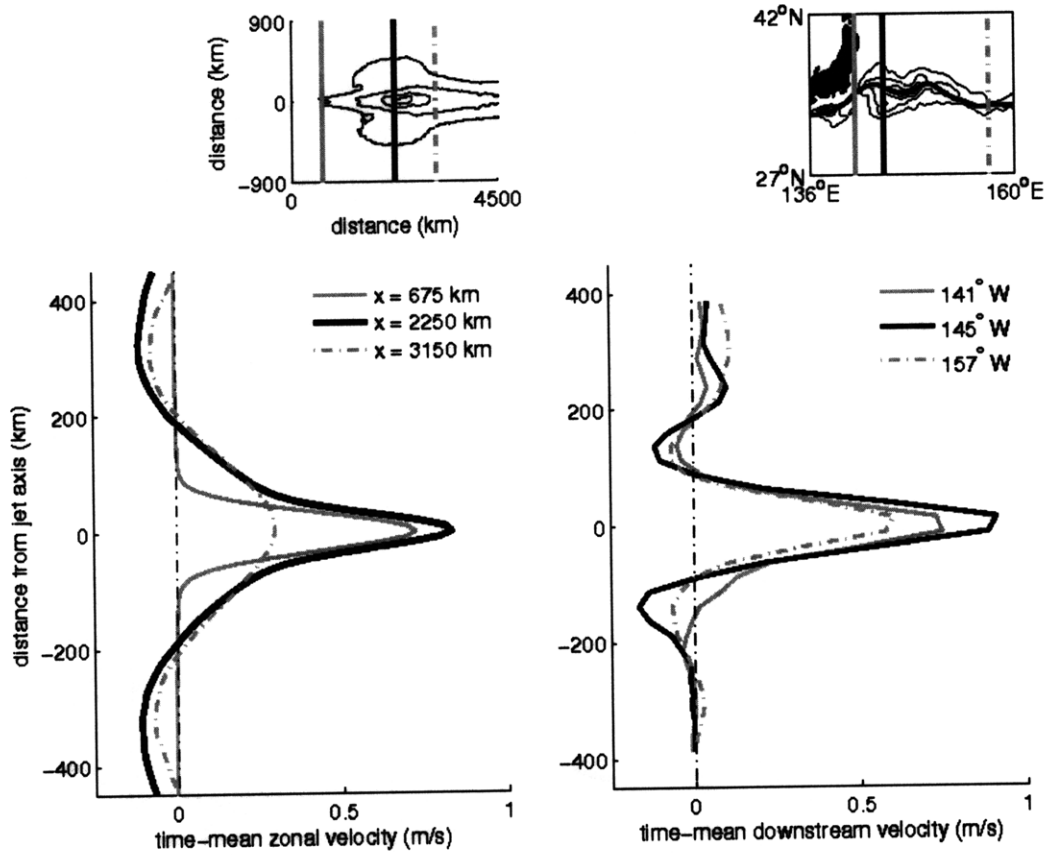
Figure 4-30: As in Figure 4-29 but with the stream-coordinate mean profiles of the KE jet derived from the 14-year altimetry record replacing the mooring observations (*right*). Corresponding model profiles are from the upper layer of a two-layer model run in a KE-like regime (*left*). Again the downstream locations for the comparison are chosen relative to the time-mean EKE distributions (*upper inserts*).

more detail by making use of the altimetry record. A comparison of the continuous downstream evolution of mean properties, in particular of the maximum mean jet velocity, the maximum mean recirculation velocity, and the maximum in EKE from the model run in a KE-like regime to that derived from the altimetry record is shown in Figure 4-31. Here again there are several consistencies in structure, including a peak in the time-mean jet velocity located downstream of the inflow/western boundary, a peak in the time-mean recirculation velocity located downstream of the peak in jet velocity, and a peak in the time-mean EKE located downstream of the peak in recirculation velocity. There are differences as well, a particularly outstanding example being the additional structure seen in the downstream evolution of EKE in the KE jet compared to the single peaked structure of the idealized model. It is potentially useful to note that the location of the multiple local maxima in the observed EKE profile are coincident with the downstream locations of the crest and trough of the first quasi-stationary meander that is present in the time-mean KE jet path (Figure 4-31 *upper right*), a feature that is not present in the idealized model. I hypothesize that the non-zonal nature of the mean jet in the region of the quasi-stationary meanders has a significant effect on the stability properties of the basic state jet and the related eddy-mean flow interactions, however this deserves further exploration.

A second important model-observations discrepancy, common to all of the comparisons, exists in the rate at which the time-mean properties evolve downstream, with the KE jet evolving much more slowly with downstream distance than its model counterpart. The fact that the model fields are viewed in the geographical frame while the observations are viewed in a stream-coordinate frame may be partially responsible for this, and this will be qualified in future work, however I suspect that the meanders in the time-mean KE jet path also contribute to the discrepancy. Time-mean sea surface height fields from the 14-year altimetry record suggest that the extent of the recirculations in the KE are modulated by the meanders of the jet path, and, as mentioned above, there are dynamical arguments that suggest that the non-zonality
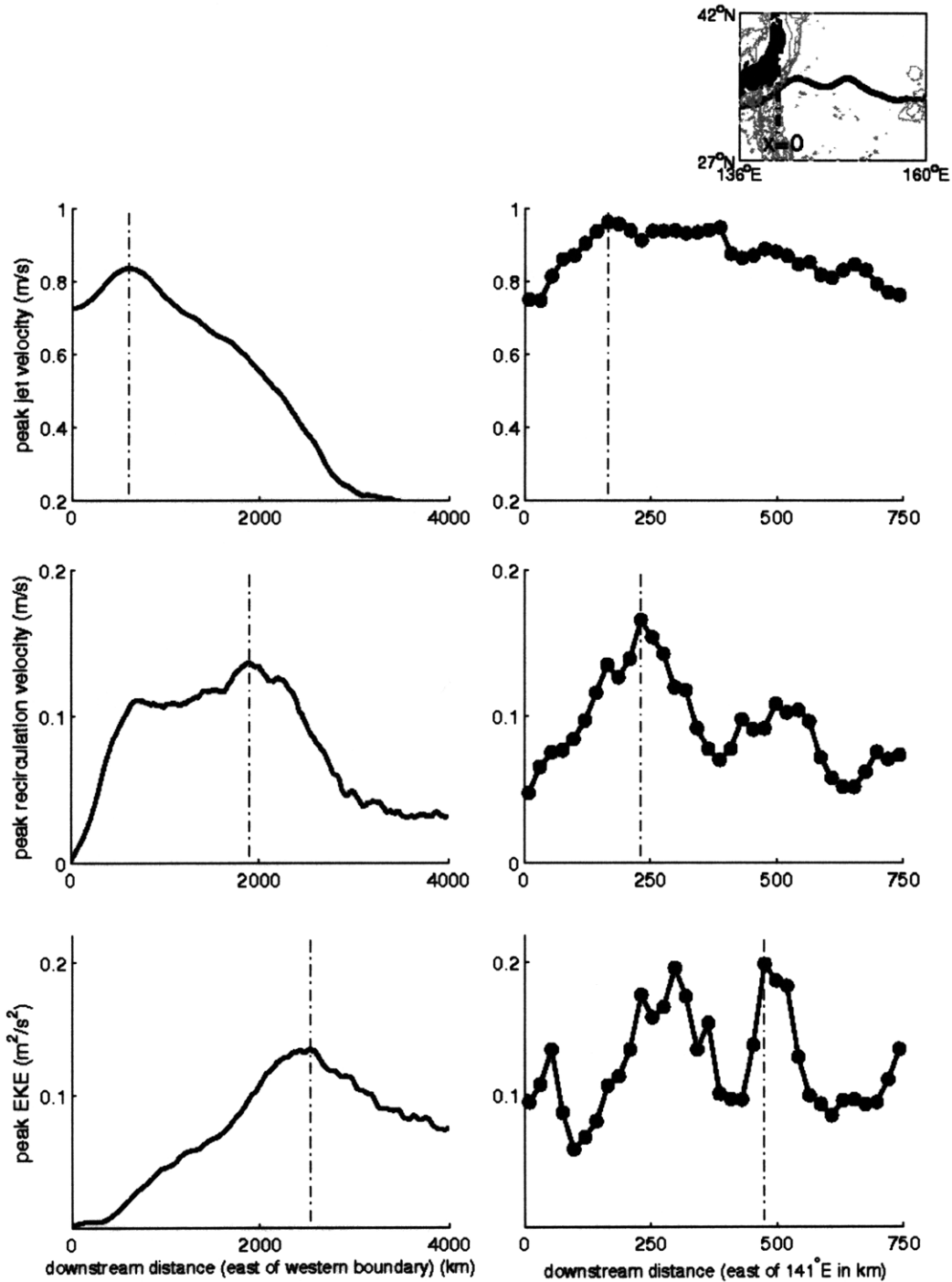
Figure 4-31: The peak time-mean jet velocity (*top*), the peak time-mean recirculation velocity (*middle*), and the peak time-mean EKE (*bottom*) as a function of downstream distance for the idealized WBC jet model (*left*) *vs.* the KE jet (*right*). Again, model values come from the upper layer of a typical two-layer run with KE-like parameters, while observed values are taken from the stream-coordinate mean velocity field derived from the 14-year altimetry record. The origin for the altimetry evolution is taken to be the approximate longitude where the KE jet enters the deep ocean as described in Figure 4-28 (*upper insert*).

of the jet that results from the presence of these meanders would have an important influence on the downstream development of the eddy-mean flow interactions. Understanding this discrepancy in the scale of downstream development, and the role that the presence of the quasi-stationary meanders in the KE path may play, is a subject left for future work.

(b) Properties of the eddy variability and signatures of eddy-mean flow interactions

Perhaps the most dynamically significant test of model-observation consistency, especially from the perspective of eddy-mean flow interactions, is that of consistency in the downstream evolution of the properties of the eddy variability, and in particular how they relate to signatures of the eddy effect on the time-mean circulation. As mentioned, diagnosing the eddy effect on the mean is much more difficult using direct observations compared to using the model output, but two insightful examples are given in Figures 4-32 and 4-33.

A comparison of the time-mean covariance ellipses (a visualization of the time-mean Reynolds stresses $\overline{u'u'}$, $\overline{v'v'}$ and $\overline{u'v'}$) between those from the KE-like two-layer model and those computed from the mooring observations is given in Figure 4-32. Here again important similarities in downstream development are seen. In particular, the dynamically significant transition from a pattern of positive ellipse tilt north of the jet axis and negative ellipse tilt south of the jet axis in the near-field of the jet (consistent with a barotropically unstable jet regime) upstream of the location of maximum EKE, to the reverse pattern (consistent with a wave-radiator regime) downstream of this location is observed. This suggests that there is potential relevance of the two-regime description of eddy effect on the mean found in the idealized WBC jet model to the downstream development of the KE jet.

Finally, using both the zonal and meridional gradient information available with the maps of altimetry measurements, it is possible to compute the eddy-mean flow interaction terms directly using observational data. Here the limitation is spatial resolution: computing the eddy forcing terms requires taking a number of derivatives
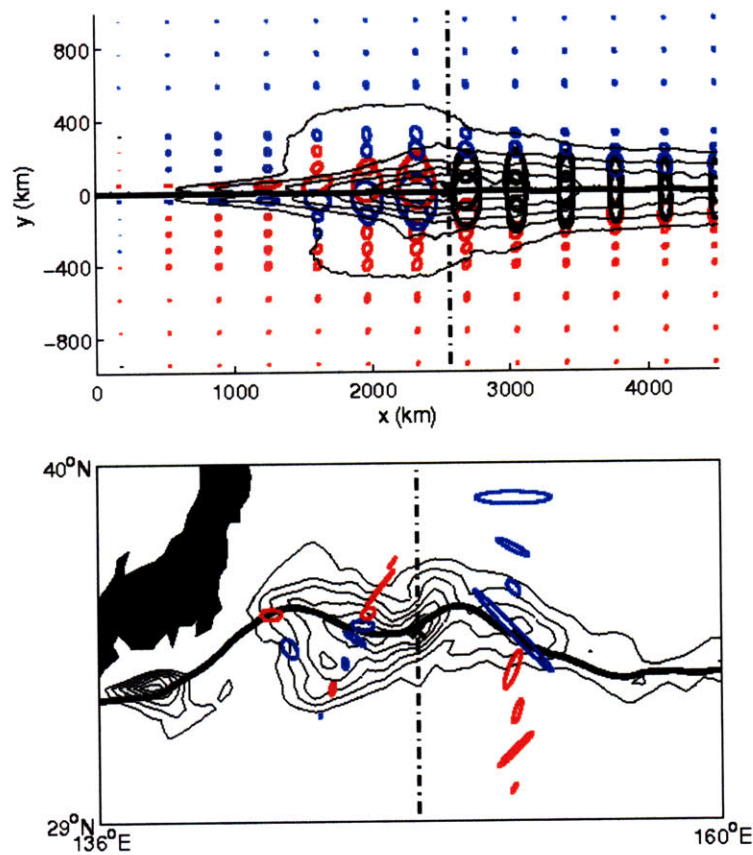
Figure 4-32: A comparison of the time-mean covariance ellipses (a visualization of the time-mean Reynolds stresses $\overline{u'u'}$, $\overline{v'v'}$ and $\overline{u'v'}$) for the layer-averaged fields in the two-layer model run in a KE-like regime (*top*) vs. those for the KE jet as derived from the depth-averaged mooring observations (*bottom*). Their location is referenced to the downstream development of the jet by the time-mean EKE distribution (derived from the upper layer in the case of the model and the 14-year altimetry record in the case of the KE jet), which is shown by the black contours. The location of the EKE maximum is indicated by the **x**, and the vertical dashed line indicates the downstream location corresponding to this maximum. Ellipses are colored red if their tilt is greater than zero (an indication of $\overline{u'v'} > 0$), blue if their tilt is less than zero (an indication of $\overline{u'v'} < 0$), and black if the tilt is not significantly different from zero (an indication of $\overline{u'v'} \sim 0$). The observed velocities were band-passed filtered in the mesoscale range (periods of 10 - 100 days) before the variances and covariances were computed to clarify the cross-jet variations.

of the SSH information, and the spatial resolution of the objectively mapped SSH fields with an approximate cutoff of length scales less than 300 km means that higher-order derivatives will be very reduced in magnitude. Despite this, investigations into the extent to which horizontal momentum fluxes can be reproduced by altimetry measurements do suggest that although the stresses are underestimated, they do show the correct general tendencies (Leeuwenburgh and Stammer, 2002), and hence such an investigation can be instructive. By computing the eddy forcing terms using the altimetry fields and comparing them to model results, I find several similarities in these quantities. An example is given in Figure 4-33, in which I compare the "effective eddy force" (the negative of the divergence of the eddy flux of zonal momentum) for a barotropic model run to that derived from the altimetry fields. There is a clear suggestion in the latter of a switch in sign of the eddy forcing across the maximum in recirculation strength, consistent with the idealized model.

4.5   Summary and Discussion

Motivated by the KESS observational program I have sought to improve our understanding of the nature and the importance of eddy-mean flow interactions in the Kuroshio Extension. I first characterized the state of the mean KE jet and its recirculation gyres, its eddy variability, and the nature of their interactions within the KESS time frame at the KESS location. I next evaluated the relevance of the idealized WBC jet model to the KE system both in terms of the model design and its findings.

My study has revealed a picture of the time-mean jet-gyre system over the KESS period. In the geographical frame, this is of a strong, surface-intensified jet oriented to the southeast with little variation with depth below the thermocline. Westward recirculations flanking the time-mean jet to both the north and the south are found to be a significant feature of the time-mean deep jet structure, but there exists no clear evidence of westward recirculations in the upper ocean. In the stream-coordinate view, as expected, the mean jet appears stronger and sharper. Its baroclinic structure
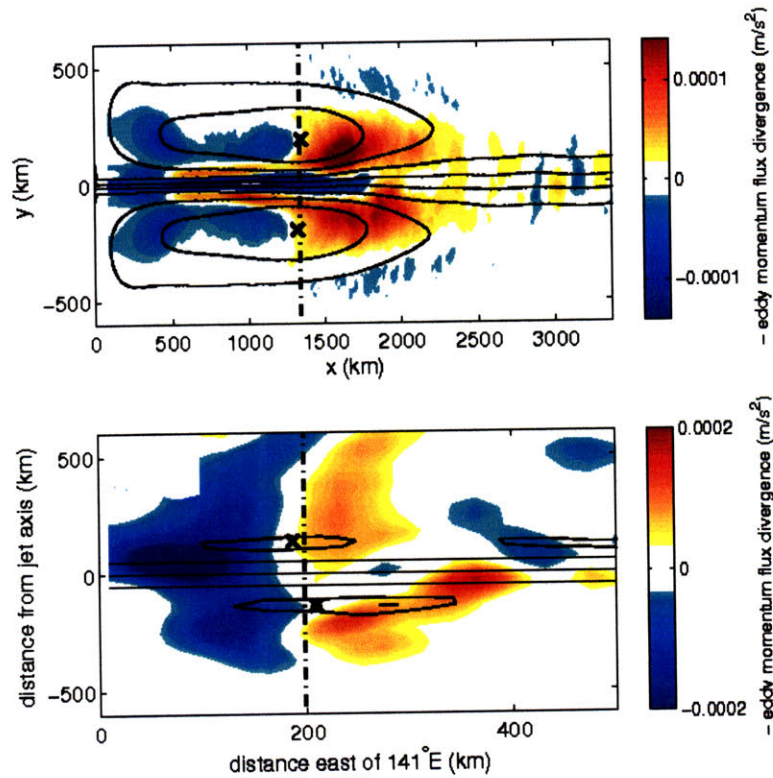
Figure 4-33: A comparison of the "effective eddy-force" (the negative of the diver-
gence of the eddy flux of zonal momentum) for a barotropic model run in a KE-like
parameter regime (*top*) *vs.* that derived from the 14-year altimetry record (*bottom*).
Color indicates the effective eddy force and black contours indicate properties of the
time-mean jet-gyre system for reference, with **x**s denoting the location of maximum
recirculation transport/velocity and the vertical dashed line indicating the down-
stream location corresponding to this maximum. In the case of the altimetry field
calculation, the eddy flux divergence was computed in geographical coordinates then
projected into the distance coordinates shown, while the contours of the time-mean
jet/gyre system are from the stream-coordinate calculation of the time-mean down-
stream velocity.

at depth is also more pronounced. This makes it much more strongly sheared in both the horizontal and the vertical than is suggested by the geographical mean picture. It also makes the existence of weakly depth-dependent recirculations that extend throughout the water column apparent to both the north and south of the time-mean jet. This observation in combination with evidence of these recirculations seen in other forms of the KESS measurements, are the first clear observational evidence of a northern recirculation gyre in the KE.

I have characterized properties of the temporal eddy variability by describing it and its effect on jet structure grouped according to some of its various sources: meandering, rings, waves and instability. In summary, first I find that, at the KESS location, the jet exhibits vigorous meandering with a range of $\pm$ 300 km from its time-mean position. One of the dominant meandering timescales is consistent with a linear stability calculation prediction, while the source of lower frequency variability is open to speculation. Meandering has a significant effect on the time-mean jet structure and its variability, resulting in a weakening and broadening of the upper layer jet, and eliminating the upper ocean recirculations from the time-mean jet structure. It accounts for a significant fraction of the EKE (approximately 50% in the deep ocean), and smears out fine structure in its cross-jet profile, eliminating a sharp maximum in EKE at the jet axis and minima inside the recirculations that are seen when the effects of meandering are removed. Second, the interaction of both warm and cold core rings also are a significant feature of the eddy variability at this location, with rings interacting with the KESS array approximately 25% of the time. Rings tend to be more frequent in winter, and although they pass to both the north and south of the jet, are more frequent to the south. Interestingly, although rings contribute significantly to the variance structure on the flanks of the jet, they do not have a significant direct effect on the mean jet structure there. Importantly, time-mean recirculations remain a feature of the time-mean jet structure whether or not ring interactions are included. Third, there are indications of waves in the KESS velocity records in the form of low frequency peaks in the velocity spectra and indications of propagating signals in Hovmöller diagrams. The observed wavenumber

associated with the 40-day period signal is consistent with the barotropic Rossby wave dispersion relation. The source of this wave activity (*i.e.* whether radiated from the jet or generated remotely) remains an open question. Finally, there are also indications of jet instability. Both spectra of velocity records and the jet meandering show enhanced energy at timescales consistent with linear stability calculations, and both synoptic mean and instantaneous snapshots of horizontal and vertical shears observed indicate that shears can far exceed the critical values for both barotropic and baroclinic instability based on idealized Rayleigh and Phillips model criteria, and the critical value for instability based on the meridional gradients of approximations to the layered PV gradients.

My study of eddy-mean flow interactions was limited, but there are some indications of the nature of these interactions that are worthy of mention. First, the time-mean cross jet distribution of the covariance $\overline{u'v'}$ observed is in the sense for eddies to drive the time-mean recirculations. This is consistent with the scenario of energy radiation from a localized source (a "wave-radiator") and the regime seen in the idealized WBC jet model downstream of mean jet stabilization (the "wave-radiator regime"). Hence the observations provide support for the hypothesis that the recirculations are, at least partially, eddy-driven. Second, although the comparison of the observed Reynolds stresses with those of idealized models of potential eddy-mean flow interaction scenarios relevant to the KE jet do not offer conclusive results, they are suggestive of an unstable jet in the upper ocean and wave radiation in the deep ocean.

The second goal of the study was to evaluate the relevance of the idealized WBC jet model of Chapter 3 to the oceanic system by considering both its set-up and its predictions relative to observations of the KE. I argued that the KE observations suggest that aspects of the idealized model design are appropriate to the KE system: a simple vertical velocity structure observed in KESS suggests a dynamical model with simplified vertical structure may suffice, indications in the KESS records of a high degree of nonlinearity suggest that a fully nonlinear dynamical model is essential, and

the horizontal and vertical shears upstream where the KE jet approximately separates from the coast suggest that a jet subject to mixed instability is a realistic forcing for the idealized study.

Further, consistencies between model predictions and observational results, in particular in the downstream development of mean and eddy properties, provide additional support for the claim of the model's potential relevance to the KE jet. Both *in situ* mooring observations and the satellite altimetry record in the KE region show important similarities in the downstream development of the mean jet-gyre system to that in the idealized model, such as a strengthening and sharpening of the jet and the development of westward recirculations up to the downstream location of maximum EKE, followed by a weakening of the jet and the recirculation strength past this downstream location. There are similarities in the downstream development of eddy properties as well, in particular in the signatures of the eddy effect on the mean. Mooring observations of Reynolds stresses suggest of a transition from an unstable jet regime upstream of the EKE maximum to a wave-radiator regime downstream of the EKE maximum, as found in the idealized WBC model. In addition, there is a suggestion of a similar transition from a westward to eastward eddy force across the maximum in recirculation strength both in the model and in the mean altimetry fields.

Taken all together, these indications and consistencies give some confidence in the idealized model's potential ability to capture the essential physics of the KE jet system. As a consequence, I hope that the understanding gained from the theoretical study is useful in teaching us about the importance of eddy-mean flow interactions in the KE and potentially other WBC jet systems as well.

The work presented here is just the beginning of an observational look at eddy-mean flow interactions with the KESS data, in the KE jet and in WBC jets in general, and there is lots more to be done. There are also several new and interesting open questions that are suggested by this initial look at the KESS data which could lead to interesting avenues to pursue in the future.

First, the various topics addressed in this study would benefit from further, more detailed analysis. The study here offers evidence of a northern recirculation gyre and the suggestion that eddies may play a role in driving it, but the dynamics are still uncertain. Hence eddy-mean flow interactions in the KESS data should be quantified. Progress can be made by incorporating other forms of the KESS data (for example the MMP and CPIES measurements) and applying the methods of Bryden (1979) and Phillips and Rintoul (2000) to the point-wise MMP measurements and the methods of Cronin (1996) and Bower and Hogg (1996) to the two-dimensional data. This will allow the diagnosis of the eddy-mean energy and PV budgets, and the characterization of the cases of up-gradient and down-gradient fluxes. The use of high resolution global circulation model output here would be useful as well, providing a larger temporal and spatial window into the KE and permitting statistical studies of the energy and PV fluxes. This at the same time would have the additional benefit of providing an excellent opportunity for the development of process-based metrics for ocean model fidelity. Interesting questions that could be addressed include the relative importance of relative vorticity *vs.* thickness fluxes in the eddy forcing, and the role of episodic events in the context of the time-averaged observed fluxes.

In addition to furthering work on the questions addressed in this study, there are also new interesting questions that have arisen from this look into the KESS data. I elaborate on two of particular interest.

The first concerns the role of external features and influences in the jet-gyre system. Some of the largest waves, meanders and ring formations in the KESS record appear to have been triggered by external features: deep synoptic eddies, warm and cold core rings, and other possibly wind-driven eddies arriving from the east. Analogous to the jet stream, this observation contributes to the debate about whether a given synoptic disturbance grows locally from infinitesimal perturbations, or rather grows from the interaction with a pre-existing smaller amplitude feature. The relative fraction of mesoscale features that develop locally *vs.* those that grow from external pre-existing disturbances could be quantified in the KESS record. The source of many

214

of these external features is also an open question that could be investigated.

The second topic that has arisen to be of particular interest during this study relates to the bimodal variability of the KE jet, and the causes and mechanisms of its regime shifts. The KE jet is observed to exhibit a bimodality in its low frequency behavior, oscillating between a quasi-steady state consisting of quasi-stationary meanders, and a highly variable state consisting of energetic meanders (the "stable" and "unstable" states respectively) (Qui and Chen, 2005). Fortuitously, the KESS field program captured a regime transition in late 2004, with the most recent weakly meandering pattern, which had begun in 2001, switching to the strongly meandering state[5]. Accompanying the shift in the state of the surface jet, was also a dramatic change in the state of the subsurface time-mean jet and its eddy variability observed by the KESS array. For example, relative to the weakly meandering state, the strongly meandering state's time-mean jet became much weaker, especially in the upper ocean, and the recirculations became less prominent (Figure 4-34 *left*). Note that these changes in the mean jet structure are observed in the stream-coordinate frame, that is with the smearing out effects of jet meandering removed, so this represents a real change in jet strength. As a consequence, both the horizontal and vertical shear in the strongly meandering period was much reduced relative to the weakly meandering state *i.e.* paradoxically the weakly meandering state jet looks much more unstable than the strongly meandering state based on the magnitudes of the velocity shears. Associated with the transition from the weakly meandering to strongly meandering state is also a dramatic increase in eddy energy, both in the upper ocean and also in the deep subthermocline ocean (Figure 4-34 *right*). One hypothesis for the cause of the change in the dynamic state of the KE jet is that it arises from a change in the PV structure of the jet-gyre system (Spall, 1996). This can be tested with the KESS data by examining the time-evolution of the PV structure and its favorability for different instability modes in the different dynamical states during the KESS pe-

---

[5]I prefer the labels "weakly meandering" and "strongly meandering" as opposed to "stable" and "unstable" as they do not make statements about the jet's hydrodynamic stability properties. As will be discussed, the two states of the KE jet are distinguished by changes in the meandering intensity of the jet, not necessarily the magnitudes of the jet shear and hence its hydrodynamic stability properties.
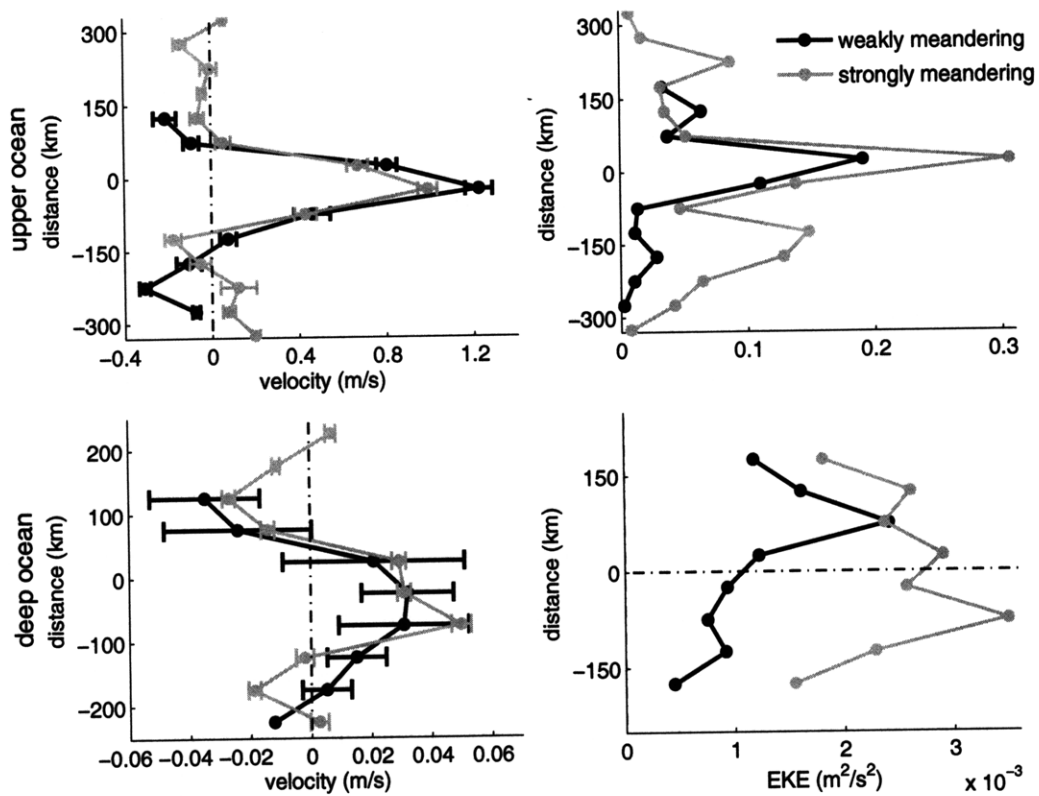
Figure 4-34: A comparison of the time-mean jet structure (*left*) and EKE distribution (*right*) computed over the time period in the KESS record during which the KE jet was in its weakly meandering state (15 June 2004 through 1 December 2004) (*black*) *vs.* that when the KE jet was in its strongly meandering state (1 December 2004 - 19 May 2006) (*gray*). The upper ocean (average of surface and 250 m depths) is shown in the upper panels and the abyssal ocean (average of 1500 m, 2000 m, 3500 m and 5000 m depths) is shown in the lower panels. Error bars on the mean velocity indicate the standard error in the mean.

riod. Insight into the question about whether changes leading to the rapid transition arise from processes generated locally or enter either from upstream or downstream can also potentially be gained from the KESS record. Comparing and contrasting the jet's structure, its eddy properties, and their interactions in the two states may provide new insight into how the transition occurs, and what its implications are for the stability of the jet and the strength and extent of the recirculations. This may potentially resolve the paradox of the highly sheared jet showing low eddy variability and vice versa.

Finally, it seems incomplete to fail to include a discussion about the GS, the KE's

much more extensively studied cousin. Eddy-mean flow interactions that drive the recirculation gyres in the GS are likely the same in the KE, however there are interesting differences that, by understanding their influences, could lead to an improved understanding of eddy-mean flow interactions in WBC jet systems generally. For instance, the presence of semi-permanent meanders in the KE jet in the upstream region (which make the "basic-state jet" distinctly non-zonal) complicates the dynamical picture in the KE relative to the GS. Distinct stratification, bathymetry, modes of variability, thermohaline circulation, and region geometry also make the KE different. Understanding similarities and differences in eddy-mean flow interactions in the GS *vs.* the KE, and even better linking differences to known differences in these influences, promises an improved understanding of the physical mechanisms involved. Past studies of the GS with a particular emphasis on eddy-mean flow interactions that would serve well as a basis for comparison with the results presented here include Dewar and Bane (1989), Hogg (1993, 1994), Shay et al. (1995), Bower and Hogg (1996), Cronin (1996), and Cronin and Watts (1996). It is a fortuitous time to pursue such a study, as KESS data plus that of SYNOP and now the CLIvar MOde Water Dynamic Experiment (CLIMODE) offer more complete views of these systems than ever before.

Chapter 5

Conclusions

Motivated by a new observational data set in the Kuroshio Extension (KE) uniquely suited to study the jet, its eddy variability and their interactions, this thesis has examined the nature and the importance of eddy mean-flow interactions in western boundary current (WBC) jets and recirculation gyre dynamics from both theoretical and observational perspectives. This has included a study of eddy mean-flow interactions in idealized configurations relevant to WBC jet systems, an observational analysis to characterize eddy-mean flow interactions in the KE jet, and an evaluation of the relevance of the theoretical understanding derived from the idealized studies to the dynamics of the actual oceanic system.

5.1   Contributions

The work has resulted in several new contributions to our understanding of the role of eddies in the dynamics of WBC jet and recirculation gyre systems, both idealized and actual.

The theoretical study of eddy-forced recirculation gyres from the rectification of a localized, transient forcing (Chapter 2) has extended our understanding of a mechanism by which eddies may drive the recirculation gyres observed in WBC jet systems. The major contributions include:

1. new insights into the rectification mechanism, in particular an understanding that the recirculation gyres are driven by an up-gradient eddy flux of potential vorticity inside the forcing region, and that the effectiveness of the process depends on the properties of the energy radiation from the forcing, which in turn depends on the population of waves excited.

2. a new understanding of the effects of stratification, a background flow, and strong nonlinearity on the mechanism, all critical features in the WBC jet-gyre application.

3. a demonstration of the mechanism in the laboratory in a rotating tank experiment (see Appendix B).

Overall, the study suggests that in a relevant parameter regime, this mechanism is capable of driving mean recirculation velocities on the order of a few to tens of centimeters per second. This is consistent with the magnitude of the deep recirculation velocities observed during KESS and in the past both in the KE and Gulf Stream (GS), making it plausible that this mechanism has relevance to the forcing of the deep recirculation gyres observed in WBC jet systems.

The theoretical study of eddy-mean flow interactions in the downstream evolution of an idealized model of a WBC jet (Chapter 3) has extended our understanding of the role of eddies in an idealized WBC jet configuration in which eddy effects and inertial effects can both play a role. Although eddy-mean flow interactions in unstable jets has been an extensively studied topic, a configuration which combines highly-variable time-dependent and highly inertial dynamics, baroclinicity, and zonal evolution, as is relevant to WBC jet systems, has thus far remained relatively unexplored. The major contributions include, all applicable to the idealized model of a WBC jet in a parameter regime appropriate to the GS and KE:

1. the identification that nonlinear eddy fluxes play two distinct and critical roles in the downstream development of the time-mean jet: first stabilizing the jet to its large-scale horizontal and/or vertical shear through a diffusive-like, down-

gradient potential vorticity flux, and second driving the time-mean recirculations through an anti-diffusive, up-gradient potential vorticity flux dynamically similar to the mechanism by which eddies drive the recirculation gyres studied in Chapter 2.

2. the understanding that zonal variation is important. In particular, the role of eddies depends critically on the downstream location relative to the position where the unstable time-mean jet first becomes stable, and the zonal advection of eddy activity is fundamental to the mechanism permitting eddies to drive the mean flows.

3. the new result that the addition of baroclinicity does not significantly alter the barotropic mechanism responsible for driving the recirculations.

4. an empirical prediction for the properties of the eddy-driven time-mean circulation (the strength and extent of the time-mean recirculations) given the stability properties of the upstream jet that was the source of the eddy variability.

Overall, these results support the hypothesis that the observed recirculations in the KE and GS are, at least partially, eddy-driven, and provide insight into what may determine the properties of the observed mean jet and its recirculations as they evolve downstream.

Finally, the observational analysis of the new KESS observations as well as past observations and satellite data in the KE region, has furthered our understanding of the nature and importance of eddy-mean flow interactions in the KE. This has been achieved both by characterizing the state of the mean jet, its eddy variability, and the nature of their interactions at the KESS location during the KESS time frame, and also by evaluating the relevance of the idealized WBC jet model to the KE system both in terms of the model design and its findings. This has resulted in:

1. the first clear evidence of a northern recirculation gyre in the KE, as well as support for the hypothesis that the recirculations are, at least partially, eddy-driven.

2. observational indications that the KE jet is potentially barotropically and baro-clinically unstable at the location observed, making jet instability a likely source of at least some of the eddy variability of the system.

3. support for the idealized model's potential success in capturing aspects of the essential physics of the KE jet system. This comes both from observational indications that the idealized model's simplified vertical structure, source of eddy variability (the mixed instability of the inflowing jet), and nonlinear dynamics are appropriate to the observed system, as well as from demonstrated consistencies between model predictions and observational results in the downstream development of both time-mean and eddy properties.

Overall, the work provides us with a new characterization of the KE jet, its variability, and their interactions at the downstream location of maximum eddy kinetic energy, as well as some confidence in the theoretical model's usefulness in teaching us the importance of eddy-mean flow interactions in the KE and potentially WBC jets in general.

5.2 Implications

The results of this work have important implications both for our understanding of large-scale ocean dynamics and for ocean modeling.

First, the results presented here contribute to an improved understanding of WBC jet dynamics. The theoretical study of the idealized WBC jet that has demonstrated relevance to the observed system has shown that eddy forcing and steady-state inertial terms are of roughly equal importance in the downstream development of the time-mean jet-gyre system. Hence including eddies in our working understanding of WBC jet dynamics, our realistic modeling of these systems, and in the design of our observational monitoring strategies of WBC jet systems is of first-order importance. This study has also suggested that properties of WBC jet recirculations, which can fundamentally alter the dynamical structure of the jet and add significantly to its net

transport, are, at least partially, linked the stability properties of the upstream jet that was the source of the eddy variability. This is useful if, for example, we wanted to understand changes we would expect to see in WBC jet transport or structure if oceanic conditions changed in such a way as to alter the stability properties of the upstream jet. Given that WBCs are one of the foremost components in global heat transport and thus in regulating the global climate, predicting changes in WBC jet transport has potentially very important climatic implications.

This work also has potentially important implications for ocean modeling. Understanding the role of eddies in WBC jets allows us to understand the importance of having various eddy processes resolved in our numerical simulations of these systems. The results presented here suggest that failure to resolve the eddies responsible for the effects discussed here will result in reduced mean WBC jet transports, with the abyssal ocean recirculations (and their significant enhancement to jet transport) missing altogether. Indeed, all eddy-driven mean flows produced by the nonlinear rectification mechanism explored here would not be represented in general circulation models with eddy effects parameterized simply as down-gradient diffusion. In addition however to indicating the importance of resolving eddies in our ocean models, this work may also suggest suitable, *process-based* parameterizations for these eddy effects in cases when resolving the eddies responsible for them explicitly is impossible. As discussed in Chapter 3, progress can potentially be made by exploiting the new understanding that eddy-mean flow interactions in these systems depends critically on the zonal variation that results from the advection of eddy activity from a region of eddy growth (where eddies provide down-gradient tracer fluxes) to a region of eddy decay (where they provide up-gradient tracer fluxes). Hence an appreciation of the eddy life-cycle can potentially help organize our understanding of the effect of eddies on the background state in WBC jets, and potentially assist in our development of realistic parameterization schemes.

5.3 Future Work

There are many more things to be done on this subject and I have several proposals for future research, some of which I hope to have the future opportunity to pursue.

Immediately, there is an opportunity to further the analysis of the KESS observations on this subject. The study here offers evidence of a northern recirculation gyre and the suggestion that eddies may play a role in driving it, but the dynamics are still uncertain. Hence the eddy-mean flow interactions in the KESS data need to be quantified. As discussed in Chapter 4, progress can be made by incorporating other forms of the KESS data (for example the MMP and CPIES measurements) and applying the methods of Bryden (1979) and Phillips and Rintoul (2000) to the point-wise MMP measurements and the methods of Cronin (1996) and Bower and Hogg (1996) to the two-dimensional data. This will allow the diagnosis of the eddy-mean energy and PV budgets, and the characterization of the cases of up-gradient and down-gradient fluxes. Interesting questions that could be addressed include the relative importance of relative vorticity *vs.* thickness fluxes in the eddy forcing, and the role of episodic events in the context of the time-averaged observed fluxes. As also discussed in Chapter 4, investigation into the role of external features and influences in the jet-gyre system, as well as the causes and mechanisms of the KE regime shift and its implications for the stability of the jet and the strength and extent of the recirculations, have both emerged from this initial look at the KESS data as additional interesting avenues to pursue.

Second, there are several opportunities to extend the theoretical studies, in particular that on the idealized WBC jet. For example, there are several interesting open questions with implications for PV dynamics and cross-frontal exchange that could potentially benefit from a Lagrangian analysis of the dynamics at play in the model. In addition, the construction of a stream-coordinate description of the idealized model jet is needed to compare with the stream-coordinate description of the KE jet that has proved so insightful in the analysis of the observations. The effect of varying friction on the time-mean recirculation properties also should be explored. In

addition however to further analysis of the theoretical model in its current configuration, progress can also be made by adding additional physics. The model is idealized in many respects. It is quasi-geostrophic, has highly simplified vertical structure, and the source of its eddy variability is restricted to the intrinsic variability of the unstable jet. This is of course by design, the aim was to isolate aspects of the physics that were of interest, and make the system otherwise as simple as possible to elucidate understanding of the essential dynamics and mechanisms. The next step is to add back various aspects of the physics, and understand their effects on the dynamics. Of particular interest is the effect of jet tilt on the mechanisms I have explored. This is relevant given the non-zonal nature of the KE jet as a consequence of the quasi-stationary meander and the non-zonal orientation of the GS path, and it is of interest given the significant effect a non-zonal tilt of the basic state jet can have on the jet's stability and radiating properties (Kamenkovich and Pedlosky, 1996). Of interest also is the effect of a time-dependent inflow, given the newly emerging paradigm of a fundamentally non-steady overturning circulation (S. Lozier, personal communication)[1]. Of course, the standard additions of primitive equation dynamics, continuous stratification, topography (in particular the influence of the Shatsky Rise in the KE), wind forcing, and atmospheric coupling all will provide valuable insight into how the eddy-mean flow interactions discussed in this work are affected by these additional influences.

Third, I believe much progress can be made on this topic via a similarly aimed study using not idealized theoretical models or observations, but instead the relatively new tool of "realistic" eddy-resolving general circulation model (EGCM) output. The relative maturation in recent years of now global, high-resolution, primitive equation numerical models which attempt to simulate the ocean circulation with a high degree of realism (with respect to geometry, topography, physics and forcing) have resulted in EGCMs with greatly improved realism in eddy processes, eddy kinetic energy level *etc.* This has created a new tool for the examination and interpretation of ocean dynamics (Stammer et al., 1996; Smith et al., 2000; McClean et al., 2002;

---

[1]See the US CLIVAR Atlantic Meridional Overturning Circulation Implementation Plan 2007.

Maltrud and McClean, 2005). EGCM studies have the potential of being especially fruitful in the investigation of eddy-mean flow interactions as they relate to realistic oceanic flows because model output can achieve sufficiently high resolution in space and time over a sufficiently long period and large area to address questions that have been difficult to examine with sparse observational data in the past. Work could build upon the EGCM analysis by Nakamura and Chao (2001, 2002) with a focus on evaluating the relevance of the mechanisms elucidated by the idealized theoretical studies presented here, conducting the EGCM analysis in concert with the analysis of direct observations, and comparing and contrasting the GS and KE systems. The EGCM study would also be a useful opportunity to evaluate the effectiveness of the idealized two-layer jet model in capturing the essential physics of the system, as well as to develop process-based metrics for ocean model fidelity. Initial work in this direction using the output of a $1/10°$, 40-level global simulation of the Parallel Ocean Program (POP) model (McClean et al., 2002; Maltrud and McClean, 2005) in the KE region suggest that this high resolution POP model can give insight into the mechanisms driving the recirculations. Figure 5-1 shows the presence of time-mean westward zonal recirculations to both the north and south of the time-mean jet at all depths in the model fields. It is expected that the processes responsible for the generation and maintenance of these features can be diagnosed by a detailed analysis of the other model variables.

Finally, I believe our understanding of eddy-mean flow interactions in WBC jets in general can be furthered by a comparison of the GS and KE systems. Relative to the KE, the GS has been extensively studied. The KESS data provides a new opportunity to compare and contrast these systems in a way that has not been possible in the past. Past studies of the GS with a particular emphasis on eddy-mean flow interactions that would serve well as a basis for comparison with the results presented here include Dewar and Bane (1989), Hogg (1993, 1994), Shay et al. (1995), Bower and Hogg (1996), Cronin and Watts (1996) and Cronin (1996). SYNOP and now the CLIvar MOde Water Dynamic Experiment (CLIMODE) data in the GS would also be a useful resource for a comparative study with KESS results. Eddy-mean flow
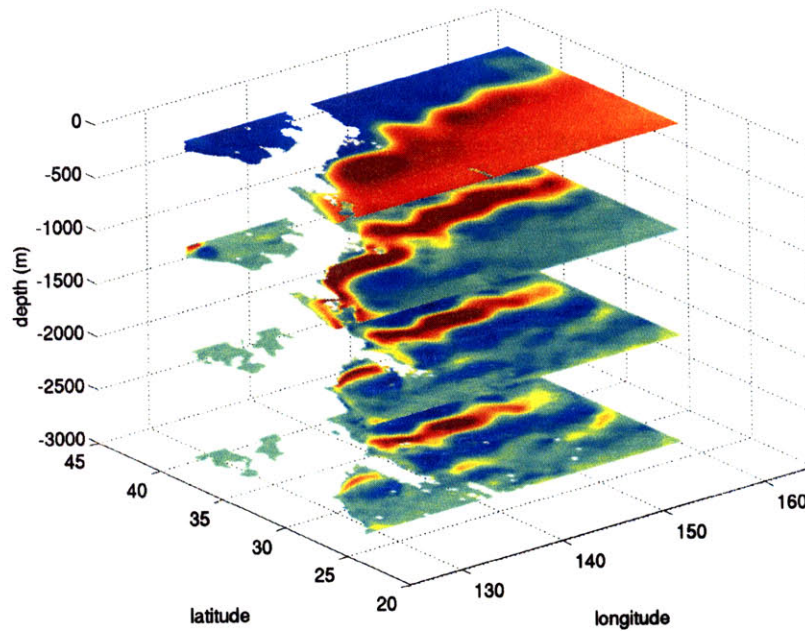
Figure 5-1: The three-year time-mean circulation (1998-2001) in the Kuroshio region from the Parallel Ocean Program (POP) EGCM model. Contours of time-mean sea surface height (*surface*) and zonal velocity (*subsurface levels*) are shown with varying color scales. For zonal velocity, red colors are positive (eastward) values and blue colors are negative (westward) values. Time-mean westward recirculations are observed flanking the jet to the north and south at all levels.

interactions that drive the recirculation gyres in the GS are likely the same in the KE, however there are interesting differences that, by understanding their influences, could lead to an improved understanding of eddy-mean flow interactions in WBC jet systems generally. For instance, the presence of semi-permanent meanders in the KE jet in the upstream region (which make the "basic-state jet" distinctly non-zonal) complicates the dynamical picture in the KE relative to the GS. Distinct stratification, bathymetry, modes of variability, thermohaline circulation, and region geometry also make the KE different. Understanding similarities and differences in eddy-mean flow interactions in the GS *vs.* the KE, and even better linking differences to known differences in these influences, promises an improved understanding of the physical mechanisms involved.

Appendix A

Analytical Analysis for the Rectification Problem

As discussed in Section 2.2.1, to gain insight into the rectification mechanism and the relation between forcing parameters and rectified flow I appeal to an analytical solution. For this purpose, like HR83, I simplify the forcing function by reducing its spatial dependence to a delta function in space (*i.e.* I seek the Green's function solution). With this simplification, the full equation I want to solve is:

$$\frac{\partial \nabla^2 \psi}{\partial t} + J(\psi, \nabla^2 \psi) + \beta \frac{\partial \psi}{\partial x} = \delta(\mathbf{x})e^{i\omega t} \tag{A.1}$$

Equation A.1 cannot however be solved in closed form because of the nonlinear self advection $J(\psi, \nabla^2 \psi)$.

Assuming the forcing amplitude is small, one can make progress by expanding the solution in powers of forcing amplitude. Hence I consider:

$$\frac{\partial \nabla^2 \psi}{\partial t} + J(\psi, \nabla^2 \psi) + \beta \frac{\partial \psi}{\partial x} = \epsilon \delta(\mathbf{x})e^{i\omega t} \tag{A.2}$$

and take ψ to have the form:

$$\psi = \epsilon \psi_1 + \epsilon^2 \psi_2 + ... \tag{A.3}$$

Substituting A.3 into A.2 and equating terms of the same order of ϵ then yields:

$$Order\ \epsilon : \frac{\partial \nabla^2 \psi_1}{\partial t} + \beta \frac{\partial \psi_1}{\partial x} = \delta(\mathbf{x}) e^{i\omega t} \tag{A.4}$$

$$Order\ \epsilon^2 : \frac{\partial \nabla^2 \psi_2}{\partial t} + J(\psi_1, \nabla^2 \psi_1) + \beta \frac{\partial \psi_2}{\partial x} = 0 \tag{A.5}$$

The order ϵ equation is a linear equation whose solution is (HR83):

$$\psi_1(x, y, t) = H_o^{(2)}(Br) e^{-i(Bx + \omega t) - \frac{1}{4}\pi} \tag{A.6}$$

where $H_o^{(2)}$ is the Hankel Function of the second kind and B is the radius of the Rossby wave dispersion relation circle $B = \frac{\beta}{2\omega}$. The time-mean flow associated with the order ϵ linear forced wave field is zero.

The first contribution to the time-mean flow enters at order ϵ^2. Taking the time-mean of Equation A.5 yields:

$$\overline{J(\psi_1, \nabla^2 \psi_1)} + \beta \frac{\partial \overline{\psi_2}}{\partial x} = 0 \tag{A.7}$$

Re-arranging to solve for $\overline{\psi_2}$, the time-mean streamfunction associated with the rectified flow, then gives:

$$\overline{\psi_2} = \frac{1}{\beta} \int_x^{x_E} \overline{J(\psi_1, \nabla^2 \psi_1)}\, dx \tag{A.8}$$

Hence one arrives at the result that the second-order time-mean flow is given by the zonal integral (to the eastern boundary, x_E) of the time-mean Jacobian (relative vorticity flux divergence) of the first order, linear forced wave field. For a delta function forcing however, $\overline{\psi_2}$ outside the immediate vicinity of the forcing is found to be zero due to the anti-symmetric pattern of the relative vorticity flux divergence.

To introduce spatial dependence to the forcing function I use the Green's function solution for ψ_1 given by Equation A.6 and compute the particular solution for a given spatial forcing dependence $F(\mathbf{x})$ by evaluating the convolution integral:

$$\psi_{1P} = \int_x^{x_E} \psi_1(\mathbf{x}, \mathbf{x}') \mathbf{F}(\mathbf{x}')\, d\mathbf{x}' \tag{A.9}$$

For the forcing function $F(\mathbf{x})$ I consider a normalized Gaussian forcing function of the form

$$F(x,y) = A \left(\frac{2 - 4\left(\frac{x}{L}\right)^2}{L^2} + \frac{2 - 4\left(\frac{x}{L}\right)^2}{L^2} \right) e^{-\left(\frac{x}{L}\right)^2 - \left(\frac{y}{L}\right)^2} \tag{A.10}$$

and compute the particular solution via numerical integration. As before, to compute the time-mean rectified flow associated with this wave field, I compute the zonal integral of the time-mean Jacobian using the particular solution ψ_{1P} in place of ψ_1.

I test the validity of the analytical approximations by comparing them to the output of the fully nonlinear numerical calculations in the limit of small forcing amplitude (Figure A-1). Here it can be seen that the Green's function solution for the order ϵ linear forced wave field (Equation A.6) captures the form of the wave field in the weakly nonlinear solution (Figure A-1 (*top*)). I also verify that the order ϵ^2 time-mean flow obtained from the integration of the time-mean Jacobian of the particular solution for a normalized Gaussian forcing function $\left(\overline{\psi}_{2P} = \frac{1}{\beta} \int_x^{x_E} \overline{J(\psi_{1P}, \nabla^2 \psi_{1P})} \, dx \right)$ also describes the gross characteristics of the mean rectified flow of the nonlinear calculation (Figure A-1 (*bottom*)). These correspondences give confidence in the utility of these analytical forms in understanding the nonlinear rectification in the weakly nonlinear limit.
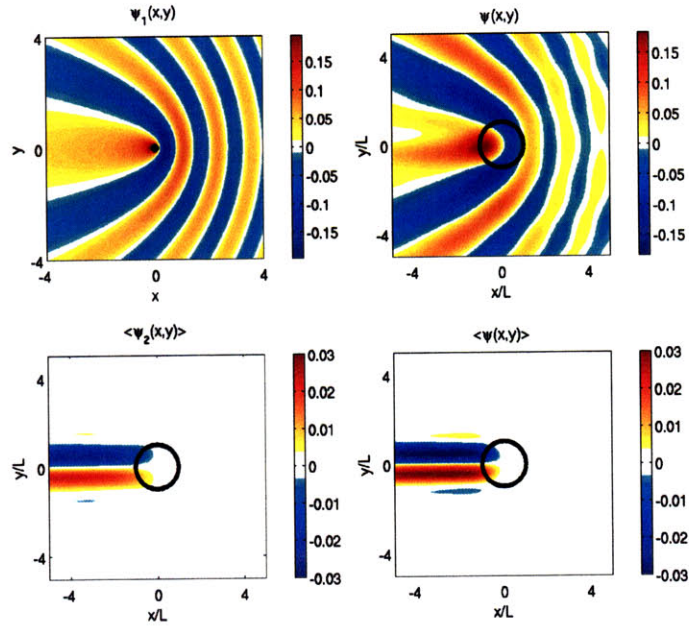
Figure A-1: A comparison of the analytical expressions derived in Appendix A (*right*) with the corresponding output from the fully nonlinear model forced by a small-amplitude forcing (*left*). The instantaneous wave fields (with the analytical solution given by the Green's function solution (Equation A.6)) is shown in the upper row. The time-mean rectified flow (with the analytical prediction given by the zonal integral of the time-mean advection of relative vorticity (time-mean Jacobian) of the linear forced wave field given by the particular solution for a Gaussian forcing function (Equation A.9)) is shown in the lower row.

Appendix B

Rectification Laboratory Study

As a supplement to the study, I test whether the localized oscillatory Ekman pumping in a closed basin that I consider numerically produces the same steady-state circulation pattern and dependence on forcing amplitude in a real fluid in the laboratory.

The experimental set-up, diagrammed in Figure B-1, consists of a rapidly rotating, homogeneous fluid in a square basin with a variable topographic beta effect. The fluid was forced by a small source of vertical velocity mid-basin at the lower boundary with variable amplitude and which alternated sign at variable frequency. Forcing amplitudes equivalent to an Ekman pumping velocity in the range of 1×10^{-5} m/s $<$ $w_{Ek} < 5\times10^{-5}$ m/s (or equivalently a wind stress of $0.05 < \tau < 0.2$ N/ms^2) and forcing periods in the range of 25 days $< T_{forcing} < 250$ days (assuming a forcing length scale of 50 km) were considered.

The first important result is the demonstration that the steady-state response of the fluid to this forcing is indeed a circulation consisting of a zonal jet at the latitude of the forcing flanked by a pair of counter-rotating recirculation gyres (Figure B-2). Hence the qualitative nature of the rectified flow in the numerical simulations is consistent with that observed in the laboratory.

The second result of note is the observation of a similar qualitative change in behavior in the mean-flow response beyond a critical forcing amplitude. In a series of laboratory experiments that varied the magnitude of the forcing, the jet velocity was observed to increase sharply with forcing amplitude for weak Ekman velocities
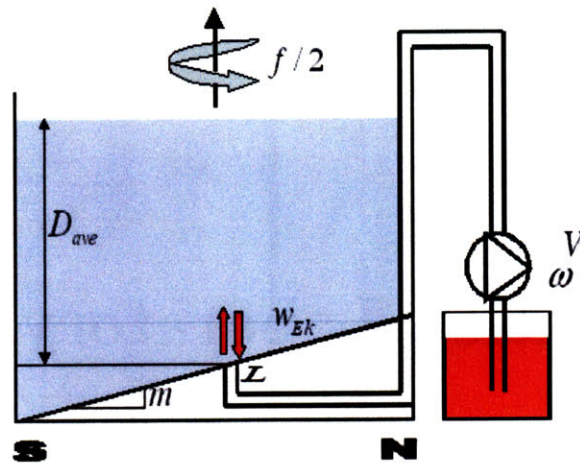
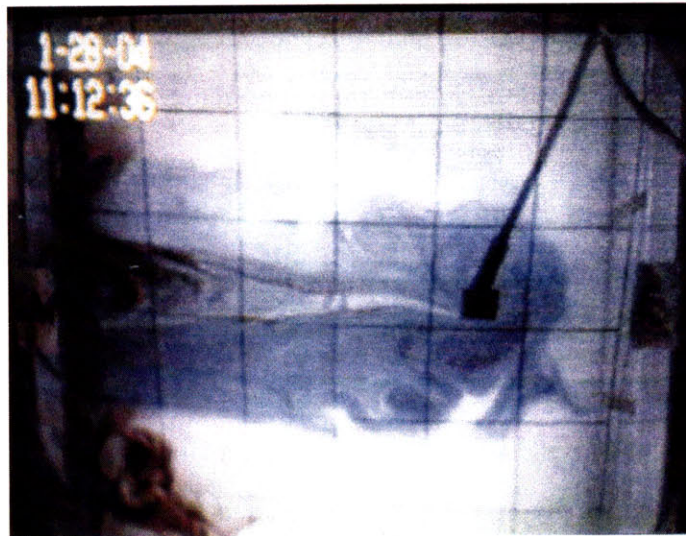Figure B-1: The laboratory set-up.

Figure B-2: A photograph of the steady state circulation pattern (visualized by colored dye) that shows a zonal jet at the latitude of the forcing flanked by a pair of counter-rotating recirculation gyres consistent with the numerical simulations.
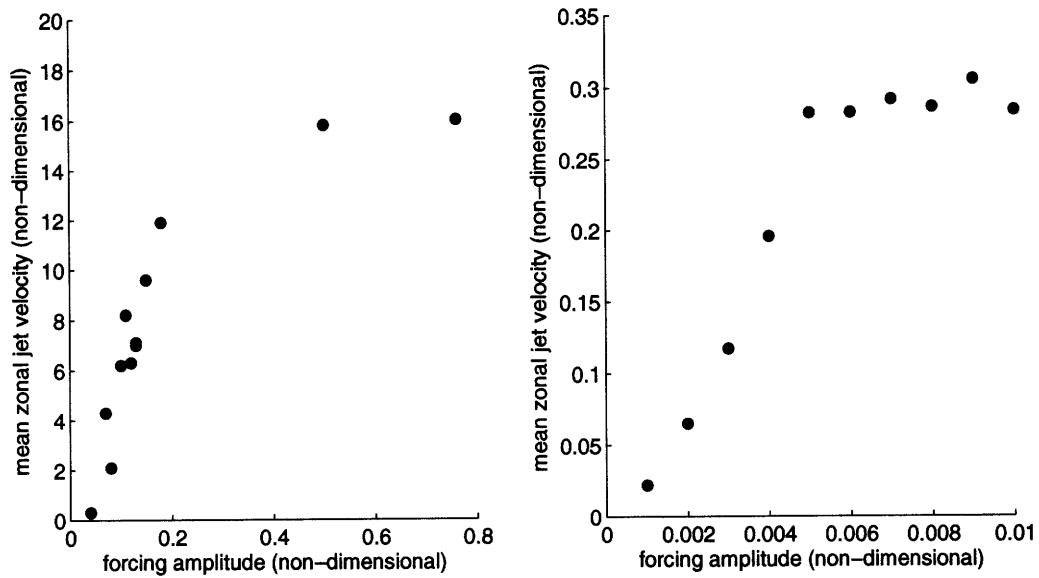
Figure B-3: The dependence of "rectification effectiveness" on the forcing amplitude in the laboratory experiments (*left*) and the numerical simulations (*right*). To allow a direct comparison, here "rectification effectiveness" is measured by the maximum eastward jet velocity (in the case of the laboratory experiments normalized by the Coriolis parameter and forcing length scale).

(virtually no turbulence in the fluid) but became insensitive to forcing strength at large Ekman velocities (excessive turbulence in the fluid) (Figure B-2 *left*). This is similar to the quadratic and saturated dependence of rectification effectiveness on forcing amplitude observed in the numerical simulations. Numerical results are represented in terms of the mean jet velocity (to make them directly comparable to the laboratory results) also in Figure B-2 (*right*). This is also consistent with the results of Whitehead (1975), who similarly saw two regimes of behavior in his experiments forced by the vertical oscillation of a circular disk.

Appendix C

The Numerical WBC Jet Model

C.1 Model Equations

The numerical model used is the one described in Jayne and Hogg (1999) modified to include two-layer dynamics. It is quasi-geostrophic, on a mid-latitude β plane, with linear bottom friction.

For barotropic runs, the model solves the fully nonlinear, barotropic quasi-geostrophic potential vorticity equation (QGPVE) in non-dimensional form:

$$\frac{\partial q}{\partial t} + J(\psi, q) = -R\,\nabla^2\psi \qquad \text{(C.1)}$$

where q, the barotropic potential vorticity, is given by:

$$q = \nabla^2\psi + \beta y \qquad \text{(C.2)}$$

Here ψ is the non-dimensional streamfunction, R is a non-dimensional bottom friction coefficient, and β is the non-dimensional β parameter, $\beta = \frac{\beta_{dim}L^2}{U}$, representing the ratio of the scales of the horizontal gradient in relative vorticity associated with the inflowing jet to that of the horizontal gradient in planetary vorticity.

In the two-layer configuration, the model solves the Burger-number weighted

237

barotropic and baroclinic equations formed from the layered version of the QGPVE ($\frac{1}{S_2}$ x layer 1 + $\frac{1}{S_1}$ x layer 2 and layer 1 - layer 2 respectively), with bottom friction acting on the lower layer vorticity, giving the barotropic vorticity prognostic equation:

$$\frac{\partial\left(\frac{1}{S_2}q_1 + \frac{1}{S_1}q_2\right)}{\partial t} + \frac{1}{S_2}J(\psi_1, q_1) + \frac{1}{S_1}J(\psi_2, q_2) = -\frac{1}{S_1}R\nabla^2\psi_2 \qquad (C.3)$$

and the baroclinic vorticity prognostic equation:

$$\frac{\partial(q_1 - q_2)}{\partial t} + J(\psi_1, q_1) - J(\psi_2, q_2) + (\frac{1}{S_1} + \frac{1}{S_2})J(\psi_1, \psi_2) = R\nabla^2\psi_2 \qquad (C.4)$$

with

$$q_n = \nabla^2\psi_n + \beta y \mp \frac{1}{S_n}(\psi_1 - \psi_2) \quad n = 1, 2 \qquad (C.5)$$

ψ_n is the non-dimensional streamfunction in the nth layer, and S_n is the nth layer Burger number, $S_n = \frac{ND_n}{fL}$, representing the ratio of the Rossby radius of deformation to the jet width in each layer, and hence the relative importance of stratification in the vertical to rotation in the horizontal.

The model is forced by the prescription of an unstable zonal jet on the western boundary. For the cases discussed here, the streamfunction at $x = 0$ in the upper layer is prescribed in the form of an error function:

$$\psi_1(x = 0, y) = A\,\mathrm{erf}(\frac{\ell}{y}) \qquad (C.6)$$

producing a Gaussian jet in zonal velocity with amplitude $\frac{2}{\sqrt{\pi}}A$ and half width ℓ. An inflow can also be prescribed in the lower layer, but given my intentions to model the WBC jet entering the open ocean from the coast, no flow was prescribed at the western boundary in the lower layer for all cases discussed.

The jet must be removed from the domain at the eastern boundary. This is done a sufficient distance downstream and in a manner that does not affect the upstream dynamics studied. In practice the jet is removed in a state of marginal barotropic stability (*i.e.* with a width given by $\ell = \left(\frac{-8Ae^{-1.5}}{\beta\sqrt{\pi}}\right)^{\frac{-1}{3}}$), but upstream results are

insensitive to outflow conditions as long as they are reasonable.

C.2   Numerical Method

Details on the numerical method can be found in Jayne and Hogg (1999). Briefly, the time-rate of change of the barotropic and baroclinic vorticity is computed from the layer streamfunction and vorticity fields and then, after solving for the barotropic and baroclinic streamfunctions from the vorticity fields, the layer streamfunctions are computed and stepped in time using a third-order Adams-Bashforth scheme (Durran, 1991). Integration in time and space is done using a scheme that is center differenced in the two spatial dimensions (an "Arakawa A-grid") and advective terms are handled using the vorticity conserving scheme of Arakawa (1966). At each time step the relative vorticity is inverted to find the streamfunction using the generalized Buneman algorithm (Adams et al., 1988).

In the domain of interest, explicit friction is chosen to be as low as possible consistent with numerical stability (a non-dimensional bottom friction coefficient of $R = 5 \times 10^{-5}$ (barotropic case) and $R = 5 \times 10^{-9}$ (baroclinic case) is used). This corresponds to a range of dimensional values for the dissipation time scale from ~ 10 years for $\beta = 0.04$ to $\sim 10^2$ years for $\beta = 0.4$ (barotropic case) and from $\sim 10^5$ years for $\beta = 0.02$ to $\sim 10^7$ years for $\beta = 0.9$ (baroclinic case).

Dissipative sponge layers, 50 grid points wide, are placed next to all lateral boundaries to absorb all waves leaving the domain. The interior dynamics are insensitive to the sponge layer width or decay constant.

The non-dimensional grid spacing is 0.2 (corresponding to a dimensional value of ~ 10 km) and the number of grid points in the domain is 751 (E-W) by 401 (N-S). With the origin at the N-S midpoint of the western boundary, this puts the eastern boundary at $x = 150$ and the northern boundary at $y = 40$ non-dimensional units. Dimensionally this corresponds to a domain of size ~ 6000 km in zonal extent and ~ 3200 km in meridional extent, of which I examine an interior domain of size ~ 3000-4000 km in zonal extent and ~ 1600 km in meridional extent.

C.3 Model Parameters

I fix the non-dimensional forcing parameters A (the jet strength) and ℓ (the jet width) ($|A| = \ell = 1.0$). Inflowing jet properties are then set by the value of non-dimensional β, which can be thought of as setting the relative size of the horizontal shear of the WBC and hence its supercriticality to barotropic instability. The WBC-typical runs discussed have a value of β of 0.05, which results in a dimensional scaling that make the inflowing jet profile consistent with the velocity and length scales of the Kuroshio jet where it separates from the coast (Figure C-1). Parameter studies discussed vary β in the range from 0.4 to 0.04 (barotropic case) and 0.9 to 0.02 (two-layer case), which correspond to (taking the scale of the jet width to be fixed) a dimensional inflowing jet strength, U, in the range of ~ 0.1 to ~ 1 m/s (barotropic case) and in the range of ~ 0.05 to ~ 1.5 m/s (two-layer case). The GS has a value for non-dimensional β in the range of 0.02-0.13 (Flierl et al., 1987).

In the case of the two-layer runs, upper and lower layer Burger numbers need also to be specified. In all cases, a value of S_1 of 1.0 and S_2 of 4.0 are used, corresponding to a thermocline depth of approximately ~ 800 m in a ~ 4000 m depth ocean, again typical of KE and GS scales. The nature of the stability explored is almost certainly dependent on the values of these parameters, although this is something not explored in this work.
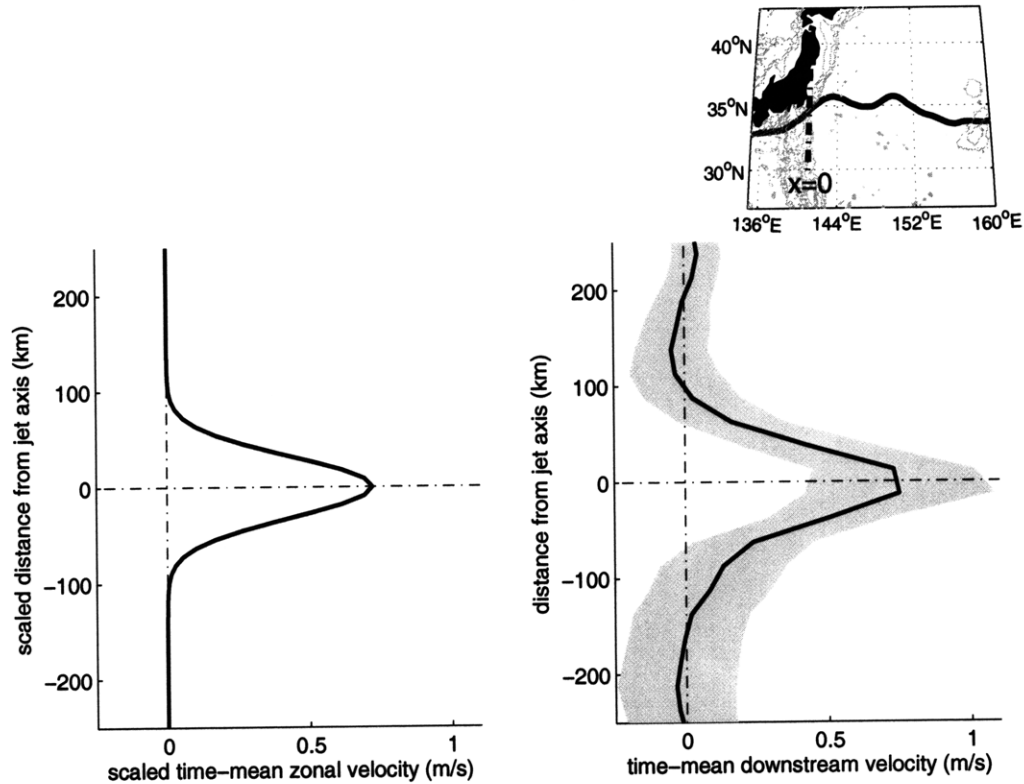
Figure C-1: Inflowing jet profile for the WBC-typical model runs dimensionalized according to the appropriate value of non-dimensional β (β=0.05 in this case) (*left*) *vs.* the synoptic mean jet profile of the Kuroshio at the point of separation from the coast (*right*). The Kuroshio profile is derived from satellite altimetry data (source: AVISO) for the period 1992-2006. The time-mean (solid black line) and the mean ± its standard deviation (gray shading) profiles are shown. The profile is taken at a longitude of 141°E (dashed line $x = 0$), corresponding to where the time-mean Kuroshio path defined by the 2.1 SSH contour (solid black line) leaves the continental slope (gray contours denote bathymetry (source: ETOPO5) with contour intervals of 2000, 4000, 6000 and 8000 m depth) (*upper right*). See Chapter 4 for a complete description of the synoptic mean calculation.

Appendix D

Observational Data Processing Procedures

D.1 Data Return

A summary of the data return for the KESS mooring array instrumentation is shown in Figure D-1. The ADCP and current meters yielded almost complete time series at all sites (>80% data return). The MMP deployment however was less successful: MMPs stopped profiling in strong currents and in the winter months when some experienced mechanical failures. This resulted in MMP data return at any given depth at any given day only 55% of the time (note that the times when the MMPs returned complete profiles was significantly less than this). It was as a consequence of the incomplete and biased records of the MMPs, that this study restricted its upper ocean analysis to satellite altimetry and ADCP data. The MMP measurements should be revisited and will be useful for case studies of individual events when there is data available.

D.2 Data Processing

Mooring measurements of velocity were corrected for mooring motion, low-passed filtered and subsampled at one day. ADCP records were processed by Luc Rainville,
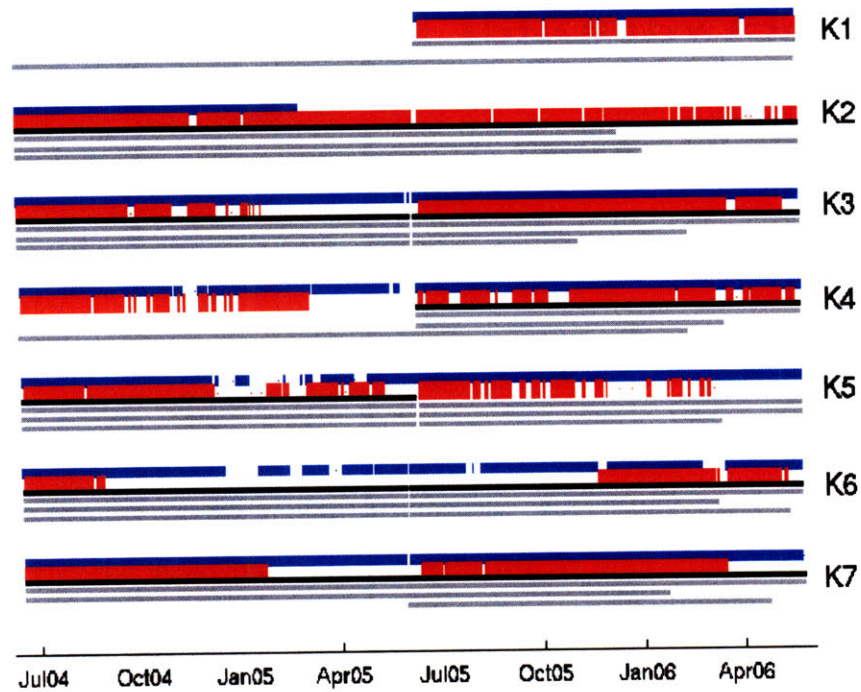
Figure D-1: A line indicates times when measurements of the various instruments on each of the moorings are good: ADCP (*blue*), MMP (*red*), VACM (*black*), and RCM-11 at 2000, 3500 and 5000 m depth (*gray*). The ADCP and current meters yielded almost complete time series at all sites (>80% data return) but MMPs returned only partial records.

VACM records by Maggie Cook, and the RCM-11 records by Nelson Hogg. RCM-11 velocities were adjusted by 10% to agree with the VACMs and Aquadopp current meters. Small gaps in the record were filled with the value of the record mean in the case of the ADCP measurements, and by a gap-filling procedure developed by Hogg that used the records at other subthermocline depths plus the vertical structure of the first EOF to reconstruct missing record values at deep levels.

D.3 Definition of a Stream-Coordinate System

To compute the stream-coordinate mean picture of the KESS mooring measurements, I take the following steps: At each time step I 1. define the location and orientation of the jet axis in the vicinity of the array; 2. calculate the distance of each mooring to the closest point on the jet axis and the orientation of the jet axis there; and 3. rotate the observed velocities based on that orientation into downstream and cross-stream components (Figure D-2). Daily values of distance and velocity are then binned according to distance from the jet axis and averaged in each bin. A bin size of 50 km width was chosen to ensure a reasonable number of observations (> 200) in each bin within ± 200 km from the jet axis (Figure D-3). The result of the procedure is a profile of mean downstream and cross-stream velocity as a function of distance from the jet axis.

To define the jet axis position and orientation in the vicinity of the mooring array, I considered three independent proxies for the jet axis location: 1. the 2.1 m SSH contour measured by satellite altimetry; 2. a proxy for thermocline depth (the 350 m depth contour of the 12° C isotherm) measured by the CPIES; and 3. the latitude where the 11° C isotherm is at 250 m depth measured by the mooring array ADCP measurements (Figure D-4). In the case of the later, because no information about the orientation of the jet axis is given by this proxy, the angle of the jet's orientation was taken to be the orientation of the velocity vector with the largest eastward zonal component measured by the array on that day. It was encouraging that all three proxies gave very consistent results for both the jet axis position (Figure 4-12), and
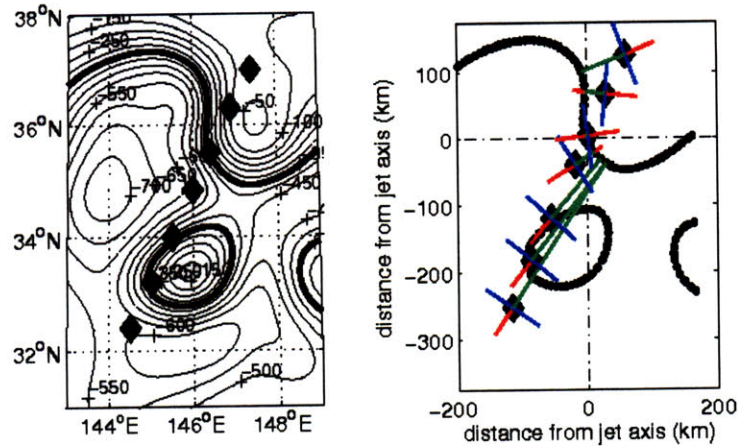
Figure D-2: An illustration of how the stream-coordinate frame is defined at each time step. The location and orientation of the jet axis in the vicinity of the mooring array is defined by a proxy (here the 350 m depth contour of the 12° C isotherm indicated by the thick black line) (*left*). Distance from each mooring to the closest point on the jet axis is calculated (green line), and velocities are rotated into downstream (blue) and cross-stream (red) components based on the jet's orientation at that point (*right*). The example shown here is the calculation for 23 December 2004.

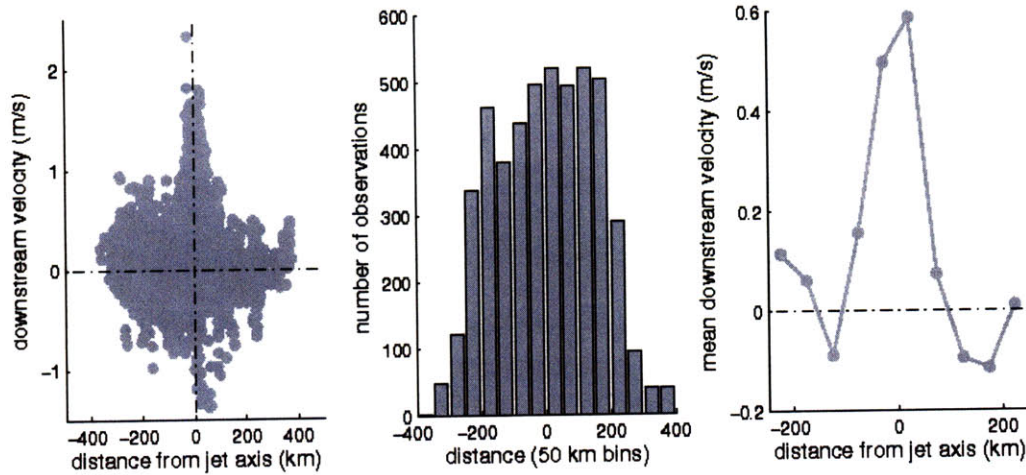Figure D-3: An illustration of the calculation of the stream-coordinate mean jet structure at 250 m depth: a superposition of all the downstream velocity measurements made by all moorings as a function of distance from the jet axis (*left*), a histogram showing the number of observations in each distance bin (*middle*), and the bin averaged downstream velocity as a function of distance from the jet axis (*right*).
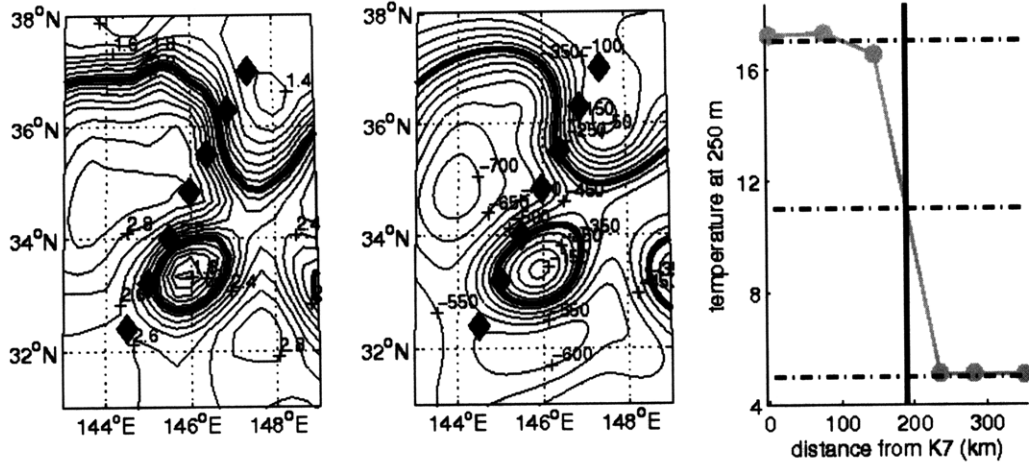
Figure D-4: An illustration of the three independent proxies for jet axis position. The 2.1 SSH contour (thick black line) in the weekly SSH field measured by satellite altimetry (*left*). The 350 m depth contour (thick black line) in the daily snapshot of the depth of the 12° C isotherm measured by the CPIES array (*middle*). The position of the 11° C isotherm (thick black line) in the daily snapshot of the cross-jet distribution of temperature at 250 m depth measured by the mooring ADCPs (*right*).

the stream-coordinate structure derived form it, including the existence of westward recirculations to both the north and south of the time-mean jet (Figure D-5). This gives confidence that each is a useful way to determine the jet axis position. Note that there are some differences between the definitions in the time-mean jet structure in terms of the jet strength/transport, in particular the jet defined using the CPIES data has significantly weaker velocity magnitudes and net transport than the jets defined using the other two proxies. Reasons for the discrepancy are not yet understood.

A stream-coordinate mean system was also defined for the WESTPAC array mooring measurements. Here neither altimetry data nor CPIES data was available, so the position of the jet axis was taken to be that given by the latitude of the 6° C isotherm at 500 m depth using the same method applied to the KESS ADCP data.

Finally, a stream-coordinate mean picture of the KE jet structure was computed using the altimetry fields from the 14-year record (Figure D-6). Like in the calculation for the mooring array observations, the stream-coordinate mean was computed by defining the jet axis by the 2.1 m SSH contour, and then computing the distance

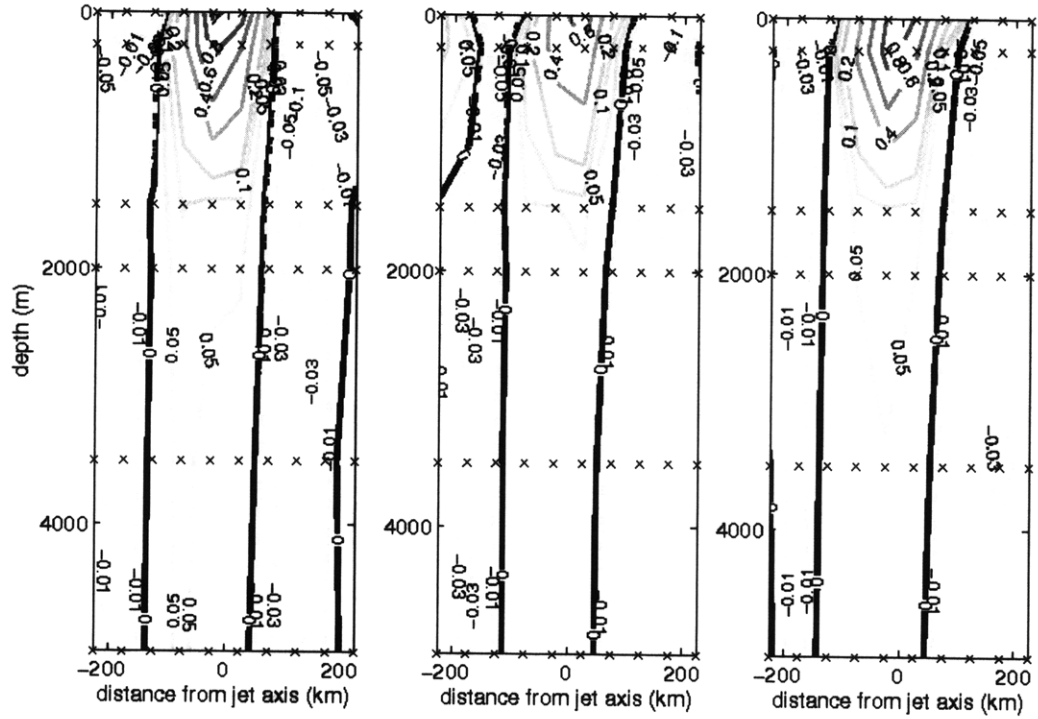Figure D-5: A comparison of the stream-coordinate description of the time-mean jet structure computed using each of the three proxies for jet axis position: using altimetry (*left*), using the CPIES data (*middle*), and using the ADCP data (*right*). As in Figure 4-10, solid contours indicate positive (downstream) values of the time-mean downstream velocity (in m/s) while dashed contours indicate negative (upstream) values.
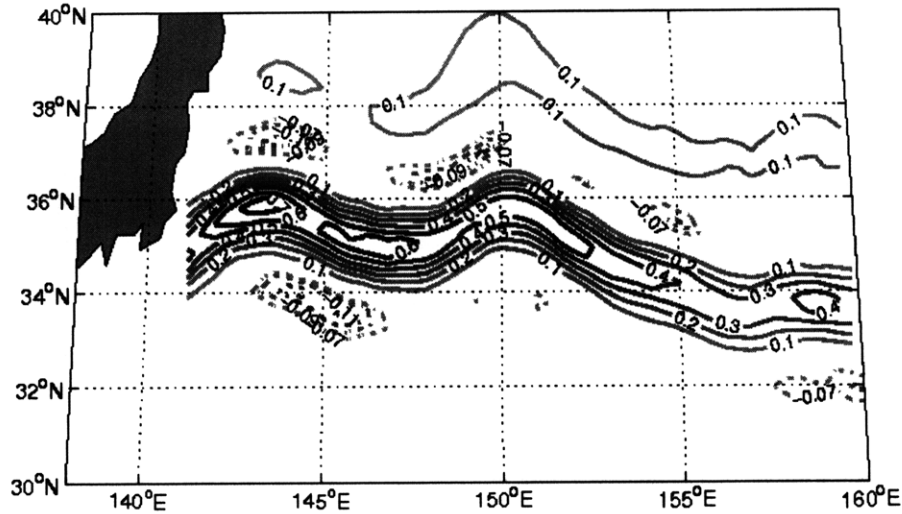
Figure D-6: The stream-coordinate description of mean KE jet structure derived from the 14-year satellite altimetry record. Contours are of the time-mean geostrophic downstream velocity (in m/s) with solid contours indicating positive (downstream) values while dashed contours indicate negative (upstream) values. For display purposes, the calculation (done in distance coordinates) has been projected back onto a latitude-longitude grid.

to the nearest point on the jet axis and rotating the velocities at each grid point. Velocities were then binned and averaged based on distance from the jet axis at each longitudinal grid point. This produced a series of meridional profiles of the time-mean stream-coordinate jet structure at each $\frac{1}{3}°$ longitude. As seen in Figure D-6, the calculation revealed a series of closed recirculation gyres flanking the jet, seemingly modulated by the quasi-stationary meanders in the time-mean jet's path.

D.4   Ring Identification and Removal

The interaction of warm core and cold core rings with the moorings were identified using a temperature criterion at 250 m depth. This was achieved by examining the cross-jet profiles of temperature as a function of distance from the jet axis as measured by the ADCPs. Large deviations from the mean temperature on the flanks

249
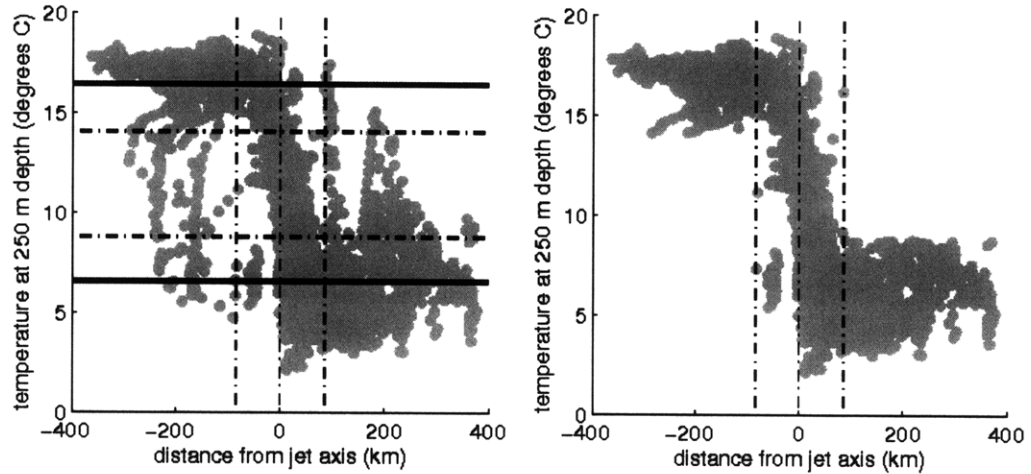
Figure D-7: Cross-jet distributions of temperature at 250 m depth as a function of distance from the jet axis for the full record (*left*) and the record with ring interactions removed (*right*). Rings were identified by times when the temperature on the flanks of the jet (outside ±85 km from the jet axis (thick dashed vertical lines)) was outside one standard deviation (thick dashed horizontal lines) from the time-mean flanking value (thick solid horizontal lines).

of the jet (specifically outside one standard deviation from the mean flanking value) were flagged as being times when rings were interacting with the array. These times were then cross-checked with altimetry snapshots. To remove times when rings were interacting with the array, measurements at all depths were removed from the record if this temperature criterion at 250 m depth was satisfied.

Appendix E

Kuroshio Extension Relevant Linear Stability Calculations

I consider KE-jet relevant linear stability calculations to compute the dynamical signatures (timescales, length scales, cross-jet distributions of Reynolds stresses) that could potentially be associated with the instability of the KE jet. By comparing observed signatures to those predicted by these calculations, is then a way to evaluate whether one sees evidence of potential jet instability. An outline of the calculations, the results, and their relation to the KESS observations are briefly presented here.

E.1 Calculations

I consider the perturbation field that arises from the linear instability of a steady, barotropically unstable jet profile in one-layer and two-layer configurations following Kamenkovich and Pedlosky (1996). I solve the linearized quasi-geostrophic potential vorticity equations for a specified basic state jet profile uniform in the along-jet direction given by $U(y) = U_0 = (1 - y^2)^3$, where U_0 is the peak jet velocity at $y = 0$ and y is the meridional direction. The solution is obtained via a numerical "shooting technique" that varies the complex phase speed until the numerical solutions in the interior match the exterior analytic solutions at the edge of the jet. In the barotropic case, this requires that the solution be continuous across the interface. In the two-

layer case, continuity of the solution and its derivative is applied. The method gives the values of the phase speed c (both real and imaginary), the meridional wavenumber l (both real and imaginary), and the eigenfunction ϕ (the y-dependent part of the perturbation stream function) inside the jet. From this, the oscillation frequency, kc_R where k is the zonal wavenumber and c_R is the real part of the complex phase speed, and the time-dependent velocity fields both inside and exterior to the jet can be computed.

I perform the calculation for a range of values of the zonal wavenumber k and examine:

- the different signatures of the sinuous *vs.* varicose mode

- the properties of the fastest growing and the most radiating mode

- the effect of tilt of the basic jet profile (of interest given the non-zonal nature of the time-mean KE jet at the KESS location as a consequence of the quasi-stationary meander)

- the effect of baroclinicity

E.2 Results and their Relation to the KESS Observations

The results of the calculations give information on the expected timescales, length scales and the variance structure of the various modes considered, and permit comparison with the KESS observations.

(a) **Time and length scales**

The expected period of oscillation $\left(\frac{2\pi}{kc_R}\right)$ and zonal wavelength $\left(\frac{2\pi}{k}\right)$ for a selection of calculations are given in Tables E.1 and E.2 for the barotropic and two-layer cases respectively. I consider both the sinuous and varicose modes for a zonal jet and one tilted 30° to the southeast (to model the orientation of the time-mean jet at

252

the KESS location). I also consider both the properties of the fastest growing mode (*i.e.* the mode with the largest growth rate kc_i where c_i is the imaginary part of the complex wave speed) and the most radiating mode (the mode with the smallest ratio of meridional wavelength to meridional decay scale given by the ratio of the imaginary and real parts of the complex meridional wavenumber, $\frac{l_i}{l_R}$).

Mode			oscillation period (days)	wavelength (km)
zonal	sinuous	fastest growing	25	300
	varicose		20	500
tilted	sinuous		20	300
	varicose		20	500
zonal	sinuous	most radiating	500	800
	varicose		400	1300
tilted	sinuous		400	800
	varicose		200	1300

Table E.1: Time and length scales for various linear instability modes: barotropic jet

Mode			oscillation period (days)	wavelength (km)
zonal	sinuous	fastest growing	5	100
	varicose		6	200
tilted	sinuous		5	100
	varicose		6	200
zonal	sinuous	most radiating	30	200
	varicose		6	2000
tilted	sinuous		50	200
	varicose		20	2000

Table E.2: Time and length scales for various linear instability modes: baroclinic jet

In general, the calculations show that the varicose modes have universally larger zonal wavelengths (smaller k) than the corresponding sinuous modes, and that the fastest-growing modes have universally shorter periods of oscillation than the corresponding most radiating modes. Adding tilt does not change the zonal wavelength, but can significantly alter the growth rate, radiating properties, period of oscillation, and the meridional wavelength and decay scales. Adding tilt tends to decrease the oscillation period, increase the meridional wavenumber (decrease the meridional

253

wavelength), and increase the meridional decay scale at least in one direction. Adding tilt also makes modes that were otherwise not strongly radiating ($\frac{l_L}{l_R} > 1$) radiating ($\frac{l_L}{l_R} < 1$) for the cases of both the sinuous and varicose modes. Finally, adding baroclinicity (here in the form of a quiescent lower layer) also can significantly alter the time and length scales, and radiation properties. Baroclinicity uniformly reduces the period and wavelength of all modes considered.

Interpreting the results in terms of their relevance to the scales of the KE allows me to highlight certain modes as consistent with the observed scales, and hence select potential candidates for the instability experienced by the KE jet. Many of the modes considered do have oscillation periods on the order of the highest frequency timescales observed as spectral peaks in the KESS velocity records. In particular, all of the fastest growing barotropic modes (sinuous and varicose, zonal and tilted) have oscillation periods that meet this criterion (*i.e.* periods on the order of 20-30 days). In general, the barotropic most radiating modes have periods much longer than those seen in observed spectra (400-500 days). Similarly, the barotropic fastest growing modes tend to have zonal wavelengths consistent with KE scales (300-500 km), while the most radiating modes tend to have unphysically long zonal wavelengths. Hence, these observations suggest a potential relevance of the barotropic fastest growing modes to the KE jet's instability, while providing an argument against the relevance of the barotropic most radiating modes.

If one considers the baroclinic results however, a different conclusion is reached. As a consequence of the uniform decrease in both oscillation period and zonal wavelength for all modes considered, with the addition of a second layer fastest growing modes now have a period that is significantly less than the 20-50 day mesoscale range, while the most radiating modes now have periods more consistent with the observed timescales. The wavelengths associated with the varicose most radiating modes remain unphysically large for KE scales, but the sinuous modes have physically reasonable length scales as well as timescales.

(b) Variance structure

I also consider the meridional structure of the solutions as potential insight about relevant instability modes can also come from the comparison of the observed cross-jet distributions of Reynolds stresses and EKE with those predicted by the linear stability calculations. Here I find that the structure of the perturbation field is not altered by whether the fastest growing or most radiating mode is considered, but rather distinguishes between the sinuous *vs.* varicose modes. Tilt plays an important role by introducing asymmetry between north and south of the jet, making both the meridional wavelength and decay scale different to the north *vs.* to the south. Changing the meridional decay scale in particular introduces asymmetry into the magnitudes of the perturbation field north *vs.* south of the jet, enhancing one flank's variance levels relative to the other.

Interpreting the results of solution structure in terms of their relevance to the KESS observations (Figure E-1) shows that the single-peaked structure of the variances observed in the upper ocean by the KESS moorings is suggestive of the sinuous mode, which is distinguishable from the varicose mode by its peak in $\overline{u'u'}$ and $\overline{EKE}$ at the jet axis as opposed to on the jet edges. This is consistent with the conclusion of the baroclinic time and length scale calculations, and offers further support for the hypothesis that the KE jet experiences a sinuous mode instability.
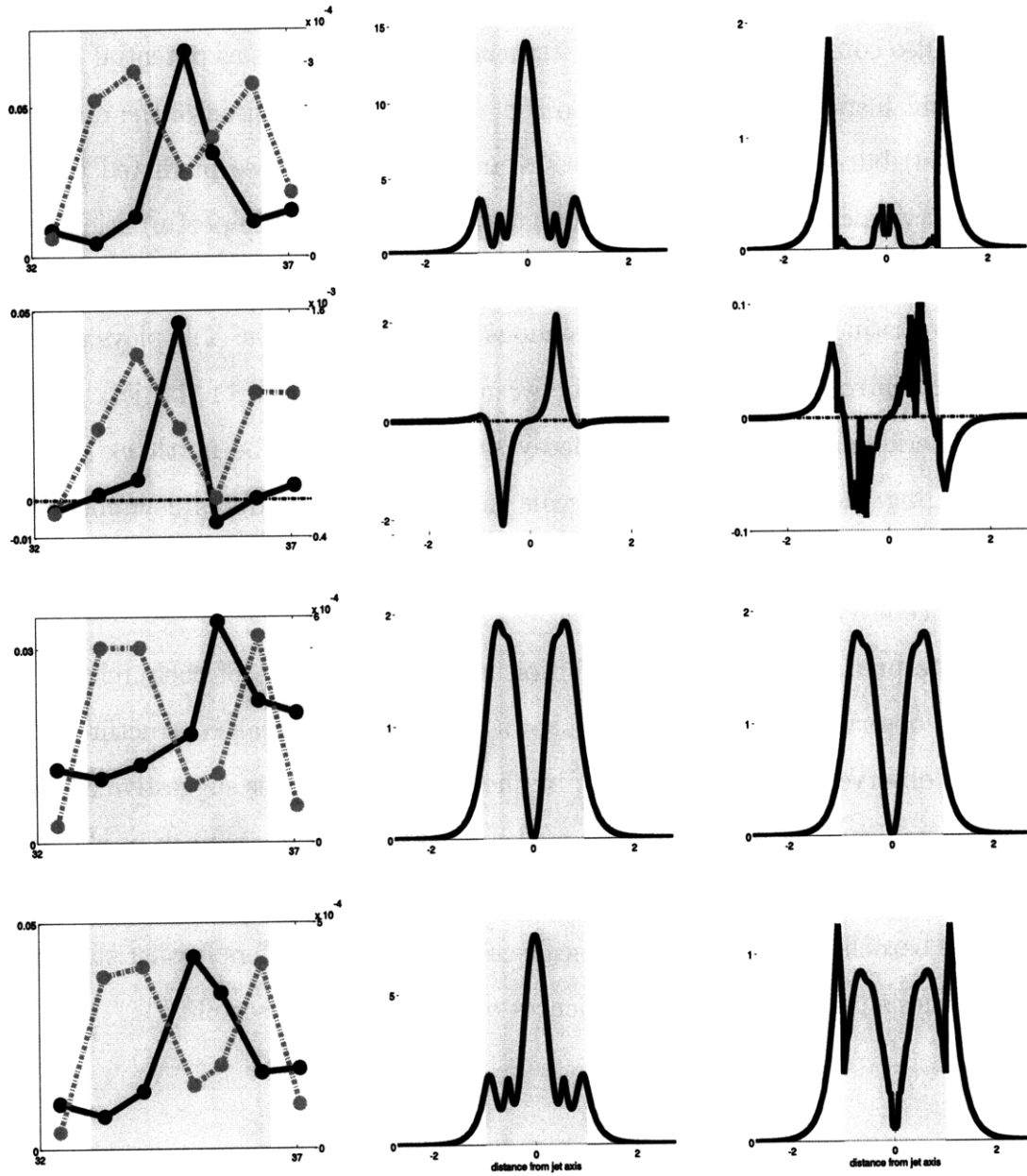
Figure E-1: The cross-jet distributions of $\overline{u'u'}$ (1st row), $\overline{u'v'}$ (2nd row), $\overline{v'v'}$ (3rd row) and $\overline{EKE} = \frac{1}{2}\left(\overline{u'u'} + \overline{v'v'}\right)$ (4th row) observed at the KESS mooring array (1st column) compared to those for the sinuous mode (2nd column) and the varicose mode (3rd column) from the linear stability calculation for a zonal, barotropic jet. As in Figure 4-24, the KESS observations are shown for the upper ocean (at 250 m depth) in black scaled by the left-hand axes, and the deep ocean (averaged over 1500 m, 2000 m, 3500 m and 5000 m depth) in gray scaled by the right-hand axes, and velocity fields were band-passed filtered in the mesoscale range (periods of 10 - 100 days) before the variances and covariances were computed to clarify the cross-jet variations. The gray shading indicates the width of the time-mean jet.

Bibliography

Adamec, D., 1998: Modulation of the seasonal signal of the Kuroshio Extension during 1994 from satellite data. *J. Geophys. Res.*, **103**, 10209–10222.

Adams, J., P. Swartztrauber, and R. Sweet, 1988: *FISHPAK: A package of FOR-TRAN subprograms for the solution of separable elliptic partial differential equations. Version 3.2.*

Andrews, D. G., and M. E. McIntyre, 1976: Planetary waves in horizontal and vertical shear: The generalized Eliassen - Palm relation and the mean zonal acceleration. *J. Atmos. Sci.*, **33**, 2031–2048.

Andrews, D. G., and M. E. McIntyre, 1978: Generalized Eliassen - Palm and Charney - Drazin theorems for waves on axisymmetric mean flows in incompressible atmospheres. *J. Atmos. Sci.*, **35**, 175–185.

Arakawa, A., 1966: Computational design for long-term numerical integration of the equations of fluid motion: Part I: Two-dimensional incompressible flow. *J. Comput. Phys.*, **1**, 119–145.

Beliakova, N., 1998: *Generation and Maintenance of Recirculations by Gulf Stream Instabilities.* Ph.D. thesis, Mass. Inst. of Technol./Woods Hole Oceanogr. Inst. Joint Program, Cambridge, Mass.

Berloff, P., 2005: On the rectification of randomly forced flows. *J. Mar. Res.*, **63**, 497–527.

Berloff, P., A. Hogg, and W. Dewar, 2007a: The turbulent oscillator: A mechanism of low-frequency variability of the wind-driven ocean gyres. *J. Phys. Oceanogr.*, **37**, 2363–2386.

Berloff, P., S. Kravtsov, W. Dewar, and J. McWilliams, 2007b: Ocean eddy dynamics in a coupled ocean-atmosphere model. *J. Phys. Oceanogr.*, **37**, 1103–1121.

Berloff, P., and J. McWilliams, 1999: Quasi-geostrophic dynamics of the western boundary current. *J. Phys. Oceanogr.*, **29**, 2607–2634.

Berloff, P., and S. Meacham, 1998: The dynamics of a simple baroclinic model of the wind-driven circulation. *J. Phys. Oceanogr.*, **28**, 361–388.

Bower, A. S., and N. G. Hogg, 1992: Evidence for barotropic wave radiation from the Gulf Stream. *J. Phys. Oceanogr.*, **22**, 42–61.

Bower, A. S., and N. G. Hogg, 1996: Structure of the Gulf Stream and its recirculations at 55°W. *J. Phys. Oceanogr.*, **26**, 1002–1022.

Bryden, H. L., 1979: Poleward heat flux and conversion of available potential energy in Drake Passage. *J. Mar. Res.*, **37**, 1–22.

Cessi, P., 1990: Recirculation and separation of boundary currents. *J. Mar. Res.*, **48**, 1–35.

Cessi, P., G. Ierley, and W. Young, 1987: A model of the inertial recirculation driven by potential vorticity anomalies. *J. Phys. Oceanogr.*, **17**, 1640–1652.

Chang, E. K. M., S. Lee, and K. L. Swanson, 2002: Storm track dynamics. *J. Climate*, **15**, 2163–2183.

Chen, S., B. Qiu, and P. Hacker, 2007: Profiling float measurements of the recirculation gyre south of the Kuroshio Extension in May-November. *J. Geophys. Res.*, **112**, C05023.

Chester, D., P. Malanotte-Rizzoli, J. Lynch, and C. Wunsch, 1994: The eddy radiation field of the Gulf Stream as measured by ocean acoustic tomography. *Geophys. Res. Lett.*, **21**, 181–184.

Cronin, M., 1996: Eddy-mean flow interaction in the Gulf Stream at 68°W: Part II: Eddy forcing on the time-mean flow. *J. Phys. Oceanogr.*, **26**, 2132–2151.

Cronin, M., and D. R. Watts, 1996: Eddy-mean flow interaction in the Gulf Stream at 68°W: Part I: Eddy energetics. *J. Phys. Oceanogr.*, **26**, 2107–2131.

Dewar, W. K., and J. M. Bane, 1989: Gulf Stream dynamics. Part II: Eddy energetics at 73°W. *J. Phys. Oceanogr.*, **19**, 1574–1587.

Ducet, N., and P. Y. Le-Traon, 2001: A comparison of surface eddy kinetic energy and Reynolds stresses in the Gulf stream and the Kuroshio current systems from merged TOPEX/Poseidon and ERS-1/2 altimetric data. *J. Geophys. Res.*, **106**, 16,603–16,622.

Durran, D. R., 1991: The third-order Adams Bashforth method: An attractive alternative to leapfrog time differencing. *Mon. Wea. Rev.*, **119**, 702–720.

Flierl, G. R., P. Malanotte-Rizzoli, and N. J. Zabusky, 1987: Nonlinear waves and coherent vortex structures in barotropic beta-plane jets. *J. Phys. Oceanogr.*, **17**, 1408–1438.

Fofonoff, N. P., 1954: Steady flow in a frictionless homogeneous ocean. *J. Mar. Res.*, **50**, 545–566.

Fofonoff, N. P., 1981: The Gulf Stream system. *Evolution in Physical Oceanography*, pp. 112–129.

Greatbatch, R. J., 1987: A model for the inertial recirculation of a gyre. *J. Mar. Res.*, **45**, 601–634.

Haidvogel, D. B., and W. R. Holland, 1978: The stability of ocean currents in eddy-resolving general circulation models. *J. Phys. Oceanogr.*, **8**, 363–392.

Haidvogel, D. B., and P. B. Rhines, 1983: Waves and circulation driven by oscillatory winds in an idealized ocean basin. *Geophys. Astrophys. Fluid Dyn.*, **25**, 1–63.

Hall, M. M., 1986: Horizontal and vertical structure of the Gulf Stream velocity field at 68°W. *J. Phys. Oceanogr.*, **16**, 1814–1828.

Hall, M. M., 1989: Velocity and transport structure of the Kuroshio Extension at 35°N, 152°E. *J. Geophys. Res.*, **94**, 14445–14459.

Hall, M. M., 1991: Energetics of the Kuroshio Extension at 35°N, 152°E. *J. Phys. Oceanogr.*, **21**, 958–975.

Hallock, Z. R., and W. J. Teague, 1995: Current meter observations during the Kuroshio Extension Regional Experiment. Tech. Rep. MR/7332-95-7592, NRL.

Hallock, Z. R., and W. J. Teague, 1996: Evidence for a North Pacific Deep western boundary current. *J. Geophys. Res.*, **101**, 6617–6624.

Hogg, N. G., 1981: Topographic waves along 70°W on the Continental Rise. *J. Mar. Res.*, **39**, 627–649.

Hogg, N. G., 1983: A note on the deep circulation of the western North Atlantic: Its nature and causes. *Deep-Sea Res.*, **30**, 945–961.

Hogg, N. G., 1985: Evidence for baroclinic instability in the Gulf Stream recirculation. *Prog. Oceanog.*, **14**, 209–229.

Hogg, N. G., 1988: Stochastic wave radiation by the Gulf Stream. *J. Phys. Oceanogr.*, **18**, 1687–1701.

Hogg, N. G., 1992: On the transport of the Gulf Stream between Cape Hatteras and the Grand Banks. *J. Mar. Res.*, **50**, 545–566.

Hogg, N. G., 1993: Toward parameterization of the eddy field near the Gulf Stream. *Deep-Sea Res.*, **40**, 2359–2376.

Hogg, N. G., 1994: Observations of Gulf Stream meander-induced disturbances. *J. Phys. Oceanogr.*, **24**, 2534–2545.

Holland, W. R., and D. B. Haidvogel, 1980: A parameter study of the mixed instability of idealized ocean currents. *Dyn. Atmos. Oceans*, **4**, 185–215.

Holland, W. R., and P. B. Rhines, 1980: An example of eddy-induced ocean circulation. *J. Phys. Oceanogr.*, **10**, 1010–1031.

Hoskins, B. J., and K. I. Hodges, 2002: New perspectives on the northern hemisphere winter storm tracks. *J. Atmos. Sci.*, **59**, 1041–1061.

Hoskins, B. J., I. N. James, and G. H. White, 1983: The shape, propagation and mean-flow interaction of large-scale weather systems. *J. Atmos. Sci.*, **40**, 1595–1612.

Howden, S. D., 2000: The three-dimensional secondary circulation in developing Gulf Stream meanders. *J. Phys. Oceanogr.*, **30**, 888–915.

Howe, P., 2008: *Stream-coordinate Structure and Variability of the Kuroshio Extension*. Master's thesis, Univ. of Rhode Island, Narragansett, R.I.

Jayne, S. R., 2006: The circulation of the North Atlantic Ocean from altimetry and the GRACE geoid. *J. Geophys. Res.*, **111**, C03005.

Jayne, S. R., and N. G. Hogg, 1999: On recirculation forced by an unstable jet. *J. Phys. Oceanogr.*, **29**, 2711–2718.

Jayne, S. R., N. G. Hogg, and P. Malanotte-Rizzoli, 1996: Recirculation gyres forced by a beta-plane jet. *J. Phys. Oceanogr.*, **26**, 492–504.

Jayne, S. R., N. G. Hogg, S. Waterman, L. Rainville, K. Donohue, R. Watts, J. McClean, M. Maltrud, B. Qiu, S. Chen, and P. Hacker, 2008: Recirculation in the Kuroshio Extension. *In preparation*.

Johns, W. E., 1988: One-dimensional baroclinically unstable waves on the Gulf Stream potential vorticity gradient near Cape Hatteras. *Dyn. Atmos. Oceans*, **11**, 323–350.

Johns, W. E., T. J. Shay, J. M. Bane, and D. R. Watts, 1995: Gulf Stream structure, transport, and recirculation near 68°W. *J. Geophys. Res.*, **100**, 817–838.

Kamenkovich, I. V., and J. Pedlosky, 1996: Radiating instability of nonzonal ocean currents. *J. Phys. Oceanogr.*, **26**, 622–643.

Kelly, K. A., M. J. Caruso, S. Singh, and B. Qui, 1996: Observations of atmosphere-ocean coupling in midlatitude western boundary currents. *J. Geophys. Res.*, **101**, 6295–6312.

Lee, T., and P. Cornillon, 1995: Temporal variation of meandering intensity and domain-wide lateral oscillations of the Gulf Stream. *J. Geophys. Res.*, **100**, 13,603–13,613.

Leeuwenburgh, O., and D. Stammer, 2002: Uncertainties in altimetry-based velocity estimates. *J. Geophys. Res.*, **107**, 3175 doi:10.1029/2001JC000937.

Luyten, J., 1977: Scales of motion in the deep Gulf Stream and across the continental rise. *J. Mar. Res.*, **35**, 49–74.

Malanotte-Rizzoli, P., N. G. Hogg, and R. E. Young, 1995: Stochastic wave radiation by the Gulf Stream: Numerical Experiments. *Deep-Sea Res.*, **42**, 389–423.

Malanottte-Rizzoli, P., 1994: *The Oceans: Physiochemical Dynamics and Resources.* Chap. The Gulf Stream System: Dynamics and Modeling. The Pennsylvania Academy of Science.

Maltrud, M. E., and J. L. McClean, 2005: An eddy-resolving global 1/10° ocean simulation. *Ocean Modelling*, **8**, 31–54.

Marshall, J., and G. Nurser, 1986: Steady, free circulation in a stratified quasi-geostrophic ocean. *J. Phys. Oceanogr.*, **16**, 1799–1813.

Maximenko, N. A., B. Bang, and H. Sasaki, 2005: Observational evidence of alternating zonal jets in the world ocean. *Geophys. Res. Lett.*, **32**, L12607.

McCalpin, J., and D. B. Haidvogel, 1996: Phenomenology of the low-frequency variability in a reduced-gravity quasi-geostrophic double-gyre model. *J. Phys. Oceanogr.*, **26**, 739–752.

McClean, J. L., P. M. Poulain, J. W. Pelton, and M. E. Maltrud, 2002: Eulerian and Lagrangian statsitics from surface drifters and a high resolution POP simulation in the North Atlantic. *J. Phys. Oceanogr.*, **32**, 2472–2491.

Meacham, S. P., 2000: Low-frequency variability in the wind-driven circulation. *J. Phys. Oceanogr.*, **30**, 269–293.

Nakamura, M., and Y. Chao, 2001: Diagnoses of an eddy-resolving Atlantic Ocean model simulation in the vicinity of the Gulf Stream. Part I: Potential vorticity. *J. Phys. Oceanogr.*, **31**, 353–378.

Nakamura, M., and Y. Chao, 2002: Diagnoses of an eddy-resolving Atlantic Ocean model simulation in the vicinity of the Gulf Stream. Part II: Eddy potential enstrophy and eddy potential vorticity fluxes. *J. Phys. Oceanogr.*, **32**, 1599–1620.

Orlanski, I., 1998: Poleward deflection of storm tracks. *J. Atmos. Sci.*, **55**, 2577–2602.

Owens, W. B., and B. A. Warren, 2001: Deep circulation in the northwest corner of the Pacific Ocean. *Deep-Sea Res.*, **48**, 959–993.

Pedlosky, J., 1963: Baroclinic instability in two-layer systems. *Tellus*, **15**, 20–25.

Pedlosky, J., 1965: A study of the time dependent ocean circulation. *J. Atmos. Sci.*, **22**, 267–272.

Pedlosky, J., 1970: Finite-amplitude baroclinic waves. *J. Atmos. Sci.*, **27**, 15–30.

Pedlosky, J., 1972: Finite-amplitude baroclinic wave packets. *J. Atmos. Sci.*, **29**, 680–686.

Pedlosky, J., 1976: Finite-amplitude baroclinic disturbances in downstream varying currents. *J. Phys. Oceanogr.*, **6**, 335–344.

Phillips, H. E., and S. R. Rintoul, 2000: Eddy variability and energetics from direct current measurements in the Antarctic Circumpolar Current south of Australia. *J. Phys. Oceanogr.*, **30**, 3050–3076.

Plumb, R. A., and R. Ferrari, 2005: Transformed Eulerian-Mean theory. Part I: Nonquasigeostrophic theory for eddies on a zonal-mean flow. *J. Phys. Oceanogr.*, **35**, 165–174.

Primeau, F. W., 1998: Multiple equilibria of a double-gyre ocean model with super-slip boundary conditions. *J. Phys. Oceanogr.*, **28**, 2130–2147.

Qui, B., 1995: Variability and energetics of the Kuroshio Extension and its recirculation gyre from the first two-years of TOPEX data. *J. Phys. Oceanogr.*, **25**, 1827–1842.

Qui, B., 2000: Interannual variability of the Kuroshio Extension system and its impact on the wintertime SST field. *J. Phys. Oceanogr.*, **30**, 1486–1502.

Qui, B., 2002: The Kuroshio Extension System: Its large-scale variability and role in the midlatitude ocean-atmosphere interaction. *J. Oceangr.*, **58**, 57–75.

Qui, B., and S. Chen, 2005: Variability of the Kuroshio Extension jet, recirculation gyre and mesoscale eddies on decadal timescales. *J. Phys. Oceanogr.*, **35**, 2090–2103.

Reverdin, G., P. Niller, and H. Valdimarsson, 2003: North Atlantic Ocean surface currents. *J. Geophys. Res.*, **108**, 3002 doi:10.1029/2001JC001020.

Rhines, P. B., 1975: Waves and turbulence on a beta-plane. *J. Fluid Mech.*, **69**, 417–443.

Rhines, P. B., 1977: *The Sea.* Vol. 6, Chap. The dynamics of unsteady currents, pp. 189–318. John Wiley, New York.

Rhines, P. B., and W. R. Holland, 1979: A theoretical discussion of eddy-driven mean flows. *Dyn. Atmos. Oceans*, **3**, 289–325.

Richards, K. J., N. A. Maximenko, F. O. Bryan, and H. Sasaki, 2006: Zonal jets in the Pacific Ocean. *Geophys. Res. Lett.*, **33**, L03605.

Richardson, P. L., 1985: Average velocity and transport of the Gulf Stream near 55°W. *J. Mar. Res.*, **43**, 83–111.

Rossby, H. T., 1987: On the energetics of the Gulf Stream at 73°W. *J. Mar. Res.*, **45**, 59–82.

Savidge, D. K., and J. M. Bane, 1999a: Cyclogenesis in the deep ocean beneath the Gulf Stream: Part I. Description. *J. Geophys. Res.*, **104**, 18111–18126.

Savidge, D. K., and J. M. Bane, 1999b: Cyclogenesis in the deep ocean beneath the Gulf Stream: Part II. Dynamics. *J. Geophys. Res.*, **104**, 18127–18140.

Schmitz, W. J., 1980: Weakly depth-dependent segments of the North Atlantic circulation. *J. Mar. Res.*, **38**, 111–133.

Schmitz, W. J., 1984: Observations of the vertical structure of the eddy field in the Kuroshio Extension. *J. Geophys. Res.*, **89**, 6355–6364.

Schmitz, W. J., 1987: Observations of new large scale and stable abyssal currents at midlatitudes along 165°E. *J. Phys. Oceanogr.*, **17**, 1309–1315.

Schmitz, W. J., 1988: Exploration of the eddy field in the midlatitude North Pacific. *J. Phys. Oceanogr.*, **18**, 459–468.

Schmitz, W. J., and M. S. McCartney, 1993: On the North Atlantic circulation. *Rev. Geophys.*, **31**, 29–49.

Schmitz, W. J., P. P. Niiler, R. L. Bernstein, and W. R. Holland, 1982: Recent long-term moored instrument observations in the western North Pacific. *J. Geophys. Res.*, **87**, 9425–9440.

Shay, T. J., J. M. Bane, D. R. Watts, and K. L. Tracey, 1995: Gulf Stream flow field and events near 68°W. *J. Geophys. Res.*, **100**, 22565–22589.

Sheremet, V. A., 2002: Inertial gyre driven by a zonal jet emerging from the western boundary. *J. Phys. Oceanogr.*, **32**, 2361–2378.

Smith, R. D., M. E. Maltrud, F. O. Bryan, and M. W. Hecht, 2000: Numerical simulation of the North Atlantic Ocean at 1/10°. *J. Phys. Oceanogr.*, **30**, 1532–1561.

Spall, M. A., 1994: Wave-induced abyssal recirculations. *J. Mar. Res.*, **52**, 1051–1080.

Spall, M. A., 1996: Dynamics of the Gulf Stream/deep western boundary current crossover. Part II: Low-frequency internal oscillations. *J. Phys. Oceanogr.*, **26**, 2169–2182.

Stammer, D., R. Tokmakian, A. Semtner, and C. Wunsch, 1996: How well does a 1/4° global circulation model simulate large-scale oceanic observations? *J. Geophys. Res.*, **101**, 25779–25811.

Starr, V. P., 1968: *Physics of Negative Viscosity Phenomena.* McGraw-Hill Book Co.

Teague, W. J., Z. R. Hallock, G. A. Jacobs, and J. L. Mitchell, 1990: Kuroshio sea surface height fluctuations observed simultaneously with inverted echo sounders and TOPEX/POSEIDON. *J. Geophys. Res.*, **100**, 24987–24994.

Thompson, R. O. R. Y., 1971: Why there is an intense eastward current in the North Atlantic but not in the South Atlantic. *J. Phys. Oceanogr.*, **1**, 235–237.

Thompson, R. O. R. Y., 1977: Observations of Rossby waves near Site D. *Prog. Oceanog.*, **7**, 1–28.

Thompson, R. O. R. Y., 1978: Reynolds stress and deep counter-currents near the Gulf Stream. *J. Mar. Res.*, **36**, 611–615.

Veronis, G., 1966: Wind-driven circulation - Part 2: Numerical solutions of the non-linear problem. *Deep-Sea Res.*, **13**, 31–55.

Watts, D. R., X. Qian, and K. L. Tracey, 2001: Mapping abyssal current and pressure fields under the meandering Gulf Stream. *J. Atmos. Oceanic Technol.*, **18**, 1052–1067.

Watts, D. R., K. L. Tracey, J. M. Bane, and T. J. Shay, 1995: Gulf Stream path and thermocline structure near 74°W and 68°W. *J. Geophys. Res.*, **100**, 18,291–18,312.

Whitehead, J., 1975: Mean flow driven by circulation on a beta-plane. *Tellus*, **27**, 358–364.

Williams, G. P., 1978: Planetary circulations: 2. The Jovian quasi-geostrophic regime. *J. Atmos. Sci.*, **36**, 932–968.

Williams, R. G., C. Wilson, and C. W. Hughes, 2007: Ocean and atmosphere storm tracks: The role of eddy forcing. *J. Phys. Oceanogr.*, **37**, 2267–2289.

Worthington, L. V., 1976: On the North Atlantic Circulation. The Johns Hopkins Oceanographic Studies, Vol. 6, 110 pp.

Wyrtki, K., L. Magaard, and J. Hagar, 1976: Eddy energy in the oceans. *J. Geophys. Res.*, **81**, 2631–2646.

Xue, H., 1991: *Stability Analyses of the Gulf Stream Front Using the Linearized Primitive Equations.* Ph.D. thesis, Princeton University, Princeton, NJ.